

BIOMASS-DERIVED CELLULOSE NANOFORMS AND THEIR FUNCTIONAL HYBRIDS

by

HASNA M A

AcSIR Registration No: 10CC18J39005

A thesis submitted to the
Academy of Scientific & Innovative Research
for the award of the degree of
DOCTOR OF PHILOSOPHY
in
SCIENCE

Under the supervision of

Dr. Saju Pillai



CSIR-National Institute for Interdisciplinary Science and Technology (NIIST)

Thiruvananthapuram -695 019



Academy of Scientific and Innovative Research

AcSIR Headquarters, CSIR-HRDC campus

Sector 19, Kamla Nehru Nagar,

Ghaziabad, U.P. – 201 002, India

July 2023

Dedicated to the Powerful

Motherhood

My Mum...



सी एस आई आर -राष्ट्रीय अंतर्विषयी विज्ञान तथा प्रौद्योगिकी संस्थान
वैज्ञानिक तथा औद्योगिक अनुसन्धान परिषद्, भारत सरकार
इंडस्ट्रियल इस्टेट पी.ओ, पाप्पनमकोड, तिरुवनंतपुरम - 695 019, केरल, भारत
CSIR-NATIONAL INSTITUTE FOR INTERDISCIPLINARY SCIENCE AND TECHNOLOGY
Council of Scientific and Industrial Research, Govt. of India
Industrial Estate PO, Pappanamcode, Thiruvananthapuram 695 019, Kerala, INDIA



डॉ. सजु पिल्लै

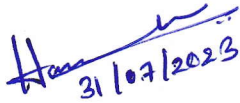
प्रमुख वैज्ञानिक एवं सह प्राध्यापक
पदार्थ विज्ञान तथा प्रौद्योगिकी प्रभाग

Dr. Saju Pillai

Principal Scientist & Associate Professor
Materials Science & Technology Division

CERTIFICATE

This is to certify that the work incorporated in this Ph.D. thesis entitled, "*Biomass-derived Cellulose Nanoforms and their Functional Hybrids*" submitted by *Ms. Hasna M A* to the Academy of Scientific and Innovative Research (AcSIR) in fulfillment of the requirements for the award of the Degree of *Doctor of Philosophy in Science*, embodies original research work carried-out by the student. We, further certify that this work has not been submitted to any other University or Institution in part or full for the award of any degree or diploma. Research materials obtained from other sources and used in this research work has been duly acknowledged in the thesis. Images, illustrations, figures, tables etc., used in the thesis from other sources, have also been duly cited and acknowledged.


31/07/2023

Hasna M A
(Candidate)


31/07/2023

Dr. Saju Pillai
(Thesis Supervisor)

STATEMENTS OF ACADEMIC INTEGRITY

I, **Hasna M A**, a Ph.D. student of the Academy of Scientific and Innovative Research (AcSIR) with Registration No.10CC18J39005, hereby undertake that the thesis entitled “**Biomass-derived Cellulose Nanoforms and their Functional Hybrids**” has been prepared by me and that the document reports original work carried out by me and is free of any plagiarism in compliance with the UGC Regulations on “*Promotion of Academic Integrity and Prevention of Plagiarism in Higher Educational Institutions (2018)*” and the CSIR Guidelines for “*Ethics in Research and in Governance (2020)*”.

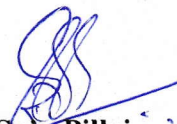


Hasna M A

31/07/2023

Thiruvananthapuram

It is hereby certified that the work done by the student, under our supervision, is plagiarism-free in accordance with the UGC Regulations on “*Promotion of Academic Integrity and Prevention of Plagiarism in Higher Educational Institutions (2018)*” and the CSIR Guidelines for “*Ethics in Research and in Governance (2020)*”.



Dr. Saju Pillai

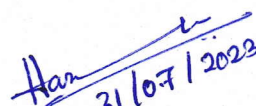
31/07/2023

Thiruvananthapuram

DECLARATION

I, **Hasna M A** bearing AcSIR Registration No. **10CC18J39005**, declare:

- (a) that my thesis entitled, “**Biomass-derived Cellulose Nanoforms and their Functional Hybrids**” is plagiarism free in accordance with the UGC Regulations on “*Promotion of Academic Integrity and Prevention of Plagiarism in Higher Educational Institutions (2018)*” and the CSIR Guidelines for “*Ethics in Research and in Governance (2020)*”.
- (b) that I would be solely held responsible if any plagiarized content in my thesis is detected, which is violative of the UGC regulations 2018.


31/07/2023
Hasna M A

Thiruvananthapuram

ACKNOWLEDGEMENTS

With great pleasure, I extend my profound gratitude and indebtedness to Dr. Saju Pillai, my thesis supervisor, for suggesting the research problem and reassuring my potential. His valuable support, encouragement, and guidance throughout the research period have led to the successful completion of this work.

I am grateful to Dr. C. Anandharamakrishnan and Dr. A. Ajayaghosh, the present and former directors of CSIR-NIIST, for providing the necessary facilities and infrastructure for carrying out the research work.

I wish to express my gratitude to Dr. S. Ananthakumar, Dr. M. Ravi, Dr. S. Savithri, Dr. Harikrishna Bhatt, and Dr. P. Prabhakar Rao, the present and former Heads of the Materials Science and Technology Division, for their valuable help in various academic and official matters.

I extend my sincere gratitude to the current and former AcSIR coordinators, Dr. Karunakaran Venugopal, Dr. C.H. Suresh, and Dr. R. Luxmi Varma, for their help during my admission and other academic activities.

I want to acknowledge my DAC members, Dr. U. S. Hareesh, Dr. Kaustabh Kumar Maiti, and Dr. T.P.D. Rajan, for their valuable comments and suggestions.

A special word of thanks to Dr. M. Padmanabhan (Department of Chemistry, Amrita University), Dr. Sreekumar Kurungot (CSIR-NCL, Pune), Dr. Sujith Kumar Ghosh (Department of Chemistry, Assam University), Dr. Achu Chandran, & Dr. Rajeev K Sukumaran (CSIR-NIIST) for the fruitful Research collaborations. I take this opportunity to express my gratitude towards Dr. Manoj Raama Varma for his constant encouragement and personal support during the entire Ph.D. tenure.

My gratitude extends to all the scientists and technical staff of CSIR-NIIST who rendered their valuable and timely help, particularly Mr. Peer Muhammed, Mr. Harish Raj, and Mr. Kiran Mohan, in sample characterization. I am also thankful to all the office and library staff at NIIST for their kind cooperation.

I am thankful to the Academy of Science and Innovative Research (AcSIR), Ghaziabad, India, for all the academic proceedings. I am obliged to UGC for the financial support to carry out this work. Special thanks to Mr. Ribin Johnson for all the timely help getting the fellowship.

I would like to express my heartfelt thanks to my senior, Dr. Aswathy Babu, for her constant support, fruitful discussions, and advice. I take this opportunity to thank all my research collaborators, including Mr. Haris Vargese, Mr. Abhilash T. K., Mr. Anas S., Mr. Adarsh V., Dr. Shilpa N., and Mr. Sudip Kumar Pal.

I thank my present and former lab mates, Dr. Parvathy R Chandran, Dr. Vipin V. V, Dr. Sumina N. B, Dr. Nabeela Kallayi, Dr. Reny Thankam Thomas, Dr. Raji V. Nair, Mr. Animesh M. R., Ms. Meghna Mary Thomas, Ms. Gopika Preethikumar, Ms. Silpa T.S, Ms. Adithya A.V, Mr. Rahul Raj, Ms. Lekshmi L, Mr. Heitor H G Matchumua, Mr. Unnikrishnan, Ms. Swetha Shaji, Mr. Akhil A. B., Mr. Jishnu, Mr. Sonu and Ms. Dheekshitha for their help and support.

I am thankful to my MSc. project students, Ms. Faseela, Ms. Anna, Ms. Sreelakshmi, Ms. Arathy, Ms. Ardra V.S., and Ms. Adrija De, who worked with me during my research period.

I cherish the time spent with my comrades Dr. Aswathi K and Ms. Bhavya A. S for their help and support during the days at NIIST. You are my secret ears! Who hears me even if I am silent. Thank you for making my half-decade more memorable.

I extend my love to Ms. Suja P., Ms. Nishna N., and Dr. P.P. Jasnamol for their support and unforgettable fun. I would like to thank my juniors Ms. Shamili C. Das, Ms. Devikrishna K. S., Ms. Anagha Ramesh, Ms. Bhavya V., Ms. Athira B.S, Ms. Syamini J, Ms. Jefin P Thomas for changing the silent hostel corridors to noisy with perfect entertainment.

I warmly thank all my magnetism lab friends for their support and companionship. I would like to extend my thanks to all my friends at the electronic materials lab, including Mr. Adarsh S.Pillai, Mr. Sumith S., Mr. Mahesh M. L, and Mr. Christan Sam, for the joyful amity.

I thank all friends and juniors at CSTD, specially Ms. Indhulekha M, Ms. Pooja Ghosh, Mr. Rahul P, Ms. Drishya Elizebath K, and Mr. Manikandan M for their help and support, primarily for AFM and electrospinning.

We could not even say thanks to some people in our life especially loved ones, my Mum, Papa, my better half, Thasni and Anu, for their unconditional love. Without their support and encouragement, I would not have reached this stage of my life. I am also indebted to my uncles, Mr. Kabeer, and Late. Mr. Sageer for their constant support and care at each stage of my life. Anyone can't replace your vacancy... Miss you... Love to heaven!!

Moreover, I thank and proud of myself for enduring all personal & carrier hardships and keeping me in spirit and happy with a piece of chocolate and a good sleep. I like to smile... smile forever.

Last but not least, I am incredibly thankful to Almighty for giving me the invisible support and strength to overcome all the struggles without losing hope throughout my life.

Thank you.....

Hasna M A

CONTENTS

	Page
CERTIFICATE	i
STATEMENT OF ACADEMIC INTEGRITY	iii
DECLARATION	v
ACKNOWLEDGEMENTS	vii
CONTENTS	xi
LIST OF ABBREVIATIONS	xvi
LIST OF FIGURES	xix
LIST OF TABLES	xxvi
PREFACE	xxix

CHAPTER 1 Introduction	1-32
-------------------------------	-------------

ABSTRACT	3
1.1. CELLULOSE	3
1.2. NANOCELLULOSE	5
1.2.1. Cellulose Nanocrystals (CNCs)	6
1.2.2. Cellulose Nanofibers (CNFs)	7
1.2.3. Bacterial Nanocellulose (BNC)	7
1.3. EXTRACTION OF NANOCELLULOSE: SOURCES AND METHODS	8
1.3.1 Mechanical Treatments	10
1.3.1.1 High-Pressure Homogenization (HPH)	10
1.3.1.2 Grinding	11
1.3.1.3 Microfluidization	11
1.3.1.4 Cryo-crushing	11

1.3.1.5.	Electrospinning	12
1.3.2.	Chemo-mechanical Treatments	13
1.3.2.1.	Acid Hydrolysis	14
1.3.2.2.	TEMPO-mediated Oxidation	15
1.3.3.	Enzymatic-mechanical Treatments	17
1.4.	PROPERTIES DEPENDENT APPLICATIONS OF NCs	17
1.4.1.	As Template/matrix for Stable Metal Nanoparticle Colloids	18
1.4.2.	Aerogels	20
1.5.	OBJECTIVES	21
1.6	REFERENCES	22

CHAPTER 2 Banana Fibers as Efficient Source for the Acid-free Synthesis of Cellulose Nanocrystals 33-56

ABSTRACT	35
2.1. INTRODUCTION	35
2.2. EXPERIMENTAL SECTION	37
2.2.1. Materials	37
2.2.2. Extraction of Holocellulose	38
2.2.3. Preparation of TEMPO-oxidized Nanocellulose (TNC)	38
2.2.4. Ultrasonication as Mechanical Disintegration	39
2.2.5. Characterizations of TNC	39
2.3. RESULTS AND DISCUSSION	40
2.3.1. Optimization of Ultrasonication Time	40
2.3.2. Effect of Ultrasonication on Degree of Oxidation	44
2.3.3. Comparison of TCNC Obtained from Different Plant Sources	48
2.4. CONCLUSIONS	53
2.5. REFERENCES	53

CHAPTER 3	Assembled Au@Ag NPs on Cellulose Nanocrystals with Tailored Plasmonic Nanogaps	57-93
------------------	---	--------------

ABSTRACT	59	
3.1.	INTRODUCTION	59
3.2.	EXPERIMENTAL SECTION	63
3.2.1.	Materials	63
3.2.2.	Synthesis of TCNC Capped Au NPs Seed (TCNC-Au NPs)	63
3.2.3.	Synthesis of TCNC Stabilized Au@Ag NPs (TCNC-Au@Ag NPs)	63
3.2.4.	SERS Sample Preparation	64
3.2.5.	Catalytic Reduction of 4-Nitrophenol (4-NP)	64
3.2.6.	Characterization Methods	65
3.3.	RESULTS AND DISCUSSION	65
3.3.1.	Morphology and Optical Properties of TCNC Templated Au and Au@Ag Nanostructures	65
3.3.2.	SERS Response	74
3.3.3.	Finite Element Modelling (FEM) Studies	81
3.3.4.	Catalytic Reduction of 4-Nitrophenol	84
3.4.	CONCLUSIONS	87
3.5.	REFERENCES	87

CHAPTER 4	CNC-directed, Stable Flower-like Au@Pd Nanostructures	95-127
------------------	--	---------------

ABSTRACT	97	
4.1.	INTRODUCTION	97
4.2.	EXPERIMENTAL SECTION	100
4.2.1.	Materials	100

4.2.2.	Synthesis of TCNC Bounded Au NPs Seed (TCNC-Au NPs)	101
4.2.3.	Synthesis of TCNC Bounded Au@Pd Nanoflowers (TCNC-Au@Pd NFs)	101
4.2.4.	Synthesis of Heterogeneous TCNC-Au@Pd Decorated NH ₂ -RGO Catalyst	101
4.2.5.	Electrocatalytic Oxygen Reduction Reaction (ORR)	102
4.2.6.	4-Nitrophenol (4-NP) Catalytic Reduction	102
4.2.7.	Characterization Methods	103
4.3.	RESULTS AND DISCUSSION	103
4.3.1.	TCNC Bounded Au@Pd Nanoflowers	103
4.3.2.	Role of TCNC in Morphology Evolution of TCNC-Au@Pd Nanoflowers	113
4.3.3.	Catalytic Performance of TCNC-Au@Pd NFs	115
4.3.4.	Oxygen Reduction Reaction in Alkaline Medium (ORR)	116
4.3.5.	Catalytic 4-Nitrophenol (4-NP) Reduction	118
4.4.	CONCLUSIONS	122
4.5.	REFERENCES	122

CHAPTER 5	Reversible Thermochromic Cobalt(II) Coordinated Malonic Acid-Nanocellulose Hybrid Aerogels	129-157
------------------	---	----------------

ABSTRACT	131
5.1. INTRODUCTION	131
5.2. EXPERIMENTAL SECTION	134
5.2.1. Materials	134
5.2.2. Preparation of TEMPO-oxidised Cellulose Nanofibers (TCNF)	134

5.2.3.	Synthesis of Cobalt(II) Induced Malonic acid-Nanocellulose Hybrid Aerogels (CoMNC)	135
5.2.4.	Physical Characterization of Aerogels	135
5.2.5.	Formulation of Humidity Sensor Android Application	136
5.3.	RESULTS AND DISCUSSION	136
5.3.1.	Cobalt(II) Coordinated Malonic acid-Nanocellulose Hybrid Aerogels	136
5.3.2.	Mechanism of Gel Formation	146
5.3.3.	Humidity Absorption of Aerogels	148
5.3.4.	Reversible Thermochromism	149
5.3.5.	Development of Humidity Sensor	150
5.3.6.	Development of an Android Mobile Application for Humidity Sensing Based on CoMNC Aerogels	150
5.4.	CONCLUSIONS	153
5.5.	REFERENCES	154
<hr/>		
CHAPTER 6	Summary and Future Perspectives	159-163
<hr/>		
6.1.	SUMMARY OF THE THESIS	161
6.2.	FUTURE PERSPECTIVES	163
<hr/>		
	ABSTRACT OF THESIS	165
	LIST OF PUBLICATIONS	167
	LIST OF CONFERENCE PRESENTATIONS	169
	ATTACHMENT OF PUBLICATIONS	

LIST OF ABBREVIATIONS

CF	Cellulose fibers
NC	Nanocellulose
RCNF	Reduced cellulose nanofibers
CMC	Cellulose microcrystals
CNCs	Cellulose nanocrystals
CNFs	Cellulose nanofibers
CNN	Cellulose nanonetworks
BNC	Bacterial nanocellulose
TEMPO	2,2,6,6-tetramethylpiperidine 1-oxyl radical
TNC	TEMPO-oxidized nanocellulose
TCNC	TEMPO-oxidised cellulose nanocrystals
TCNF	TEMPO-oxidised cellulose nanofibers
TCNC-A	TEMPO-oxidised cellulose nanocrystals from Areca nut leaf sheath
TCNC-W	TEMPO-oxidised cellulose nanocrystals from Mahogany wood
TCNC-B	TEMPO-oxidised cellulose nanocrystals from banana pseudo-stem fibers
HPH	High-pressure homogenization
wt%	Weight percentage
DI	Deionized
DMF	Dimethylformamide
DMA	Dimethylacetamide
DCM	Dichloromethane
BSA	Bovine serum albumin
4-NP	4-Nitrophenol
4-AP	4-Aminophenol
CTAC	Cetyltrimethylammonium chloride
CTAB	Cetyltrimethylammonium bromide

PVP	Polyvinylpyrrolidone
TSC	Trisodium citrate tribasic dihydrate
AA	L-ascorbic acid
MG	Malachite green
MB	Methylene blue
IPA	Iso-propyl alcohol
NPs	Nanoparticles
Au@Ag NPs	Gold-silver core-shell nanoparticles
NWs	Nanowires
NFs	Nanoflowers
Au@Pd NFs	Gold-palladium core-shell nanoflowers
RGO	Reduced graphene oxide
NH₂-RGO	Amino-functionalized reduced graphene oxide
CNT	Carbon nanotube
MOFs	Metal-organic frameworks
MA	Malonic acid
CoMNC	Cobalt(II) induced malonic acid-nanocellulose aerogels
CoNC	Cobalt(II) induced nanocellulose aerogels
Ref.	Reference
3D	Three-dimensional
CI	Crystallinity Index
I₂₀₀	Intensity of diffraction peak at $2\theta = 22.5^\circ$
I_{am}	Intensity diffraction peak from the amorphous region
λ_{max}	Absorption maxima
ICAR-NRCB	Indian Council of Agricultural Research -National Research Centre for Banana
IDEs	Integrated development environment
PDI	Polydispersity Index
SERS	Surface Enhanced Raman Spectra
LSPR	Localized Surface Plasmon Resonance
AEF	Analytical Enhancement Factor

LOD	Limit of detection
FEM	Finite Element Modelling
FTIR	Fourier Transform Infrared spectroscopy
WAXS	Wide-angle X-ray Scattering
AFM	Atomic Force Microscope
TEM	Transmission Electron Microscope
SEM	Scanning Electron Microscope
HR-TEM	High-resolution Transmission Electron Microscope
SAED	Selected Area Electron Diffraction
FFT	Fast Fourier Transform
DLS	Dynamic Light Scattering
XRD	X-ray diffractometer
XPS	X-ray Photoelectron Spectroscopy
ICP-MS	Inductively Coupled Plasma Mass Spectrometry
ORR	Oxygen Reduction Reaction
LSV	Linear Sweep Voltammetry
RDE	Rotating Disc Electrode
RHE	Reversible Hydrogen Electrode
E_{1/2}	Half-wave potential
BET	Brunauer-Emmett-Teller
BJH	Barrett-Joyner-Halenda
TGA	Thermogravimetric analysis

LIST OF FIGURES

Figure No:	Title of Figure	Page No
CHAPTER 1		
Figure 1.1.	The hierarchical structure of cellulose from Plant cell wall to monomer.	4
Figure 1.2.	Morphology of (a) cellulose nanocrystals (CNCs), (b) cellulose nanofibers (CNFs), and (c) bacterial nanocellulose (BNC).	5
Figure 1.3.	Morphology and fiber diameter of electrospun (a) cellulose acetate fibers and (b) deacetylated cellulose fibers.	13
Figure 1.4.	Preparation of CNC by regioselective acid hydrolysis of cellulose microfibril.	15
Figure 1.5.	Mechanism of TEMPO- mediated oxidation of cellulose.	16
CHAPTER 2		
Figure 2.1.	(a) FTIR spectra and (b) WAXS patterns of TNC at different ultrasonication duration from 0 h to 4 h.	40
Figure 2.2.	AFM height images of TNC samples treated at different ultrasonication times, 0 h to 4 h.	43
Figure 2.3.	(a) DLS spectra, (b) UV-Visible transmittance spectra, and (c) yield of nanofibrillation of TNC samples at different ultrasonication times.	44
Figure 2.4.	XPS survey spectra of TNC at different ultrasonication treatments from 0 h to 4 h.	45
Figure 2.5.	The deconvoluted high-resolution C1s spectra of TNC at	47

different ultrasonication times, from 0 h to 4 h.

Figure 2.6.	Deconvoluted high-resolution O1s spectra of TNC at different ultrasonication times, from 0 h to 4 h (a-e).	48
Figure 2.7.	(a-c) WAXS and (d-f)) FTIR spectra of TNC from Areca nut leaf sheaths, Mahogany wood, and banana pseudo-stem fibers, respectively.	50
Figure 2.8.	AFM height images of CNC from different plant sources.	51
Figure 2.9.	a) DLS, b) UV-Visible transmittance spectra, and c) nanofibrillation yields of TCNC-A, TCNC-W, and TCNC-B.	52

CHAPTER 3

Figure 3.1.	The preparation procedure of TCNC stabilized Au@Ag nanostructures.	66
Figure 3.2.	a) UV-Visible absorption spectra of TCNC-Au NPs with varying wt% of TCNC (0.05, 0.1, 1.5, 0.2 and 0.25), b) TEM images of TCNC-Au NPs; inset shows the high resolution TEM image of spherical TCNC-Au NP, and c) UV-Vis absorption spectra of TCNC-Au NPs at different time periods.	67
Figure 3.3.	(a) UV-Vis spectra of TCNC-Au@Ag nanostructures with varying shell thickness 't' (t_0 , t_1 , t_2 , t_3 , t_4 , and t_5) obtained by adding 0, 60, 90, 110, 150, and 210 μL 0.01 M AgNO_3 to 3 mL Au seed solution; (b) equivalent magnified TEM images.	68
Figure 3.4.	TEM images of TCNC-Au@Ag nanostructures prepared by adding (a) 60, (b) 90, (c) 110, (d-e) 150, and (f) 210 μL 0.01 M AgNO_3 to 3 mL Au seed solutions; insets in (a-d & f) shows corresponding magnified TEM images.	69

Figure 3.5.	(a) HR-TEM image of TCNC-Au@Ag nanostructures (average Ag shell thickness- 3.5 nm); inset shows the magnified images of red marked area; (b) FFT spot pattern of TCNC-Au@Ag nanostructures enclosed by (111) facets.	70
Figure 3.6.	a) TEM, and b) HR-TEM images of 0.25 wt% TCNC-Au@Ag NPs.	70
Figure 3.7.	XRD pattern of a) TCNC-Au seeds and b) TCNC-Au@Ag NPs; c) UV-Vis absorption spectra of TCNC-Au NPs at different time periods.	71
Figure 3.8.	XPS narrow scans corresponding to (a) Ag 3d; (b) Au 4f; (c) C1s and (d) O1s for TCNC- Au@Ag nanostructures.	72
Figure 3.9.	XPS narrow scan of TCNC-Au NPs	74
Figure 3.10.	SERS response of malachite green (a and b) in solid-state with varying shell thickness of TCNC-Au@Ag nanostructures; comparison of SERS sensing in dispersion solution and solid-state (c and d); comparison of solid-state SERS sensing (e and f) with control substrates (TCNC-Au and citrate stabilized Au@Ag NPs).	75
Figure 3.11.	Mechanism of SERS detection using TCNC-Au@Ag nanostructures with numerous hotspot regions	78
Figure 3.12.	AFM images of TCNC templated Au@Ag nanostructures after drying.	78
Figure 3.13.	Sensitivity of TCNC-Au@Ag (t_4) nanostructures towards SERS detection of malachite green (a and b) and methylene blue (c and d).	79
Figure 3.14.	Finite element modelling showing the electric field distribution corresponding to the 2D geometry of (a) TCNC-Au and (b) isolated TCNC-Au@Ag nanostructures; (c-d) at the junction between two TCNC-Au@Ag nanostructures; (d) represents the	83

magnified image of (c); and (e) depicts the surface with height expression where it shows a sharp peak at the junction between two core-shell nanostructures.

- Figure 3.15.** a) Comparison of 4-NP reduction efficacy of TCNC-Au@Ag NPs with different shell thickness of Ag (t_0 - t_5) after 1-minute duration (b-c) The time-dependent UV-Vis absorption spectra of 4-NP reduction with NaBH_4 catalyzed by different amounts of TCNC-Au@Ag (t_4) nanostructures and (d) corresponding kinetic plots of the reduction reaction. 85

CHAPTER 4

- Figure 4.1.** Cartoon describing various steps for synthesis of Au@Pd nanoflowers bounded with the TCNC. 104
- Figure 4.2.** TEM images of TCNC-Au NPs seed. 105
- Figure 4.3.** TEM images (a) TCNC-Au NP seeds, (b-f) TCNC-Au@Pd NFs containing an Au core and Pd petal-like shells obtained after mixing of different quantities of equimolar ascorbic acid (50, 100, 150, 200 and 250 μL) and Pd precursor at pH, 8. 106
- Figure 4.4.** TEM image of TCNC-Au NPs seed at low magnification. 107
- Figure 4.5.** HR-TEM images and their corresponding FFT patterns of TCNC-Au@Pd NFs at various Pd shell coating: Pd-50 (a-c) and Pd-200 (d-g). 107
- Figure 4.6.** (a-f) The TEM images of single TCNC-Au@Pd NF showing an increment in the number of the Pd petals obtained after the coating with different quantities of the Pd precursors, (g) TCNC-Au@Pd NFs at low magnification and (h) the corresponding UV-Visible absorption spectra. 108
- Figure 4.7.** (a) UV-Visible absorption spectra of TCNC-Au@Pd NFs (Pd- 110

- 200) suspension at different time durations (inset: the photographs showing the stability of TCNC-Au@Pd NFs colloid); XRD patterns of (b) TCNC-Au NPs seed and (c) TCNC-Au@Pd NFs (Pd-200).
- Figure 4.8.** Figure 4.8. XPS narrow scans of TCNC-Au@Pd NFs (Pd-200) (a) deconvoluted spectra of Pd 3d, (b) Au 4f, (c) C1s, and (d) O1s, respectively. 111
- Figure 4.9.** (a) Deconvoluted XPS spectra of Au(0) 4f of TCNC-Au NPs and TSC-Au NPs, and (b) FTIR spectra of TCNC and TCNC-Au@Pd NFs. 113
- Figure 4.10.** TEM images of (a) TCNC-Au@Pd NFs (Pd-200); (b) cluster-like small Pd NPs (3-5 nm) captured during Pd shell coating over Au NPs seed solution and (c-d) citrate capped Au@Pd NPs (Pd-200). 115
- Figure 4.11.** (a-c) TEM images of TCNC-Au@Pd NFs decorated NH₂-RGO nanosheets. 116
- Figure 4.12.** The ORR polarization curves of commercial Pd/C (20 wt%), TCNC-Au@Pd NFs/NH₂-RGO, TSC-Au@Pd NPs/ NH₂-RGO, and TCNC-Pd NPs/ NH₂-RGO catalysts in 0.1 M KOH solution recorded at a scan rate of 10 mV/s and an electrode rotation speed of 1600 rpm. 118
- Figure 4.13.** UV-Vis absorption spectra of 4-NP reduction catalysed with (a) varying shell thickness of TCNC-Au@Pd NFs/NH₂-RGO, (b) comparison with different control and standard catalysts in same amount and at same time interval. 118
- Figure 4.14.** Real-time spectroscopic monitoring of 4-NP catalyzed by (a) 0.05 mg, (b) 0.1 mg of TCNC-Au@Pd NFs/NH₂-RGO, (c) corresponding reaction kinetic plots, and (d) recyclability of TCNC-Au@Pd NFs/NH₂-RGO for 4-NP reduction (inset shows the photograph of catalyst recovered by centrifugation after the completion of the 5th cycle). 120

CHAPTER 5

Figure 5.1.	(a) AFM height image and (b) DLS spectrum of TCNF.	137
Figure 5.2.	Synthesis of Cobalt(II) coordinated malonic acid/nanocellulose hybrid aerogels and schematic illustration of possible coordination and crosslinking in the formed aerogels.	138
Figure 5.3.	(a) FT-IR spectra, (b) PXRD of malonic acid (MA), TEMPO-oxidised nanocellulose (TCNF), CoNC and CoMNC aerogels, (c) SEM micrographs and (d) physical appearance of fibrous CoMNC aerogels.	141
Figure 5.4.	(a) XPS survey, deconvoluted XPS spectra of (b) Co2p, (c) C1s and (d) O1s of CoMNC aerogels.	142
Figure 5.5.	Deconvoluted XPS spectra for (a) Co2p of CoNC and CoMNC aerogels, and (b) O1s spectra of TCNF and CoMNC aerogels showing the shift in terms of binding energy after gel formation.	143
Figure 5.6.	(a) BET N ₂ adsorption–desorption analysis, (b) corresponding BJH pore-size distribution curves, (c) TG curves, and (d) Compression performance of CoNC and CoMNC aerogels.	144
Figure 5.7.	XPS survey spectra of CoMNC aerogels (a) before and (b) after washing step.	146
Figure 5.8.	Physical characterization of CoMNC aerogels without washing step before freez drying. a) XRD pattern, b-c) SEM micrographs.	147
Figure 5.9.	(a-b) FT-IR spectra of CoMNC and CoNC aerogels after 2 min exposure to atmosphere at room temperature for humidity absorption rate comparison.	148
Figure 5.10.	(a) Reversible thermochromism of CoMNC aerogels, (b) UV-Visible absorption spectrum of CoMNC aerogels at different standard humidity, and (c) developed a prototype of Java-based android mobile app for humidity sensing utilizing CoMNC	149

aerogels.

Figure 5.11. Logistic curve fit for the data between humidity and hue along with the parameters

CHAPTER 6

Nil

LIST OF TABLES

Table No:	Title	Page No:
CHAPTER 1		
Table 1.1.	Overview of reported nanocellulose production from agricultural residues.	8
Table 1.2.	Overview of reported nanoparticles systems supported with nanocellulose template.	18
CHAPTER 2		
Table 2.1.	Yield of nanofibrillation and other properties of TNC samples treated at 0 h to 4 h ultrasonication time durations.	42
Table 2.2.	Carboxylate content and O/C ratio obtained from XPS for TNC at different ultrasonication times, 0 h to 4 h.	46
Table 2.3.	% Peak area of individual or deconvoluted peaks in the peak-fitted high-resolution C1s spectra of TNC at different ultrasonication times, from 0 h to 4 h.	47
Table 2.4.	Compositions of nanocellulose source.	49
Table 2.5.	Consolidated properties of CNC from selected sources.	52
CHAPTER 3		
Table 3.1.	Zeta-potential values of different samples.	68
Table 3.2.	Analytical enhancement factor (AEF) for different shell thickness	76

Table 3.3. An overview of diverse SERS substrates with their LOD for malachite green. 80

Table 3.4. An overview of different SERS substrates with their LOD for methylene blue. 81

CHAPTER 4

Table 4.1. Zeta-potential values of TCNC-Au@Pd NFs with different Pd shell thickness. 105

Table 4.2. An overview of different catalysts for 4-NP reduction with rate constants. 121

CHAPTER 5 & 6

Nil

PREFACE

Plant-derived nanostructures are renowned for their biocompatibility and sustainability. Among them, cellulose nanoforms occupy ideal position which is based on factors such as their abundance, diversified forms with unique physicochemical properties, processibility, etc. From ancient times, wood is always considered as the main resource for the paper industry, timber industry, furniture, and so on. Due to human activity's degradation of natural ecosystems, the number of trees globally is declining at an alarming pace. Despite the fact that nanocellulose is a contemporary sustainable candidate, it is critical for researchers to identify more suitable cellulose sources that do not degrade the natural ecosystem. Worldwide, nearly eight billion people and other animals rely on food to survive. Because of this, agriculture now ranks as the largest industry in the world, producing food valued at several trillion dollars each year. This sheds light on the use of agricultural wastes as a bio-renewable source for nanocellulose production. In order to isolate nanocellulose efficiently and at a reasonable cost, more development is therefore necessary in this era of increasing sustainability requirements. With this focus, further interventions in this field for valorization of biomass to nanocellulose-based high-value products will be the scope of present research.

The current thesis mainly investigated the isolation of cellulose nanoforms from banana pseudo-stem fibers, an agricultural waste with simplification as well as the exploitation of great potentials of nanocellulose in the generation of functional hybrid materials for different application platforms. More emphasis is given to explore the template, reducing, shape-directing, and stabilizing abilities of nanocellulose in metal-based systems.

CHAPTER 1

Introduction

ABSTRACT

In this chapter, we discuss the material termed ‘nanocellulose’ and its subcategories, including cellulose nanocrystals (CNCs), cellulose nanofibers (CNFs), and bacterial nanocellulose (BNC), as well as its synthesis from different sources and properties. As a unique, sustainable material for various bio-based applications, we present the past and recent developments in the field of nanocellulose-based research as a versatile bio-template and flexible hydrogels/aerogels with good mechanical stability. We foresee nanocellulose as an excellent alternative to petroleum-based polymers and a plethora of nanocellulose in a galaxy of applications. For this, an economically viable pilot-scale production of nanocellulose is necessary to commercialize these research outcomes, and more advancements are likely to come in the future.

1.1. CELLULOSE

Cellulose is the most available natural hierarchical structure consisting of D-glucose as its structural units connected together by β -1-4 glycosidic bonds.¹ The number of monomeric units or degree of polymerization in cellulose may vary from source to source and fall in the range of 10000 -15000.² Cellulose includes in the class of semi-crystalline polysaccharides with a crystallinity of about 70%. This semi-crystallinity arises due to the presence of disordered amorphous regions together with highly ordered crystalline regions that are combined together to form cellulose chains and further bundled to microfibrils by Van der Waals forces and hydrogen bonds. Molecular alignment and dense packing of these microfibrils are mainly attributed to the overall Young’s modulus and tensile strength of cellulose.³ It has a width in the range from 5 to 20 μm and a length ranging from 0.5 to several millimeters. Due to the presence of free -OH groups in cellulose, it will tend to form strong inter-chain hydrogen bonding and align into some parallel assemblies with better mechanical strength. Morphological level of the structure of cellulose is a natural intricacy that starts from the elemental fibrils (length \sim 100 nm;

Introduction

width $\sim 1\text{-}3\text{ nm}$), which are bundled into microfibrils (diameter $\sim 10\text{-}30\text{ nm}$) which will further assemble to microfibrillar bands (length \sim few micrometers; width $\sim 100\text{ nm}$).²

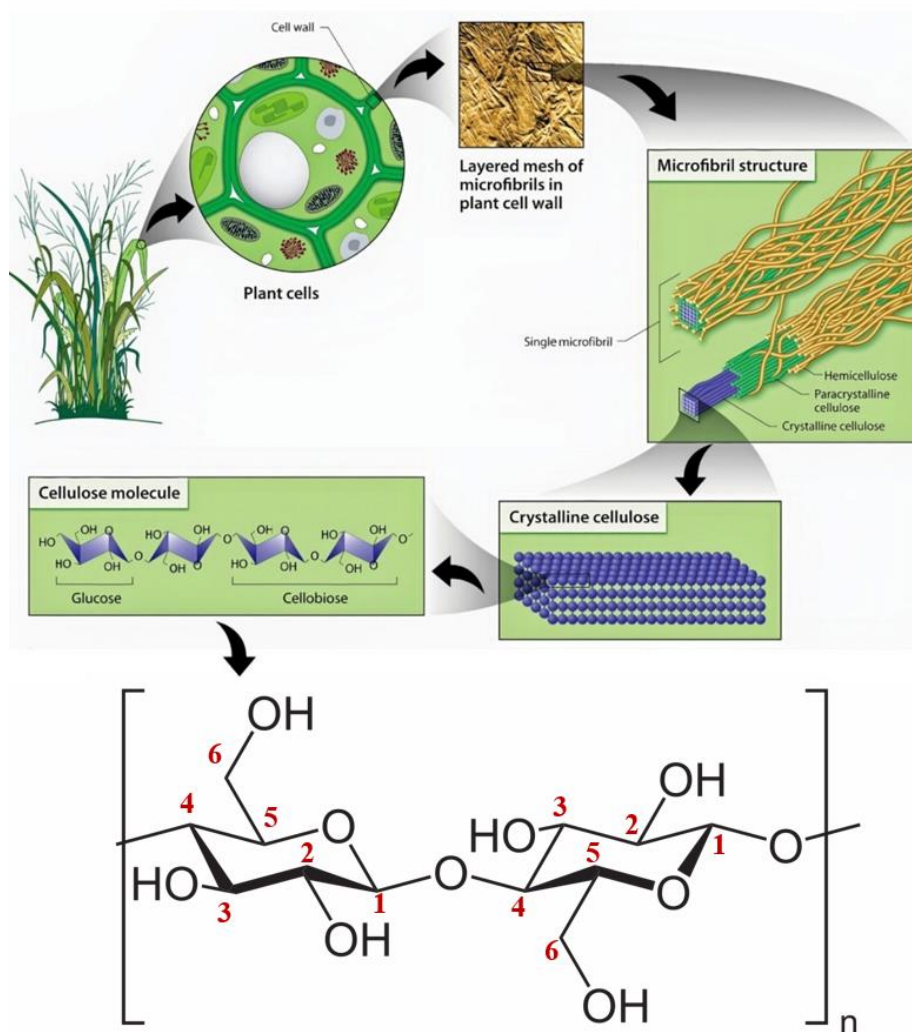


Figure 1.1. The hierarchical structure of cellulose from Plant cell wall to monomer.⁴

Generally, elementary cellulose chains exhibit different allomorphs depending on the crystal packing and spatial orientations. Mainly cellulose exists in four allomorphs like namely, cellulose I, II, III, and IV, in which cellulose I is only naturally born. This original natural cellulose I contains the combination of two allomorphs, cellulose I α (triclinic) and I β (monoclinic), in different quantities purely pertaining to the source of cellulose.⁵ Especially, cellulose I α form predominates in algae and bacteria, whereas plants contain I β

in major fractions.⁶ Cellulose I α can be converted into I β by tedious procedures at high temperatures and inert atmosphere, but 100% efficiency is still not attained. Mercerization or regeneration after solubilization of cellulose I result in cellulose II forms with a monoclinic structure generally called regenerative cellulose. It is thermodynamically stable and can be processed into different applications and also known for its mechanical stability resulting from antiparallel or irreversible chain rearrangement.⁷ Cellulose III is also produced by the chemical treatment using liquid ammonia at -80 °C from cellulose I and II. It exists in two analogs, namely cellulose III₁ and III₂, derived from their starting sources significantly the parallel and antiparallel arrangements of cellulose chains.⁸ Cellulose III can be further converted to cellulose IV allomorphs by heating in glycerol at a higher temperature (260 °C) for 20-30 min time. This again exists in two analogs, cellulose IV₁, and IV₂, with the same source dependency.⁹ Even though the scientific world found different allomorphs of cellulose, still cellulose I and II are mainly adopted for further processing and applications.

1.2. NANOCELLULOSE

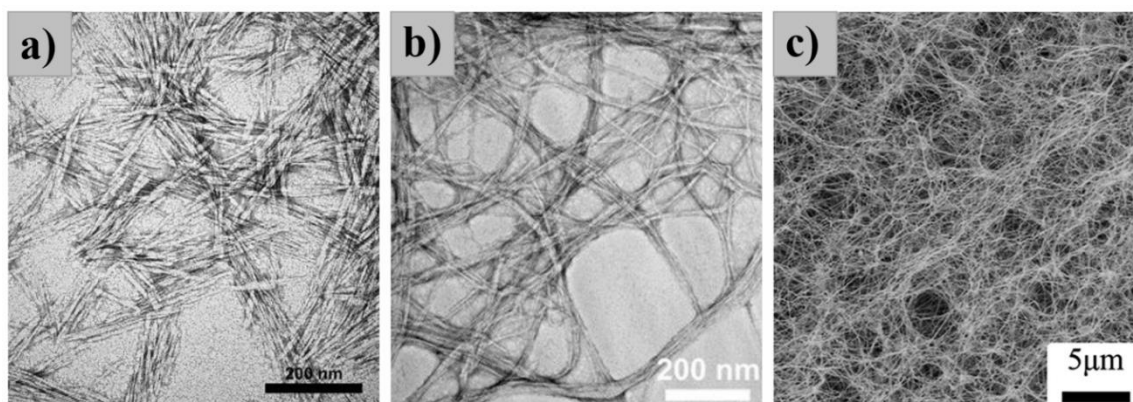


Figure 1.2. Morphology of (a) cellulose nanocrystals (CNCs), (b) cellulose nanofibers (CNFs), and (c) bacterial nanocellulose (BNC).¹⁰

The nano-designed cellulose, termed nanocellulose (NCs), is obtained from biomass via mechanical or chemical top-down approaches. Nanocellulose not only tightly holds the desirable properties of cellulose like nontoxicity, sustainability, low density,

Introduction

biodegradability, etc. but also exhibits desirable properties like high strength and modulus, flame retardancy, dimensional stability, thermal stability, thixotropic behavior, high optical transparency, high thermal conductivity, liquid crystalline nature, etc. These exciting properties of nanocellulose made it an inevitable material in many nanotechnologies, including applications like catalysis, sensing, aerogel, hydrogels, electronics, etc. Nanocellulose mainly exists in three forms - cellulose nanocrystals (CNCs), cellulose nanofibers (CNFs), and bacterial nanocellulose (BNC) based on morphology (aspect ratio), crystallinity, and other properties. Production of type of nanocellulose is dependent on the sources and method of preparation. CNCs and CNFs are produced by the breakdown of cellulose fibers into nanoscale particles; however, BNC is formed from low molecular weight sugars by bacteria. Thus large-scale manufacturing of BNC is complex, and commercialization is challenging. Nanofibrillated cellulose and cellulose nanocrystals are more promising among nano-sized cellulose materials. In contrast, bacterial nanocellulose is more favorable towards biomedical applications owing to its high mechanical strength, purity, flexibility, etc.

1.2.1. Cellulose Nanocrystals (CNCs)

Cellulose nanocrystals (CNCs), often referred to as cellulose nanowhiskers, with rod-like morphology, are usually isolated from cellulose fibers via acid hydrolysis. Since acid hydrolysis conduces to the destruction of most of the amorphous regions in cellulose, CNCs are shorter than CNFs. CNCs also generated by enzymatic hydrolysis¹¹ in addition to acid hydrolysis using H_2SO_4 ¹², HCl ¹³, H_3PO_4 ¹⁴, HBr ¹⁵, etc.

Holocellulose obtained from biomass after alkali treatment and bleaching is subjected to acid hydrolysis. Washing, centrifugation, dialysis, and freeze-drying (if required) are compulsory after hydrolysis as post-treatment after acid hydrolysis.¹⁶ CNCs liberated from acid hydrolysis may differ in degree of crystallinity, aspect ratio, and morphology due to their strong influence on the source and method of isolation.¹⁶ Lu *et al.* discussed that the synthesis of CNCs by acid hydrolysis from cotton resulted in different morphologies: rods, spheres, and networks.¹⁷ CNCs are generally observed in the needle or spindle-like morphology with a low aspect ratio (width about 5-50 nm; length about

100-200 nm). The absence of amorphous regions made CNCs an advanced material with exciting properties like liquid crystalline nature¹⁸, high Young's modulus¹⁹, high tensile strength²⁰, high thermal stability²¹, low coefficient of thermal expansion, etc. For example, Nypelo *et al.* fabricated self-standing nanocellulose Janus-type films from CNCs by acid hydrolysis.²² In another work, Biswas *et al.* reported the generation of highly thermally stable nanocomposites of CNCs and transparent polymer matrix.²³

1.2.2. Cellulose Nanofibers (CNFs)

Cellulose nanofibers (CNFs) are nanocellulose with a high aspect ratio (5-20 nm width; 500-1000 nm length) and flexibility imparted by the presence of a significant amount of amorphous region, unlike CNCs.²⁴ Mechanical, chemo-mechanical, and enzymatic-mechanical processes are the three primary ways that CNFs are made, with mechanical processes being the most well-known. Similar to CNCs, the morphology, degree of crystallinity, and properties of CNFs are well influenced by the source material and method of isolation.²⁵ CNFs are promising materials for the fabrication of gels and films since they can create complete skeletons with long fibers. For example, Isobei *et al.* fabricated TEMPO-oxidized cellulose-based hydrogels for heavy metal adsorption.²⁶ And Kobayashi *et al.* reported tough and transparent aerogels of cellulose nanofiber derivatives for insulating applications.²⁷

1.2.3. Bacterial Nanocellulose (BNC)

Bacterial nanocellulose (BNC) is the pure form of nanocellulose that is produced by the bacteria cultivated in glucose-containing cultural media. Generally, *Gluconoacetobacter xylinus*, *Agrobacterium*, *Pseudomonas*, *Rhizobium*, and *Sarcina* are the bacteria used for the production of BNC.²⁸ BNC is a cross-linked network of cellulose nanofibers of 3-5 nm width and several micron lengths with less density, high crystallinity (84-89%), better mechanical properties, surface area, etc. BNC is extensively applied in biomedical fields like implants and biomedical devices due to its pure non-cytotoxic nature.²⁹ For example, Badshah *et al.* modified and applied BNC for drug delivery.³⁰ Wang

Introduction

et al. developed anodes for lithium-ion batteries from carbon aerogels from BC.³¹ Nogi *et al.* fabricated BNC-based composite transparent films for electronic device applications.³²

1.3. EXTRACTION OF NANOCELLULOSE: SOURCES AND METHODS

Wood-based sources can be utilized for the preparation of nanocellulose by chemical treatments followed by mechanical disintegration.³³ Since wood is commercially overused in the paper and furniture sectors, it makes sense to choose agricultural waste and natural fibers with lower lignin contents instead of wood-based sources. Overall production processes are easy and energy effective by using natural fibers due to fewer lignin contents. There are a lot of approaches regarding the preparation of nanocellulose from different natural sources.

Sources for nanocellulose extraction	Nanocellulose type	Extraction method	Ref.
Wheat straw	Cellulose nanocrystals	Steam explosion	34
	Cellulose nanofibers	Steam explosion and high-shear homogenization	35
	Cellulose nanofibers	Acid hydrolysis (HCl) and Mechanical Treatment	36
Hemp	Cellulose nanocrystals	Acid hydrolysis	37
	Cellulose nanofibers	High-pressure homogenization	38
	Cellulose nanofibers	Oxidation by NaClO	39
Sugar beet	Cellulose nanofibers	TEMPO-oxidation	40

	Cellulose nanocrystals	Acid hydrolysis	41
Jute	Cellulose nanofibers	TEMPO-oxidation	42
	Cellulose nanocrystals	Acid hydrolysis	43
Banana rachis	Cellulose nanofibers	Homogenization and organosolv treatment	44
	Cellulose nanofibers	Peroxide oxidation	45
Kenaf fibers	Cellulose nanocrystals	Acid hydrolysis	46
Rice husk	Cellulose nanocrystals	Acid hydrolysis	47
Pineapple leaves	Cellulose nanofibers	Steam explosion	48
Coconut husk	Cellulose nanowhiskers	Acid hydrolysis	49
Cotton	Cellulose nanowhiskers	Microbial hydrolysis	50
Coir	Cellulose nanowhiskers	Acid hydrolysis	51

Table 1.1. Overview of reported nanocellulose production from agricultural residues.

Several approaches have been developed for the extraction of nanocellulose from cellulosic materials by combining chemical and mechanical treatments. This multistage synthesis involves the elimination of lignin since lignin hinders defibrillation.⁵² Different extraction techniques led to differences in the kinds and characteristics of the resulting nanocellulose. Three of the major methods of extraction are classified as pretreatments, chemical modification, and defibrillation.

Alkaline pretreatments are well known as an initial step in nanocellulose production because of their efficiency in deteriorating energy usage during the mechanical breakdown

Introduction

of cellulose fibers.^{38, 46a, 53} Elimination of lignin and hemicellulose contents in the biomass can be done by alkaline pretreatment and also results in swelling of cellulose fibers, which makes defibrillation easier. However, excessive alkaline treatments may cause cellulose degradation.⁵⁴

Due to its exceptional qualities, nanocellulose was introduced as a potential green material, which caused a stir in both the scientific community and the private sector. This opened up new avenues for researchers to create practical, affordable ways of making nanocellulose. Two major types of nanocellulose can be extracted from variable cellulose sources in different treatments: mechanical, chemo-mechanical, and enzymatic-mechanical treatments. Several highly useful methods are included in these three categories.

1.3.1. Mechanical Treatments

1.3.1.1. High-Pressure Homogenization (HPH)

High-pressure homogenization encompasses the subjection of cellulose pulp into the machine under high pressure, and shear forces will generate nanofibers. This process is repeated several times, specifically depending on the cellulose source, pressure drop, and length of fibers. For example, Andresen *et al.* extracted micro-fibrillated cellulose fibers by passing 2 wt% cellulose pulp suspension through a homogenizer 10 times at 600 bar.⁵⁵ Stenstad *et al.* subjected bleached spruce sulfite cellulose pulp with 2 wt% consistency with 600 bar pressure drop about 20 passes for the production of micro-fibrillated cellulose.⁵⁶ Syverud *et al.* reported the isolation of micro-fibrillated cellulose from cellulose pulp at 1 wt% consistency by using a homogenizer at 600 bar.⁵⁷ High energy consumption turns to high production cost, and also the clogging issues in machines tend the researchers to think about other alternatives or primary treatments before homogenization which makes defibrillation easier.⁵⁸

1.3.1.2. Grinding

Excessive hydrogen bonding in cellulose makes defibrillation very difficult and energy-consuming. In grinding, shear forces are utilized for the defibrillation of cellulose by breaking hydrogen bonds. Cellulose pulp suspension is passed through a setup containing high-speed rotating grindstone and static grindstone.⁵⁹ Bandera *et al.* reported the synthesis of nanofibers from microcrystalline cellulose by grinding at 1500 rpm with a motor load of 15 kW by passing about 12 times through the grinder.⁶⁰ Panthapulakkal *et al.* reported the isolation of nanofiber from wood pulp by grinding for the fabrication of cellulose nanofibril films.⁶¹

1.3.1.3. Microfluidization

Microfluidization setup is almost similar to high-pressure homogenization discussed above by solving the clogging problems in HPH by avoiding any in-line moving parts and also by reverse flow through the setup.^{59a} This technique is more efficient towards the production of nanofibers with equal size distribution by inducing a shear rate in the flow of pulp suspension, which leads to interparticle collision followed by the defibrillation of cellulose. However, frequent maintenance and replacement of discs may be required. For example, Ferrer *et al.* reported the production of cellulose nanofibers from empty palm fruit bunch fibers using a microfluidizer operating at 55 MPa by passing 1.8 wt% suspension about 5 times.⁶²

1.3.1.4. Cryo-crushing

As the term means, the pulp was frozen at cryogenic temperature by liquid nitrogen, followed by the rupture of cell walls by applying high applied shear forces. Chakraborty *et al.* put forward this method in 2005 for the production of cellulose microfibrils.^{33a} Wang *et al.* synthesized nanofibers by cryo-crushing from soybean stock at about 500–1000 bar for 20 passes, which resulted in defibrillation caused by the pressure exerted by ice crystals.^{54a} Alemdar *et al.* proposed the production of cellulose nanofibers from agricultural wastes

Introduction

such as wheat straw and soy hulls by cryo-crushing at 300 bar by about 20 passes.⁶³ Many researchers also reported the isolation of nano and microfibers by cryo-crushing.^{54b, 64} However, incapability of generating fine fibers and non-scalability are limited to this technique.^{59a}

1.3.1.5. Electrospinning

Electrospinning, first developed in 1934 by Formhals, is a simple process for creating ultrafine fibers with a diameter ranging from nano to micrometers.⁶⁵ Apart from melt spinning and wet spinning, electrospinning has achieved great attention due to its robustness and processing versatility and has resulted in long nanofibers with large aspect ratios from polymer solutions. The electrospinning setup includes a high-voltage source, a syringe pump, and a rotating disc collector. Electrospinning is a method for processing nanofibers using an electrically charged polymer solution jet. This technique involves applying an electric field to the solution. When the electric field's intensity is increased, a polymer drop released from the tip of a pipette elongates to form the Taylor cone. The ejection of polymer fibers from the tip of the Taylor cone is induced by a further rise in the applied voltage and collected on the oppositely charged drum. Subsequently, solvent evaporation leaves the fibers on the drum with proper orientation and directionality.⁶⁶ In general, a variety of factors, including the viscosity and surface tension of the polymer solution, the polarity of the solvent, the applied voltage, the solution temperature, humidity, the rpm of the drum collector, the distance between the needle tip and the collector, the diameter of the needle, and most importantly the concentration, are significant for the fibers without beads.⁶⁷ For the application of facemask material, electrospun nanofibers are a righteous option due to the excellent permeability of oxygen, the high degree of adsorption, the capture of small particulate materials by physical entanglement, etc., imparted from the large surface-to-volume ratio and interconnected porous geometry. Nanofibers by electrospinning are among the most interesting nanostructures so far.

Electrospinning of pristine cellulose is not possible because of the insolubility of cellulose in polar solvents. The generation of cellulose nanofibers by electrospinning of cellulose derivatives like cellulose acetate is well-known. Cellulose acetate nanofibrous

mats produced by electrospinning is popular in the field of filtration and biomedical areas.⁶⁸ Selection of suitable solvents plays an essential role in the bead-free development of homogeneous nanofibers. In the case of cellulose acetate, a binary mixture of solvents like DMA/Acetone, DMF/Acetone, and DCM/Acetone are commonly used.⁶⁹ Regeneration of cellulose nanofibers by deacetylation is also possible by alkaline treatments.⁷⁰ Ma *et al.* used an electrospun cellulose nanofiber mat produced by electrospinning of cellulose acetate and subsequent deacetylation as affinity membranes for the filtration of biomolecules like bovine serum albumin (BSA) and bilirubin. Tungprapa *et al.* well-illustrated the Impact on morphology and fiber diameter of the solvent system in electrospinning of cellulose acetate.^{69a}

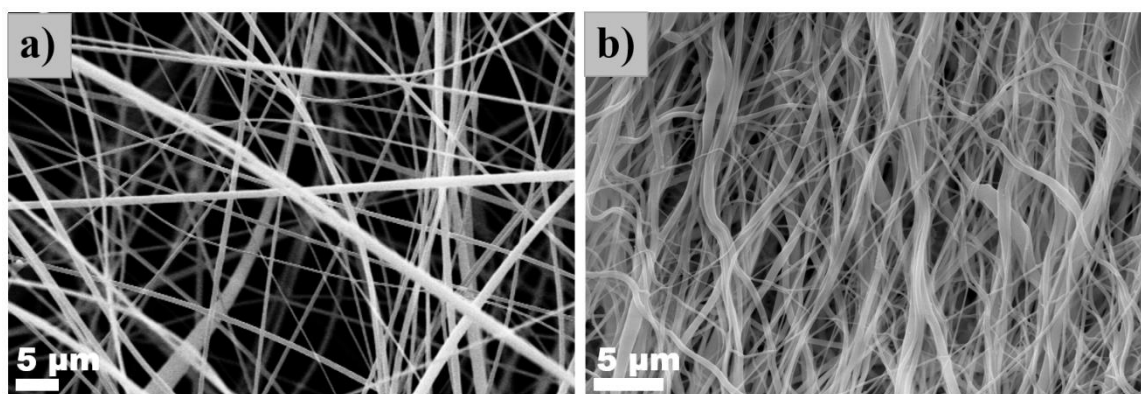


Figure 1.3. Morphology and fiber diameter of electrospun (a) cellulose acetate fibers and (b) deacetylated cellulose fibers.

1.3.2. Chemo-mechanical Treatments

Incomplete defibrillation and high energy consumption of mechanical treatments open the benign of chemo-mechanical treatments, which combine chemical treatments before mechanical treatments. Acid hydrolysis⁷¹ and TEMPO-mediated oxidation⁷² are popular in this category which also functionalized cellulose and induces hydrophilic nature.

1.3.2.1. Acid Hydrolysis

This method is mainly assigned to the development of cellulose nanocrystals with exciting properties. This method offers the production of cellulose nanocrystals by abolishing the amorphous part that is incorporated in the semi-crystalline pristine cellulose.⁷³ Reagents like strong acids rupture the hydrogen bonds between fibrils and highly disordered amorphous regions caused by the penetration of the hydronium (H_3O^+) ions, followed by the hydrolytic cleavage. However, the highly ordered crystalline region remained as intact and resulted in crystals with a low aspect ratio.⁷⁴ Most popular among acid hydrolysis is H_2SO_4 hydrolysis (~64%) not only produces the cellulose nanocrystals but also functionalized CNCs with anionic sulfate ester groups, which induces well-dispersion of individual CNCs in water by the electrostatic interaction.¹² However, these sulfate ester groups also diminish its thermal stability. Above a critical concentration of sulfate ester functionalized CNCs colloidal suspension in aqueous medium shows an ordered chiral nematic phase, which opens the way to an entirely advanced area of optically active films.^{18, 75} H_2SO_4 hydrolyzed CNCs are in spindle-like morphology with a low aspect ratio (5–10 nm width and 50–200 nm length).⁷⁶ However, Wang *et al.* reported CNCs with spherical morphology produced by the synergic action of H_2SO_4 and HCl .⁷⁷ Acid hydrolysis of cellulose also reported with other acids like hydrochloric acid¹³, nitric acid (~30%), phosphoric acid (~85%, functionalized by anionic phosphate ester groups)¹⁴, hydrobromic acid^{15, 78}, acetic acid (acetylation)⁷⁹, chloroacetic acid, etc., without any functionalization. CNCs isolated by HCl is thermally more stable, but stability in aqueous media will be decreased by the lack of any electrostatic interaction.⁸⁰ Nevertheless, the exciting properties of acid hydrolysed CNCs neutralization, washing, purification, filtration, centrifugation, dialysis, and drying makes this method very time-consuming. There are several reports regarding the isolation of cellulose nanocrystals from different sources by acid hydrolysis.^{14, 46b, 81} Besides that, there are several industries like CelluForce (Canada), American Process Inc (USA), Melodea/Holmen (Sweden), Blue Goose Biorefineries (Canada), Alberta Innovates (Canada), US forest products lab (USA), Indian Council for Agricultural Research – CIRCOT (India), FPInnovation (Canada)

commercialized CNCs in large scale.⁸² However, its cost cost-effectiveness is still questionable.

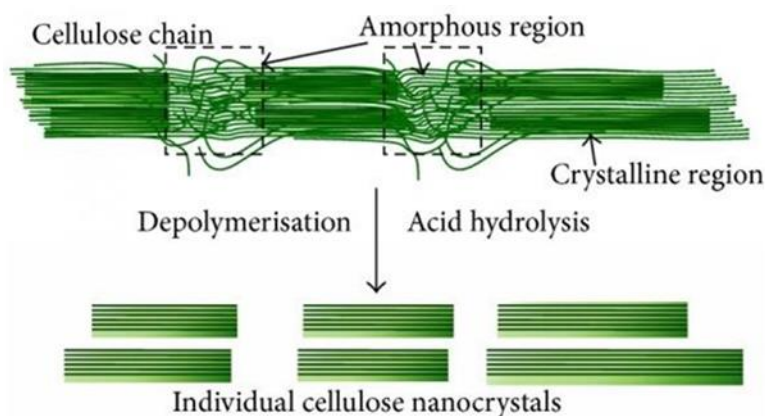


Figure 1.4. Preparation of CNC by regioselective acid hydrolysis of cellulose microfibril.⁸³

1.3.2.2. TEMPO-mediated Oxidation

Cellulose nanofibers (CNFs) with an aspect ratio >100 can be generated by TEMPO-mediated oxidation and subsequent mild mechanical treatments.⁸⁴ TEMPO-mediated oxidation of cellulose carried out by NaClO as the primary oxidant in the presence of the catalytic amount of TEMPO and NaBr at a pH 10-11. The exact mechanism of TEMPO-mediated oxidation is well demonstrated by Isogai *et al.* shown in the figure.⁷² The process of oxidation can be well observed by the consumption of NaOH to maintain pH 10-11. Functionalization of cellulose is attained by the regioselective conversion of the C-6 primary hydroxyl group to sodium carboxylated groups.⁸⁵ TEMPO-mediated oxidation by TEMPO/NaClO/NaClO₂ system was also employed for CNFs preparation where the synergic effect of NaClO and NaClO₂ were utilized.⁸⁶ TEMPO-mediated oxidation combined with mild mechanical treatment is the most efficient method for the production of nanocellulose with the surface functionalization of pristine cellulose and about 90% yield.⁷²

Apart from TEMPO-oxidised cellulose nanofibers (TCNF) produced by TEMPO-oxidation followed by homogenization, Zhou *et al.* reported the synthesis of TEMPO-

Introduction

oxidised cellulose nanocrystals with a spindle-like morphology (low aspect ratio) by replacing homogenization with ultra-sonication.⁸⁷ This acid-free method of production of CNCs is up-and-coming in the sense that it overcomes complex synthetic and purification steps in acid hydrolysis with high yield, greater quantities of surface anionic groups, and shorter and more uniform widths (~ 3 nm) of nanocellulose crystals. Zhou *et al.* also studied the gelation behavior of TEMPO-CNCs by dynamic light scattering.⁸⁸ In 2019, Isogai *et al.* reported an interesting review article regarding the different forms of nanocellulose like nanonetwork, nanofibers, and nanocrystals generated by TEMPO-mediated oxidation and subsequent slight variations in the controlled mechanical treatments.⁸⁹ Production of nanocellulose by oxidation by ammonium persulfate⁹⁰, and by hydrogen peroxide in ethanol⁹¹ have also been reported.

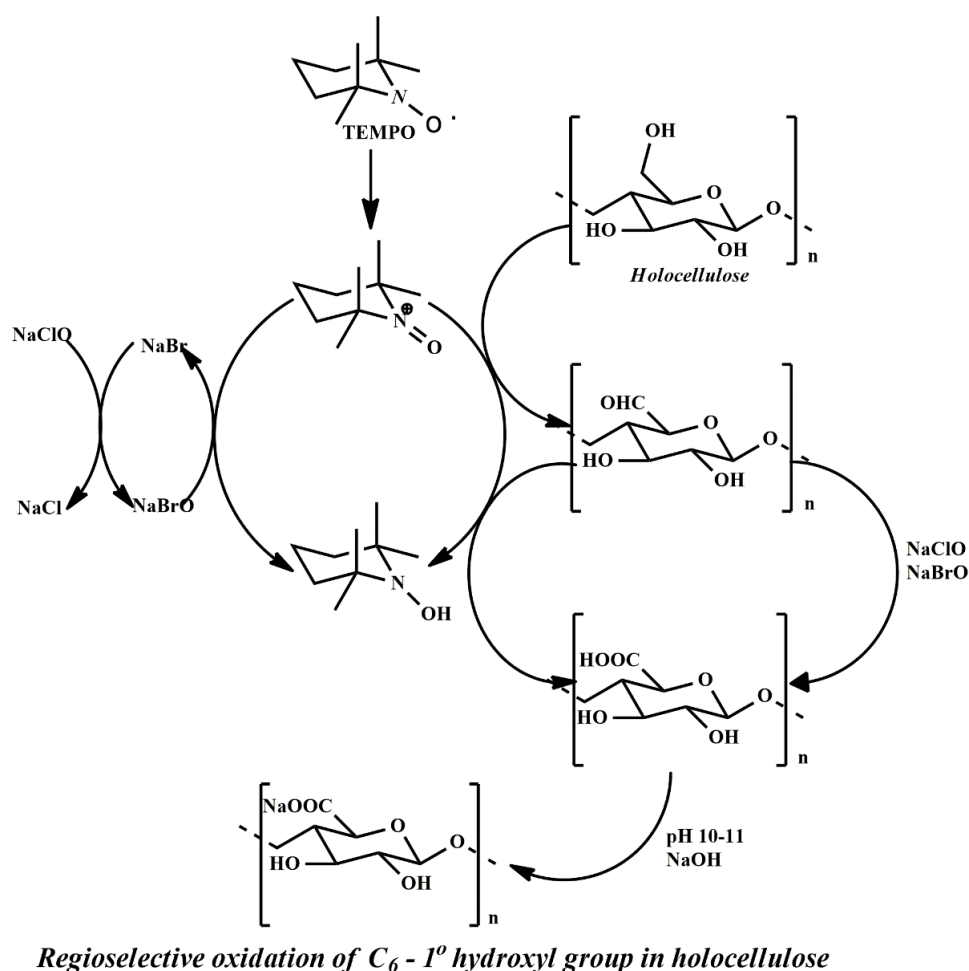


Figure 1.5. Mechanism of TEMPO-mediated oxidation of cellulose.

1.3.3. Enzymatic-mechanical Treatments

Enzymatic hydrolysis is a more environmentally friendly method of cellulose disintegration than chemical procedures, and it can be used to synthesize nanocellulose. Henriksson *et al.* reported the fabrication of nanocellulose paper by synthesizing nanocellulose through pretreatment followed by coupling of enzymatic hydrolysis and mechanical beating.⁹² They utilized endoglucanase enzyme for the enzymatic hydrolysis of the cellulose from softwood pulp. Paakko *et al.* also prepared nanocellulose fibers by enzymatic hydrolysis coupled with mechanical shearing and high-pressure homogenization.⁹³ Nanocellulose fibers resulting from enzymatic hydrolysis had a more favorable morphology that is different from nanocellulose fibers prepared by other methods.⁹⁴ However, the low yield of nanocellulose from this method tarnished its highlights over chemical treatments.

1.4. PROPERTIES DEPENDENT APPLICATIONS OF NCs

Nano design of cellulose termed ‘nanocellulose’ is a promising bio-based candidate with unprecedented properties and applications. Existence of nanocellulose in diverse morphology and properties turned to categorize them as cellulose nanocrystals (CNCs), cellulose nanofibers (CNFs), and bacterial nanocellulose (BNC). The behavior of nanocellulose products obtained from pristine cellulose after several pre and post-treatments extensively influenced by a variety of cellulose sources and method of preparation. Since all three types of nanocellulose have various structures, physical states, and properties, choosing the right kind is crucial and solely reliant on the application. For example, for the development of a gel CNFs and BNC are the best choices, whereas applications need better transparency and alignment spurred towards CNCs. Additionally, since cellulose has a complex chemical structure and a large number of functional groups, it is possible to alter its characteristics chemically. These changes to the chemical structure of cellulose at the ends may lead to new and intriguing possibilities. Applications of nanocellulose are not still fully discovered, and this field is still growing since

Introduction

nanocellulose is a precious stone from bio-waste. Here, we will discuss a few nanocellulose applications that are directly connected to the findings of the study in the remaining chapters of this thesis.

1.4.1. As Template/matrix for Stable Metal Nanoparticle Colloids

Biomass or plant-based synthesis of metal nanoparticles (NPs) are profound in various applications like medical diagnostics, environmental monitoring, food security, and homeland security. In photonics, when a material goes into diminutive size, especially to nano size, its entire properties will differ compared to the bulk. These properties are always pertaining to the tremendous increment in the surface area for minute quantities of materials. These nanostructures are imperative in a galaxy of industries, including electronics, optical, biomedical, energy storage devices, drugs, cosmetics, and so on.⁹⁵ Even though there are several chemical and other methods that are applicable to the synthesis of nanoparticles, plant-based methods always capture the interest due to their biocompatibility and sustainability. Cellulose is a highly ordered hierarchical structure produced by plants effortlessly and in abundance. Nanocellulose can mediate the eco-friendly production of bio-compatible and ultra-stable NPs. In 2016, Kaushik *et al.* tried to comprehend the papers published in the area of nanocellulose supported metal nanoparticles for catalytic applications.⁹⁶ This review illustrates the use of nanocellulose as bio-based template metal nanoparticles. Compared to traditional supports, the shelf-life and biocompatibility of nanocellulose-supported nanoparticles make them more appealing. An overview of some recent publications emanating from the development of nanoparticles supported with nanocellulose templates is listed below.

Nanocellulose	Features	Ref.
/NPs system		
CNF/Ag NPs	Spherical in shape with a particle size between 10- 50 nm	⁹⁷

CNF/Au/Ag NPs	Au nanostars and Ag NPs were prepared separately and mixed with CNF for better stability. Zeta potential for Au NSs: -12.9 mV, Ag NPs: -23.80 mV	98
NC/Pd NPs	Spherical in shape with an average particle size of 10.6 nm	99
CMC/ CNC@Ag NPs	Spherical in shape with a particle size between 10-20 nm	100
CNF/Cu₂O NPs	Spherical in shape with particle size between 20-40 nm	101
BNC/Ag NPs	Spherical in shape with a particle size between 20-40 nm	102
BNC/Ag NPs	Quasi-spherical nanoparticles (66 ± 27 nm)	103
CNF/Ag NPs	Spherical	104
CNF/Ag NWs	Ag NWs were prepared separately and mixed with CNF for better stability.	105
BNC/AgNPs/Mo O₃ NPs	Spherical in shape with an average particle size in the range from 1 nm to 10 nm	106
CF/Pd NPs	Nearly spherical	107
CNC/CAR/Ag NPs	Spherical	108
BNC/Ag NPs	Tried to achieve anisotropic morphology by using H ₂ O ₂ redox post-treatment. (triangle)	109
CNF/Ag NPs	Spherical in shape	110

Introduction

CNF/Ag NPs	Tried to achieve anisotropic morphology by using H ₂ O ₂ redox post-treatment.	111
CNF/Ag NPs	Tried to achieve anisotropic morphology	112
CNC/Ag NPs	Spherical in shape	113
CNF/Ag NPs	Spherical in shape	114
CNF/Ag NPs	Anisotropic morphology attained Shape-directing activity of nanocellulose was discussed	115
BNC/Au@Fe₂O₃	Nearly spherical in shape	116
RCNF/Au@Ag NPs	Nearly spherical in shape	117
CNF/Au@Ag NPs	Au@Ag NPs were prepared separately and mixed with CNF for better stability.	118

Table 1.2. Overview of reported nanoparticle systems supported with nanocellulose template.

1.4.2. Aerogels

Aerogels are material structures having the majority contribution from the air in their volume. These ultimate porous structures are known for their unusual low density (0.004–0.500 g cm⁻³), high specific surface area (100 -1000 m² g⁻¹), and about 99% porosity. Aerogels are originated from wet gels or hydrogels by drying under supercritical conditions. These materials are first developed by S. Kistler in 1930.¹¹⁹ Aerogels are an amazing candidate for applications that require lightweight materials like aerospace field, and high surface, especially in catalysis, insulation materials¹²⁰, 3D printing, medical scaffolds¹²¹, adsorption or separation¹²², etc. Flexibility and other mechanical properties

made polymers inevitable materials in aerogels developments compared to the inorganic materials in which nanocellulose-based aerogels captured the minds of researchers due to their biocompatibility. Among the different types of nanocellulose CNFs and BNC are more amenable for both hydrogel and aerogels applications due to their long fibrous nature with a high aspect ratio that can form cross-linked and entangled networks. Handful of hydroxyl groups in cellulose makes suitable bonds for the formation of mechanically stable and robust hydrogel networks by inter and intra-molecular hydrogen bonding and other electrostatic interactions towards additive components.¹²³ For example, Zander *et al.* utilized Ca^{2+} and Fe^{3+} ions cross-linked CNFs hydrogels ideal for tissue engineering applications.¹²¹ Ram *et al.* examined the use of aerogels based on CNCs and the manufacture of such devices in the context of aerogels.¹²⁴

1.5. OBJECTIVES

The valorization of agricultural biomass and industrial wastes must be strongly encouraged since a future with limited natural resources is not far off. A country like India produces tons of various agricultural biomass every year due to its diverse geography and agricultural areas. Utilization of these bio-wastes to value-added products in a sustainable way is inevitable for a better tomorrow. Nanocellulose is such a kind of candidate with unprecedented applicability in different fields. It is ideal for our country with enormous precious agricultural products, especially in this current period of the ‘*One District One Product*’ approach or other schemes by the Ministry of food processing industries. Although nanocellulose can be produced from biomass waste and is known for its sustainability, and eye-catching processabilities, in order to meet the commercial application requirements, the cost of production needs to be minimized. In order to produce nanocellulose in large quantities, energy efficiency, and process simplicity are crucial. In the first working chapter, our objectives are to isolate cellulose nanocrystals in a more effective and efficient way. In briefly,

- ❖ Value-added and energy-saving production of cellulose nanocrystals CNCs from biomass waste of banana plant (banana pseudo-stem fibers) instead of complex and hazardous acid hydrolysis

Introduction

- ❖ To determine the viability of extracting nanocellulose from banana plant waste in comparison with other plant wastes for optimal yield
- ❖ The physiochemical characteristics of nanocellulose are being optimized and investigated to help choose the best form for applications with particular structural and characteristic requirements

Our major goals in the other working chapters are to develop functional hybrids based on nanocellulose, including CNC-supported bimetallic nanostructures and the use of metal ions-CNF coordination for gel formation. Applicabilities of these nanocellulose metallic hybrids towards application areas like SERS, catalysis, electrocatalysis, and humidity sensing, etc., are also illustrated.

1.6. REFERENCES

1. Brännvall, E., Aspects on strength delivery and higher utilisation of the strength potential of softwood kraft pulp fibres. *Royal Institute of Technology* **2007**, *31*, 1-20.
2. Muddasar, M.; Beaucamp, A.; Culebras, M.; Collins, M. N., Cellulose: Characteristics and applications for rechargeable batteries. *International Journal of Biological Macromolecules* **2022**.
3. Mohanty, A. K.; Misra, M.; Drzal, L. T., *Natural fibers, biopolymers, and biocomposites*. CRC press: 2005.
4. US DOE. 2005. Genomics:GTL Roadmap, D. S.-., U.S. Department of Energy Office of Science. (p. 204).
5. Santmartí, A.; Lee, K.-Y., Crystallinity and thermal stability of nanocellulose. In *Nanocellulose and sustainability*, CRC Press: 2018; pp 67-86.
6. Wang, T.; Yang, H.; Kubicki, J. D.; Hong, M., Cellulose structural polymorphism in plant primary cell walls investigated by high-field 2D solid-state NMR spectroscopy and density functional theory calculations. *Biomacromolecules* **2016**, *17* (6), 2210-2222.
7. Klemm, D.; Heublein, B.; Fink, H. P.; Bohn, A., Cellulose: fascinating biopolymer and sustainable raw material. *Angewandte chemie international edition* **2005**, *44* (22), 3358-3393.
8. Huber, T.; Müssig, J.; Curnow, O.; Pang, S.; Bickerton, S.; Staiger, M. P., A critical review of all-cellulose composites. *Journal of Materials Science* **2012**, *47* (3), 1171-1186.
9. Zugenmaier, P., *Crystalline cellulose and derivatives: characterization and structures*. Springer: 2008.
10. (a) Schiavi, D.; Francesconi, S.; Taddei, A. R.; Fortunati, E.; Balestra, G. M., Exploring cellulose nanocrystals obtained from olive tree wastes as sustainable crop protection tool against bacterial diseases. *Scientific Reports* **2022**, *12* (1),

- 6149; (b) Nissilä, T.; Wei, J.; Geng, S.; Teleman, A.; Oksman, K., Ice-templated cellulose nanofiber filaments as a reinforcement material in epoxy composites. *Nanomaterials* **2021**, *11* (2), 490; (c) Li, G.; Nandgaonkar, A. G.; Habibi, Y.; Krause, W. E.; Wei, Q.; Lucia, L. A., An environmentally benign approach to achieving vectorial alignment and high microporosity in bacterial cellulose/chitosan scaffolds. *RSC advances* **2017**, *7* (23), 13678-13688.
11. Filson, P. B.; Dawson-Andoh, B. E.; Schwegler-Berry, D., Enzymatic-mediated production of cellulose nanocrystals from recycled pulp. *Green Chemistry* **2009**, *11* (11), 1808-1814.
 12. Nascimento, D. M.; Nunes, Y. L.; Figueirêdo, M. C.; de Azeredo, H. M.; Aouada, F. A.; Feitosa, J. P.; Rosa, M. F.; Dufresne, A., Nanocellulose nanocomposite hydrogels: technological and environmental issues. *Green Chemistry* **2018**, *20* (11), 2428-2448.
 13. Battista, O. A., Hydrolysis and crystallization of cellulose. *Industrial & Engineering Chemistry* **1950**, *42* (3), 502-507.
 14. Camarero Espinosa, S.; Kuhnt, T.; Foster, E. J.; Weder, C., Isolation of thermally stable cellulose nanocrystals by phosphoric acid hydrolysis. *Biomacromolecules* **2013**, *14* (4), 1223-1230.
 15. Lee, S.-Y.; Mohan, D. J.; Kang, I.-A.; Doh, G.-H.; Lee, S.; Han, S. O., Nanocellulose reinforced PVA composite films: effects of acid treatment and filler loading. *Fibers and Polymers* **2009**, *10* (1), 77-82.
 16. Habibi, Y.; Lucia, L. A.; Rojas, O. J., Cellulose nanocrystals: chemistry, self-assembly, and applications. *Chemical reviews* **2010**, *110* (6), 3479-3500.
 17. Lu, P.; Hsieh, Y.-L., Preparation and properties of cellulose nanocrystals: rods, spheres, and network. *Carbohydrate polymers* **2010**, *82* (2), 329-336.
 18. Xiong, R.; Yu, S.; Smith, M. J.; Zhou, J.; Krecker, M.; Zhang, L.; Nepal, D.; Bunning, T. J.; Tsukruk, V. V., Self-assembly of emissive nanocellulose/quantum dot nanostructures for chiral fluorescent materials. *ACS nano* **2019**, *13* (8), 9074-9081.
 19. Usov, I.; Nyström, G.; Adamcik, J.; Handschin, S.; Schütz, C.; Fall, A.; Bergström, L.; Mezzenga, R., Understanding nanocellulose chirality and structure-properties relationship at the single fibril level. *Nature communications* **2015**, *6* (1), 1-11.
 20. Zhang, J.; Luo, N.; Zhang, X.; Xu, L.; Wu, J.; Yu, J.; He, J.; Zhang, J., All-cellulose nanocomposites reinforced with in situ retained cellulose nanocrystals during selective dissolution of cellulose in an ionic liquid. *ACS Sustainable Chemistry & Engineering* **2016**, *4* (8), 4417-4423.
 21. Petersson, L.; Kvien, I.; Oksman, K., Structure and thermal properties of poly (lactic acid)/cellulose whiskers nanocomposite materials. *Composites Science and Technology* **2007**, *67* (11-12), 2535-2544.
 22. Nypelö, T.; Amer, H.; Konnerth, J.; Potthast, A.; Rosenau, T., Self-standing nanocellulose janus-type films with aldehyde and carboxyl functionalities. *Biomacromolecules* **2018**, *19* (3), 973-979.
 23. Biswas, S. K.; Tanpichai, S.; Witayakran, S.; Yang, X.; Shams, M. I.; Yano, H., Thermally superstable cellulosic-nanorod-reinforced transparent substrates featuring microscale surface patterns. *ACS nano* **2019**, *13* (2), 2015-2023.

Introduction

24. Li, P.; Sirviö, J. A.; Haapala, A.; Liimatainen, H., Cellulose nanofibrils from nonderivatizing urea-based deep eutectic solvent pretreatments. *ACS applied materials & interfaces* **2017**, *9* (3), 2846-2855.
25. Desmaisons, J.; Boutonnet, E.; Rueff, M.; Dufresne, A.; Bras, J., A new quality index for benchmarking of different cellulose nanofibrils. *Carbohydrate Polymers* **2017**, *174*, 318-329.
26. Isobe, N.; Chen, X.; Kim, U.-J.; Kimura, S.; Wada, M.; Saito, T.; Isogai, A., TEMPO-oxidized cellulose hydrogel as a high-capacity and reusable heavy metal ion adsorbent. *Journal of hazardous materials* **2013**, *260*, 195-201.
27. Kobayashi, Y.; Saito, T.; Isogai, A., Titelbild: Aerogels with 3D Ordered Nanofiber Skeletons of Liquid-Crystalline Nanocellulose Derivatives as Tough and Transparent Insulators (Angew. Chem. 39/2014). *Angewandte Chemie* **2014**, *126* (39), 10419-10419.
28. El-Saied, H.; Basta, A. H.; Gobran, R. H., Research progress in friendly environmental technology for the production of cellulose products (bacterial cellulose and its application). *Polymer-Plastics Technology and Engineering* **2004**, *43* (3), 797-820.
29. (a) Wiegand, C.; Moritz, S.; Hessler, N.; Kralisch, D.; Wesarg, F.; Müller, F. A.; Fischer, D.; Hipler, U.-C., Antimicrobial functionalization of bacterial nanocellulose by loading with polihexanide and povidone-iodine. *Journal of Materials Science: Materials in Medicine* **2015**, *26* (10), 245; (b) Czaja, W. K.; Young, D. J.; Kawecki, M.; Brown, R. M., The future prospects of microbial cellulose in biomedical applications. *biomacromolecules* **2007**, *8* (1), 1-12; (c) Wan, W.; Hutter, J.; Milton, L.; Guhados, G., Bacterial cellulose and its nanocomposites for biomedical applications. ACS Publications: 2006.
30. Badshah, M.; Ullah, H.; Khan, A. R.; Khan, S.; Park, J. K.; Khan, T., Surface modification and evaluation of bacterial cellulose for drug delivery. *International journal of biological macromolecules* **2018**, *113*, 526-533.
31. Wang, L.; Schütz, C.; Salazar-Alvarez, G.; Titirici, M.-M., Carbon aerogels from bacterial nanocellulose as anodes for lithium ion batteries. *Rsc Advances* **2014**, *4* (34), 17549-17554.
32. Nogi, M.; Yano, H., Transparent nanocomposites based on cellulose produced by bacteria offer potential innovation in the electronics device industry. *Advanced materials* **2008**, *20* (10), 1849-1852.
33. (a) Chakraborty, A.; Sain, M.; Kortschot, M., Cellulose microfibrils: a novel method of preparation using high shear refining and cryocrushing. *Holzforschung* **2005**, *59* (1), 102-107; (b) Isogai, A., Wood nanocelluloses: fundamentals and applications as new bio-based nanomaterials. *Journal of wood science* **2013**, *59* (6), 449-459; (c) Zhao, J.; Zhang, W.; Zhang, X.; Zhang, X.; Lu, C.; Deng, Y., Extraction of cellulose nanofibrils from dry softwood pulp using high shear homogenization. *Carbohydrate Polymers* **2013**, *97* (2), 695-702.
34. Dufresne, A.; Cavallé, J. Y.; Helbert, W., Thermoplastic nanocomposites filled with wheat straw cellulose whiskers. Part II: effect of processing and modeling. *Polymer composites* **1997**, *18* (2), 198-210.

-
35. Kaushik, A.; Singh, M., Isolation and characterization of cellulose nanofibrils from wheat straw using steam explosion coupled with high shear homogenization. *Carbohydrate research* **2011**, *346* (1), 76-85.
 36. Alemdar, A.; Sain, M., Biocomposites from wheat straw nanofibers: Morphology, thermal and mechanical properties. *Composites Science and Technology* **2008**, *68* (2), 557-565.
 37. Cao, X.; Chen, Y.; Chang, P. R.; Stumborg, M.; Huneault, M. A., Green composites reinforced with hemp nanocrystals in plasticized starch. *Journal of Applied Polymer Science* **2008**, *109* (6), 3804-3810.
 38. Wang, B.; Sain, M.; Oksman, K., Study of structural morphology of hemp fiber from the micro to the nanoscale. *Applied Composite Materials* **2007**, *14* (2), 89.
 39. Dai, D.; Fan, M.; Collins, P., Fabrication of nanocelluloses from hemp fibers and their application for the reinforcement of hemp fibers. *Industrial Crops and Products* **2013**, *44*, 192-199.
 40. Habibi, Y.; Vignon, M. R., Optimization of cellouronic acid synthesis by TEMPO-mediated oxidation of cellulose III from sugar beet pulp. *Cellulose* **2008**, *15* (1), 177-185.
 41. Mandal, A.; Chakrabarty, D., Isolation of nanocellulose from waste sugarcane bagasse (SCB) and its characterization. *Carbohydrate Polymers* **2011**, *86* (3), 1291-1299.
 42. Cao, X.; Ding, B.; Yu, J.; Al-Deyab, S. S., Cellulose nanowhiskers extracted from TEMPO-oxidized jute fibers. *Carbohydrate polymers* **2012**, *90* (2), 1075-1080.
 43. Kasyapi, N.; Chaudhary, V.; Bhowmick, A. K., Bionanowhiskers from jute: Preparation and characterization. *Carbohydrate polymers* **2013**, *92* (2), 1116-1123.
 44. Zuluaga, R.; Putaux, J.-L.; Restrepo, A.; Mondragon, I.; Gañán, P., Cellulose microfibrils from banana farming residues: isolation and characterization. *Cellulose* **2007**, *14* (6), 585-592.
 45. Zuluaga, R.; Putaux, J. L.; Cruz, J.; Vélez, J.; Mondragon, I.; Gañán, P., Cellulose microfibrils from banana rachis: Effect of alkaline treatments on structural and morphological features. *Carbohydrate Polymers* **2009**, *76* (1), 51-59.
 46. (a) Kargarzadeh, H.; Ahmad, I.; Abdullah, I.; Dufresne, A.; Zainudin, S. Y.; Sheltami, R. M., Effects of hydrolysis conditions on the morphology, crystallinity, and thermal stability of cellulose nanocrystals extracted from kenaf bast fibers. *Cellulose* **2012**, *19* (3), 855-866; (b) Zaini, L. H.; Jonoobi, M.; Tahir, P. M.; Karimi, S., Isolation and characterization of cellulose whiskers from kenaf (*Hibiscus cannabinus* L.) bast fibers. **2013**; (c) Shi, J.; Shi, S. Q.; Barnes, H. M.; Pittman Jr, C. U., A chemical process for preparing cellulosic fibers hierarchically from kenaf bast fibers. *BioResources* **2011**, *6* (1), 879-890.
 47. (a) Johar, N.; Ahmad, I.; Dufresne, A., Extraction, preparation and characterization of cellulose fibres and nanocrystals from rice husk. *Industrial Crops and Products* **2012**, *37* (1), 93-99; (b) Ludueña, L. N.; Fasce, D. P.; Alvarez, V. A.; Stefani, P. M., Nanocellulose from rice husk following alkaline treatment to remove silica. **2011**.
 48. Cherian, B. M.; Leão, A. L.; De Souza, S. F.; Thomas, S.; Pothan, L. A.; Kottaisamy, M., Isolation of nanocellulose from pineapple leaf fibres by steam explosion. *Carbohydrate polymers* **2010**, *81* (3), 720-725.
-

Introduction

49. Fahma, F.; Iwamoto, S.; Hori, N.; Iwata, T.; Takemura, A., Effect of pre-acid-hydrolysis treatment on morphology and properties of cellulose nanowhiskers from coconut husk. *Cellulose* **2011**, *18* (2), 443-450.
50. Satyamurthy, P.; Jain, P.; Balasubramanya, R. H.; Vigneshwaran, N., Preparation and characterization of cellulose nanowhiskers from cotton fibres by controlled microbial hydrolysis. *Carbohydrate Polymers* **2011**, *83* (1), 122-129.
51. Nascimento, D. M.; Almeida, J. S.; Dias, A. F.; Figueirêdo, M. C. B.; Morais, J. P. S.; Feitosa, J. P.; Rosa, M. d. F., A novel green approach for the preparation of cellulose nanowhiskers from white coir. *Carbohydrate polymers* **2014**, *110*, 456-463.
52. Hubbe, M. A.; Rojas, O. J.; Lucia, L. A.; Sain, M., Cellulosic nanocomposites: a review. *BioResources* **2008**, *3* (3), 929-980.
53. (a) Sheltami, R. M.; Abdullah, I.; Ahmad, I.; Dufresne, A.; Kargarzadeh, H., Extraction of cellulose nanocrystals from mengkuang leaves (*Pandanus tectorius*). *Carbohydrate Polymers* **2012**, *88* (2), 772-779; (b) Karimi, S.; Dufresne, A.; Tahir, P. M.; Karimi, A.; Abdulkhani, A., Biodegradable starch-based composites: effect of micro and nanoreinforcements on composite properties. *Journal of Materials Science* **2014**, *49* (13), 4513-4521.
54. (a) Wang, B.; Sain, M., Dispersion of soybean stock-based nanofiber in a plastic matrix. *Polymer International* **2007**, *56* (4), 538-546; (b) Bhatnagar, A.; Sain, M., Processing of cellulose nanofiber-reinforced composites. *Journal of Reinforced Plastics and Composites* **2005**, *24* (12), 1259-1268.
55. Andresen, M.; Johansson, L.-S.; Tanem, B. S.; Stenius, P., Properties and characterization of hydrophobized microfibrillated cellulose. *Cellulose* **2006**, *13* (6), 665-677.
56. Stenstad, P.; Andresen, M.; Tanem, B. S.; Stenius, P., Chemical surface modifications of microfibrillated cellulose. *Cellulose* **2008**, *15* (1), 35-45.
57. Syverud, K.; Stenius, P., Strength and barrier properties of MFC films. *Cellulose* **2009**, *16* (1), 75.
58. (a) Zimmermann, T.; Bordeanu, N.; Strub, E., Properties of nanofibrillated cellulose from different raw materials and its reinforcement potential. *Carbohydrate Polymers* **2010**, *79* (4), 1086-1093; (b) Eriksen, Ø.; Syverud, K.; Gregersen, Ø., The use of microfibrillated cellulose produced from kraft pulp as strength enhancer in TMP paper. *Nordic Pulp & Paper Research Journal* **2008**, *23* (3), 299-304.
59. (a) Spence, K. L.; Venditti, R. A.; Rojas, O. J.; Habibi, Y.; Pawlak, J. J., A comparative study of energy consumption and physical properties of microfibrillated cellulose produced by different processing methods. *Cellulose* **2011**, *18* (4), 1097-1111; (b) Abe, K.; Iwamoto, S.; Yano, H., Obtaining cellulose nanofibers with a uniform width of 15 nm from wood. *Biomacromolecules* **2007**, *8* (10), 3276-3278.
60. Bandera, D.; Sapkota, J.; Josset, S.; Weder, C.; Tingaut, P.; Gao, X.; Foster, E. J.; Zimmermann, T., Influence of mechanical treatments on the properties of cellulose nanofibers isolated from microcrystalline cellulose. *Reactive and Functional Polymers* **2014**, *85*, 134-141.

-
61. Panthapulakkal, S.; Sain, M., Preparation and characterization of cellulose nanofibril films from wood fibre and their thermoplastic polycarbonate composites. *International Journal of Polymer Science* **2012**, *2012*.
 62. Ferrer, A.; Filpponen, I.; Rodríguez, A.; Laine, J.; Rojas, O. J., Valorization of residual Empty Palm Fruit Bunch Fibers (EPFBF) by microfluidization: production of nanofibrillated cellulose and EPFBF nanopaper. *Bioresource Technology* **2012**, *125*, 249-255.
 63. Alemdar, A.; Sain, M., Isolation and characterization of nanofibers from agricultural residues—Wheat straw and soy hulls. *Bioresource technology* **2008**, *99* (6), 1664-1671.
 64. Wang, B.; Sain, M., Isolation of nanofibers from soybean source and their reinforcing capability on synthetic polymers. *Composites Science and Technology* **2007**, *67* (11-12), 2521-2527.
 65. (a) Reneker, D. H.; Chun, I., Nanometre diameter fibres of polymer, produced by electrospinning. *Nanotechnology* **1996**, *7* (3), 216; (b) Reneker, D. H.; Yarin, A. L.; Fong, H.; Koombhongse, S., Bending instability of electrically charged liquid jets of polymer solutions in electrospinning. *Journal of Applied physics* **2000**, *87* (9), 4531-4547; (c) Yarin, A. L.; Koombhongse, S.; Reneker, D. H., Bending instability in electrospinning of nanofibers. *Journal of applied physics* **2001**, *89* (5), 3018-3026.
 66. (a) Bhardwaj, N.; Kundu, S. C., Electrospinning: a fascinating fiber fabrication technique. *Biotechnology advances* **2010**, *28* (3), 325-347; (b) Deitzel, J. M.; Kleinmeyer, J.; Harris, D.; Tan, N. B., The effect of processing variables on the morphology of electrospun nanofibers and textiles. *Polymer* **2001**, *42* (1), 261-272.
 67. (a) Pham, Q. P.; Sharma, U.; Mikos, A. G., Electrospinning of polymeric nanofibers for tissue engineering applications: a review. *Tissue engineering* **2006**, *12* (5), 1197-1211; (b) Venugopal, J.; Zhang, Y.; Ramakrishna, S., Electrospun nanofibres: biomedical applications. *Proceedings of the institution of mechanical engineers, Part N: Journal of nanoengineering and nanosystems* **2004**, *218* (1), 35-45.
 68. (a) Ma, Z.; Kotaki, M.; Ramakrishna, S., Electrospun cellulose nanofiber as affinity membrane. *Journal of membrane science* **2005**, *265* (1-2), 115-123; (b) Lee, K. Y.; Jeong, L.; Kang, Y. O.; Lee, S. J.; Park, W. H., Electrospinning of polysaccharides for regenerative medicine. *Advanced drug delivery reviews* **2009**, *61* (12), 1020-1032.
 69. (a) Tungprapa, S.; Puangparn, T.; Weerasombut, M.; Jangchud, I.; Fakum, P.; Semongkhon, S.; Meechaisue, C.; Supaphol, P., Electrospun cellulose acetate fibers: effect of solvent system on morphology and fiber diameter. *Cellulose* **2007**, *14* (6), 563-575; (b) Celebioglu, A.; Uyar, T., Electrospun porous cellulose acetate fibers from volatile solvent mixture. *Materials Letters* **2011**, *65* (14), 2291-2294.
 70. (a) Liu, H.; Hsieh, Y. L., Ultrafine fibrous cellulose membranes from electrospinning of cellulose acetate. *Journal of Polymer Science Part B: Polymer Physics* **2002**, *40* (18), 2119-2129; (b) Liu, H.; Hsieh, Y. L., Surface methacrylation and graft copolymerization of ultrafine cellulose fibers. *Journal of Polymer Science Part B: Polymer Physics* **2003**, *41* (9), 953-964; (c) Son, W. K.; Youk, J. H.; Lee, T. S.; Park, W. H., Electrospinning of ultrafine cellulose acetate fibers: studies of a
-

Introduction

- new solvent system and deacetylation of ultrafine cellulose acetate fibers. *Journal of Polymer Science Part B: Polymer Physics* **2004**, *42* (1), 5-11.
71. Boldizar, A.; Klason, C.; Kubat, J.; Näslund, P.; Saha, P., Prehydrolyzed cellulose as reinforcing filler for thermoplastics. *International Journal of Polymeric Materials* **1987**, *11* (4), 229-262.
72. Isogai, A.; Saito, T.; Fukuzumi, H., TEMPO-oxidized cellulose nanofibers. *nanoscale* **2011**, *3* (1), 71-85.
73. (a) Dufresne, A., *Nanocellulose: from nature to high performance tailored materials*. Walter de Gruyter GmbH & Co KG: 2017; (b) Dufresne, A., Cellulose nanomaterial reinforced polymer nanocomposites. *Current Opinion in Colloid & Interface Science* **2017**, *29*, 1-8.
74. Thielemans, W.; Warbey, C. R.; Walsh, D. A., Permselective nanostructured membranes based on cellulose nanowhiskers. *Green Chemistry* **2009**, *11* (4), 531-537.
75. Mu, X.; Gray, D. G., Formation of chiral nematic films from cellulose nanocrystal suspensions is a two-stage process. *Langmuir* **2014**, *30* (31), 9256-9260.
76. Dong, X. M.; Revol, J.-F.; Gray, D. G., Effect of microcrystallite preparation conditions on the formation of colloid crystals of cellulose. *Cellulose* **1998**, *5* (1), 19-32.
77. Wang, N.; Ding, E.; Cheng, R., Preparation and liquid crystalline properties of spherical cellulose nanocrystals. *Langmuir* **2008**, *24* (1), 5-8.
78. Filpponen, I.; Argyropoulos, D. S., Regular linking of cellulose nanocrystals via click chemistry: synthesis and formation of cellulose nanoplatelet gels. *Biomacromolecules* **2010**, *11* (4), 1060-1066.
79. Trifol, J.; Sillard, C.; Plackett, D.; Szabo, P.; Bras, J.; Daugaard, A. E., Chemically extracted nanocellulose from sisal fibres by a simple and industrially relevant process. *Cellulose* **2017**, *24* (1), 107-118.
80. Gopi, S.; Balakrishnan, P.; Chandradhara, D.; Poovathankandy, D.; Thomas, S., General scenarios of cellulose and its use in the biomedical field. *Materials Today Chemistry* **2019**, *13*, 59-78.
81. (a) Teixeira, E. d. M.; Pasquini, D.; Curvelo, A. A.; Corradini, E.; Belgacem, M. N.; Dufresne, A., Cassava bagasse cellulose nanofibrils reinforced thermoplastic cassava starch. *Carbohydrate polymers* **2009**, *78* (3), 422-431; (b) Chen, Y.; Liu, C.; Chang, P. R.; Anderson, D. P.; Huneault, M. A., Pea starch-based composite films with pea hull fibers and pea hull fiber-derived nanowhiskers. *Polymer Engineering & Science* **2009**, *49* (2), 369-378; (c) Mathew, A. P.; Thielemans, W.; Dufresne, A., Mechanical properties of nanocomposites from sorbitol plasticized starch and tunicin whiskers. *Journal of Applied Polymer Science* **2008**, *109* (6), 4065-4074.
82. (a) Xie, H.; Du, H.; Yang, X.; Si, C., Recent strategies in preparation of cellulose nanocrystals and cellulose nanofibrils derived from raw cellulose materials. *International Journal of Polymer Science* **2018**, *2018*; (b) Trache, D.; Tarchoun, A. F.; Derradji, M.; Mehelli, O.; Hussin, M. H.; Bessa, W., Cellulose Fibers and Nanocrystals: Preparation, Characterization, and Surface Modification. In *Functionalized Nanomaterials I*, CRC Press: 2020; pp 171-190.

-
83. Lee, H.; Hamid, S. B. A.; Zain, S., Conversion of lignocellulosic biomass to nanocellulose: structure and chemical process. *The Scientific World Journal* **2014**, 2014.
84. (a) Lasseguette, E.; Roux, D.; Nishiyama, Y., Rheological properties of microfibrillar suspension of TEMPO-oxidized pulp. *Cellulose* **2008**, 15 (3), 425-433; (b) Saito, T.; Hirota, M.; Tamura, N.; Kimura, S.; Fukuzumi, H.; Heux, L.; Isogai, A., Individualization of nano-sized plant cellulose fibrils by direct surface carboxylation using TEMPO catalyst under neutral conditions. *Biomacromolecules* **2009**, 10 (7), 1992-1996; (c) Saito, T.; Isogai, A., Introduction of aldehyde groups on surfaces of native cellulose fibers by TEMPO-mediated oxidation. *Colloids and Surfaces A: Physicochemical and Engineering Aspects* **2006**, 289 (1-3), 219-225.
85. (a) Isogai, T.; Yanagisawa, M.; Isogai, A., Degrees of polymerization (DP) and DP distribution of cellouronic acids prepared from alkali-treated celluloses and ball-milled native celluloses by TEMPO-mediated oxidation. *Cellulose* **2009**, 16 (1), 117-127; (b) da Silva Perez, D.; Montanari, S.; Vignon, M. R., TEMPO-mediated oxidation of cellulose III. *Biomacromolecules* **2003**, 4 (5), 1417-1425.
86. Saito, T.; Hirota, M.; Tamura, N.; Isogai, A., Oxidation of bleached wood pulp by TEMPO/NaClO/NaClO₂ system: effect of the oxidation conditions on carboxylate content and degree of polymerization. *Journal of wood science* **2010**, 56 (3), 227-232.
87. Zhou, Y.; Saito, T.; Bergström, L.; Isogai, A., Acid-free preparation of cellulose nanocrystals by TEMPO oxidation and subsequent cavitation. *Biomacromolecules* **2018**, 19 (2), 633-639.
88. Zhou, Y.; Fujisawa, S.; Saito, T.; Isogai, A., Characterization of concentration-dependent gelation behavior of aqueous 2, 2, 6, 6-tetramethylpiperidine-1-oxyl-cellulose nanocrystal dispersions using dynamic light scattering. *Biomacromolecules* **2018**, 20 (2), 750-757.
89. Isogai, A.; Zhou, Y., Diverse nanocelluloses prepared from TEMPO-oxidized wood cellulose fibers: Nanonetworks, nanofibers, and nanocrystals. *Current Opinion in Solid State and Materials Science* **2019**, 23 (2), 101-106.
90. (a) Leung, A. C.; Hrapovic, S.; Lam, E.; Liu, Y.; Male, K. B.; Mahmoud, K. A.; Luong, J. H., Characteristics and properties of carboxylated cellulose nanocrystals prepared from a novel one-step procedure. *Small* **2011**, 7 (3), 302-305; (b) Castro-Guerrero, C. F.; Gray, D. G., Chiral nematic phase formation by aqueous suspensions of cellulose nanocrystals prepared by oxidation with ammonium persulfate. *Cellulose* **2014**, 21 (4), 2567-2577.
91. Li, Y.; Liu, Y.; Chen, W.; Wang, Q.; Liu, Y.; Li, J.; Yu, H., Facile extraction of cellulose nanocrystals from wood using ethanol and peroxide solvothermal pretreatment followed by ultrasonic nanofibrillation. *Green Chemistry* **2016**, 18 (4), 1010-1018.
92. Henriksson, M.; Berglund, L. A.; Isaksson, P.; Lindstrom, T.; Nishino, T., Cellulose nanopaper structures of high toughness. *Biomacromolecules* **2008**, 9 (6), 1579-1585.
93. Pääkkö, M.; Ankerfors, M.; Kosonen, H.; Nykänen, A.; Ahola, S.; Österberg, M.; Ruokolainen, J.; Laine, J.; Larsson, P. T.; Ikkala, O., Enzymatic hydrolysis combined with mechanical shearing and high-pressure homogenization for
-

Introduction

- nanoscale cellulose fibrils and strong gels. *Biomacromolecules* **2007**, 8 (6), 1934-1941.
94. (a) Siró, I.; Plackett, D., Microfibrillated cellulose and new nanocomposite materials: a review. *Cellulose* **2010**, 17 (3), 459-494; (b) Tibolla, H.; Pelissari, F. M.; Rodrigues, M. I.; Menegalli, F. C., Cellulose nanofibers produced from banana peel by enzymatic treatment: Study of process conditions. *Industrial Crops and Products* **2017**, 95, 664-674.
 95. Mohammadinejad, R.; Karimi, S.; Irvani, S.; Varma, R. S., Plant-derived nanostructures: types and applications. *Green Chemistry* **2016**, 18 (1), 20-52.
 96. Kaushik, M.; Moores, A., Nanocelluloses as versatile supports for metal nanoparticles and their applications in catalysis. *Green Chemistry* **2016**, 18 (3), 622-637.
 97. Zhong, C.; Zajki-Zechmeister, K.; Nidetzky, B., Reducing end thiol-modified nanocellulose: Bottom-up enzymatic synthesis and use for templated assembly of silver nanoparticles into biocidal composite material. *Carbohydrate Polymers* **2021**, 260, 117772.
 98. Sun, L.; Yu, Z.; Alsammarraie, F. K.; Lin, M.-H.; Kong, F.; Huang, M.; Lin, M., Development of cellulose nanofiber-based substrates for rapid detection of ferbam in kale by surface-enhanced Raman spectroscopy. *Food Chemistry* **2021**, 347, 129023.
 99. Dewan, A.; Sarmah, M.; Bharali, P.; Thakur, A. J.; Boruah, P. K.; Das, M. R.; Bora, U., Pd nanoparticles-loaded honeycomb-structured bio-nanocellulose as a heterogeneous catalyst for heteroaryl cross-coupling reaction. *ACS Sustainable Chemistry & Engineering* **2021**, 9 (2), 954-966.
 100. He, Y.; Li, H.; Fei, X.; Peng, L., Carboxymethyl cellulose/cellulose nanocrystals immobilized silver nanoparticles as an effective coating to improve barrier and antibacterial properties of paper for food packaging applications. *Carbohydrate polymers* **2021**, 252, 117156.
 101. Su, X.; Chen, W.; Han, Y.; Wang, D.; Yao, J., In-situ synthesis of Cu₂O on cotton fibers with antibacterial properties and reusable photocatalytic degradation of dyes. *Applied surface science* **2021**, 536, 147945.
 102. Huo, D.; Chen, B.; Meng, G.; Huang, Z.; Li, M.; Lei, Y., Ag-nanoparticles@ bacterial nanocellulose as a 3D flexible and robust surface-enhanced Raman scattering substrate. *ACS Applied Materials & Interfaces* **2020**, 12 (45), 50713-50720.
 103. Parnsubsakul, A.; Ngoensawat, U.; Wutikhun, T.; Sukmanee, T.; Sapcharoenkun, C.; Pienpinijtham, P.; Ekgasit, S., Silver nanoparticle/bacterial nanocellulose paper composites for paste-and-read SERS detection of pesticides on fruit surfaces. *Carbohydrate Polymers* **2020**, 235, 115956.
 104. Chen, J.; Huang, M.; Kong, L., Flexible Ag/nanocellulose fibers SERS substrate and its applications for in-situ hazardous residues detection on food. *Applied Surface Science* **2020**, 533, 147454.
 105. Zeng, Z.; Wu, T.; Han, D.; Ren, Q.; Siqueira, G.; Nyström, G., Ultralight, flexible, and biomimetic nanocellulose/silver nanowire aerogels for electromagnetic interference shielding. *Acs Nano* **2020**, 14 (3), 2927-2938.

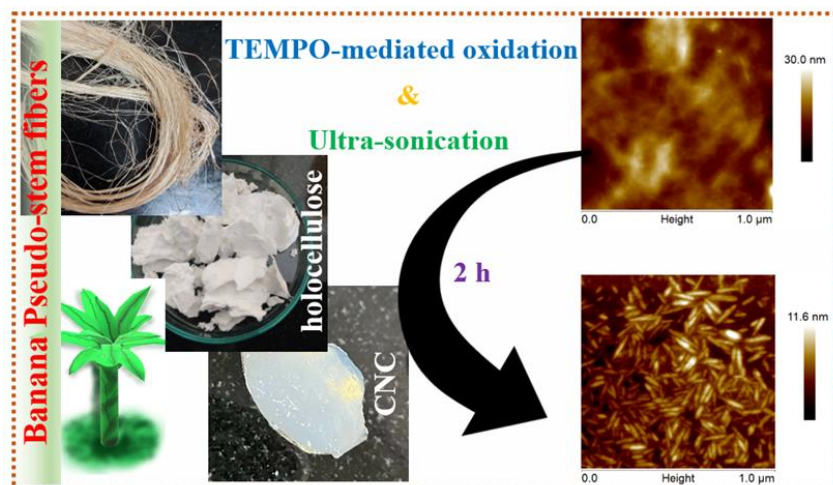
106. Sukhavattanakul, P.; Manuspiya, H., Fabrication of hybrid thin film based on bacterial cellulose nanocrystals and metal nanoparticles with hydrogen sulfide gas sensor ability. *Carbohydrate polymers* **2020**, *230*, 115566.
107. Easson, M. W.; Jordan, J. H.; Bland, J. M.; Hinchliffe, D. J.; Condon, B. D., Application of Brown Cotton-Supported Palladium Nanoparticles in Suzuki–Miyaura Cross-Coupling Reactions. *ACS Applied Nano Materials* **2020**, *3* (7), 6304-6309.
108. Abdelgawad, A. M.; El-Naggar, M. E.; Elsherbiny, D. A.; Ali, S.; Abdel-Aziz, M. S.; Abdel-Monem, Y. K., Antibacterial carrageenan/cellulose nanocrystal system loaded with silver nanoparticles, prepared via solid-state technique. *Journal of Environmental Chemical Engineering* **2020**, *8* (5), 104276.
109. Musino, D.; Rivard, C.; Landrot, G.; Novales, B.; Rabilloud, T.; Capron, I., Hydroxyl groups on cellulose nanocrystal surfaces form nucleation points for silver nanoparticles of varying shapes and sizes. *Journal of Colloid and Interface Science* **2021**, *584*, 360-371.
110. Rusin, C. J.; El Bakkari, M.; Du, R.; Boluk, Y.; McDermott, M. T., Plasmonic cellulose nanofibers as water-dispersible surface-enhanced Raman scattering substrates. *ACS Applied Nano Materials* **2020**, *3* (7), 6584-6597.
111. Gu, J.; Dichiaro, A., Hybridization between cellulose nanofibrils and faceted silver nanoparticles used with surface enhanced Raman scattering for trace dye detection. *International Journal of Biological Macromolecules* **2020**, *143*, 85-92.
112. Cieśla, J.; Chylińska, M.; Zdunek, A.; Szymańska-Chargot, M., Effect of different conditions of synthesis on properties of silver nanoparticles stabilized by nanocellulose from carrot pomace. *Carbohydrate Polymers* **2020**, *245*, 116513.
113. Bergamonti, L.; Potenza, M.; Poshtiri, A. H.; Lorenzi, A.; Sanangelantoni, A. M.; Lazzarini, L.; Lottici, P. P.; Graiff, C., Ag-functionalized nanocrystalline cellulose for paper preservation and strengthening. *Carbohydrate Polymers* **2020**, *231*, 115773.
114. Chen, X.; Lin, H.; Xu, T.; Lai, K.; Han, X.; Lin, M., Cellulose nanofibers coated with silver nanoparticles as a flexible nanocomposite for measurement of flusilazole residues in Oolong tea by surface-enhanced Raman spectroscopy. *Food Chemistry* **2020**, *315*, 126276.
115. Jiang, F.; Hsieh, Y.-L., Synthesis of cellulose nanofibril bound silver nanoprism for surface enhanced Raman scattering. *Biomacromolecules* **2014**, *15* (10), 3608-3616.
116. Kang, S.; Rahman, A.; Boeding, E.; Vikesland, P. J., Synthesis and SERS application of gold and iron oxide functionalized bacterial cellulose nanocrystals (Au@ Fe₃O₄@ BCNCs). *Analyst* **2020**, *145* (12), 4358-4368.
117. Gopiraman, M.; Saravanamoorthy, S.; Baskar, R.; Ilangovan, A.; Ill-Min, C., Green synthesis of Ag@ Au bimetallic regenerated cellulose nanofibers for catalytic applications. *New Journal of Chemistry* **2019**, *43* (43), 17090-17103.
118. Asgari, S.; Sun, L.; Lin, J.; Weng, Z.; Wu, G.; Zhang, Y.; Lin, M., Nanofibrillar cellulose/Au@ Ag nanoparticle nanocomposite as a SERS substrate for detection of paraquat and thiram in lettuce. *Microchimica Acta* **2020**, *187* (7), 1-11.
119. Kistler, S. S., Coherent expanded aerogels and jellies. *Nature* **1931**, *127* (3211), 741-741.

Introduction

120. Mathew, A. P.; Oksman, K.; Pierron, D.; Harmand, M. F., Biocompatible fibrous networks of cellulose nanofibres and collagen crosslinked using genipin: potential as artificial ligament/tendons. *Macromolecular Bioscience* **2013**, *13* (3), 289-298.
121. Zander, N. E.; Dong, H.; Steele, J.; Grant, J. T., Metal cation cross-linked nanocellulose hydrogels as tissue engineering substrates. *ACS applied materials & interfaces* **2014**, *6* (21), 18502-18510.
122. (a) Jiang, F.; Hsieh, Y.-L., Cellulose nanofibril aerogels: synergistic improvement of hydrophobicity, strength, and thermal stability via cross-linking with diisocyanate. *ACS applied materials & interfaces* **2017**, *9* (3), 2825-2834; (b) Zhang, F.; Ren, H.; Dou, J.; Tong, G.; Deng, Y., Cellulose nanofibril based-aerogel microreactors: A high efficiency and easy recoverable W/O/W membrane separation system. *Scientific Reports* **2017**, *7* (1), 1-7.
123. De France, K. J.; Hoare, T.; Cranston, E. D., Review of hydrogels and aerogels containing nanocellulose. *Chemistry of Materials* **2017**, *29* (11), 4609-4631.
124. Ram, F.; Biswas, B.; Torris, A.; Kumaraswamy, G.; Shanmuganathan, K., Elastic piezoelectric aerogels from isotropic and directionally ice-templated cellulose nanocrystals: comparison of structure and energy harvesting. *Cellulose* **2021**, *28* (10), 6323-6337.

CHAPTER 2

Banana Fibers as Efficient Source for the Acid-free Synthesis of Cellulose Nanocrystals



ABSTRACT

Currently, polymers derived from petroleum byproducts are still employed in a majority of technologies and commercial items. These lead to the quest for alternatives that are environmental friendly with low health and safety risks within affordable prices. The use of natural resources is important for the growth and advancement of a sustainable economy around the world. In this chapter, we present an efficient and energy-saving method for the synthesis of cellulose nanocrystals (CNC) from banana pseudo-stem fibers by TEMPO-mediated oxidation followed by ultrasonication. In addition to chemical functionalization, subsequent mechanical disintegration also plays an important role in the derived nanocellulose. Optimization, structure, and properties of CNC were conducted at varying ultrasonication durations. Since the quantity of conversion is vital in every synthesis method, yield, and the material properties of CNC from banana pseudo-stem fibers were compared with other plant parts like Areca nut leaf sheaths and Mahogany hardwood. This study highlights the utilization of banana pseudo-stem fibers as an appropriate choice of source for the production of CNC by an acid-free route where TEMPO-mediated oxidation followed by ultrasonication.

2.1. INTRODUCTION

Nanocellulose emerged as the ‘nano’ prototype of the ubiquitous natural polymer cellulose by overcoming most of its hindrances towards the processability and applicability. Nanocellulose is well-known in three different faces, namely cellulose nanofiber (CNF), cellulose nanocrystal (CNC), and bacterial cellulose (BNC), regarding their aspect ratio and origin.¹ CNCs are crystalline with a low aspect ratio, whereas CNFs are semi-crystalline, having amorphous along with crystalline parts and a high aspect ratio. In addition to these, BNCs are high-purity cellulose fibers produced by bacteria.² These comprising subclasses in the nanocellulose make it more adaptable and servable in any applications requiring remindful properties.³ The present age is passing through a strong mission among global countries to cut down carbon emissions effectively by welcoming

Acid-free synthesis of CNC

sustainable alternatives. Here comes the prominence of modified cellulose-based materials, but from the past decade, cellulose is always pointed towards wood, and it has become the most exploited source of cellulose. These increasing demands lead to deforestation, which made a huge impact on landscapes globally. Since cellulose is the major component in the plant kingdom, agricultural residues can be considered as resources of cellulose with the bonus mark of waste to product approach. Hemp, banana fibers, flax, pineapple leaf, jute, ramie, and cotton are some of the known resources of cellulose in unnegotiable amounts. There are several top-down synthetic procedures to transform natural cellulose form into custom-made functional materials so as to exploit their intrinsic physical and chemical properties. All these methods include energy-consuming steps that are necessary to break the bundle of microfibrils to the end form of nano.⁴ Crops as cellulose sources for the production of nanocellulose not only avoid the use of valuable commodities but also low energy consumption for processing due to the decrease in the lignin content.⁵

Even though Bananas are mainly cultivated in tropical countries, this fruit is unavoidable and the second most consuming fruit worldwide. As a Musaceae plant family member, more than 60% of banana trees become agricultural wastes after harvesting, including its pseudo-stem.⁶ As a result, more than 100 million metric tons of banana plant wastes are produced worldwide, especially in India, China, Indonesia, Brazil, Ecuador, Philippines, Colombia, etc., being the main global banana producers. These can be fruitfully utilized in different value-added products, such as biodegradable packaging materials, bioplastics, etc.⁷ In 2022, ICAR-NRCB, India, has developed and licensed their sustainable technology for banana fiber processing from its pseudo-stem wastes.⁸

Banana fibers are attractive candidate for plant-derived cellulose containing almost 50-65% cellulose. These high amounts of cellulose can be systematically isolated and can be converted into nanocellulose with more energy-saving benefits. Chemically treated banana fibers are known for their higher crystallinity index of about 62% beneficial for cellulose nanocrystal (CNC) production. Acid hydrolysis is the most adapted method for the isolation of CNC from cellulose, in which the fraction of amorphous parts in the semi-crystalline polymer gets hydrolyzed by H₂SO₄, and crystalline parts get untouched.⁹ The main obstacles to this method arise from the handling of concentrated acids, heavy and

prolonged neutralization, and low yield. In 2019, Isogai *et al.* put forward the isolation of CNF, CNC, and cellulose nanonetworks (CNN) by TEMPO-mediated oxidation.¹⁰ Production of CNC from TEMPO-mediated oxidation can be particularly achieved by ultrasonication. Benefits of choosing ultrasonication as the mechanical disintegration method serve the simple and minimum requirement of an ultrasonication bath apart from high-pressure homogenization, microfluidization, sonication, mechanical grinding, etc., adopted in other production strategies.¹¹

Herein, we investigate an acid-free TEMPO-mediated oxidation process for the synthesis of cellulose nanocrystals (CNCs) with a relatively high yield (95%) from untapped banana pseudo-stem wastes. The time duration for cavitation force treatment using ultrasonication after TEMPO-mediated oxidation is very well studied to get the maximum yield of CNC from banana fibers. Properties of CNC at different sonication durations were also discussed systematically by using Fourier Transform Infrared spectroscopy (FTIR), Wide-angle X-ray Scattering (WAXS), Atomic Force Microscope (AFM), Dynamic Light Scattering (DLS), UV-Visible Spectrophotometer, and X-ray Photoelectron Spectroscopy (XPS) as characterization techniques. Feasibility of banana fiber as a cellulose source was compared with two other plant parts, hardwood (Mahogany wood) and leaves (Areca nut leaf sheath). We verified that the exact oxidation procedure and mechanical disintegration may not work on different sources depending upon their recalcitrant behavior. Breakthroughs in terms of yield with less energy consumption make this material, a source for CNC production without compromising sustainability and quality.

2.2. EXPERIMENTAL SECTION

2.2.1. Materials

Banana pseudo-stem fibers (NaOH treated), Areca nut leaf sheaths, and Mahogany hardwood chips were collected from agricultural and timber industry wastes and used as cellulose sources. Sodium chlorite (NaClO_2), 2,2,6,6-tetramethyl piperidine-1-oxyl radical (TEMPO; $\text{C}_9\text{H}_{18}\text{NO}$), sodium hypochlorite (NaClO), sodium bromide (NaBr) used for

Acid-free synthesis of CNC

bleaching and subsequent TEMPO-mediated oxidation of the holocellulose purchased from Sigma-Aldrich, India. Sodium hydroxide for pretreatment was brought from Rankem. Ultrapure deionized (DI) water (Milli-Q purifier system, Merck, Germany) was consumed as the solvent in the complete synthesis procedure.

2.2.2. Extraction of Holocellulose

The ultimate strategy for extracting holocellulose by abolishing both lignin and hemicellulose content explained in the literature has been slightly modified as adequate as starting material.¹² Banana pseudo-stem fibers were initially pre-treated with excess NaOH during the extraction process. Subsequently, delignification was done at a minimum of two times with 1.7 wt% NaClO₂ at pH 4 at 150 °C until the biomass turned into a white cotton-like substance. The obtained holocellulose was washed thoroughly with DI water, dried, and kept for further experiments. Removal of non-cellulosic contents from the banana fibers were done by pretreatment and delignification steps for three repeated cycles. The exact same procedure is also adopted for other sources, Areca nut leaf sheaths and Mahogany hardwood for comparison.

2.2.3. Preparation of TEMPO-oxidized Nanocellulose (TNC)

TEMPO-oxidation was performed by the procedure put forward by Isogai and co-workers.¹³ Concisely, a catalytic quantity of TEMPO (0.032 g) was accurately weighed and dissolved in DI water by stirring for 5 min in a 500 mL flat bottom flask. Then 0.32 g of NaBr and 1.00 g of holocellulose were added, and the water content was increased to 270 mL by adding additional DI water. The oxidation process was initiated by adding a 30 mL ice-cooled NaClO solution at pH 10–11 range. Due to the presence of excess NaOH in the holocellulose, further addition of NaOH was not required. The reaction was conducted for 1 h. During the reaction, region-selective conversion of carbon-6 (C6) hydroxyl to carboxyl group was monitored from the way of consumption of NaOH or pH measured at regular 5 min intervals.

2.2.4. Ultrasonication as Mechanical Disintegration

A 350 W ultrasonication bath was used for the mechanical disintegration of the TEMPO-oxidized cellulose containing reaction mixture. Ultrasonication was carried out in cooled water at a frequency of 40 kHz under the low strength of the ultrasonic wave. Suspension after TEMPO-oxidation was transferred to an ultrasonication bath and subjected to sonication for 0, 0.5, 1, 2, and 4 h keeping at ice-cold condition. Further oxidation process was quenched by adding 5 mL of ethanol. The final product was separated by washing and followed by freeze-drying. The exfoliated nanocellulose form was denoted as TNC since it was not confirmed as CNF or CNC.

2.2.5. Characterizations of TNC

The FTIR spectrometer (PerkinElmer) was used to study the chemical structure of TNC by scanning in the range from 4000 to 400 cm^{-1} . Wide-Angle X-ray Scattering (WAXS) pattern of TNC and holocellulose was recorded using XEUSS SAXS/WAXS system from Xenocs operated with Cu $K\alpha$ ($\lambda = 1.54 \text{ \AA}$), 50 kV. The crystallinity index (CI) of holocellulose and TNC were measured using the equation:

$$CI = \frac{I_{200} - I_{am}}{I_{200}}$$

Where I_{200} is the intensity of diffraction peak at $2\theta = 22.5^\circ$, and I_{am} is the minimum intensity diffraction peak from the amorphous region between (1-10) and (200) planes. Aspect ratio or dimension of nanocellulose is very crucial for confirming the type of nanocellulose (CNC or CNF) were obtained using Atomic Force Microscopy in tapping mode (AFM, Multimode 8 atomic force microscope linked to Nanoscope V controller (Bruker, Santa Barbara, CA). Si cantilevers (NSG 01, NT-MDT) with a 10 nm radius of curvature and a scan rate of 1 Hz were used. The resonance frequencies ranged from 120 to 180 kHz, and the force constant of the AFM probe ranged from 2.5 to 10 N/m. Scan size from $10 \times 10 \mu\text{m}^2$ to $800 \times 800 \text{ nm}^2$ at 512×512 -pixel resolution were recorded. Samples were deposited on an ultra-smooth mica substrate and dried under vacuum for 24 h prior to the AFM measurements. The dynamic light scattering (DLS) data and zeta potential were obtained

Acid-free synthesis of CNC

from Zetasizer Nano ZS, Malvern equipment. Transmittance of TNC dispersed in water were recorded by UV-2600 spectrophotometer by Shimadzu, Kyoto, Japan. Samples for DLS, zeta potential, and transmittance measurements were prepared by dispersing 0.1% (w/v) in water. The carboxyl content of TNC were experimentally estimated using conductometric titration. X-ray photoelectron spectroscopy (XPS) study was performed using PHI 5000 VersaProbe II, ULVAC-PHI Inc., USA. The binding energies of XPS peaks were referenced to the C1s peak at 284.8 eV.

2.3. RESULTS AND DISCUSSION

2.3.1. Optimization of Ultrasonication Time

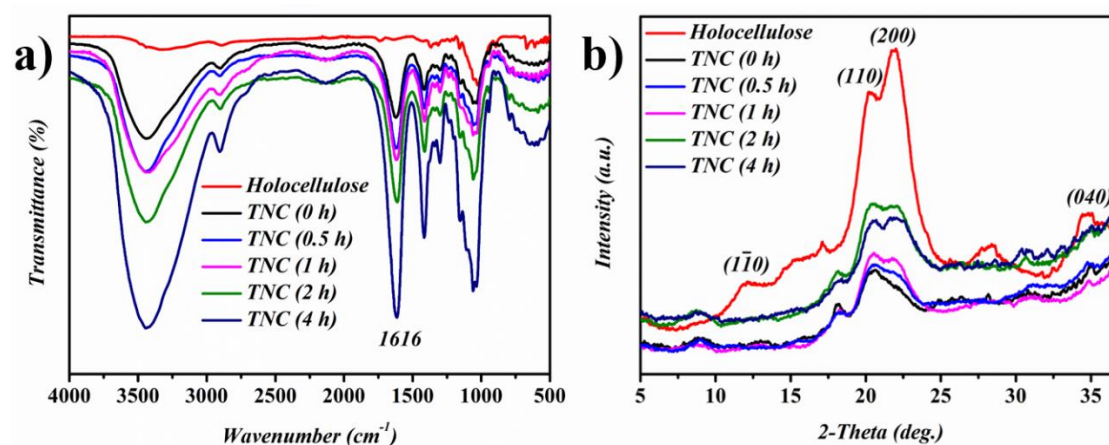


Figure 2.1. (a) FTIR spectra and (b) WAXS patterns of TNC at different ultrasonication duration from 0 h to 4 h.

TEMPO/NaBr/NaClO oxidation can effectively graft carboxyl groups on the selective positions of cellulose chains, thereby imparting better processability and solubility properties. Maintaining the pH between 10-11 is very important for this functionalization because non-selective and aggressive oxidation properties may occur at lower pH. Sometimes, TEMPO also becomes less active or inactive at lower pH.¹⁴ Post-mechanical treatments also play very crucial in the type and properties of nanocellulose produced. Very low energy consumption is required for oxidized cellulose via TEMPO/NaBr/NaClO system, and it needs to be optimized for every source of cellulose since nature builds a diverse and hierarchical organization of cellulose chains in plant

varieties. In the case of banana pseudo-stem fibers, our assumption is that nanofibrillation occurs at very low energy consumption due to the simple and parallel arrangement of cellulose chains via hydrogen bonding and Van der Waals forces. We attempted several different time durations from 0 to 4 h for ultrasonication to select the optimum period, and all its properties are evaluated in detail.

Figure 2.1 depicts the effect of ultrasonication on the chemical modification and crystallinity of TNC. Functionalization or chemical modifications of cellulose after TEMPO-oxidation can be confirmed from FTIR analysis. The absence of peaks at 1242 cm^{-1} , 1500 cm^{-1} , and 1700 cm^{-1} in the FTIR spectra of TNC (**Figure 2.1a**) indicated that the pretreatment and bleaching processes could remove lignin and hemicellulose contents from the fiber.¹⁵ The introduction of carboxyl functional groups by the regio-selective oxidization of the C6 primary hydroxyl group is evident from the intense peak at 1616 cm^{-1} .¹⁶ Other prominent peaks at 3300-3500 (broad), 2900, 1400-1450, and 1055 cm^{-1} bloated from the -OH stretching, C-H stretching, C-H bending, and C-O stretching vibrations, respectively.¹⁷ After the ultrasonication process, there is a considerable increment in the carboxyl peak intensity with the increase in the ultrasonication time. This implies that oxidation continues throughout the ultrasonication treatment, and the degree of oxidation also depends on the duration of ultrasonication. This needs to be investigated further. WAXS pattern (**Figure 2.1b**) of holocellulose and TNC confirmed the modification of Cellulose I to Cellulose II phase by mercerization as indicated by three peaks at $2\theta = 12.5^\circ$, 20.7° , and 22.1° that are indexed as (110), (110) and (200) planes of Cellulose II.¹⁸ CI values corresponding to TNC from time 0 h to 4 h were estimated by Segal's method, as shown in **Table 2.1**. CI values estimated from WAXS patterns of TNC samples treated at different ultrasonication times 0 h to 4 h were 60%, 61.9%, 62%, 63%, and 62.9%, respectively.

To gain more insight into the morphology and dimension of TNC samples, AFM analysis were carried out. Accordingly, the AFM height images of TNC (**Figure 2.2**) showed that on increasing the duration of ultrasonication treatment, the average length of nanocellulose fibers significantly reduced and fell in the category of CNC with the low aspect ratio. At 2 h of ultrasonication, the formation of crystals becomes more profound,

Acid-free synthesis of CNC

with excellent spindle-like morphology having a length of about 150 ± 20 nm and a width of about 15 ± 5 nm (**Figure 2.2d**). Further, a longer ultrasonication would destroy the structure of CNC, as observed in the AFM height images in 4 h of ultrasonication (**Figure 2.2e**).

Sample	Yield (%)	PDI	Average Particle Size (nm)	Zeta Potential (mV)	XRD crystallinity (%)
TNC (0 h)	43	0.211	1065	-59.43	60
TNC (0.5 h)	50	0.403	377.4	-55.41	61.9
TNC (1 h)	58	0.403	197	-53.45	62
TNC (2 h)	95	0.343	160	-51.68	63
TNC (4 h)	15	0.377	198	-44.86	62.9

Table 2.1. Yield of nanofibrillation and other properties of TNC samples treated at 0 h to 4 h ultrasonication time durations.

Figure 2.3a exhibits a nearly similar size distribution of TNC as observed in AFM height images at different ultrasonication time. At the time 0 h, the size distribution of TNC fell in the category of CNF due to its high aspect ratio. Later, the size decreased upon the increase in the ultrasonication time and dropped in the category of CNC. Detailed data obtained from DLS and zeta potential recorded with 0.1% (w/v) TNC dispersion is shown in **Table 2.1**. Zeta potential values of TNC dispersions from 0 h to 4 h ultrasonication treatment were -59.43, -55.41, -53.45, -51.68, and -44.86 mV, respectively. Zeta potential values showed a descending order upon increasing the ultrasonication time. This is because ultrasonication is always a disintegration process which can reduce the colloidal stability. However, these zeta potential values are very closer and pretty much good, indicating the stability of TNC dispersion compared to other reports.¹⁹ **Figure 2.3b** displays the UV-Visible transmittance spectra of 0.1% (w/v). On increasing the ultrasonication time, the light transparency of TNC suspensions also increased up to 2 h. At 4 h sonication time,

transparency again follows the path of low. An increase in the transmittance is always considered as the fingerprint of the increase in crystallinity and a decrease in the particle size.²⁰ Likewise, an increase in transmittance also can be correlated to the increase in carboxyl content or degree of oxidation.¹⁹ Electrostatic interaction between the induced COO^- groups also provides better dispersibility or solubility in water. This observation in the UV-Visible transmittance spectra also signifies the formation of CNC instead of CNF by this method. In terms of reaction yield (**Figure 2.3c**), results showed that on increasing ultrasonication treatment time from 0 to 2 h, the quantity of CNC generated also increased from 43 to 95% and then drastically disappeared with 4 h, caused by the complete disruption of cellulose. This may have resulted from the rupture of even the crystalline regions of cellulose by the high amount of cavitation force treatment using ultrasonication and increasing temperature. Nanofibrillation yield of only 15% at 4 h and its disrupted structure of crystals as observed in the AFM analysis (**Figure 2.2e**) which is in good agreement with that of time, 2 h as optimum ultrasonication period for CNC from banana pseudo-stem fibers with the excellent yield of production.

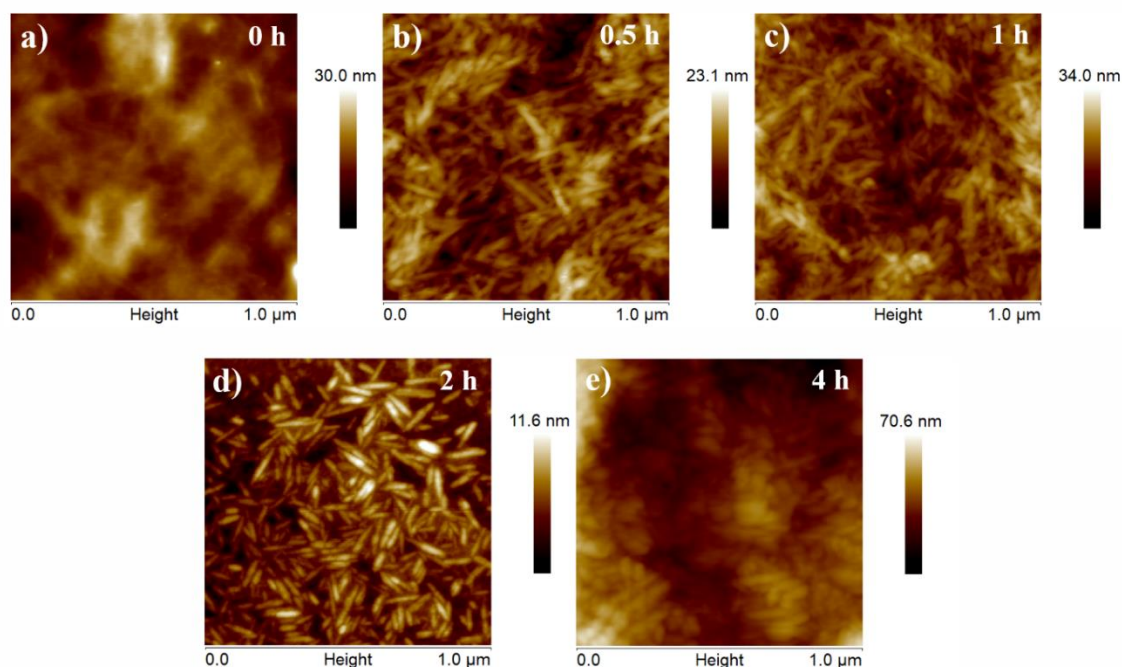


Figure 2.2. AFM height images of TNC samples treated at different ultrasonication times, 0 h to 4 h.

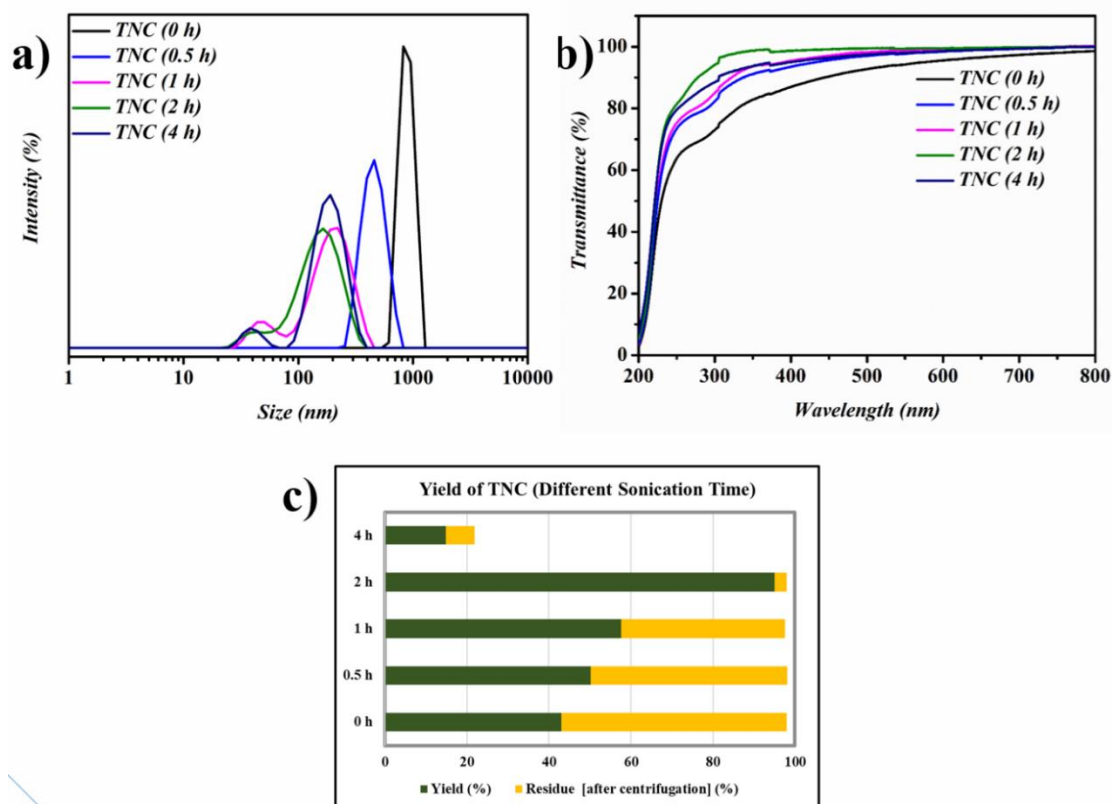


Figure 2.3. (a) DLS spectra, (b) UV-Visible transmittance spectra, and (c) yield of nanofibrillation of TNC samples at different ultrasonication times.

2.3.2. Effect of Ultrasonication on Degree of Oxidation

According to Isogai *et al.*, even though CNF, CNC, or CNW prepared from TEMPO-oxidation followed by any mechanical treatments, all would have the same carboxyl content despite the power of mechanical disintegration.¹⁰ TEMPO-mediated oxidation is always rendered at the surface of cellulose microfibrils. In our detailed literature study, they subjected cellulose to mechanical disintegration as a second step after quenching and washing of product from TEMPO-oxidation.^{13c} Therefore, the introduction of the ultrasonication process before the quenching of the TEMPO-oxidation step could improve or change the carboxyl content of the entire system. In order to study the effect of the ultrasonication time on the degree of oxidation, we estimated the carboxyl content at different ultrasonication times. The results were interesting, and the carboxyl content was

improved by increasing the ultrasonication duration (**Table 2.2**). This observation suggests that a post-ultrasonication treatment also can promote oxidation or carboxyl functionalization. The XPS analysis of samples at the corresponding ultrasonication time has been carried out to find out the surface elemental composition in the system. **Figure 2.4** shows the XPS survey spectra displayed C and O are major elements with peaks, at 532 eV for O 1s and 284 eV for C 1s.

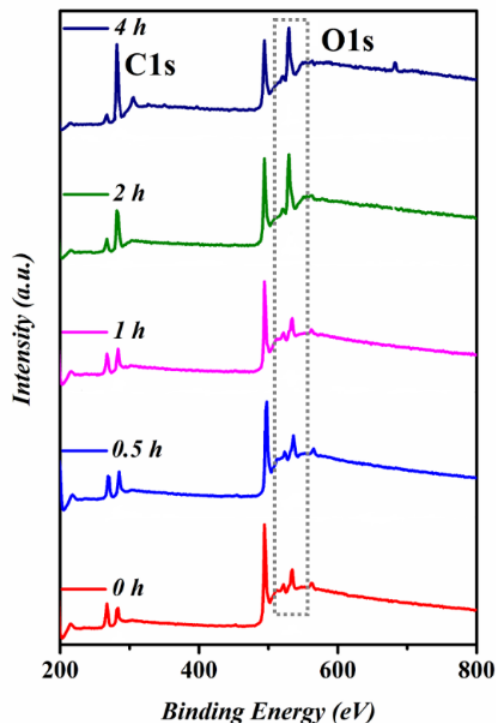


Figure 2.4. XPS survey spectra of TNC at different ultrasonication treatments from 0 h to 4 h.

The trend of increase in the elemental oxygen content is also in agreement with the increment in the carboxyl content obtained by simple conductometric titrations. Respective of carboxyl content, the O/C ratio estimated at different ultrasonication durations were summarized below (**Table 2.2**). The increase in the O/C ratio depicts the utilization of cavitation force in the progress of TEMPO-mediated oxidation in bulk too. Interestingly, compared to the O/C ratio of holocellulose from banana pseudo-stem fiber was significantly increased from 0.41 to 0.7 for TNC for 2 h ultrasonication. The obtained O/C ratio for TNC for 2 h ultrasonication was higher than the O/C ratio reported for TEMPO-

Acid-free synthesis of CNC

oxidized nanocellulose in the literature.²¹ The O/C ratio obtained were 0.02, 0.07, 0.3, and 0.7 for ultrasonication time from 0 h, 0.5h, 1 h, and 2 h, respectively. At the sonication time 4 h, the O/C ratio was decreased to 0.3, ascribed to the destruction of the entire system.

Sample	Carboxyl content (mmol/g)	O/C Ratio from XPS
Holocellulose	-----	0.41
TNC (0 h)	0.04	0.02
TNC (0.5 h)	0.16	0.07
TNC (1 h)	0.59	0.3
TNC (2 h)	1.32	0.7
TNC (4 h)	0.53	0.3

Table 2.2. Carboxylate content and O/C ratio obtained from XPS for TNC at different ultrasonication times, 0 h to 4 h.

In order to obtain more elucidations from XPS, deconvoluted C1s XPS spectra of TNC at different ultrasonication times from 0 to 4 h were plotted and presented in **Figure 2.5(a-e)**. We could fit four distinct peaks attributed to C-C/C-H, C-O, O-C-O/C=O, and O-C=O chemical bonds at 284.7, 286.2, 288, and 289.2 eV, respectively.²² The peak areas of deconvoluted peaks in the C1s spectra exhibited a decrease in the percentage area corresponding to C-C/C-H and a gradual increase in the peak area of C-O, O-C-O/C=O, and O-C=O chemical bonds with the increase in the ultrasonication time. The area under the deconvoluted peaks corresponds to C-C/C-H, C-O, O-C-O/C=O, and O-C=O chemical bonds were tabulated below. (**Table 2.3**) This increment in the area corresponding to these oxygen-containing bonds strengthens and proves the increase in the carboxyl content and respective degree of oxidation by the post-ultrasonication process. Specifically, the % area of the peak corresponding to C-C/C-H bonds of TNC decreased from 79.7 to almost 54.2 by post-ultrasonication treatment. On the other hand, compared with the % peak area of all the initial C-O, O-C-O/C=O, and O-C=O bonds (10.4, 5.2, and 2.2) were increased to 29.4,

11.3, and 4.9, respectively by 2 h ultrasonication time. Further increase in ultrasonication duration to 4 h would completely ruin the cellulose system resulting in a decrease in the % area of peaks of C-O, O-C-O/C=O, and O-C=O bonds to 16, 8, and 1, respectively.

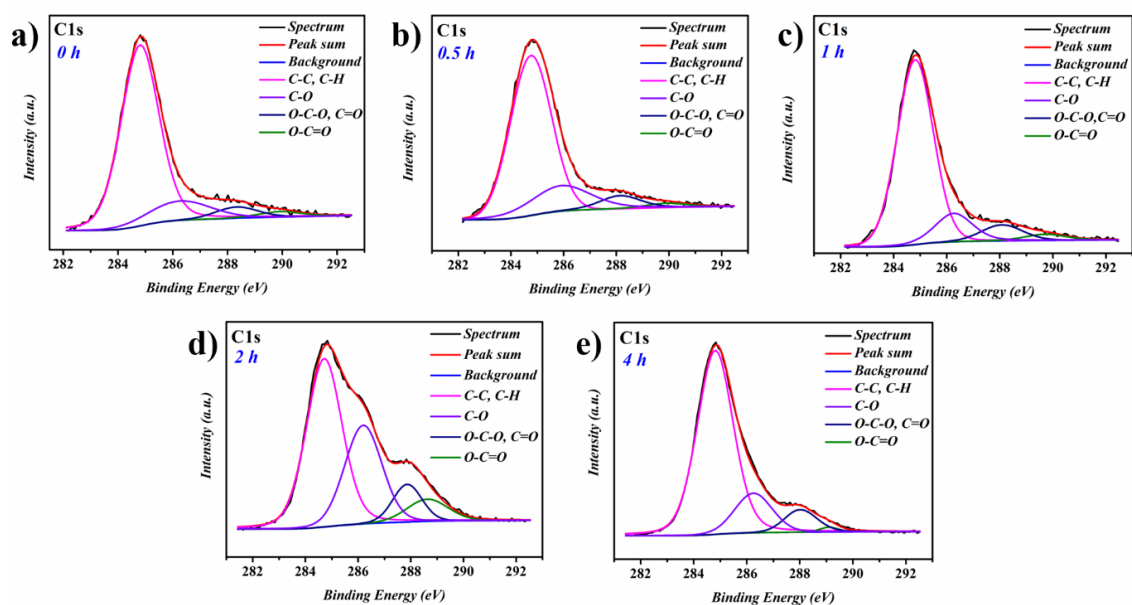


Figure 2.5. The deconvoluted high-resolution C1s spectra of TNC at different ultrasonication times, from 0 h to 4 h.

Sample	Peak Area C-C/C-H (%)	Peak Area C-O (%)	Peak Area O-C-O/C=O (%)	Peak Area O-C=O (%)
TNC (0 h)	79.7	10.4	5.2	2.2
TNC (0.5 h)	78.8	13.1	6.7	2.4
TNC (1 h)	72	19.1	7.47	2.8
TNC (2 h)	54.2	29.4	11.3	4.9
TNC (4 h)	75	16	8	1

Table 2.3. % Peak area of individual or deconvoluted peaks in the peak-fitted high-resolution C1s spectra of TNC at different ultrasonication times, from 0 h to 4 h.

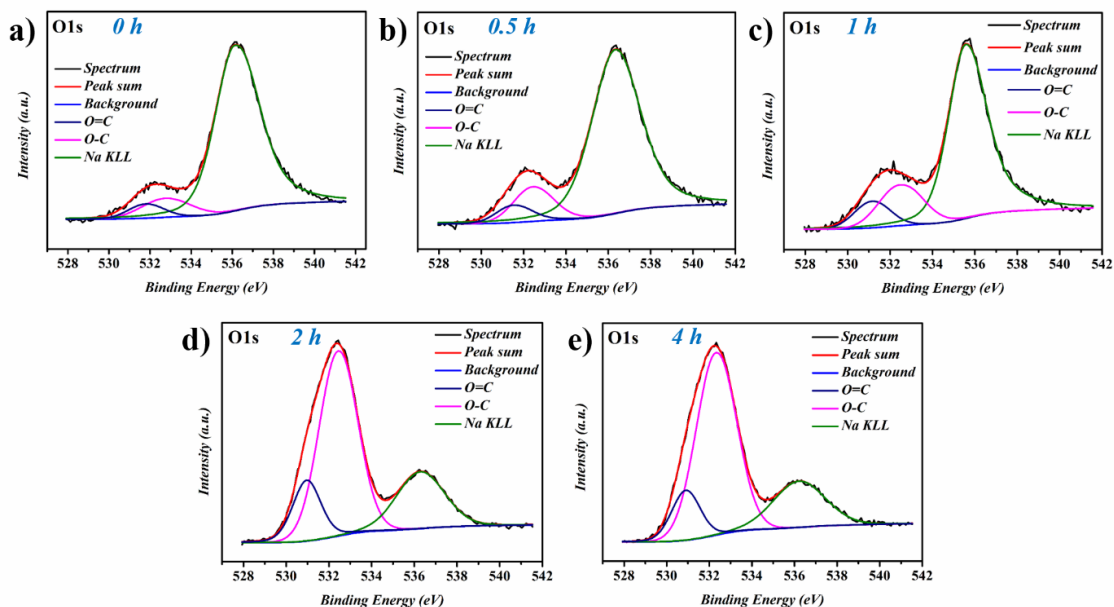


Figure 2.6. Deconvoluted high-resolution O1s spectra of TNC at different ultrasonication times, from 0 h to 4 h (a-e).

The deconvoluted O1s survey spectra of all samples of TNC at different ultrasonication time is shown in **Figure 2.6**. The peak at 532.6 and 530.7 eV corresponds to the O–C and O=C bonds, respectively.²³ When comparing with respect to the Na KLL peak at 535 eV, an increase in the intensity of peaks attributed to the O-C, and O=C groups was significantly noticeable. These observations from XPS analysis of samples of TNC at different sonication also confirmed and validated the increase in the carboxyl content by the post-ultrasonication process observed in the conductometric titrations. Therefore, we could infer that the ultrasonication process can affect the degree of oxidation and resulting prominent properties if TEMPO-mediated oxidation is not quenched before the mechanical disintegration process, and this can be utilized in a better way.

2.3.3. Comparison of TCNC Obtained from Different Plant Sources

To investigate the prominence of banana fiber as a better source for the synthesis of CNC, the synthesis procedure was repeated for cellulose obtained from Areca nut leaf sheaths (TCNC-A) and Mahogany wood (TCNC-W). These two bio-sources were selected

for representing the leaf part and hardwood of the plant kingdom. The entire TEMPO-mediated oxidation step and a 2 h ultrasonication step (where maximum successful CNC formation was observed for banana fiber, TCNC-B) were carried out for these two sources.

Source	Cellulose (%)	Lignin (%)	Hemicellulose (%)	Reference
Areca nut leaf sheath	50-65	17-20	5-10	24
Mahogany wood	50-60	25-30	-----	25
Banana pseudo-stem fibers	50-68	5-10	6-20	26

Table 2.4. Compositions of nanocellulose source.

Table 2.4 shows a composition of different sources (Areca nut leaf sheath, Mahogany wood, Banana pseudo-stem fibers) utilized for the synthesis of nanocellulose found in the literature. However, it may differ in values from one landscape to another. In our experiments, the holocellulose yield obtained from Areca nut leaf sheath, Mahogany wood, and banana pseudo-stem fibers from Kerala (India) region were 49, 35, and 59%, respectively. To understand the crystallinity and chemical modification, WAXS and FTIR spectroscopic analyses have been conducted. A similar WAXS pattern (**Figure 2.7 a-c**) of three samples, TCNC-A, TCNC-W, and TCNC-B obtained were corresponding to Cellulose II. Even though all WAXS patterns show the typical peaks for Cellulose II, dramatic variation in crystallinity was observed. Crystallinity strongly depends upon the source of cellulose. It is observable that TCNC-W shows lower crystallinity than others; this can affect the nanofibrillation yield. The percentage of crystallinity for each sample was calculated from the WAXS pattern and added in **Table 2.5**. Carboxyl functionalization was confirmed by the peak in the range from 1600 to 1620 cm^{-1} in the FTIR spectra of samples (**Figure 2.7 d-f**). The intensity of this carboxyl peak is different in these three sources and significantly very less in the case of TCNC-W. Difficulties in the conversion

Acid-free synthesis of CNC

and functionalization of cellulose from Mahogany wood may be due to the higher amount of lignin present as compared to the other two (**Table 2.4**).

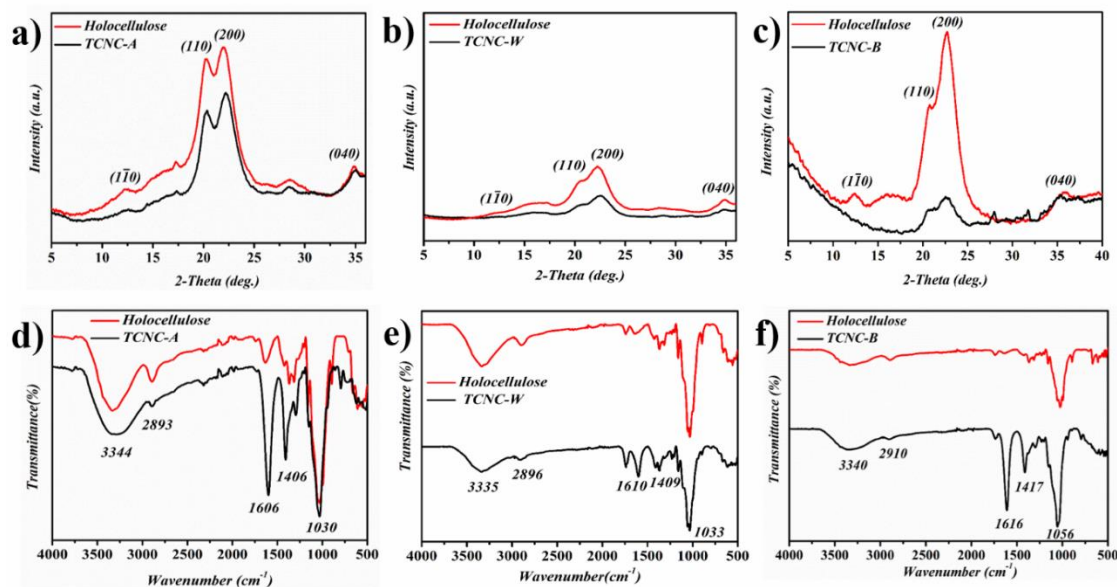


Figure 2.7. (a-c) WAXS and (d-f) FTIR spectra of TNC from Areca nut leaf sheaths, Mahogany wood, and banana pseudo-stem fibers, respectively.

To understand and compare the nanostructure of the cellulosic materials after TEMPO-mediated oxidation and 2 h ultrasonication, AFM analysis has been carried out (**Figure 2.8**). Successful disintegration of cellulose to CNC is attained in all three sources. CNC showed an order in size TCNC-A > TCNC-W > TCNC-B. Significantly, CNC from the banana fiber was observed to have a more distinct and smaller needle-like nanostructure. To evaluate the size distribution, DLS analysis were done since CNC are aggregated and varied in a broad range in AFM height images (**Figure 2.9a**). TCNC-A, TCNC-W, and TCNC-B seemed to have an average size of 249.4, 204.6, and 160, respectively (**Table 2.5**). These results are in good agreement with the AFM images of respective classes. Zeta potential values for all three samples of TCNC were measured: -56.7, -58.2, and -52 mV for TCNC-A, TCNC-W, and TCNC-B, respectively. These higher zeta potential values above -50 mV highlight the ultra-high stability of as-prepared CNCs using our method.

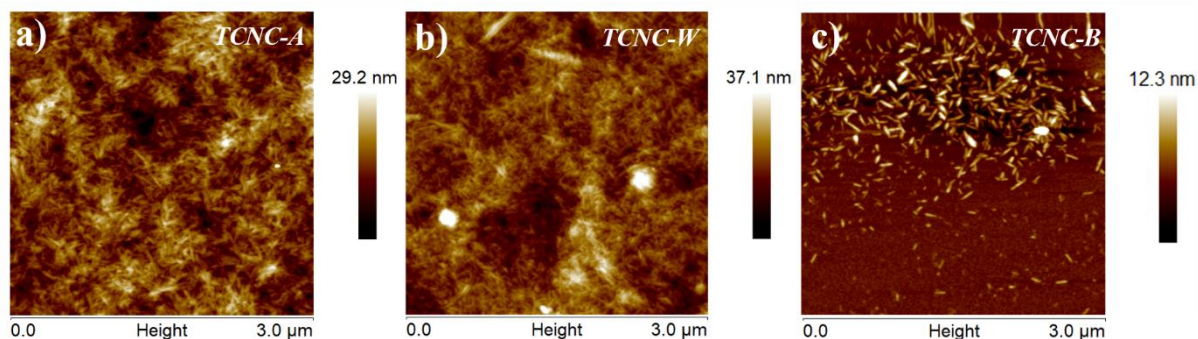


Figure 2.8. AFM height images of CNC from different plant sources.

The light transmittance of 0.1% (w/v) of TCNC-A, TCNC-B, and TCNC-B dispersions were recorded and shown in **Figure 2.9b**. Among the three samples, CNC from banana pseudo-stem fibers showed maximum transmittance. This trend of transmittance of samples is dependent on their carboxyl functionalization or degree of oxidation.¹⁹ Carboxyl contents were estimated for three samples and obtained a value of 1.02, 0.88, and 1.32 mmol/g for TCNC-A, TCNC-W, and TCNC-B, respectively (**Table 2.5**). The lower value in the carboxyl content of TCNC-W can be attributed to all other results, which showed the complexity and resistance of hardwood towards the TEMPO-oxidation and ultrasonication process due to their strong and healthy hierarchical alignment of cellulose. Both carboxyl content and transmittance were observed to be showing the same trend of TCNC-W < TCNC-A < TCNC-B, highlighting the benefits of banana pseudo-stem fibers as an efficient and good choice of source for CNC. The yield of fibrillation achieved after TEMPO-mediated oxidation and 2 h ultrasonication treatment time was compared for all three sources (**Figure 2.9c**). Since the same oxidation and post-mechanical disintegration strategy were used for all three sources, the yield of CNCs were completely correlated to the complexity of alignment of cellulose chains in different sources by Van der Waals interactions and hydrogen bonding, which provide resistance to chemical reactions and mechanical treatments. Hardwoods are always known for their mechanical strength inherent in their hierarchical structure of cellulose and lignin as plant cell walls. These same advantages of hardwood affect oppositely on our applications and treatments can be observed by a low yield of 36% (**Table 2.5**). Areca nut leaf sheath shows a higher yield of

Acid-free synthesis of CNC

about 50% on nanofibrillation than Mahogany wood, even though it is significantly lower than banana pseudo-stem fibers (94%).

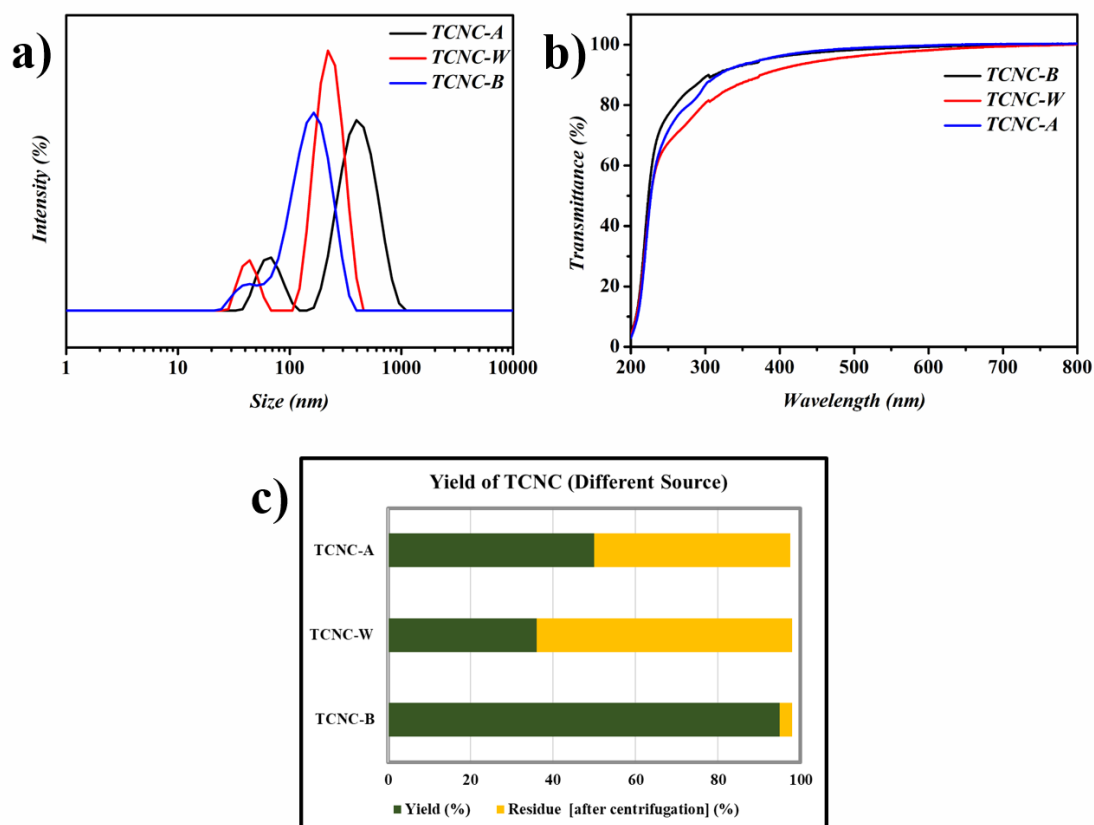


Figure 2.9. a) DLS, b) UV-Visible transmittance spectra, and c) nanofibrillation yields of TCNC-A, TCNC-W, and TCNC-B.

Sample	Yield (%)	PDI	Average Particle Size (nm)	Zeta Potential (mV)	Carboxylate content (mmol /g)	XRD crystallinity (%)
TCNC-A	50	0.356	249.4	-56.7	1.02	72
TCNC-W	36	0.343	204.6	-58.2	0.88	59
TCNC-B	95	0.343	160	-52	1.32	63

Table 2.5. Consolidated properties of CNC from selected sources.

This study reveals that Mahogany wood and Areca nut leaf sheaths showed higher recalcitrance as compared to banana pseudo-stem fibers since it is a crop variety. Results obtained from this comprehensive comparison between the ease of preparation of CNC from different plant parts displayed that banana pseudo-stem fibers are much more reactive toward TEMPO oxidation mainly due to the less complex hierarchical structure and stacking of cellulose chains than other plant parts.²⁷ TEMPO-mediated oxidation is always more active and progressing inaccessible and/or disordered regions.

2.4. CONCLUSIONS

Nanocellulose with desirable properties was born in the twentieth century as a part of research for sustainable alternatives from the most abundant natural source, cellulose. Along with chemical functionalization, subsequent mechanical disintegration plays an important role in the nanocellulose that was derived. This study enlightens the applicability of banana pseudo-stem fibers as a favorable origin for the acid-free synthesis of CNC efficiently and energy-saving manner. Nanofibrillation yield, carboxyl content, crystallinity, adequate morphology, transparency, and other properties were investigated at different levels of ultrasonication treatment time as post-mechanical disintegration. TEMPO-oxidation followed by 2 h ultrasonication was optimized to be best for banana pseudo-stem fibers for the preparation of CNC with properties. A similar strategy was adopted to evaluate the prominence of banana fiber as a source for the CNC against Areca nut leaf sheath and Mahogany wood as a model representative for diverse and bio-originated plant parts. Both sources under the same procedures did not exhibit excellent results from banana pseudo-stem fibers due to their recalcitrant nature. This method can be adapted to produce diverse nanocellulose with required properties from banana fiber in an efficient and energy-conservative way.

2.5. REFERENCES

1. Das, R.; Lindström, T.; Sharma, P. R.; Chi, K.; Hsiao, B. S., Nanocellulose for sustainable water purification. *Chemical Reviews* **2022**, *122* (9), 8936-9031.

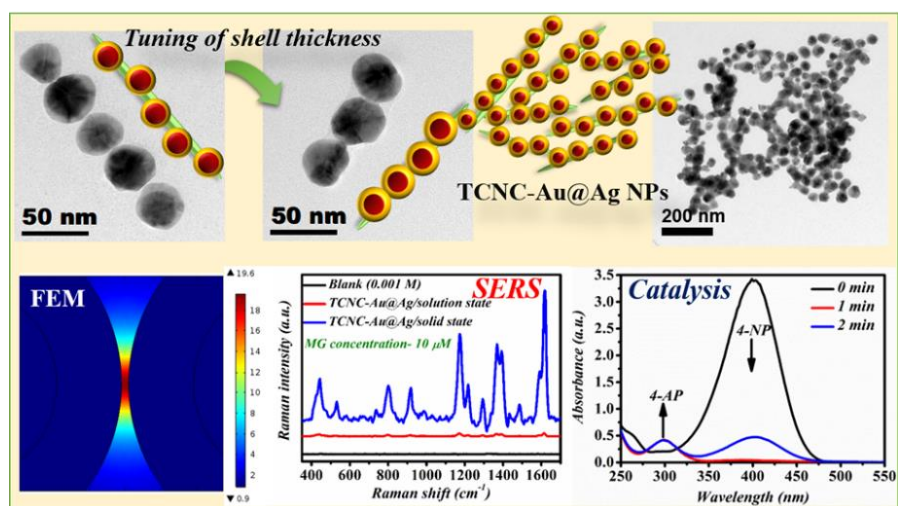
2. Etale, A.; Onyianta, A. J.; Turner, S. R.; Eichhorn, S. J., Cellulose: A Review of Water Interactions, Applications in Composites, and Water Treatment. *Chemical Reviews* **2023**.
3. Thomas, B.; Raj, M. C.; Joy, J.; Moores, A.; Drisko, G. L.; Sanchez, C., Nanocellulose, a versatile green platform: from biosources to materials and their applications. *Chemical reviews* **2018**, *118* (24), 11575-11625.
4. Pinto, L. O.; Bernardes, J. S.; Rezende, C. A., Low-energy preparation of cellulose nanofibers from sugarcane bagasse by modulating the surface charge density. *Carbohydrate polymers* **2019**, *218*, 145-153.
5. Mohammadinejad, R.; Karimi, S.; Iravani, S.; Varma, R. S., Plant-derived nanostructures: types and applications. *Green Chemistry* **2016**, *18* (1), 20-52.
6. Alzate Acevedo, S.; Díaz Carrillo, Á. J.; Flórez-López, E.; Grande-Tovar, C. D., Recovery of banana waste-loss from production and processing: a contribution to a circular economy. *Molecules* **2021**, *26* (17), 5282.
7. García, R.; Quevedo, J.; Socorro, A., Practices for the use of solid waste in banana plantations and results of its implementation. *Univ. Soc* **2020**, *12*, 280-291.
8. <https://nrcb.icar.gov.in/Entrepreneur.php>.
9. Tibolla, H.; Pelissari, F. M.; Martins, J. T.; Vicente, A.; Menegalli, F. C., Cellulose nanofibers produced from banana peel by chemical and mechanical treatments: characterization and cytotoxicity assessment. *Food Hydrocolloids* **2018**, *75*, 192-201.
10. Isogai, A.; Zhou, Y., Diverse nanocelluloses prepared from TEMPO-oxidized wood cellulose fibers: Nanonetworks, nanofibers, and nanocrystals. *Current Opinion in Solid State and Materials Science* **2019**, *23* (2), 101-106.
11. Chen, Y.; Zhang, L.; Yang, Y.; Pang, B.; Xu, W.; Duan, G.; Jiang, S.; Zhang, K., Recent progress on nanocellulose aerogels: Preparation, modification, composite fabrication, applications. *Advanced Materials* **2021**, *33* (11), 2005569.
12. (a) Rosli, N. A.; Ahmad, I.; Abdullah, I., Isolation and Characterization of Cellulose Nanocrystals from Agave angustifolia Fibre. *BioResources* **2013**, *8* (2); (b) Lani, N.; Ngadi, N.; Johari, A.; Jusoh, M., Isolation, characterization, and application of nanocellulose from oil palm empty fruit bunch fiber as nanocomposites. *Journal of Nanomaterials* **2014**, *2014*, 13-13.
13. (a) Isogai, A.; Saito, T.; Fukuzumi, H., TEMPO-oxidized cellulose nanofibers. *nanoscale* **2011**, *3* (1), 71-85; (b) Zhou, Y.; Fujisawa, S.; Saito, T.; Isogai, A., Characterization of concentration-dependent gelation behavior of aqueous 2, 2, 6, 6-tetramethylpiperidine-1-oxyl– cellulose nanocrystal dispersions using dynamic light scattering. *Biomacromolecules* **2018**, *20* (2), 750-757; (c) Zhou, Y.; Saito, T.; Bergström, L.; Isogai, A., Acid-free preparation of cellulose nanocrystals by TEMPO oxidation and subsequent cavitation. *Biomacromolecules* **2018**, *19* (2), 633-639.
14. Praskalo, J.; Kostic, M.; Potthast, A.; Popov, G.; Pejic, B.; Skundric, P., Sorption properties of TEMPO-oxidized natural and man-made cellulose fibers. *Carbohydrate polymers* **2009**, *77* (4), 791-798.
15. Saurabh, C. K.; Dungani, R.; Owolabi, A.; Atiqah, N.; Zaidon, A.; Aprilia, N. S.; Sarker, Z. M.; Khalil, H. A., Effect of hydrolysis treatment on cellulose

- nanowhiskers from oil palm (*Elaeis guineensis*) fronds: Morphology, chemical, crystallinity, and thermal characteristics. *BioResources* **2016**, *11* (3), 6742-6755.
16. Nabeela, K.; Thomas, R. T.; Nair, J. B.; Maiti, K. K.; Warriar, K. G. K.; Pillai, S., TEMPO-oxidized nanocellulose fiber-directed stable aqueous suspension of plasmonic flower-like silver nanoconstructs for ultra-trace detection of analytes. *ACS Applied Materials & Interfaces* **2016**, *8* (43), 29242-29251.
 17. Hop, T. T. T.; Mai, D. T.; Cong, T. D.; Nhi, T. T. Y.; Loi, V. D.; Huong, N. T. M.; Tung, N. T., A comprehensive study on preparation of nanocellulose from bleached wood pulps by TEMPO-mediated oxidation. *Results in Chemistry* **2022**, *4*, 100540.
 18. Tang, Z.; Li, W.; Lin, X.; Xiao, H.; Miao, Q.; Huang, L.; Chen, L.; Wu, H., TEMPO-oxidized cellulose with high degree of oxidation. *Polymers* **2017**, *9* (9), 421.
 19. Lv, T.; Luo, Y.; Chen, Y.; Dai, D.; Feng, X.; Chen, H.; Yu, Y.; Ma, L.; Zhang, Y.; Dai, H., Tuning the properties of pineapple peel cellulose nanofibrils by TEMPO-mediated oxidation and ball milling. *Cellulose* **2022**, *29* (18), 9609-9625.
 20. Levanic, J.; Šenk, V. P.; Nadrah, P.; Poljanšek, I.; Oven, P.; Haapala, A., Analyzing TEMPO-oxidized cellulose fiber morphology: new insights into optimization of the oxidation process and nanocellulose dispersion quality. *ACS Sustainable Chemistry & Engineering* **2020**, *8* (48), 17752-17762.
 21. (a) Benkaddour, A.; Jradi, K.; Robert, S.; Daneault, C., Study of the effect of grafting method on surface polarity of tempo-oxidized nanocellulose using polycaprolactone as the modifying compound: Esterification versus click-chemistry. *Nanomaterials* **2013**, *3* (4), 638-654; (b) Barazzouk, S.; Daneault, C., Amino acid and peptide immobilization on oxidized nanocellulose: spectroscopic characterization. *Nanomaterials* **2012**, *2* (2), 187-205.
 22. Fei, Y.; Liang, M.; Yan, L.; Chen, Y.; Zou, H., Co/C@ cellulose nanofiber aerogel derived from metal-organic frameworks for highly efficient electromagnetic interference shielding. *Chemical Engineering Journal* **2020**, *392*, 124815.
 23. Hakkeem, H. M. A.; Babu, A.; Shilpa, N.; Venugopal, A. A.; Mohamed, A.; Kurungot, S.; Pillai, S., Tailored synthesis of ultra-stable Au@ Pd nanoflowers with enhanced catalytic properties using cellulose nanocrystals. *Carbohydrate Polymers* **2022**, *292*, 119723.
 24. (a) Poddar, P.; Islam, M. S.; Sultana, S.; Nur, H.; Chowdhury, A., Mechanical and thermal properties of short arecanut leaf sheath fiber reinforced polypropylene composites: TGA, DSC and SEM analysis. *Journal of Material Science & Engineering* **2016**, *5* (5), 1-7; (b) Poddar, P.; Sultana, S.; Akbar, M., Environmentally sustainability of short Areca-nut leaf sheath fiber reinforced polypropylene composites. *MOJ Poly Sci* **2018**, *2* (3), 48-50.
 25. Colares, C. J.; Pastore, T.; Coradin, V. T.; Camargos, J. A.; Moreira, A. C.; Rubim, J. C.; Braga, J. W., Exploratory analysis of the distribution of lignin and cellulose in woods by raman imaging and chemometrics. *Journal of the Brazilian Chemical Society* **2015**, *26*, 1297-1305.
 26. (a) Shroff, A.; Karolia, A.; Shah, J., Bio-softening of banana fiber for nonwoven application. *Int J Sci Res* **2015**, *4* (4), 1524-1527; (b) Pujari, S.; Ramakrishna, A.; Kumar, M. S., Comparison of jute and banana fiber composites: A review.

- International Journal of Current Engineering and Technology* **2014**, 2 (2), 121-126.
27. Saito, T.; Isogai, A., TEMPO-mediated oxidation of native cellulose. The effect of oxidation conditions on chemical and crystal structures of the water-insoluble fractions. *Biomacromolecules* **2004**, 5 (5), 1983-1989.

CHAPTER 3

Assembled Au@Ag NPs on Cellulose Nanocrystals with Tailored Plasmonic Nanogaps



This chapter has been adopted from the following publication,

H. M. Abdul Hakkeem *et al.*, *Microchemical Journal*, 2021, 168, 106393.

ABSTRACT

Bio-template-directed synthesis of shell-engineered plasmonic nano-assemblies has attracted extensive research interest due to their profound opto-electronic properties and sustainability. In this chapter, we discuss the potential of TEMPO-oxidized cellulose nanocrystals (TCNC) as a promising bio-template for the in-situ synthesis of assembled Au_{core}-Ag_{shell} nanoparticles (Au@Ag NPs) with tunable optical and catalytic properties. By modulating Ag shell thickness, TCNC promoted the assembly of Au@Ag nanostructures and resulted in abundant plasmonic hotspots. The resultant hotspot engineered Au@Ag nano-assemblies on TCNC exhibited consequential SERS activity in solid-state and could detect malachite green and methylene blue concentrations down to 10 fM and 100 fM, respectively. Importantly, here the TCNC not only acts as a bio-template for the synthesis of core-shell nano-assemblies but also provides higher colloidal stability, as revealed by its zeta potential value of -49.7 mV. The astounding SERS enhancement is further validated by finite element modelling (FEM) studies, which revealed an enhanced electric field concentrates at the junction between two adjacent TCNC-Au@Ag NPs having a separation distance of 1 nm. Further, TCNC-Au@Ag NPs nano-assemblies displayed enhanced catalytic activity towards 4-nitrophenol reduction with a rate constant of $32.33 \times 10^{-3} \text{ s}^{-1}$.

3.1. INTRODUCTION

Morphology-dependant plasmonic features of Au and Ag nanoparticles (NPs) make them enablers for interdisciplinary areas such as SERS¹, catalysis², sensing³, biomedicine⁴, etc. Bimetallic core-shell nanostructures, in particular Au-Ag, have gained noticeable recognition over the past few years due to their excellent opto-electronic properties resulting from the synergic electronic effects, which are dissimilar from their monometallic counterparts.⁵ The fact that surface-enhanced Raman scattering (SERS) is highly reliant on the structures of NPs promotes the researchers to optimize NPs size, shape, and composition to achieve high SERS enhancement. Among the several bimetallic nanostructures, Au@Ag core-shell nanostructures possess improved chemical stability,

Assembled TCNC - Au@Ag NPs

greater plasmonic properties, and excellent electromagnetic enhancement in the visible region, which is widely exploited in the field of SERS.⁶ Besides, when these plasmonic core-shell nanostructures are positioned adjacent to each other to form organized assemblies, the coupling of localized surface plasmon resonance of individual core-shell nanoparticles will occur. It brings exceptionally high electric field enhancements at the junctions of NPs.⁷ It is being established that the SERS responsiveness relies heavily on the electromagnetic (EM) field enhancement persuaded by the hotspots (nanogap junctions between the plasmonic nanostructures) generated by localized surface plasmon resonance (LSPR).⁸ In the domain of SERS, generating these hotspot regions in plasmonic structures that can produce a significant enhancement in Raman signal intensities remains an obstacle.⁹

Catalysts, known as the backbone of the chemical industry, have become a major area of research in industry and academia due to their extensive use. Since catalysis is a surface area influenced phenomenon, top-down conversion from macroscopic to nanoscopic size is essential.¹⁰ Despite the SERS application of bimetallic Au-Ag NPs, it is known that the Au@Ag systems having a variable surface composition and particle size will modify the overall electronic and ensemble effects of the catalyst and, thereby, subsequent high catalytic activity.⁵ Results have shown that the diameter of the core and thickness of the shell plays a prominent part in the catalytic efficiencies as well as SERS properties of Au@Ag NPs.¹¹ The efficacy of Au-Ag bimetallic NPs in various catalytic applications has been investigated in quite a few studies.¹¹⁻¹² However, the greater tendency of nanostructures towards agglomeration may significantly deteriorate their plasmonic properties and catalytic activity.¹³ Plasmonic nanostructures with long shelf-life, which hold their plasmonic properties and high surface area, are essential for catalytic activity. Even though some progress was made in the area of spherically shaped Au@Ag NPs, controlled growth of nanostructures with stability, uniformity in size, and morphology remains a challenge. Uniformity and anisotropy in nanostructures can be achieved by using capping agents like CTAB, CTAC, PVP, etc., which are well known but may reduce the catalytic or SERS activities of nanostructures since they prevent reactant molecule adsorption on the surface of the nanostructures or hinder with the identification of

compounds of concern.¹⁴ Further, to improve the SERS sensitivity of the nanosubstrates, it can be fabricated into ordered arrays by lithography, self-assembly, and template methods.¹⁵ Nevertheless, some of these methods are time consuming, expensive, and have minimal output. Hence for practical applications, an efficient SERS substrate is required to have i) superior stability, ii) numerous hotspots to ensure high sensitivity, iii) uniform dissemination of the hotspots to achieve better reproducibility of the signal, and iv) method of preparation should be easy and green. Whereas in catalysis, high surface area, optimum size, and stability of nanostructures are relevant.

Various biomaterials based templates for metal nanostructures synthesis have been emerged recently as green candidates. In which nanocellulosic materials are emerging as a promising sustainable biomaterial for the in-situ synthesis of plasmonic nanostructures. Nanocellulose can prevent the uncontrolled aggregation of metal NPs even in low pH environments.¹⁶ However, the impact of nanocellulose as a nano-designer in the NPs synthesis is only found lately, and has not been fully explored. For example, *Wei et al.* described the preparation of Au/nanocellulose composite by in-situ reduction of Au³⁺ in BC hydrogel for SERS applications.¹⁷ *Johnson et al.* studied the nanocomposite of crystalline cellulose nanofiber-Ag NPs and demonstrated for its electro-catalytic properties in the oxygen reduction reaction.¹⁸ Nanocellulose has great potential for chemical modification and functionalization through the hydroxyl groups and TEMPO-mediated oxidation of cellulose is considered as the best cost-effective approach for nanocellulose extraction from plant sources.¹⁹ TEMPO-oxidized nanocellulose fibers with high densities of carboxylate groups on the surface offer anchor sites for metal NPs. Apart from TEMPO-oxidised nanocellulose fibers (TCNF) produced by TEMPO-oxidation followed by homogenization, TEMPO-oxidised cellulose nanocrystals (TCNC) with spindle-like morphology (low aspect ratio) can be prepared by replacing homogenization with ultrasonication and it is recently proposed by *Isogai et al.*²⁰ The inherent -OH, induced -COOH functional groups, good water dispersibility, and self-assembling behavior enable TCNC as the right option for NPs synthesis.²¹

There have been several reports dealing with cellulose nanocrystals (CNC) to prepare metallic NPs, whereas limited studies have been reported for the synthesis of

Assembled TCNC - Au@Ag NPs

bimetallic Au-Ag nanostructures.²² Seed-mediated synthesis of nanostructures of Au@Ag core-shell by growing an appropriate quantity of Ag shell over Au core is proven to be an effective option for achieving a highly potential bimetallic system. Recently, *Asgari et al.* prepared Au@Ag/cellulose nanofibers (CNF) nanocomposite by simply mixing CNF suspension with Au@Ag NPs in an equimolar ratio for SERS applications.²³ In another report, *Gopiraman et al.* utilized CNF produced by electrospinning of cellulose acetate to generate CNF/Au@Ag bimetallic nanocomposites for catalytic applications.²⁴ However, none of these studies has investigated the utility of CNF or CNC for the in-situ preparation of Au@Ag NPs due to the complexity of achieving control over the morphology in the nanocellulose matrix. The advantage of in-situ synthesis of core-shell NPs on TCNC bio-template would be the control over the assembly of plasmonic nanostructures, which allows for maximum SERS enhancement.

In this chapter, we discuss a facile bio-supported method for the in-situ preparation and assembly of Au@Ag core-shell NPs on carboxylated cellulose nanocrystals and demonstrate its dual role as a susceptible SERS platform and catalytic support. It provides a straightforward and robust green route for generating core-shell nanostructures in the aqueous medium over organic solvents. The synthesis procedure relies on the controlled reduction of Ag(I) ions over TCNC stabilized Au NPs through a seed-mediated method, resulting in Au@Ag nanostructures with tunable optical properties. Subsequently, the resultant Au@Ag nanostructures are effectively assigned as a substrate for the trace-level SERS detection of two carcinogenic adulterant dyes: malachite green and methylene blue, widely used as colorants and biocides in the aquaculture industry. Furthermore, the catalytic properties of optimized TCNC-Au@Ag nano-assemblies are studied kinetically following the reduction of 4-nitrophenol as a typical catalytic reduction reaction. This context would also bring new insight into the various functions of TCNC, such as (1) an environmentally benign template for the synthesis of Au@Ag NPs with excellent colloidal stability and longer shelf-life, (2) regulated growth of core-shell nanostructures and subsequent inter-particle coupling, (3) more importantly, astounding enhancement in SERS especially in solid-state by TCNC enabled hotspot engineering, and (4) superior homogeneous catalytic performance.

3.2. EXPERIMENTAL SECTION

3.2.1. Materials

TCNC prepared from banana pseudo-stem fibers by TEMPO-mediated oxidation and 2h ultra-sonication (Chapter 2, section 2.2.), aurochloric acid ($\text{HAuCl}_4 \cdot 2\text{H}_2\text{O}$), trisodium citrate tribasic dihydrate (TSC; $\text{C}_6\text{H}_5\text{Na}_3\text{O}_7 \cdot 2\text{H}_2\text{O}$), silver nitrate (AgNO_3), L-ascorbic acid (AA; $\text{C}_6\text{H}_8\text{O}_6$), malachite green (MG; $\text{C}_{23}\text{H}_{25}\text{N}_2$), methylene blue (MB; $\text{C}_{16}\text{H}_{18}\text{ClN}_3\text{S} \cdot 3\text{H}_2\text{O}$), 4-nitrophenol (4-NP; $\text{C}_6\text{H}_5\text{NO}_3$) and sodium borohydride (NaBH_4) and were bought from Sigma-Aldrich, India. Ultrapure deionized (DI) water (Milli-Q purifier system, Merck, Germany) was utilized throughout the synthesis.

3.2.2. Synthesis of TCNC Capped Au NPs Seed (TCNC-Au NPs)

Synthesis of Au seed solution was initiated by TEMPO-oxidized cellulose nanocrystals (TCNC), and the reduction process was augmented by the addition of TSC. Briefly, 60 mL 0.1 wt% TCNC aqueous solution was taken in a 250 mL conical flask followed by 750 μL of 0.01 M HAuCl_4 , was gradually added, and the mixture is heated up to 100 °C with continuous magnetic stirring. When boiling pioneered, 1 mL of 1 wt% trisodium citrate was added, and the mixture was heated for an extra 20 min. The colorless solution gradually converted to purple, and the subsequent solution was used to synthesize core-shell Au@Ag NPs as Au seeds. The TCNC capped Au seed solution was cooled at room temperature and preserved at 5 °C for further use. To investigate the impact of TCNC the reaction is carried out with different weight percentages of TCNC, while keeping all other reagent concentration constant. Hence, Au seeds with different sizes were synthesized by controlling the wt% of TCNC solution, ranging from 0.05 to 0.25.

3.2.3. Synthesis of TCNC Stabilized Au@Ag NPs (TCNC-Au@Ag NPs)

TCNC stabilized Au@Ag core-shell NPs have been synthesized by employing a modified seed-mediated approach.²⁵ In brief, 150 μL of 0.01 M aqueous ascorbic acid solution have been added to 3 mL TCNC capped Au NPs seeds prepared above and magnetically stirred for 2 min. Followed by an equivalent volume (150 μL) of 0.01 M

Assembled TCNC-Au@Ag NPs

AgNO₃ aqueous solution was then applied drop by drop with vigorous stirring. The solution color slowly shifted from purple to yellowish-orange with 10 min of magnetic stirring. The quantity of AA and AgNO₃ varied from 60 to 210 μL, led to the production of core-shell TCNC-Au@Ag NPs with various Ag shell thicknesses. All the synthesis was done at 25 °C. The samples were cooled and stored at 5 °C in amber-colored storage bottles. For comparison, the standard Turkevich method adapted citrate capped Au and Au@Ag NPs were synthesized.²⁶ Except for Trisodium citrate, all other reaction parameters were kept constant for evaluating the role of TSC as reducing and capping agent.

3.2.4. SERS Sample Preparation

Samples for SERS were prepared by mixing analytes and substrate colloids (without any concentrating by centrifuging) in a 1:3 (V/V) ratio one day prior to the measurement. For solution phase measurements, 10 μL samples were pipetted out on a pre-cleaned glass slide (cleaned by washing with chromic acid, sonicating in ethanol, and acetone afterward accompanied by UV-Ozone treatment for 10 min) at the time of measurement. In the case of solid state, drops on glass slide were dried in a desiccator. Especially for SERS spectra in the solid state, Raman signals were captured from minimum 5 different positions, and all were repeated at least three times.

3.2.5. Catalytic Reduction of 4-Nitrophenol (4-NP)

First, 4 mL of freshly prepared 15 mM aqueous solution of NaBH₄ is well mixed with 80 μL, 10 mM aqueous 4-NP solution in a quartz cuvette. Then the specific amount of TCNC-Au@Ag NPs colloid were added to the above solution and well mixed.²⁴ The reduction reaction is monitored by the change in the yellow color of 4-NP to colorless and was analyzed spectrometrically at regular intervals of time. Time dependent absorption spectra was measured until the completion of the reaction indicated by the absence of absorption peak of the 4-nitrophenolate ion at 400 nm.

3.2.6. Characterization Methods

Transmission electron microscopy (TEM) images of TCNC-Au NPs, TCNC-Au@Ag NPs, and subsequent selected area electron diffraction (SAED) captured using a FEI-Tecnai 30 G2S-TWIN transmission electron microscope, 300 kV. The plasmonic properties of colloids of NPs and spectrometric monitoring of 4-NP catalytic reduction were acquired using a UV-Visible spectrometer (Shimadzu UV-2700, Shimadzu, Japan) with a spectral range of 200-700 nm by using a 1cm path length quartz cell. Powder X-ray diffraction (XRD) pattern of the TCNC-Au and TCNC-Au@Ag samples were taken using PANalyticalX' pert pro equipped with Cu K α ($\lambda=1.54 \text{ \AA}$), 45 kV. X-ray photoelectron spectra (XPS) was obtained using PHI 5000 VersaProbe II, ULVAC-PHI Inc., USA. Samples were prepared by concentrating colloidal samples on a pre-cleaned glass slide using an O-ring. Zeta potential of colloids were measured with Zetasizer Nano ZS, Malvern instruments. Elemental content of Au and Ag were estimated utilizing inductively coupled plasma mass spectrometry (ICP-MS) by Thermo scientific iCAP-RQ. Studies of Raman spectroscopy (SERS) were carried out using a 20X objective on a WI-Tec Raman microscope (WI-Tec, Inc., Germany, alpha 300R); 600 g/mm grating; Peltier-cooled charge-coupled detector; 633 nm laser; resolution of 1 cm^{-1} ; 2s integration time; 5 accumulations in the range of $0\text{-}3000 \text{ cm}^{-1}$.

3.3. RESULTS AND DISCUSSION

3.3.1. Morphology and Optical Properties of TCNC Templated Au and Au@Ag Nanostructures

Preparation of TCNC-Au and TCNC-Au@Ag NPs was demonstrated in **Figure 3.1**. Our synthetic approach relies on the convergence of two concepts: initially, TCNC templated synthesis of Au NPs as the core of the nanostructure on which the growth of Ag shell occurs; secondly, the sequential variation of Ag ion concentration in the reaction mixture during synthesis. During the synthesis of Au NPs seed, carboxyl groups in TCNC act as anchor sites for Au³⁺ ions, and reduction is facilitated by the combined reduction action of TCNC and citrate.²⁷ At the same time, the TCNC network in aqueous media

Assembled TCNC - Au@Ag NPs

provides more steric stabilization to Au NPs by significantly preventing the fusion of Au NPs formed on the TCNC templates.²⁸ Such interaction promotes the creation of adjacent and tightly packed Au NPs in the TCNC matrix. The size of the Au core formed was regulated by varying wt% of TCNC from 0.05 to 0.1, 0.15, 0.2, and 0.25 wt% by keeping all other reaction parameters constant (**Figure 3.2a**). It is found that the wt% TCNC plays a critical role in the size distribution and morphology of the resulting Au NPs. Due to the highly spherical morphology and monodispersed nature, 0.1 wt% TCNC stabilized Au NPs were taken as the optimized seed system for further Ag shell coating. The as-prepared TCNC-Au NPs seed possesses a diameter of 25.0 ± 5 nm and a surface plasmon resonance band located at 524 nm (**Figure 3.2a-b**). In addition, a zeta potential value of -45 mV makes TCNC-Au colloids super stable without any signs of aggregation and flocculation for at least up to 6 months (**Table 3.1, Figure 3.2c**).

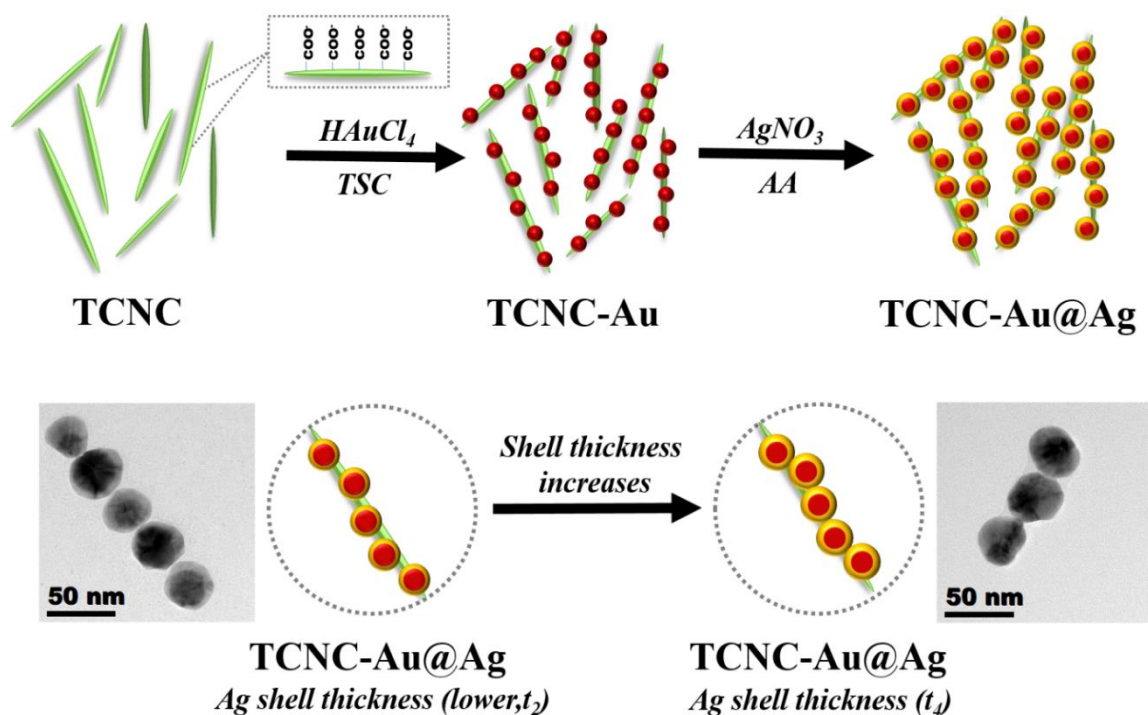


Figure 3.1. The preparation procedure of TCNC stabilized Au@Ag nanostructures.

TCNC-Au@Ag core-shell NPs with varying shell thickness is prepared by introducing different quantities of AgNO_3 and ascorbic acid dropwise into an equal volume

of TCNC-Au seeds (25.0 ± 5 nm) colloids. It has been demonstrated that due to the fine match of lattice constants of Ag and Au, Ag can selectively adsorb and develop on the Au core surface to form the core-shell structure.²⁹ **Figure 3.3a** showed the UV-Visible absorption spectra obtained from TCNC-Au@Ag NPs colloids with different Ag shell thickness prepared by different amounts of Ag precursor and AA (from 60, 90, 110, 150, and 210 μL). After adding AgNO_3 solution, the resultant Au@Ag nanostructures displayed two plasmonic bands, one at 390 nm (Ag shell) and the other at 520 nm (Au core), which specifies the partial coverage of Au core by Ag NPs. When the thickness of Ag shell increased, the typical plasmonic absorption intensity of Ag enhanced and was inclined to redshift.³⁰ As the thickness of the Ag shell increased from t_1 to t_5 , the location of the LSPR band of Ag was switched from 390 nm to 420 nm and the LSPR of Au core was gradually suppressed, and even completely screened as the Ag shell grew.

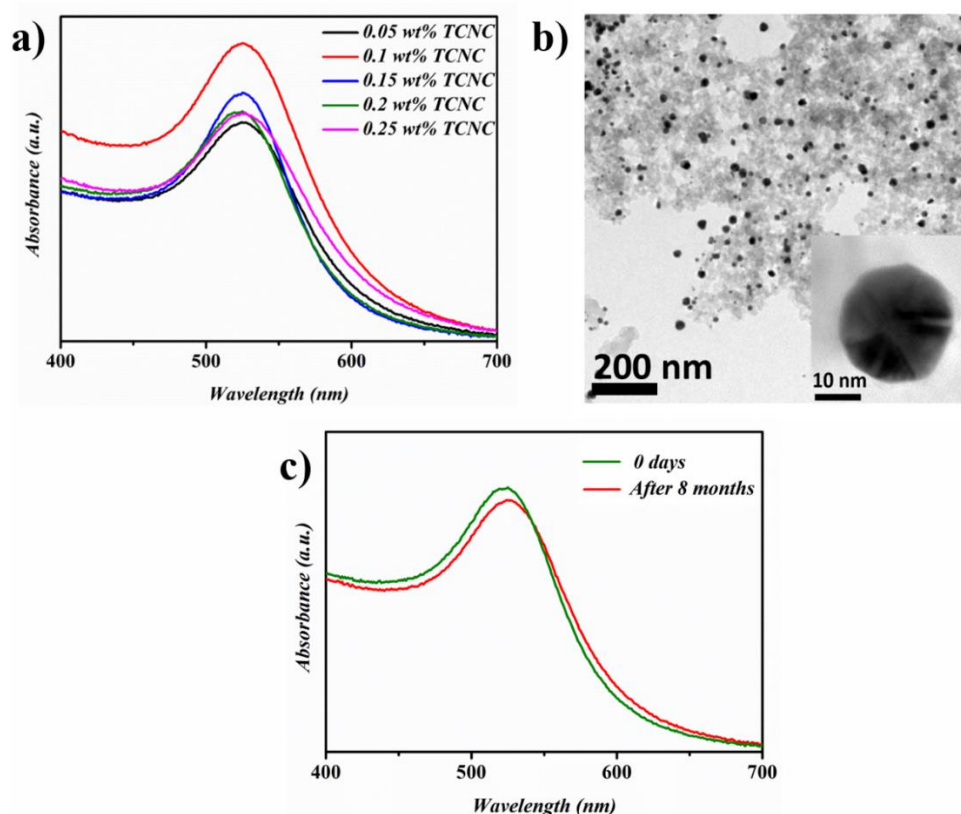


Figure 3.2a. a) UV-Visible absorption spectra of TCNC-Au NPs with varying wt% of TCNC (0.05, 0.1, 1.5, 0.2, and 0.25), b) TEM images of TCNC-Au NPs; inset shows the high-resolution TEM image of spherical TCNC-Au NP, and c) UV-Vis absorption spectra of TCNC-Au NPs at different time periods.

Samples	Zeta potential (mV)
TCNC	-40.3
TCNC-Au	-45.0
TCNC-Au@Ag (t_4)	-49.7

Table 3.1. Zeta-potential values of different samples.

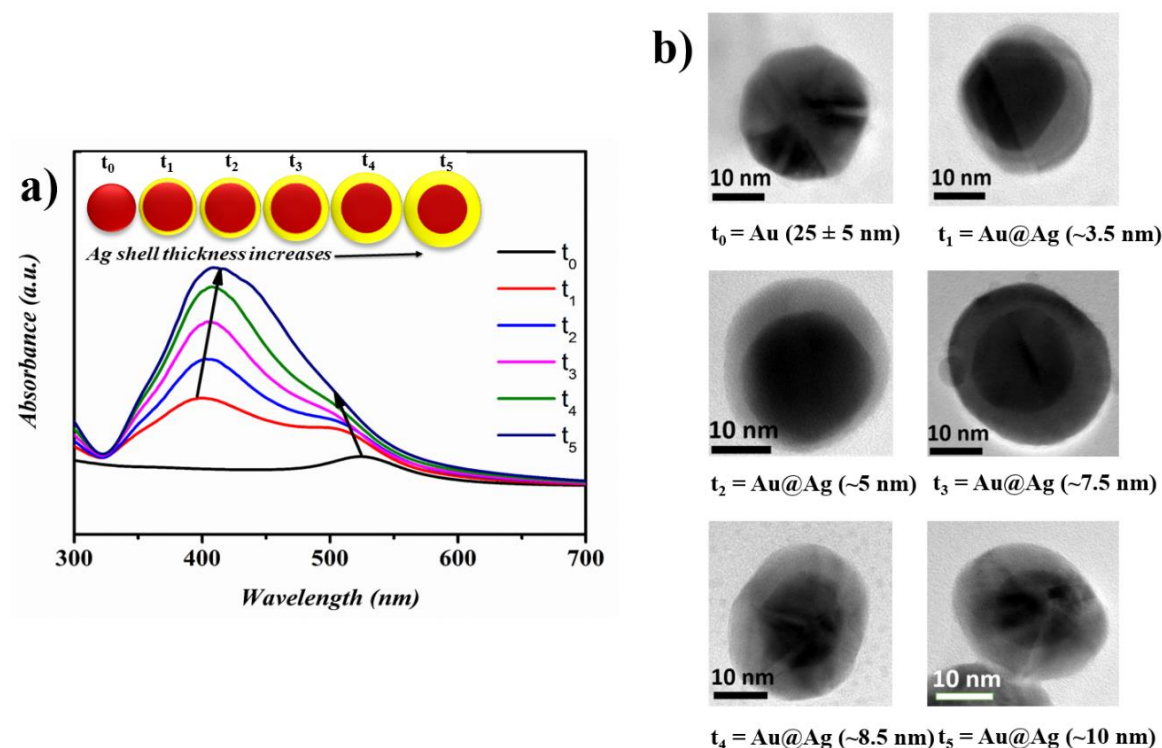


Figure 3.3. (a) UV-Vis spectra of TCNC-Au@Ag nanostructures with varying shell thickness ‘t’ (t_0 , t_1 , t_2 , t_3 , t_4 , and t_5) obtained by adding 0, 60, 90, 110, 150, and 210 μL 0.01 M AgNO_3 to 3 mL Au seed solution; (b) equivalent magnified TEM images.

Figure 3.3b & Figure 3.4 displays the TEM micrographs of TCNC-Au@Ag nanostructures acquired at respective shell thickness from t_0 to t_5 . A gradual increase in the Ag shell thickness from around 3.5 nm (t_1) to 5.5 (t_2), 7.5 (t_3), 8.5 (t_4), and 10 nm (t_5) can be observed with a collateral rise in the total diameter of NPs from 28.5 ± 2 nm to 35.5 ± 2 nm. The nanostructure of the core-shell would be distinguished by the contrast in electron

density between the Au (dark) and the Ag (bright).³¹ Interestingly, a gradual reduction in the interparticle distance can be seen with an increase in shell thickness, offering numerous plasmonic hotspot junctions. A highly cross-linked Au@Ag nanostructure assemblies were obtained onto TCNC templates with an Ag shell thickness of ~ 8.5 nm (t_4) (**Figure 3.4d-e**). Therefore, it should be noted that the formation of core-shell nanochains could be efficiently tailored by tuning the shell thickness of Ag. This morphological change of isolated Au@Ag NPs into necklace-like nanoassemblies could be well correlated with the gradual redshift of the Ag plasmon band that arises due to the interparticle coupling between adjacent core-shell NPs. However, at higher shell thickness (~ 10 nm), the ordered arrangements were found to be slightly disrupted due to the formation of larger sized Au@Ag nanostructures on TCNC templates. **Figure 3.5a** depicted a typical HR-TEM image of TCNC-Au@Ag NPs obtained with an Au core size of 25.0 ± 5 nm and Ag shell thickness of around 3.5 nm. HR-TEM and the FFT spot pattern (**Figure 3.5b**) show that the Ag (0) formed typically along the direction of the Au (111) plane.

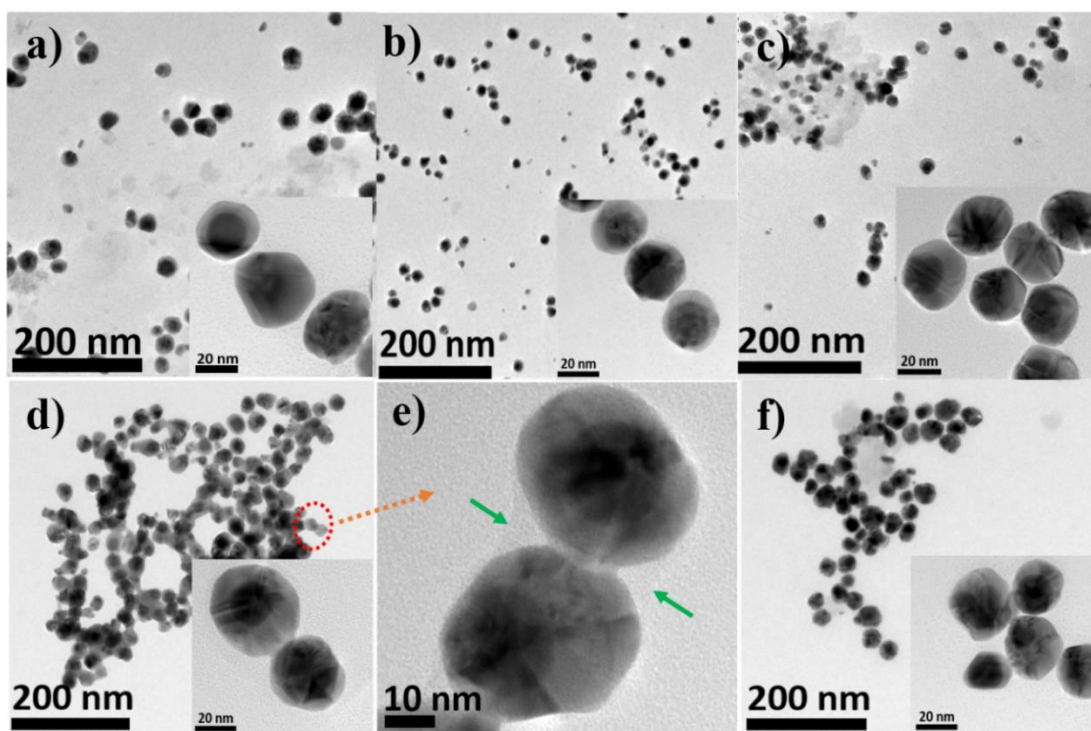


Figure 3.4. TEM images of TCNC-Au@Ag nanostructures prepared by adding (a) 60, (b) 90, (c) 110, (d-e) 150, and (f) 210 μL 0.01 M AgNO_3 to 3 mL Au seed solutions; insets in (a-d & f) shows corresponding magnified TEM images.

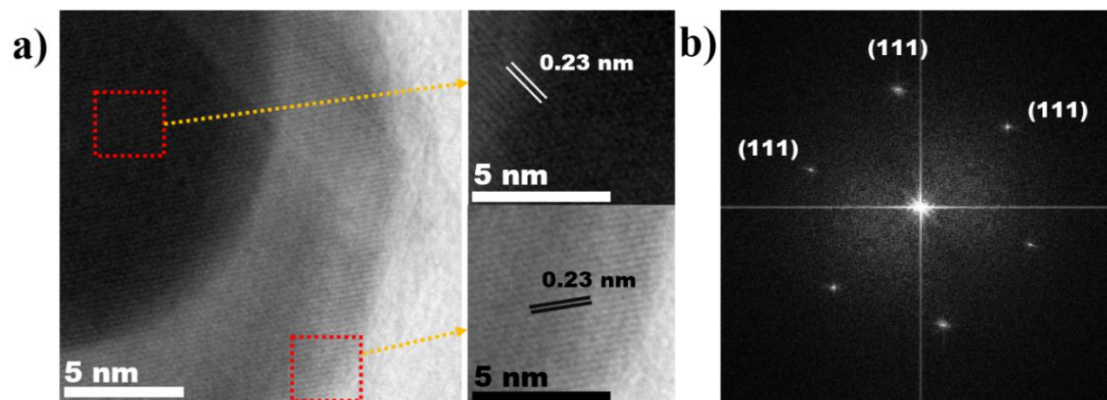


Figure 3.5. (a) HR-TEM image of TCNC-Au@Ag nanostructures (average Ag shell thickness- 3.5 nm); inset shows the magnified images of the red marked area; (b) FFT spot pattern of TCNC-Au@Ag nanostructures enclosed by (111) facets.

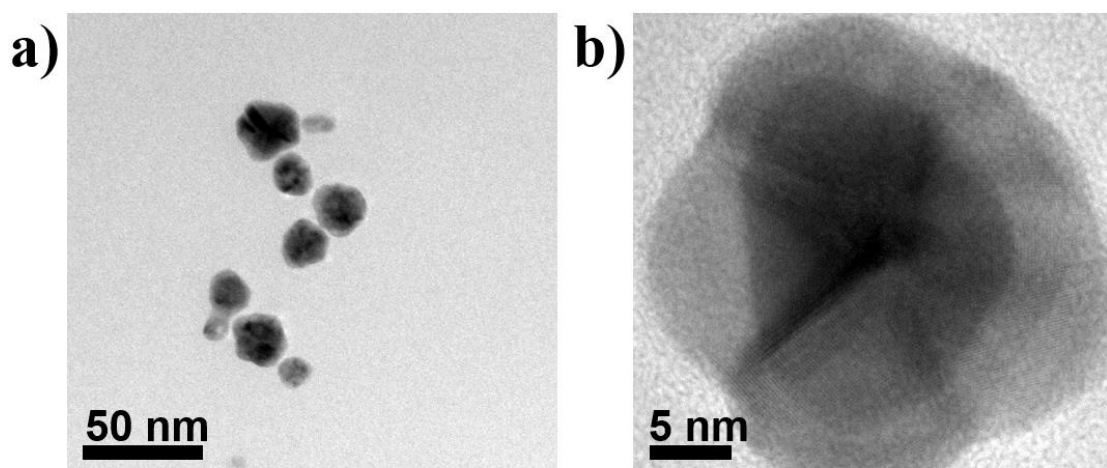


Figure 3.6. a) TEM, and b) HR-TEM images of 0.25 wt% TCNC-Au@Ag NPs.

Here, nanocellulose act as a backbone which introduces new metamorphosis of Au@Ag core-shell nanostructures in both properties and structural aspects. We highlight the TCNC as a green template for the preparation of Au@Ag NPs with controlled shell thickness. At an optimum shell thickness of Ag, interparticle coupling between core-shell NPs resulted in the formation of coupled chain-like core-shell nanostructures templated over TCNC instead of forming bulk agglomerates. Subsequently, to get more insight into

the role of TCNC in morphological transformation, we repeated the experiments with a higher wt% of TCNC (0.25 wt%) for preparing Au@Ag NPs. Interestingly, larger Au@Ag NPs were found with irregular morphology (**Figure 3.6**) instead of forming spherical nanostructures. This could be ascribed to the presence of more nucleation sites offered by a higher amount of TCNC, and different reaction kinetics followed. These results imply that the formation of discrete and close-packed core-shell nanostructures could be efficiently tailored by altering the Ag shell thickness and wt% of TCNC. Our present study can therefore offer a good method that uses the green candidate nanocellulose to prepare not only the discrete Au@Ag NPs with various shell thicknesses but also the coupled Au@Ag NPs with tunable plasmon bands.

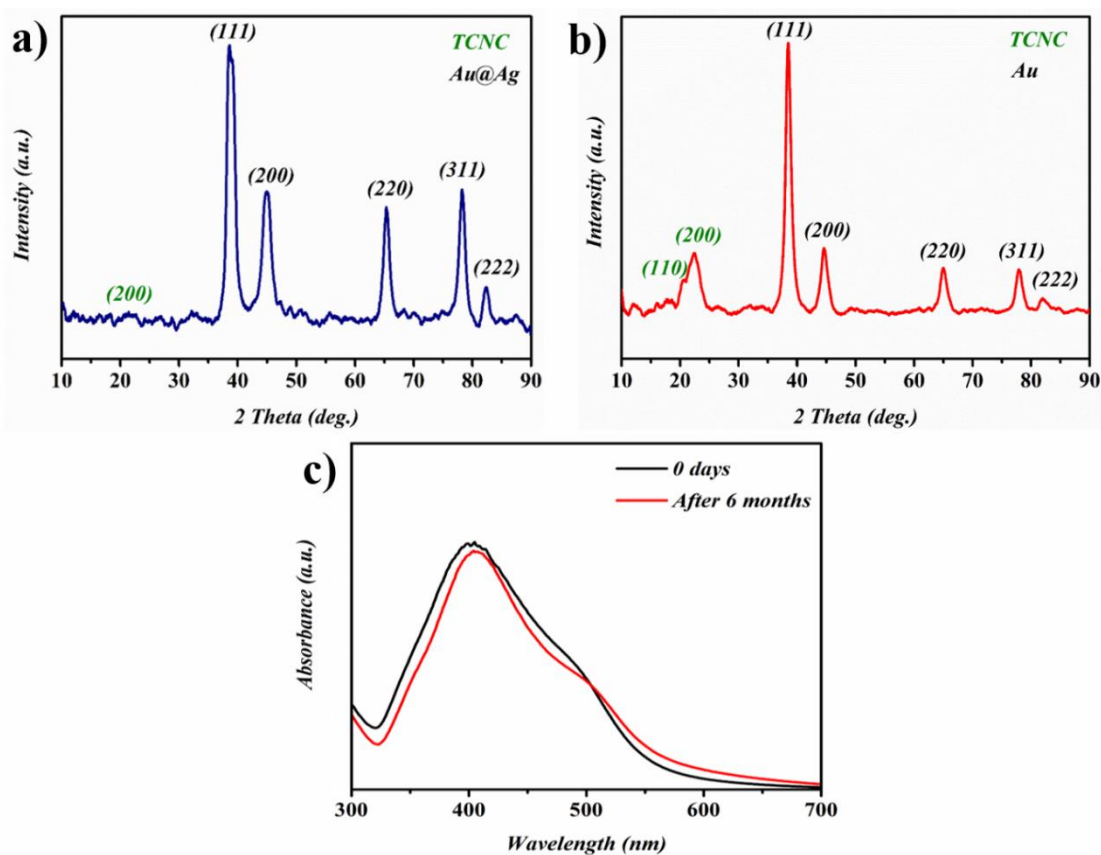


Figure 3.7. XRD pattern of a) TCNC-Au seeds and b) TCNC-Au@Ag NPs; c) UV-Vis absorption spectra of TCNC-Au NPs at different time periods.

The XRD spectra were recorded for validation of Ag nanocrystal shell coating on the TCNC-Au seed surface. XRD pattern of TCNC-Au NPs showed (**Figure 3.7a**) four specific diffraction peaks in the 2θ range of 10° - 90° at 38.42° , 44.39° , 64.93° and 77.89°

Assembled TCNC-Au@Ag NPs

respectively indexing the planes (111), (200), (220) and (311) of the cubic face-centered Au accompanied by a weak-intensity peak at 81.81° , indexed as (222) plane (JCPDS no. 00-004-0784). Additional peaks at 20.31° and 22.36° are from the TCNC as the template of Au NPs indexing the planes (110) and (200) of cellulose II, respectively. Meanwhile, the diffracted peaks in the XRD pattern of TCNC-Au@Ag NPs presented in **Figure 3.7b** showed peaks at 38.9° , 44.9° , 65.3° , 78.2° and 82.2° that could be well assigned to the (111), (200), (220), (311) and (222) planes of the Ag FCC crystal structure (JCPDS no. 00-004-0783). The diffraction patterns of Au NPs and Au@Ag NPs are almost similar due to their 2θ values residing very adjacent to one another.³¹ Nevertheless, the XRD patterns displayed sharper characteristic peaks for TCNC-Au@Ag NPs than those for TCNC-Au NPs, indicating that Ag shell grown over Au seeds surface with high crystallinity.

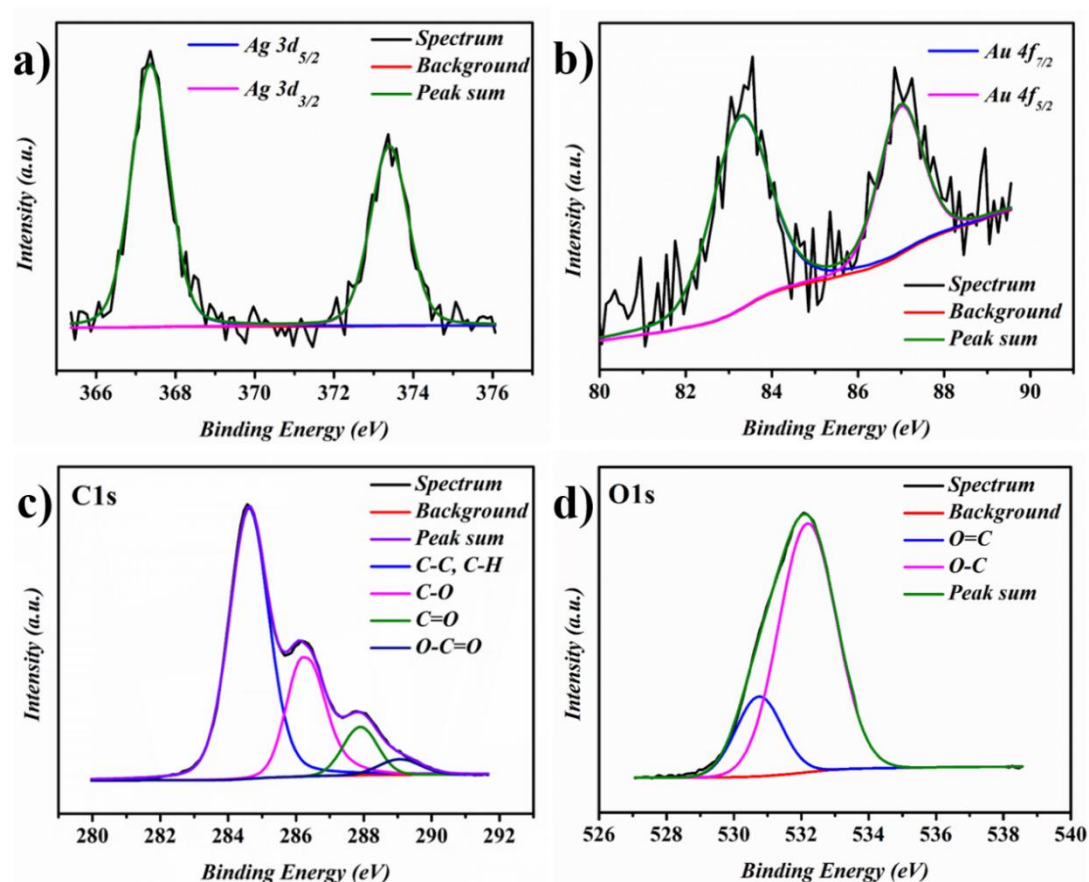


Figure 3.8. XPS narrow scans corresponding to (a) Ag 3d; (b) Au 4f; (c) C1s, and (d) O1s for TCNC- Au@Ag nanostructures.

The as-prepared TCNC-Au@Ag colloid exhibited a zeta potential value of -49.7 mV, indicating excellent stability and longer shelf-life, as evident from the minor changes in the UV-vis absorption band (**Table 3.1, Figure 3.7c**). X-ray photoelectron spectroscopy (XPS) studies were carried out to identify the oxidation states and the chemical composition of the core-shell nanostructures. In the case of TCNC-Au@Ag NPs, the two characteristic Ag 3d components are observed at BEs 367.4 eV (Ag 3d_{5/2}) and 373.4 eV (Ag 3d_{3/2}) with 6 eV difference confirming the formation of metallic Ag (**Figure 3.8a**).³² Additionally, the narrow scan of Au 4f core-level exhibited two peaks at 83.8 eV (Au 4f_{7/2}) and 87.5 eV (4f_{5/2}) with an energy difference of 3.7 eV, inferring the zero-valent state of Au NPs (**Figure 3.8b**). Further, the presence of carboxyl functionalized TEMPO-oxidised cellulose nanocrystals (TCNC) was also investigated by XPS. Strong peaks of O1s and C1s appeared at 532.1 eV, and 284.8 eV confirmed the presence of TCNC as the template in our system. **Figure 3.8c** displayed the high-resolution spectrum of C1s of TCNC. The peaks at 284.8 eV, 285.9 eV, 288, and 289.1 eV were assigned to C-C/C-H, C-O, O-C-O/C=O, and O-C=O respectively, which are the main chemical states of carboxyl functionalized cellulose.³³ Deconvoluted spectra of O1s (**Figure 3.8d**) revealed two peaks at 532.2 and 530.7 eV corresponding to O-C, and O=C/O-C-O respectively also infer the presence of TCNC as the backbone of Au@Ag Nps.³⁴ The XPS narrow scans of Au 4f core-level of TCNC-Au NPs (**Figure 3.9**) showed two peaks due to spin-orbit splitting at binding energies (BEs) 83.4 eV (Au 4f_{7/2}) and 87.1 eV (4f_{5/2}) inferring the zero-valent state of Au NPs. The relative peak intensity of bulk Au 4f spectrum in the Au@Ag (**Figure 3.8b**) gets suppressed compared to Au seed, which further authenticates the formation of core-shell nanostructures. It must be noted that we should have observed prominent signals corresponding to both Au and Ag components in the XPS spectra in the case of probable formation of Au/Ag mixed bimetallic structure compared to that of Au@Ag core-shell structures.³⁵

From the above observations, we could infer that TCNC acted as a template introducing a new transformation to Au@Ag NPs in both properties and structural aspects. Based on these findings, the TCNC can be highlighted as a soft-template for constructing ordered assemblies of Au@Ag nanostructures by tuning the shell thickness. With an optimized TCNC content and Ag shell thickness, the interparticle coupling between core-

Assembled TCNC - Au@Ag NPs

shell NPs enabled the formation of ordered assemblies of Au@Ag over TCNC instead of forming bulk agglomerates. Therefore, the present study can offer a versatile method that introduces TCNC as a plasmonic engineer and shape directing template to prepare the discrete spherical Au@Ag NPs with diverse shell thicknesses and the coupled Au@Ag nanostructures with numerous plasmonic nanogaps.

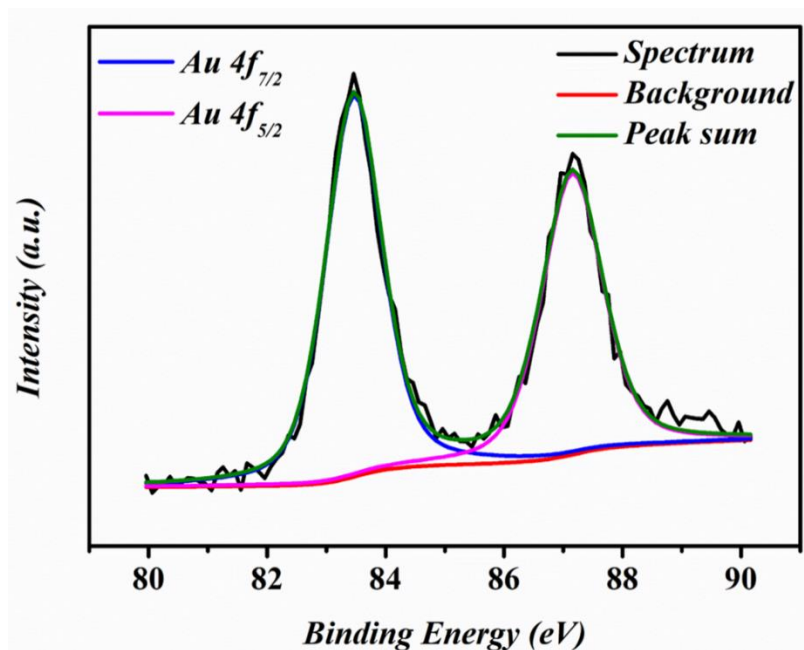


Figure 3.9. XPS narrow scan of TCNC-Au NPs.

3.3.2. SERS Response

The plasmonic effect of TCNC-Au@Ag NPs in SERS enhancement was evaluated using a cationic dye malachite green (MG), a carcinogenic fungicide and parasiticide in aquaculture, as the Raman probe molecule. TCNC templated Au@Ag nanoassemblies offer numerous hotspot junctions, which take a major share in amplifying electromagnetic field compared to isolated NPs. Moreover, the positively charged MG dye would readily get adsorbed on the surface of negatively charged TCNC via electrostatic interaction, which further contributes to SERS enhancement. Firstly, the SERS spectra of MG are recorded at least from five random spots of dried TCNC-Au@Ag substrates having different shell thickness, ~3.5 to ~10 nm (t_1 - t_5), and are presented in **Figure 3.10a**. The significant bands at 1617, 1368, 1174, 918, and 445 cm^{-1} can be attributed to the in-plane

stretching of the ring-C-C, N-phenyl stretching, N-C stretching vibration coupled with the C-C and C-H in-plane motions at 1394 cm^{-1} , aromatic C-H in-plane bending vibrations, ring skeletal vibrations of the phenyl-C modes of MG.³⁶ The peak at 1617 cm^{-1} was used to assess the enhancement in Raman signal intensity, and the bar diagram (**Figure 3.10b**) shows relative intensity. With shell thickness rising from ~ 3.5 to 10 nm , the SERS intensity of MG adsorbed on TCNC-Au@Ag nanostructures underwent a gradual increase and reached a maximum at 8.5 nm . However, further increase of the Ag shell thickness caused a decrease of Raman signal intensity since the LSPR properties of Au core became masked at higher Ag shell thickness ($>8.5\text{ nm}$).²⁵

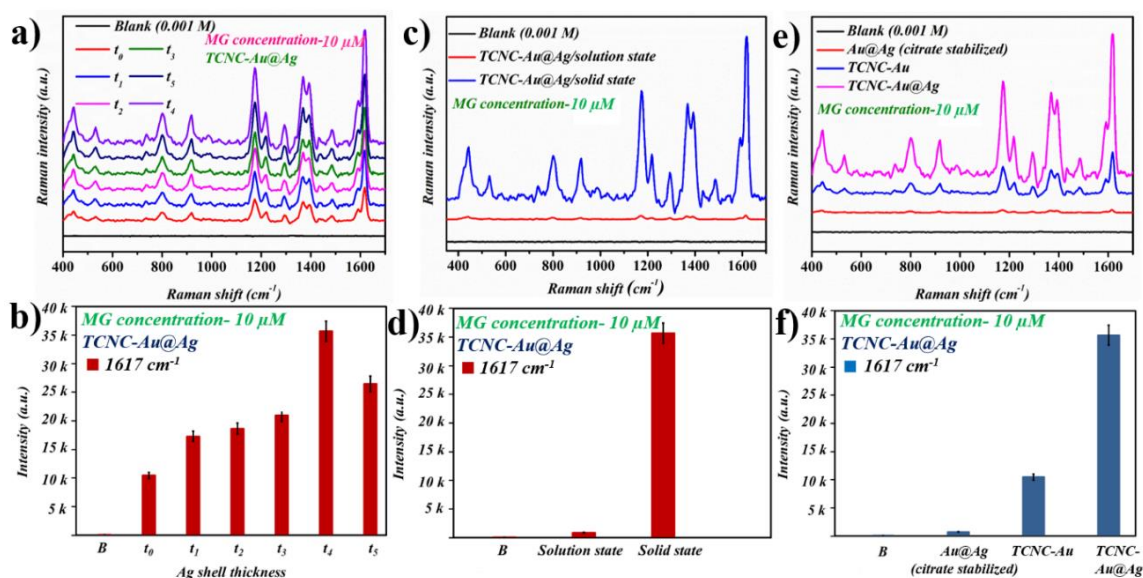


Figure 3.10. SERS response of malachite green (a and b) in solid-state with varying shell thickness of TCNC-Au@Ag nanostructures; comparison of SERS sensing in dispersion solution and solid-state (c and d); comparison of solid-state SERS sensing (e and f) with control substrates (TCNC-Au and citrate stabilized Au@Ag NPs).

The analytical enhancement factor (AEF) for different shell thickness is calculated based on the specific equation,

$$AEF = \frac{I_{SERS}}{I_{RAMAN}} - \frac{C_{RAMAN}}{C_{SERS}}$$

Assembled TCNC - Au@Ag NPs

where I_{SERS} is the intensity of the sample with concentration C_{SERS} in the presence of metal NPs as a substrate, while I_{RAMAN} and C_{RAMAN} are in the absence of NPs substrate.³⁷ Focused on the intense peak of MG at 1617 cm^{-1} , AEFs for different TCNC-Au@Ag NPs were estimated to be 2.01×10^5 , 3.3×10^5 , 3.61×10^5 , 4.03×10^5 , 6.85×10^5 , and 5.08×10^5 for t_0 , t_1 , t_2 , t_3 , t_4 , and t_5 , respectively (**Table 3.2**). All these experimental outcomes were in agreement with the findings reported in the case of core-shell Au@Ag NPs and nanocubes.^{38,38b} It has been stated that the incident light can only penetrate the Ag shell up to a specific thickness.³⁹ Accordingly, in this ongoing analysis, it was assumed that when the mean Ag shell thickness exceeds 8.5 nm, the excitation of Au core electrons will be difficult, resulting in lesser SERS intensity. In addition, the TCNC-Au@Ag NPs become unstable when the Ag shell coated over the surface of AuNPs is too thick.²⁵ Hence, taking into account the SERS behavior and stability, the TCNC-Au@Ag (t_4) NPs with about 8.5 nm Ag shell thickness was selected as the optimum SERS substrate for more investigations.

Sample	AEF
TCNC-Au(t_0)	2.01×10^5
TCNC-Au@Ag(t_1)	3.33×10^5
TCNC-Au@Ag(t_2)	3.61×10^5
TCNC-Au@Ag(t_3)	4.03×10^5
TCNC-Au@Ag(t_4)	6.85×10^5
TCNC-Au@Ag(t_5)	5.08×10^5
Au@Ag (citrate stabilized)	1.40×10^4

Table 3.2. Analytical enhancement factor (AEF) for different shell thickness

Subsequently, we compared the SERS efficiency of this optimized substrate in the solution phase and solid state using the same probe molecule, MG, and are presented in (**Figure 3.10c-d**). Interestingly, it is evident that the SERS peak intensity of MG in dried substrate exhibited 45 times enhancement when compared with the SERS signal intensity

in the solution state. In order to substantiate the role of cellulose nanocrystals in hotspot generation, SERS spectra of MG were recorded using different control substrates such as TCNC-Au, TCNC-Au@Ag (~8.5 nm (t_4)) and citrate capped-Au@Ag (~8.5 nm shell thickness) NPs in the dried state (**Figure 3.10e-f**). The peak intensity at 1617 cm^{-1} versus different substrates revealed the role of TCNC in SERS, which is several times higher than that of other control systems. It is also evident that TCNC capped Au NPs exhibited 10 times SERS enhancement when compared with citrate stabilized Au@Ag core-shell nanostructures. This shows that the TCNC template and the shell thickness play a key role in controlling the amplified electric fields created near the core-shell NPs.⁴⁰ Further, the higher SERS enhancement of the t_4 substrate could be a consequence of the enhanced near-field produced either by single core-shell NPs or from the hotspots produced within the core-shell NP assemblies having an interparticle distance of less than 1nm. The hotspot engineering ability of TCNC in SERS has been illustrated in **Figure 3.11**. Upon drying, the entangled Au@Ag NPs decorated TCNC payloads come close together, inherited by its self-assembling property, leading to the creation of a highly dense hotspot region augmented electromagnetic field and the dramatic enhancement in SERS signal intensity.^{17, 41} The effective pre-concentration of the targeted analytes while drying and creating high-density hotspot regions facilitated by the closely packed array of TCNC-Au@Ag plasmonic payloads is an added advantage. From the AFM analysis, we could see numerous Au@Ag NPs (bright contrast) adhering over the TCNC surface even after drying (**Figure 3.12**). Such findings shed light on the significance of TCNC in modulating the plasmonic effects while comparing it with the plasmonic properties of classical mono or bimetallic systems prepared with conventional capping agents.

We further evaluated the applicability of the developed TCNC-Au@Ag core-shell substrate for the trace-level detection of MG. MG is a triphenylmethane dye that has been widely used in aquaculture as an antifungal and antiparasite. But this ominous chemical can be readily absorbed by fish tissues which causes many genetical mutations and cancer in animals.³⁷ With the decrease in concentration, the prominence of MG Raman peaks steadily decreased as expected (**Figure 3.13a-b**). The switch between the presence and the

Assembled TCNC-Au@Ag NPs

absence of six characteristic peaks in these two runs suggests that the practical limit of detection (LOD) of MG is below 10 fM.

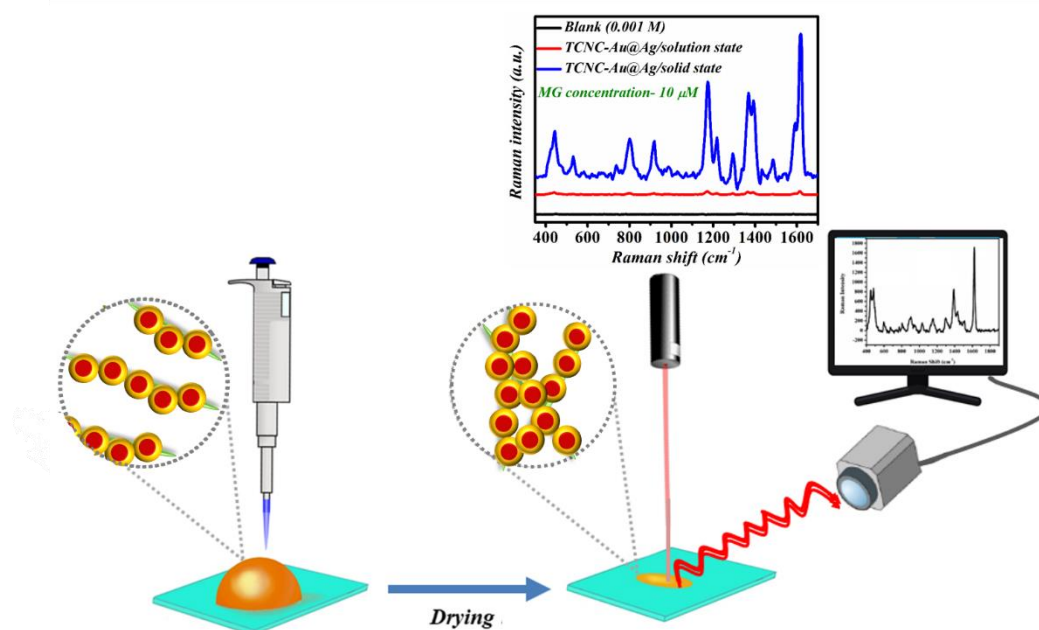


Figure 3.11. Mechanism of SERS detection using TCNC-Au@Ag nanostructures with numerous hotspot regions.

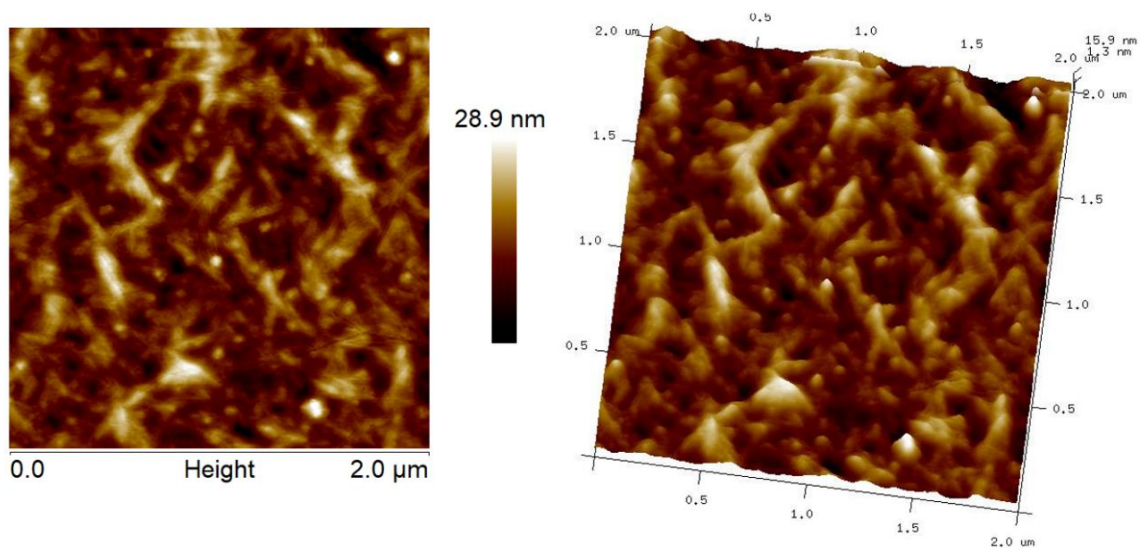


Figure 3.12. AFM images of TCNC templated Au@Ag nanostructures after drying.

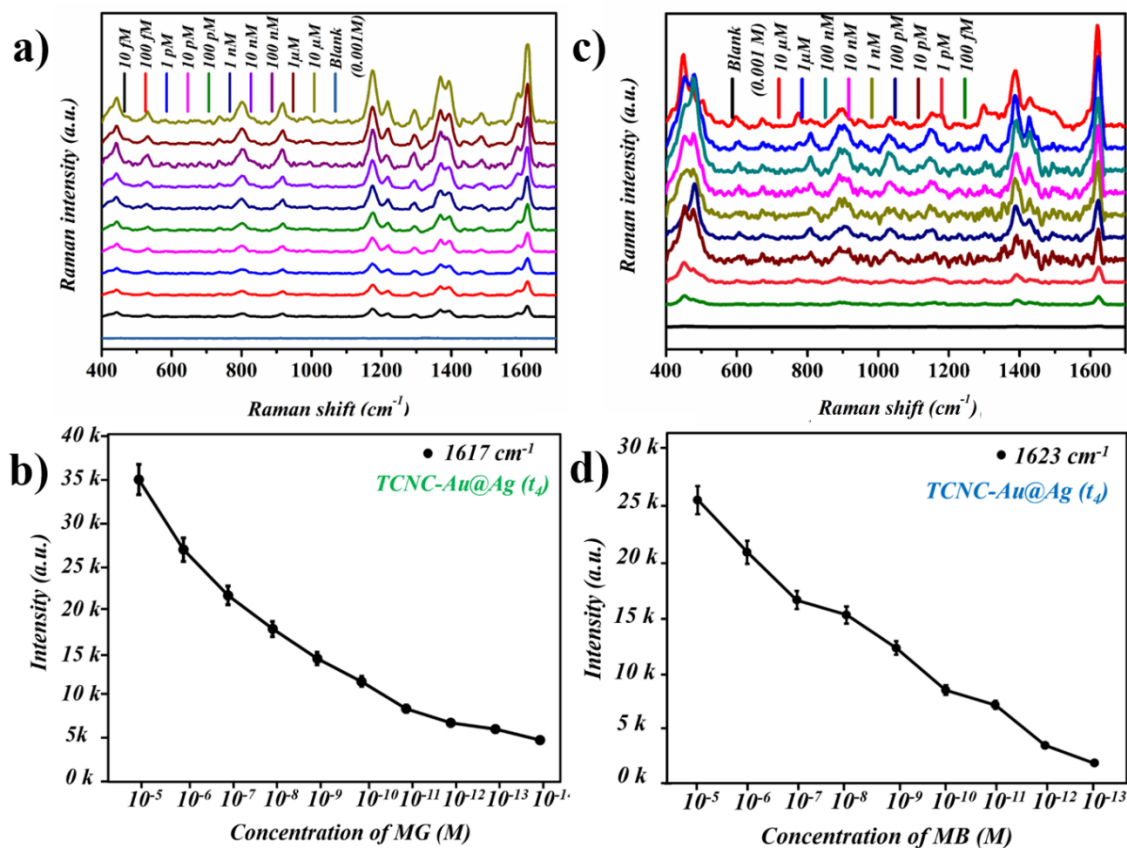


Figure 3.13. Sensitivity of TCNC-Au@Ag (t₄) nanostructures towards SERS detection of malachite green (a and b) and methylene blue (c and d).

An overview of the sensitivity studies with the LOD of MG with various types of Au@Ag substrates has been tabulated (**Table 3.3**). Practical application of the substrate solely lies on the reproducibility criterion. Hence, the reproducibility of the developed substrate has been evaluated using methylene blue (MB), as shown in **Figure 3.13c**. The significant bands at 1623, 1394, 1302, 1174, 1154, 770, 501, and 448 cm⁻¹ can be attributed to the in-plane stretching of the ring-C-C, C-N symmetrical stretching, C-H in-plane ring deformation, C-H in-plane bending vibrations (1154 & 770), and C-N-C deformation vibrations (501 & 448) of MB.⁴² Plot for comparison of the SERS intensity at 1623 cm⁻¹ versus concentration of MG with standard deviation also given (**Figure 3.13d**). It could be found that blank MB solution Raman spectra with a concentration of 10⁻³ M are not qualitative and recognizable, whereas SERS spectra in the presence of 0.1 wt% TCNC-Au@Ag (t₄) NPs in solid-state displayed strongly amplified SERS signals even at a

Assembled TCNC - Au@Ag NPs

concentration below 100 fM. An overview of the sensitivity studies with the lowest detection limit of MG and MB with various types of Au@Ag substrates has been tabulated (Table 3.4). It is worthy of notice that the SERS platform specified in this report exhibits higher sensitivity when compared with other substrates. It suggests that this method is green, cost-effective, nontoxic, and affords sustainable alternatives to known methods and their applicability in biomedical, diagnosis, and environmental monitoring.

SERS substrate	LOD (M)	Reference
GO/Au nanocomposite	2.5×10^{-6}	43
Ag NPs/paper (SILAR)	10^{-12}	37
TiO ₂ NRs/Ag NPs	10^{-12}	44
Ag/Graphene	2.7×10^{-11}	45
Ag NCs/ZnO nanodome array	10^{-17}	46
Fe ₃ O ₄ @SiO ₂ @Ag	2×10^{-15}	47
Au@4-MBA@Ag NRs	5×10^{-8}	48
ZnO NRs/Au@4-ATP@Ag core-shell NPs	1.9×10^{-9}	49
Au/Ag concave nanolayers	5×10^{-14}	50
Bacterial cellulose/Au nanocomposite	4×10^{-13}	17
Ag NPs/ Nanocrystalline cellulose	5.2×10^{-9}	51
Ag NPs/ SiO ₂ /Nanocrystalline cellulose	9×10^{-10}	51
TCNC-Au@Ag NPs	10^{-14}	Present work

Table 3.3. An overview of diverse SERS substrates with their LOD for malachite green.

SERS substrate	LOD (M)	Reference
Ag/RGO	10^{-8}	52
MWCNTs/Ag nanocomposite	3.2×10^{-5}	53
Au NPs	1.5×10^{-11}	42
MoO ₃ /MoO ₂ nanosheets	10^{-9}	54
ZnO@Au NRs	10^{-12}	55
Ag/Au alloy (laser ablation)	10^{-10}	56
Ag@Au core-shell	2×10^{-7}	57
Ag/TEMPO-oxidised cellulose nanofibers	10^{-15}	27
TCNC-Au@Ag NPs	10^{-13}	Present work

Table 3.4. An overview of different SERS substrates with their LOD for methylene blue.

3.3.3. Finite Element Modelling (FEM) Studies

For plasmonic nanomaterials like Au@Ag NPs, augmented electromagnetic fields are the key factor for SERS applications. For TCNC templated Au@Ag nanostructures, the nanogap between two adjacent Au@Ag NPs could be modulated by varying the shell thickness, and then the resultant hotspot phenomenon can be modulated. Hence, it is vital to examine how well the Ag shell affects the near-field properties. Therefore, we calculated the rate of electromagnetic energy (W) experienced by the analyte molecule near the isolated Au@Ag NPs surface and at the junctions of two Au@Ag NPs, referring to the entire wavelength region via finite element modelling (FEM) utilizing commercially accessible COMSOL Multiphysics software.⁵⁸ Primarily, we have used the RF module to articulate and solve the differential form of Maxwell equations in conjunction with the

initial and boundary conditions. In conjunction with state-of-the-art algorithms for preconditioning and solution, the equations are formulated by using a finite element approach, including numerically stable edge element discretization. The scattering amplitude at the far-field (E_{far}) is invoked in the prologue of this calculation as a limiting extrapolation of their near-field action, commonly described as $E_{far} = \lim_{r \rightarrow \infty} r E_{sca}$. Therefore, the extent of electromagnetic energy dissipation could be obtained by adding the incident scattering amplitude and integrating over the Poynting vector over the whole surface as,

$$W_{abs} = \frac{1}{2} \int_0^a \int_0^b \int_0^c Re [J_{tot} \cdot E^* + i\omega B \cdot H^*] dv \quad (1)$$

$$W_{sca} = \frac{1}{2} \iint_S Re [E_{sca} \times H_{sca}] \cdot nds \quad (2)$$

That is correlated with the optical cross-section $\sigma = W/P$; where P is the incident irradiance. The electric field patterns calculated through FEM showing the surface plots corresponding to the 2D geometry of Au core, isolated, and dimers of Au@Ag nanostructures were presented in **Figure 3.14**. The surface profile corresponding to TCNC-Au@Ag (**Figure 3.14b**) displays strong localization of surface charge at the Au-Ag interface. It is observed that the enhanced local field concentrates on the outer surface of the Ag-shell (for $\lambda = 410$ nm) and polarizes parallel to the incident polarization. The electric field's strength on the Ag outer shell surface is greater than that of the Au NPs of the same size (**Figure 3.14a**). This would be due to the interaction of the various kinds of charges centered on the Ag shell interface and surface along with the incident polarization and can be ascribed to the electron transfer from the Au core to the Ag shell in the nanostructures. It was observed that the maximum $|E^2|$ value is 19.20018 eV at the outer surface of the Ag shell. However, in the case of bare TCNC-Au NPs ($\lambda = 524$ nm), the electric field is shown only at the two sides of the outer surface with a maximum of $|E^2|$ value at 5.02678 eV, which is lesser than the core-shell nanostructures.

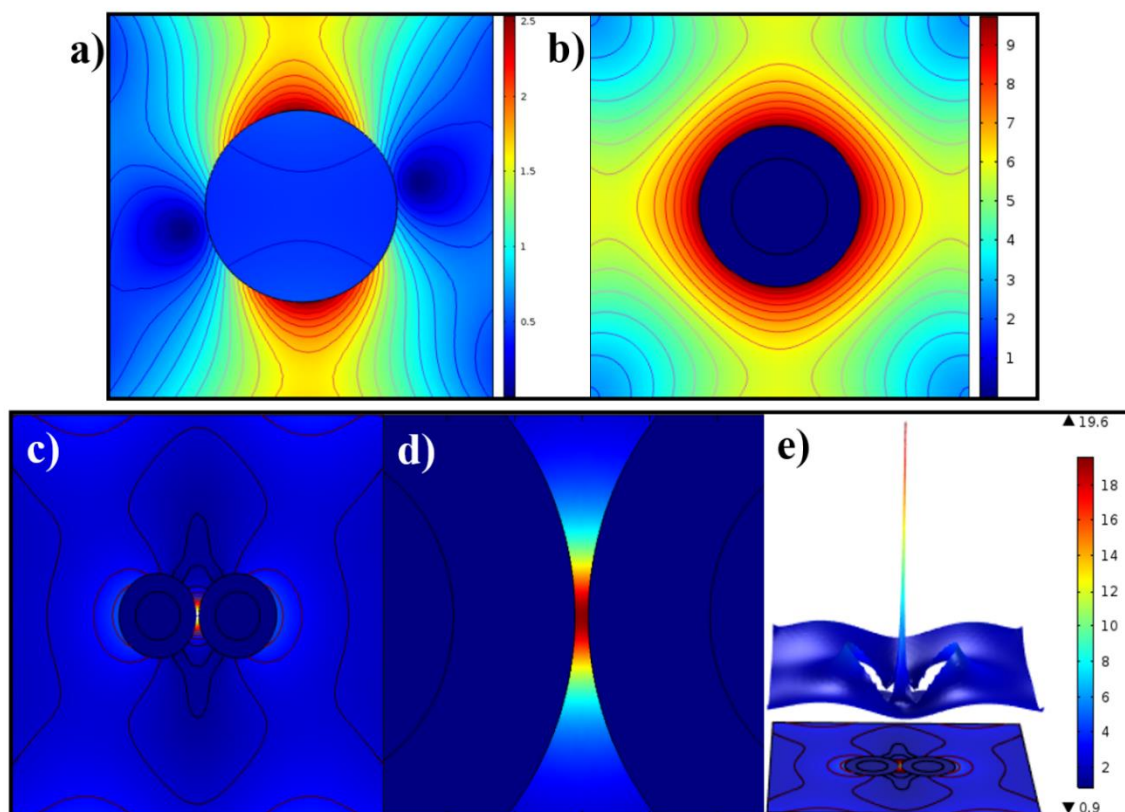


Figure 3.14. Finite element modelling showing the electric field distribution corresponding to the 2D geometry of (a) TCNC-Au and (b) isolated TCNC-Au@Ag nanostructures; (c-d) at the junction between two TCNC-Au@Ag nanostructures; (d) represents the magnified image of (c); and (e) depicts the surface with height expression where it shows a sharp peak at the junction between two core-shell nanostructures.

Further, the electric field distribution in the vicinity of two TCNC-Au@Ag (t_4) NPs was shown in **Figure 3.14c-e**. The field polarization value is higher at the junctions of two Au@Ag NPs, which shows that electromagnetic coupling is more sensitive than the isolated core-shell NPs. It could be noted that the region at the junctions of TCNC-Au@Ag ($t=8.5$ nm) nanostructures with a nanogap ~ 1 nm, concentrates the highest electric field (hotspots). When caught at these hotspots, the analyte molecules give rise to incredible Raman intensities. Further, it shows a maximum $|E^2|$ value of 39.2268 eV at the junction of the two core-shell NPs and is two orders of magnitude higher than that of isolated Au@Ag NPs and eight-fold higher than that of monometallic Au NPs. The simulated SERS

enhancement factor ($EF \sim |E^4|$) agrees with the experimentally calculated EF ($\sim 10^5$) values of TCNC-Au@Ag nanostructures.

3.3.4. Catalytic Reduction of 4-Nitrophenol

Catalytic reduction of 4-Nitrophenol by NaBH_4 is considered as one of the foremost model systems to evaluate the efficiency of catalysts by real-time spectroscopic monitoring. Moreover, nitrophenols are intractable pollutants commonly present in industrial wastes, especially from factories of pesticides, insecticides, and synthetic dyes.⁵⁹ Due to the toxic, carcinogenic nature of nitrophenols, conversion followed by disposal is necessary. The aminophenols formed in the reduction of nitrophenols by NaBH_4 are an inevitable components in the pharmaceutical industry, and the conversion is simple and efficient.⁶⁰ In order to concrete the knowledge of size and surface area specific catalysis reduction reaction of 4-NP in an excess amount of NaBH_4 in the presence of TCNC-Au@Ag NPs with different shell thickness (t_0 - t_5) were performed, and reduction was monitored by UV-Visible absorption spectra after a fixed time interval, 1 min using a constant amount of catalysts (12 μL , ~ 0.1 mg) (**Figure 3.15a**). With excess concentration of NaBH_4 , the reduction rate can be assumed to be independent of borohydride concentration.⁶¹

The absorption maximum of 4-NP in the presence of NaBH_4 is located at 400 nm due to the formation of 4-nitrophenolate ions in alkaline media.⁶² In our study, when small aliquots of TCNC-Au@Ag NPs was added to the mixture of 4-NP and NaBH_4 in a cuvette, the reduction process can be monitored by the gradual decrease in the absorption peak of 4-nitrophenolate ions at 400 nm followed by a concomitant rise at 300 nm indicating the successful formation of 4-aminophenol.⁶³ The results are unprecedented in the way that we got a maximum reduction rate for coupled chain structured TCNC-Au@Ag (t_4 , ~ 8.5 nm), which exhibited maximum enhancement in SERS. Although, in the presence of pure 25 nm TCNC-Au (t_0), negligible variation in the absorption band of 4-NP observed indicates a weak 4-NP reduction. The catalytic reaction efficacy is estimated as 11% for TCNC-Au (t_0) and 91% TCNC-Au@Ag (t_4) nanostructures. The superior catalytic action of TCNC-Au@Ag (t_4) nano assemblies could be ascribed to the synergistic electronic effect, size,

and composition.⁶⁴ Since the Fermi level for Au (-5.0 eV) is slightly lesser than that of Ag (-4.6 eV), an electron-rich area near the Au@Ag interface is created by the transfer of electrons from Ag to Au.⁶⁵

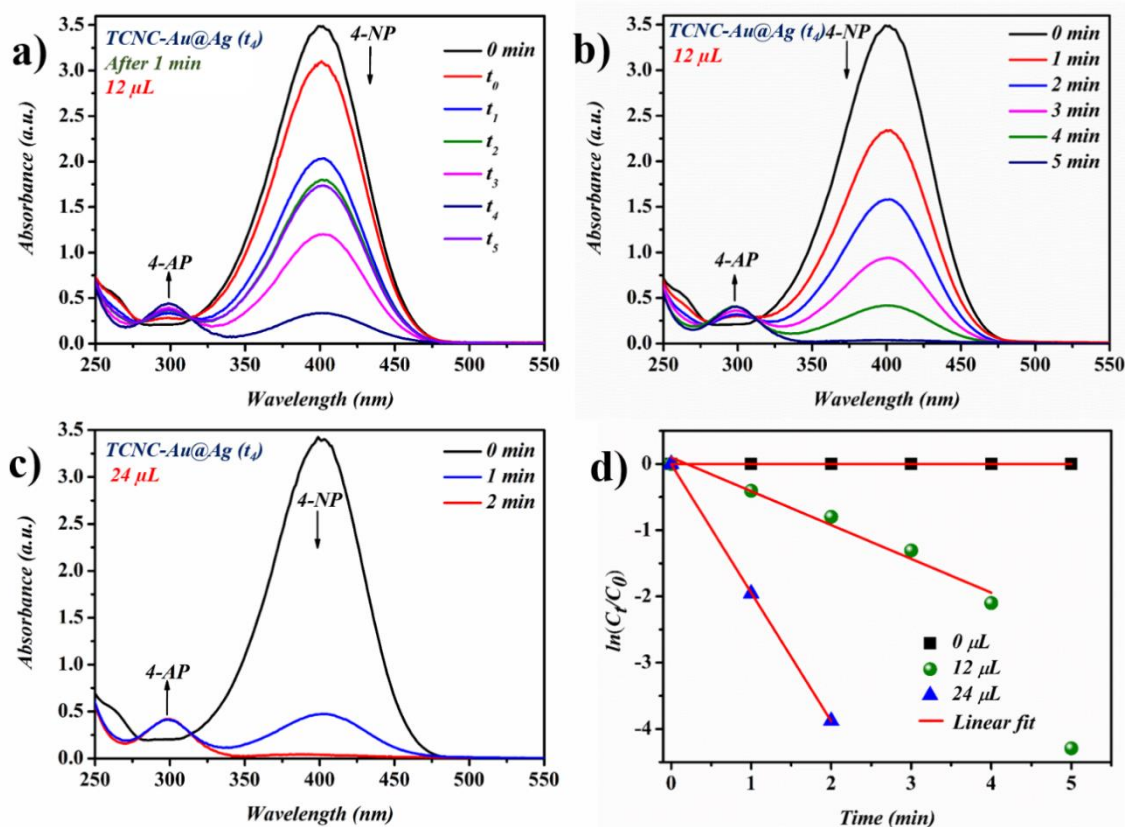


Figure 3.15. a) Comparison of 4-NP reduction efficacy of TCNC-Au@Ag NPs with a different shell thickness of Ag (t₀-t₅) after 1-minute duration (b-c) The time-dependent UV-Vis absorption spectra of 4-NP reduction with NaBH₄ catalyzed by different amounts of TCNC-Au@Ag (t₄) nanostructures and (d) corresponding kinetic plots of the reduction reaction.

Figure 3.15b-c shows UV-Visible absorption spectra of time dependent reduction of 4-NP in the presence of NaBH₄ by using TCNC-Au@Ag (t₄, ~8.5 nm) homogeneous catalyst for which we got maximum efficacy. Completion of reduction can be ensured not only by the vanishing of the absorption peak at 400 nm but also by the change of color of the solution from yellow to colorless by the naked eye. With the addition of 12 μL (~0.1

Assembled TCNC - Au@Ag NPs

mg) of catalyst, the reduction was completed within 5 min, whereas with an increased amount of catalyst, 24 μL (0.2 mg) reaction was completed within 3 min. This short time period of time for the reduction process, even with very minute quantities of TCNC-Au@Ag (t_4), signifies its applicability in the field of catalysis. Regeneration of catalyst can also have done by providing suitable heterogeneous support to the NPs. Moreover, the electron transfer between Au and Ag is ambiguous, which could be further explained by the electron compensation effect.⁶⁶ The distorted electron balance between Au and Ag is compensated for the back-donation of electrons from Au to Ag, causing a reduced d-electron in the Au core with an augmented d-electron in the Ag shell, which is predominant at interfaces of Au and Ag. Hence, for TCNC templated Au@Ag nano-assemblies with Ag shell thickness of ~ 8.5 nm, numerous accessible electron-rich regions could be present on the TCNC surface. These highly active surface sites lead to more adsorption of 4-NP, thus leading to an enhanced catalytic rate. However, in the case of bare Au NPs (TCNC-Au NPs), such localization of electrons does not occur, and the electron density is distributed throughout the entire particle.

Reaction kinetics of this reduction was analyzed from $\ln C_t/C_0$ versus time plot, and the linear fit was done with a correlation coefficient of 0.9672 (12 μL) and 0.9999 (24 μL), which revealed that the reduction of 4-NP by NaBH_4 followed a pseudo first-order kinetics (**Figure 3.15d**). Kinetic reaction rate (k_{app}) was estimated from the slope of the linear relationship ($\ln(C_t/C_0)$ over time).⁶⁷ A high k_{app} value of $32.33 \times 10^{-3} \text{ s}^{-1}$ was calculated for 24 μL (~ 0.2 mg) of TCNC-Au@Ag (t_4) catalysed reduction of 4-Nitrophenol.

Efficacy of a catalyst has become ultimately reliant on the nanostructure and composition that promote atom surface arrangement.⁶⁸ The donor and acceptor species derived from borohydride and 4-NP are first adsorbed onto the surface of the TCNC-Au@Ag NPs. Here, the large surface area associated with the coupled nanostructures provides an active surface for the reduction and serves as a dynamic electron transfer mediator. After the reaction, the newly produced 4-aminophenol molecules rapidly desorb from the catalyst's surface.^{24, 68} Hence, the merits of the large surface area of TCNC, along with the presence of numerous electron-dense regions profited from Au@Ag nanostructures, will provide novel avenues for homogeneous catalysis.

3.4. CONCLUSIONS

In summary, we presented a green synthesis of discrete as well as assembled Au@Ag core-shell nanostructures on carboxylated cellulose nanocrystal templates using a facile seed-mediated approach. Here, TCNC is critical to obtain core-shell nano-assemblies having abundant plasmonic hotspot junctions resulting in excellent SERS activity in solid-state with remarkable colloidal shelf-life. Correlation with theoretical FEM field simulations confirmed an enhanced local field at the junctions of adjacent TCNC-Au@Ag nanostructures, which can significantly enhance the Raman intensities. Moreover, the presence of several electron-dense regions in the assembled TCNC-Au@Ag nanostructures enabled enhanced catalytic activity. We envisage that our method could pave the way for designing innovative complex nano-architectures of core-shell systems decorated on TCNC bio-templates with dense plasmonic hotspots and exceptional colloidal stability. This could open up enormous possibilities for maneuvering various multifunctional plasmonic bimetallic nano-systems suitable for biomedical, energy, and environmental applications.

3.5. REFERENCES

1. Zhang, X.; Xiao, X.; Dai, Z.; Wu, W.; Zhang, X.; Fu, L.; Jiang, C., Ultrasensitive SERS performance in 3D “sunflower-like” nanoarrays decorated with Ag nanoparticles. *Nanoscale* **2017**, *9* (9), 3114-3120.
2. Yao, Y.; Zhang, X.; Peng, J.; Yang, Q., One-pot fabrication of yolk-shell nanospheres with ultra-small Au nanoparticles for catalysis. *Chemical Communications* **2015**, *51* (18), 3750-3753.
3. Kim, W.; Lee, J.-C.; Shin, J.-H.; Jin, K.-H.; Park, H.-K.; Choi, S., Instrument-free synthesizable fabrication of label-free optical biosensing paper strips for the early detection of infectious keratoconjunctivitis. *Analytical chemistry* **2016**, *88* (10), 5531-5537.
4. (a) Kong, F.-Y.; Zhang, J.-W.; Li, R.-F.; Wang, Z.-X.; Wang, W.-J.; Wang, W., Unique roles of gold nanoparticles in drug delivery, targeting and imaging applications. *Molecules* **2017**, *22* (9), 1445; (b) Miclăuş, T.; Beer, C.; Chevallier, J.; Scavenius, C.; Bochenkov, V. E.; Enghild, J. J.; Sutherland, D. S., Dynamic protein coronas revealed as a modulator of silver nanoparticle sulphidation in vitro. *Nature Communications* **2016**, *7* (1), 1-10.
5. Arora, N.; Mehta, A.; Mishra, A.; Basu, S., 4-Nitrophenol reduction catalysed by Au-Ag bimetallic nanoparticles supported on LDH: Homogeneous vs. heterogeneous catalysis. *Applied Clay Science* **2018**, *151*, 1-9.

6. Guo, R.; Yin, F.; Sun, Y.; Mi, L.; Shi, L.; Tian, Z.; Li, T., Ultrasensitive simultaneous detection of multiplex disease-related nucleic acids using double-enhanced surface-enhanced Raman scattering nanosensors. *ACS applied materials & interfaces* **2018**, *10* (30), 25770-25778.
7. (a) Ghosh, S. K.; Pal, T., Interparticle coupling effect on the surface plasmon resonance of gold nanoparticles: from theory to applications. *Chemical reviews* **2007**, *107* (11), 4797-4862; (b) Shanthil, M.; Thomas, R.; Swathi, R.; George Thomas, K., Ag@ SiO₂ core-shell nanostructures: distance-dependent plasmon coupling and SERS investigation. *The journal of physical chemistry letters* **2012**, *3* (11), 1459-1464.
8. (a) Jiang, T.; Wang, X.; Tang, J.; Tang, S., Seed-mediated synthesis of floriated Ag nanoplates as surface enhanced Raman scattering substrate for in situ molecular detection. *Materials Research Bulletin* **2018**, *97*, 201-206; (b) Rycenga, M.; Cobley, C. M.; Zeng, J.; Li, W.; Moran, C. H.; Zhang, Q.; Qin, D.; Xia, Y., Controlling the synthesis and assembly of silver nanostructures for plasmonic applications. *Chemical reviews* **2011**, *111* (6), 3669-3712.
9. Tang, L.; Li, S.; Han, F.; Liu, L.; Xu, L.; Ma, W.; Kuang, H.; Li, A.; Wang, L.; Xu, C., SERS-active Au@ Ag nanorod dimers for ultrasensitive dopamine detection. *Biosensors and Bioelectronics* **2015**, *71*, 7-12.
10. Feng, J.; Su, L.; Ma, Y.; Ren, C.; Guo, Q.; Chen, X., CuFe₂O₄ magnetic nanoparticles: A simple and efficient catalyst for the reduction of nitrophenol. *Chemical engineering journal* **2013**, *221*, 16-24.
11. Tsao, Y.-C.; Rej, S.; Chiu, C.-Y.; Huang, M. H., Aqueous phase synthesis of Au-Ag core-shell nanocrystals with tunable shapes and their optical and catalytic properties. *Journal of the American Chemical Society* **2014**, *136* (1), 396-404.
12. Sun, Y.; Lei, C., Synthesis of Out-of-Substrate Au-Ag Nanoplates with Enhanced Stability for Catalysis. *Angewandte Chemie* **2009**, *121* (37), 6956-6959.
13. Wu, X.; Qiu, L.; Yang, Z.; Yan, F., Imidazolium functionalized NT-Im-Au-Ag hybrids for surface-enhanced Raman scattering and catalytic reduction of 4-nitrophenol. *Applied Catalysis A: General* **2014**, *478*, 30-37.
14. (a) Jiang, Y.; Wu, X.-J.; Li, Q.; Li, J.; Xu, D., Facile synthesis of gold nanoflowers with high surface-enhanced Raman scattering activity. *Nanotechnology* **2011**, *22* (38), 385601; (b) Samal, A. K.; Polavarapu, L.; Rodal-Cedeira, S.; Liz-Marzán, L. M.; Pérez-Juste, J.; Pastoriza-Santos, I., Size tunable Au@ Ag core-shell nanoparticles: synthesis and surface-enhanced Raman scattering properties. *Langmuir* **2013**, *29* (48), 15076-15082.
15. (a) Wang, H.; Levin, C. S.; Halas, N. J., Nanosphere arrays with controlled sub-10-nm gaps as surface-enhanced Raman spectroscopy substrates. *Journal of the American Chemical Society* **2005**, *127* (43), 14992-14993; (b) Yap, F. L.; Thoniyot, P.; Krishnan, S.; Krishnamoorthy, S., Nanoparticle cluster arrays for high-performance SERS through directed self-assembly on flat substrates and on optical fibers. *Acs Nano* **2012**, *6* (3), 2056-2070.
16. Liou, P.; Nayigiziki, F. X.; Kong, F.; Mustapha, A.; Lin, M., Cellulose nanofibers coated with silver nanoparticles as a SERS platform for detection of pesticides in apples. *Carbohydrate polymers* **2017**, *157*, 643-650.

17. Wei, H.; Rodriguez, K.; Renneckar, S.; Leng, W.; Vikesland, P. J., Preparation and evaluation of nanocellulose–gold nanoparticle nanocomposites for SERS applications. *Analyst* **2015**, *140* (16), 5640-5649.
18. Johnson, L.; Thielemans, W.; Walsh, D. A., Nanocomposite oxygen reduction electrocatalysts formed using bioderived reducing agents. *Journal of Materials Chemistry* **2010**, *20* (9), 1737-1743.
19. Isogai, A.; Saito, T.; Fukuzumi, H., TEMPO-oxidized cellulose nanofibers. *nanoscale* **2011**, *3* (1), 71-85.
20. Isogai, A.; Zhou, Y., Diverse nanocelluloses prepared from TEMPO-oxidized wood cellulose fibers: Nanonetworks, nanofibers, and nanocrystals. *Current Opinion in Solid State and Materials Science* **2019**, *23* (2), 101-106.
21. (a) Uddin, K. M. A.; Lokanathan, A. R.; Liljeström, A.; Chen, X.; Rojas, O. J.; Laine, J., Silver nanoparticle synthesis mediated by carboxylated cellulose nanocrystals. *Green Materials* **2014**, *2* (4), 183-192; (b) Musino, D.; Rivard, C.; Landrot, G.; Novales, B.; Rabilloud, T.; Capron, I., Hydroxyl groups on cellulose nanocrystal surfaces form nucleation points for silver nanoparticles of varying shapes and sizes. *Journal of Colloid and Interface Science* **2020**, *584*, 360-371; (c) Hoeng, F.; Denneulin, A.; Neuman, C.; Bras, J., Charge density modification of carboxylated cellulose nanocrystals for stable silver nanoparticles suspension preparation. *Journal of Nanoparticle Research* **2015**, *17* (6), 244; (d) Liu, L.; Wang, L.; Luo, S.; Qing, Y.; Yan, N.; Wu, Y., Chiral nematic assemblies of silver nanoparticles in cellulose nanocrystal membrane with tunable optical properties. *Journal of Materials Science* **2019**, *54* (8), 6699-6708.
22. Shin, Y.; Bae, I.-T.; Arey, B. W.; Exarhos, G. J., Facile stabilization of gold-silver alloy nanoparticles on cellulose nanocrystal. *The Journal of Physical Chemistry C* **2008**, *112* (13), 4844-4848.
23. Asgari, S.; Sun, L.; Lin, J.; Weng, Z.; Wu, G.; Zhang, Y.; Lin, M., Nanofibrillar cellulose/Au@Ag nanoparticle nanocomposite as a SERS substrate for detection of paraquat and thiram in lettuce. *Microchimica Acta* **2020**, *187* (7), 1-11.
24. Gopiraman, M.; Saravanamoorthy, S.; Baskar, R.; Ilangovan, A.; Ill-Min, C., Green synthesis of Ag@Au bimetallic regenerated cellulose nanofibers for catalytic applications. *New Journal of Chemistry* **2019**, *43* (43), 17090-17103.
25. Liu, B.; Han, G.; Zhang, Z.; Liu, R.; Jiang, C.; Wang, S.; Han, M.-Y., Shell thickness-dependent Raman enhancement for rapid identification and detection of pesticide residues at fruit peels. *Analytical chemistry* **2012**, *84* (1), 255-261.
26. Olson, T. Y.; Schwartzberg, A. M.; Orme, C. A.; Talley, C. E.; O'Connell, B.; Zhang, J. Z., Hollow gold–silver double-shell nanospheres: structure, optical absorption, and surface-enhanced Raman scattering. *The Journal of Physical Chemistry C* **2008**, *112* (16), 6319-6329.
27. Nabeela, K.; Thomas, R. T.; Nair, J. B.; Maiti, K. K.; Warriar, K. G. K.; Pillai, S., TEMPO-oxidized nanocellulose fiber-directed stable aqueous suspension of plasmonic flower-like silver nanoconstructs for ultra-trace detection of analytes. *ACS Applied Materials & Interfaces* **2016**, *8* (43), 29242-29251.
28. Fukuzumi, H.; Tanaka, R.; Saito, T.; Isogai, A., Dispersion stability and aggregation behavior of TEMPO-oxidized cellulose nanofibrils in water as a function of salt addition. *Cellulose* **2014**, *21* (3), 1553-1559.

29. Toro, M. C. G.; Schlegel, J. P.; Giraldo, C. H., Radioactive Bimetallic Gold–Silver Nanoparticles Production in a Research Nuclear Reactor. *ChemistrySelect* **2018**, *3* (31), 8936-8941.
30. Hu, Y.; Zhang, A.-Q.; Li, H.-J.; Qian, D.-J.; Chen, M., Synthesis, study, and discrete dipole approximation simulation of Ag-Au bimetallic nanostructures. *Nanoscale research letters* **2016**, *11* (1), 209.
31. Mahmud, S.; Satter, S. S.; Singh, A. K.; Rahman, M. M.; Mollah, M. Y. A.; Susan, M. A. B. H., Tailored Engineering of Bimetallic Plasmonic Au@ Ag Core@ Shell Nanoparticles. *ACS omega* **2019**, *4* (19), 18061-18075.
32. Jia, K.; Khaywah, M. Y.; Li, Y.; Bijeon, J. L.; Adam, P. M.; D eturche, R. g.; Guelorget, B.; Fran ois, M.; Louarn, G.; Ionescu, R. E., Strong improvements of localized surface plasmon resonance sensitivity by using Au/Ag bimetallic nanostructures modified with polydopamine films. *ACS Applied Materials & Interfaces* **2014**, *6* (1), 219-227.
33. Sun, F.; Liu, W.; Dong, Z.; Deng, Y., Underwater superoleophobicity cellulose nanofibril aerogel through regioselective sulfonation for oil/water separation. *Chemical Engineering Journal* **2017**, *330*, 774-782.
34. Yang, J.; Ma, C.; Tao, J.; Li, J.; Du, K.; Wei, Z.; Chen, C.; Wang, Z.; Zhao, C.; Ma, M., Optimization of polyvinylamine-modified nanocellulose for chlorpyrifos adsorption by central composite design. *Carbohydrate Polymers* **2020**, 116542.
35. Malathi, S.; Ezhilarasu, T.; Abiraman, T.; Balasubramanian, S., One pot green synthesis of Ag, Au and Au–Ag alloy nanoparticles using isonicotinic acid hydrazide and starch. *Carbohydrate polymers* **2014**, *111*, 734-743.
36. Zhang, K.; Zhao, J.; Xu, H.; Li, Y.; Ji, J.; Liu, B., Multifunctional paper strip based on self-assembled interfacial plasmonic nanoparticle arrays for sensitive SERS detection. *ACS applied materials & interfaces* **2015**, *7* (30), 16767-16774.
37. Kim, W.; Kim, Y.-H.; Park, H.-K.; Choi, S., Facile fabrication of a silver nanoparticle immersed, surface-enhanced Raman scattering imposed paper platform through successive ionic layer absorption and reaction for on-site bioassays. *ACS applied materials & interfaces* **2015**, *7* (50), 27910-27917.
38. (a) Wang, H.; Guo, X.; Fu, S.; Yang, T.; Wen, Y.; Yang, H., Optimized core–shell Au@ Ag nanoparticles for label-free Raman determination of trace Rhodamine B with cancer risk in food product. *Food chemistry* **2015**, *188*, 137-142; (b) Liu, Y.; Zhou, J.; Wang, B.; Jiang, T.; Ho, H.-P.; Petti, L.; Mormile, P., Au@ Ag core–shell nanocubes: epitaxial growth synthesis and surface-enhanced Raman scattering performance. *Physical Chemistry Chemical Physics* **2015**, *17* (10), 6819-6826.
39. Ma, Y.; Li, W.; Cho, E. C.; Li, Z.; Yu, T.; Zeng, J.; Xie, Z.; Xia, Y., Au@ Ag core–shell nanocubes with finely tuned and well-controlled sizes, shell thicknesses, and optical properties. *ACS nano* **2010**, *4* (11), 6725-6734.
40. (a) Zhang, S.; Xiong, R.; Mahmoud, M. A.; Quigley, E. N.; Chang, H.; El-Sayed, M.; Tsukruk, V. V., Dual-excitation nanocellulose plasmonic membranes for molecular and cellular SERS detection. *ACS applied materials & interfaces* **2018**, *10* (21), 18380-18389; (b) Ren, S.; Dong, L.; Zhang, X.; Lei, T.; Ehrenhauser, F.; Song, K.; Li, M.; Sun, X.; Wu, Q., Electrospun nanofibers made of silver nanoparticles, cellulose nanocrystals, and polyacrylonitrile as substrates for surface-enhanced Raman scattering. *Materials* **2017**, *10* (1), 68; (c) Xiong, Z.;

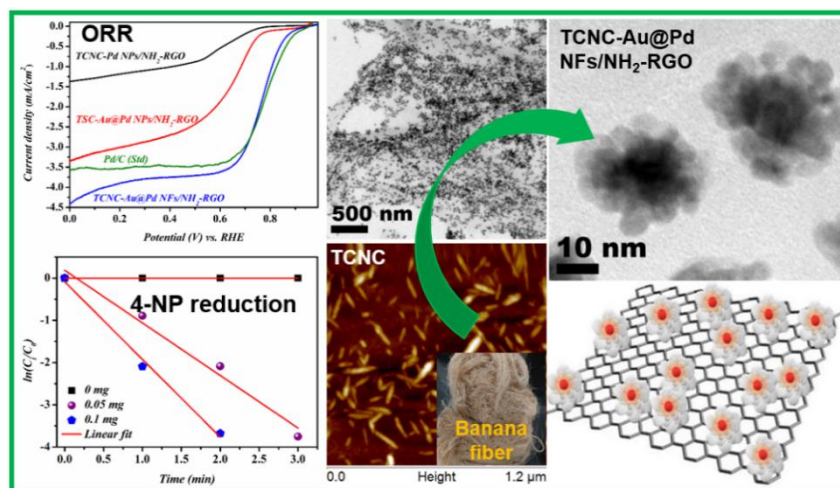
- Chen, X.; Liou, P.; Lin, M., Development of nanofibrillated cellulose coated with gold nanoparticles for measurement of melamine by SERS. *Cellulose* **2017**, *24* (7), 2801-2811.
41. Nabeela, K.; Thomas, R. T.; Mohamed, A.; Pillai, S., Nanocellulose-silver ensembles for ultrasensitive SERS: An investigation on the role of nanocellulose fibers in the generation of high-density hotspots. *Applied Materials Today* **2020**, *20*, 100672.
42. Li, C.; Huang, Y.; Lai, K.; Rasco, B. A.; Fan, Y., Analysis of trace methylene blue in fish muscles using ultra-sensitive surface-enhanced Raman spectroscopy. *Food Control* **2016**, *65*, 99-105.
43. Fu, W. L.; Zhen, S. J.; Huang, C. Z., One-pot green synthesis of graphene oxide/gold nanocomposites as SERS substrates for malachite green detection. *Analyst* **2013**, *138* (10), 3075-3081.
44. Tan, E.-Z.; Yin, P.-G.; You, T.-t.; Wang, H.; Guo, L., Three dimensional design of large-scale TiO₂ nanorods scaffold decorated by silver nanoparticles as SERS sensor for ultrasensitive malachite green detection. *ACS applied materials & interfaces* **2012**, *4* (7), 3432-3437.
45. Ouyang, L.; Yao, L.; Zhou, T.; Zhu, L., Accurate SERS detection of malachite green in aquatic products on basis of graphene wrapped flexible sensor. *Analytica chimica acta* **2018**, *1027*, 83-91.
46. Sivashanmugan, K.; Liao, J.-D.; Liu, B. H.; Yao, C.-K.; Luo, S.-C., Ag nanoclusters on ZnO nanodome array as hybrid SERS-active substrate for trace detection of malachite green. *Sensors and Actuators B: Chemical* **2015**, *207*, 430-436.
47. Song, D.; Yang, R.; Wang, C.; Xiao, R.; Long, F., Reusable nanosilver-coated magnetic particles for ultrasensitive SERS-based detection of malachite green in water samples. *Scientific reports* **2016**, *6* (1), 1-9.
48. Lin, S.; Hasi, W.; Lin, X.; Han, S.; Xiang, T.; Liang, S.; Wang, L., Lab-On-Capillary Platform for On-Site Quantitative SERS Analysis of Surface Contaminants Based on Au@ 4-MBA@ Ag Core-Shell Nanorods. *ACS sensors* **2020**, *5* (5), 1465-1473.
49. Sun, L.; Zhang, M.; Natarajan, V.; Yu, X.; Zhang, X.; Zhan, J., Au@ Ag core-shell nanoparticles with a hidden internal reference promoted quantitative solid phase microextraction-surface enhanced Raman spectroscopy detection. *RSC advances* **2017**, *7* (38), 23866-23874.
50. Huang, W.-S.; Sun, I.-W.; Huang, C.-C., Promotion of SERS and catalytic activities with bimetallic and ternary concave nanolayers. *Journal of Materials Chemistry A* **2018**, *6* (27), 13041-13049.
51. Ogundare, S. A.; van Zyl, W. E., Amplification of SERS “hot spots” by silica clustering in a silver-nanoparticle/nanocrystalline-cellulose sensor applied in malachite green detection. *Colloids and Surfaces A: Physicochemical and Engineering Aspects* **2019**, *570*, 156-164.
52. Chettri, P.; Vendamani, V.; Tripathi, A.; Singh, M. K.; Pathak, A. P.; Tiwari, A., Green synthesis of silver nanoparticle-reduced graphene oxide using Psidium guajava and its application in SERS for the detection of methylene blue. *Applied Surface Science* **2017**, *406*, 312-318.

53. Dinh, N. X.; Huy, T. Q.; Le, A.-T., Multiwalled carbon nanotubes/silver nanocomposite as effective SERS platform for detection of methylene blue dye in water. *Journal of Science: Advanced Materials and Devices* **2016**, *1* (1), 84-89.
54. Ren, P.; Zhou, W.; Ren, X.; Zhang, X.; Sun, B.; Chen, Y.; Zheng, Q.; Li, J.; Zhang, W., Improved surface-enhanced Raman scattering (SERS) sensitivity to molybdenum oxide nanosheets via the lightning rod effect with application in detecting methylene blue. *Nanotechnology* **2020**, *31* (22), 224002.
55. Sinha, G.; Depero, L. E.; Alessandri, I., Recyclable SERS substrates based on Au-coated ZnO nanorods. *ACS applied materials & interfaces* **2011**, *3* (7), 2557-2563.
56. Olea-Mejía, O.; Fernández-Mondragón, M.; Rodríguez-de la Concha, G.; Camacho-López, M., SERS-active Ag, Au and Ag–Au alloy nanoparticles obtained by laser ablation in liquids for sensing methylene blue. *Applied Surface Science* **2015**, *348*, 66-70.
57. Guo, X.; Guo, Z.; Jin, Y.; Liu, Z.; Zhang, W.; Huang, D., Silver–gold core-shell nanoparticles containing methylene blue as SERS labels for probing and imaging of live cells. *Microchimica Acta* **2012**, *178* (1-2), 229-236.
58. Yee, K., Numerical solution of initial boundary value problems involving Maxwell's equations in isotropic media. *IEEE Transactions on antennas and propagation* **1966**, *14* (3), 302-307.
59. Revathy, T.; Dhanavel, S.; Sivaranjani, T.; Narayanan, V.; Maiyalagan, T.; Stephen, A., Highly active graphene-supported palladium-nickel alloy nanoparticles for catalytic reduction of 4-nitrophenol. *Applied Surface Science* **2018**, *449*, 764-771.
60. Tian, Y.; Cao, Y.-y.; Pang, F.; Chen, G.-q.; Zhang, X., Ag nanoparticles supported on N-doped graphene hybrids for catalytic reduction of 4-nitrophenol. *RSC Advances* **2014**, *4* (81), 43204-43211.
61. Scott, R. W.; Sivadinarayana, C.; Wilson, O. M.; Yan, Z.; Goodman, D. W.; Crooks, R. M., Titania-supported PdAu bimetallic catalysts prepared from dendrimer-encapsulated nanoparticle precursors. *Journal of the American Chemical Society* **2005**, *127* (5), 1380-1381.
62. Ma, M.; Yang, Y.; Li, W.; Feng, R.; Li, Z.; Lyu, P.; Ma, Y., Gold nanoparticles supported by amino groups on the surface of magnetite microspheres for the catalytic reduction of 4-nitrophenol. *Journal of materials science* **2019**, *54* (1), 323-334.
63. Liu, Y.; Jiang, G.; Li, L.; Chen, H.; Huang, Q.; Jiang, T.; Du, X.; Chen, W., Preparation of Au/PAN nanofibrous membranes for catalytic reduction of 4-nitrophenol. *Journal of materials science* **2015**, *50* (24), 8120-8127.
64. (a) Wang, D.; Li, Y., Bimetallic nanocrystals: liquid-phase synthesis and catalytic applications. *Advanced Materials* **2011**, *23* (9), 1044-1060; (b) Guo, X.; Zhang, Q.; Sun, Y.; Zhao, Q.; Yang, J., Lateral etching of core–shell Au@ metal nanorods to metal-tipped Au nanorods with improved catalytic activity. *ACS nano* **2012**, *6* (2), 1165-1175.
65. Yang, Y.; Shi, J.; Kawamura, G.; Nogami, M., Preparation of Au–Ag, Ag–Au core-shell bimetallic nanoparticles for surface-enhanced Raman scattering. *Scripta Materialia* **2008**, *58* (10), 862-865.

66. Feng, Y.; Wang, G.; Chang, Y.; Cheng, Y.; Sun, B.; Wang, L.; Chen, C.; Zhang, H., Electron Compensation Effect Suppressed Silver Ion Release and Contributed Safety of Au@ Ag Core–Shell Nanoparticles. *Nano letters* **2019**, *19* (7), 4478-4489.
67. Liang, M.; Su, R.; Qi, W.; Yu, Y.; Wang, L.; He, Z., Synthesis of well-dispersed Ag nanoparticles on eggshell membrane for catalytic reduction of 4-nitrophenol. *Journal of Materials Science* **2014**, *49* (4), 1639-1647.
68. Menumarov, E.; Hughes, R. A.; Neretina, S., Catalytic reduction of 4-nitrophenol: a quantitative assessment of the role of dissolved oxygen in determining the induction time. *Nano letters* **2016**, *16* (12), 7791-7797.

CHAPTER 4

CNC-directed, Stable Flower-like Au@Pd Nanostructures



This chapter has been adopted from the following publication,

H. M. Abdul Hakkeem *et al.*, Carbohydrate Polymers, 2022, 292, 119723.

ABSTRACT

Au@Pd is conjoined pair of bimetallic nanoparticles recognized as a prominent candidate in catalysis. Apart from the composition, specific surface area and electronic distribution also endowed pronounced contributions in further enhancement of catalytic performance. In this chapter, we discuss a sustainable way of designing core-shell Au@Pd nanoflowers (NFs) employing banana pseudo-stem-derived TEMPO-oxidized cellulose nanocrystals (TCNC) as both capping and shape-directing agent via seed-mediated method. Dimensions of Au@Pd NFs were well controlled by the Pd precursor ratio as an experimental variable. According to our study, carboxyl groups of TCNC induced the selective adsorption of TCNC over Au NPs, and after the consumption of -COOH, rich -OH groups on TCNC will become active nucleation sites for later introduced Pd ions, thereby hindering the epitaxial growth of Pd shell over Au NPs directly resulted in the evolution of flower-like morphology. Importance of heterogeneous catalysts in catalysis signified the further modification of TCNC-Au@Pd NFs by decorating over amino-functionalized graphene (NH₂-RGO) sheets without losing their unique structure. Performance of resultant TCNC-Au@Pd NFs/NH₂-RGO heterogeneous catalyst were investigated in electrocatalytic ORR and reduction of 4-Nitrophenol by considering best model reactions in fuel cell and industrial catalytic applications, respectively.

4.1. INTRODUCTION

Bimetallic nanoparticles with tailored morphologies have been extensively studied due to their unprecedented demand in variety of fields like catalysis¹, sensing², plasmonics³, biomedical⁴ etc., owing to their excellent combined optical and electronic properties of monometallic counterparts.⁵ Apart from isotropic spherical morphologies, anisotropic morphologies have a profound influence on their intrinsic physicochemical properties.⁶ Numerous techniques like electrodeposition, sono-chemical methods, co-precipitation, etc., were reported regarding the preparation of nanomaterials, but achieving controllable geometries and stability is still questionable. Moreover, most of these methods are expensive and low yield. Chemical reduction methods, especially colloidal synthesis

TCNC - Au@Pd Nanoflowers

utilizing various capping agents, are generally employed for the synthesis of metallic nanostructures of well-defined morphologies with comparable shelf life since efficient strategies for tailoring desired morphologies of nanoparticles are gaining significant attention. CTAB⁷, CTAC⁸, PVP⁹ are a few well established and explored capping as well as shape-directing agents for modulating specific geometries of nanoparticles. Many of the synthesis methods utilizing conventional capping agents are complex, time-consuming, require high temperatures, and utilize toxic organic solvents. Nevertheless, the above-mentioned conventional capping agents are the pillars of the synthesis of anisotropic nanostructures. However, there exist only a few promising eco-friendly or sustainable strategies capable of the controlled morphology generation of metallic nanoparticles that perform with completely inherent properties. Presenting them as a sustainable alternative to conventional shape-directing agents is a challenge in the realm of nanotechnology, which is completely ruled by conventional ones.

Nano version of the most abundant biopolymer cellulose with a less amorphous nature, known as cellulose nanocrystals (CNC), upsurged in recent years. Realm of CNC goes far beyond merely due to the applicability that arises from the congregate of remarkable properties like easy functionalization¹⁰, mechanical properties¹¹, sustainability, and high surface area¹², etc. Regardless of labyrinth acid hydrolysis synthetic way, Zhou *et al.* proposed a modified way by TEMPO-mediated oxidation followed by cavitation which enables the ease of formation of CNC.¹³ Carboxyl groups confined by TEMPO-mediated oxidation and inborn abundant -OH groups ascertained the robustness of TCNC towards good carriers of metal nanoparticles avoiding any undesirable aggregation that crevasse its performances.¹⁴ Moreover, apart from conventional polymer capping agents, criteria of desirable surface area for both nanoparticles and template (TCNC) is well ascertained due to the nano range physical dimensions.¹⁵ Electrostatic interactions between metal ions and functionalized hydrophilic TCNC confine the controlled growth and distribution of metal nanoparticles over TCNC with high surface area.¹⁶ There are several reports regarding the CNC-assisted synthesis of ultra-stable metal nanoparticles, especially Au and Ag, for various applications. Notably, Kaushik *et al.* integrated the template, stabilizer, and reducing actions of CNC reported in the area of

catalysis.¹⁴ To the best of our knowledge, there are only a few recent researches on the preparation of CNC supported Pd nanoparticles for catalytic application that made an upsurge in activity; however, morphology control and modification is still not attained.¹⁷

Au@Pd anisotropic nanoparticles unambiguously showed their catalytic properties in various fields endowed from electronic couplings and geometric effects.¹⁸ Au-Pd bimetallic nanostructures can be designed as alloys or core-shell morphologies by co-reduction and seed-mediated synthesis, respectively. In which seed-mediated synthesis for core-shell morphology is complex and pronounced due to the judicious control over the intrinsic physicochemical properties simply by tuning the composition, shell morphology, and thickness.¹⁹ Numerous new strategies are evolved for the synthesis of Au@Pd core-shell NPs with flower-like morphologies utilizing shape-directing agents through seed-mediated synthesis envisioned from the pronounced applicability of this bimetallic system in the field of catalysis. Xu *et al.* demonstrated the synthesis of Au-Pd NFs by the formation of Pd petal-like shell over PVP capped Au seed.¹⁴ Lee *et al.* reported the fabrication of flower shaped porous Au-Pd alloy nanoparticles by the reduction of ascorbic acid and employing the PVP as stabilizing agent.⁹

Apart from Pt, Pd is also popular as an efficient metal catalyst that shows excellent electrochemical activity in fuel cells.²⁰ Moreover, bimetallic NPs comprising Pd and other metals often exhibit better electrocatalytic efficacies than their monometallic counterparts. Au-Pd NPs are well known as an alternative for expensive and scarce Pt catalysts.²¹ Several reports are published focussing on this bimetallic system having dramatic electro-catalytic activity emerging from the corporative catalytic properties of both Au and Pd since Au acts as a promoter to electron transfer to Pd.²² Au-Pd bimetallic NPs are also well known for its catalytic activity towards reduction of 4-NP to 4-AP, a model catalytic reaction that took as the backbone of pharmaceutical industry.²³

Incorporation of Au@Pd NPs onto a carbon support material is required for the fabrication of heterogeneous recyclable catalysis applications. Mixing of metallic NPs with vulcanized carbon were adopted by many people for the construction of heterogeneous recyclable catalysts.²⁴ However, this may be become formidable challenge for the stability of NPs. These might be the reason for choosing reduced graphene oxide (RGO)²⁵, CNT²⁶

as the versatile support for the metal NPs which further improves the catalytic activity of immobilized nanoparticles.²⁷ There arises another difficulty is that metal NPs have a tendency of spontaneous aggregation at the edges of defects of these materials, which may lead to the destruction of the anisotropic morphology of metal nanoparticles. These can be solved by the addition of surfactants; however, it may be lead to the reduction in catalytic activity.²⁸

In this chapter, we demonstrate a novel, sustainable and controllable synthetic strategy for Au@Pd NFs, well bounded by TEMPO-oxidised cellulose nanocrystals imitating a flower garland that impart ultra-stability to the colloidal system. The novelty of the present report is the remarkable shape-directing and capping activity of a bio-derived material, nanocellulose as a new competitor to conventional capping agents. For the applicability as green/sustainable, efficient and recyclable heterogeneous catalyst, TEMPO-oxidised cellulose nanocrystals bounded Au@Pd (TCNC-Au@Pd) flower-like nanoconstructs have been decorated over amino-functionalized graphene (NH₂-RGO) without losing its interesting structure. Performance of our heterogeneous catalyst in two parallel on-going model catalysis areas, that is oxygen reduction reaction (ORR) in alkaline electrolyte solution and reduction of 4-Nitrophenol were successfully attempted. This assignment will open a new door to further renovations and investigations of this green catalyst in the realm of catalysis.

4.2. EXPERIMENTAL SECTION

4.2.1. Materials

TCNC prepared from banana pseudo-stem fibers by TEMPO-mediated oxidation and 2h ultra-sonication (Chapter 2, section 2.2). Gold(III) chloride trihydrate (HAuCl₄. 2H₂O), trisodium citrate tribasic dihydrate (TSC; C₆H₅Na₃O₇. 2H₂O), Palladium chloride (PdCl₂), L-ascorbic acid (AA; C₆H₈O₆), Graphite powder < 150 μm, Sodium nitrite (NaNO₂), Sulphuric acid (H₂SO₄, 98%), Hydrogen Peroxide (H₂O₂, 30 wt%), 4-nitrophenol (4-NP; C₆H₅NO₃) and sodium borohydride (NaBH₄) were purchased from Sigma-Aldrich and used without any further purifications. Hydrochloric acid (HCl, 35 %) was purchased from Rankem, whereas potassium permanganate (KMNO₄), ethylene glycol (C₆H₆O₂) and ammonia solution (NH₄OH, 99 %) were purchased from TCI chemicals.

Ultrapure deionized (DI) water (Milli-Q purifier system, Merck, Germany) was used as solvents for all experiments.

4.2.2. Synthesis of TCNC Bounded Au NPs Seed (TCNC-Au NPs)

A typical synthesis of carboxyl functionalized cellulose nanocrystals bounded Au seed solution proceeded by the combined reduction capabilities of both TCNC and TSC with minor modifications (Chapter 3, section 3.2.2).²⁹ In detail, 600 μL of 0.05 M HAuCl_4 mixed with 50 mL aqueous solution of 0.1 wt% TCNC in a 100 mL round-bottom flask by sonication followed by rapid boiling while stirring at 400 rpm. Subsequently, 4 mL of 0.04 M of citrate was added to the boiling solution, and the purple color solution was removed from hotplate after 20 min. As-formed TCNC bounded Au seed solution had been cooled and preserved at 4 $^\circ\text{C}$ for further use. This wine red colored Au seed was used for Pd shell coatings after the solution was allowed to reach room temperature.

4.2.3. Synthesis of TCNC Bounded Au@Pd Nanoflowers (TCNC-Au@Pd NFs)

To synthesize TCNC bounded Au@Pd NFs, a seed-mediated approach was employed with minor modifications by adding 400 μL of 0.05 M aqueous ascorbic acid solution (AA) and 0.05 M PdCl_2 to as-prepared 6 mL TCNC capped Au NPs seed solution dropwise with slow stirring. Progress of reaction can be monitored by the change in the colour of the solution from purple to blackish brown. Variable amounts equimolar AA and PdCl_2 from 50 to 250 μL leads to the formation of TCNC-Au@Pd NFs with increasing number of Pd petals. The samples should be stored at 4 $^\circ\text{C}$ for long self-life. For comparison purpose, the standard Turkevich method adapted citrate capped Au@Pd NPs and TCNC bounded Pd NPs were also synthesized.

4.2.4. Synthesis of Heterogeneous TCNC-Au@Pd Decorated NH_2 -RGO Catalyst

GO was synthesized by modified Hummers method³⁰, then it was amine functionalized and reduced by using one step hydrothermal treatment. Here we adopted the in-situ hydrothermal reduction method using ethylene glycol as solvent. The amine functionalization was done using ammonia solution. Briefly, 30 mg GO was mixed with

TCNC-Au@Pd Nanoflowers

30 mL ethylene glycol solvent and was made into uniform solution by sonication for 15 min. Then the uniform solution was transferred to the Teflon lined autoclave after adding 0.5 ml ammonia solution at 170 °C for 10 h. Resultant dark brown colored solution was filtered, washed and dried at 60 °C for 24 h to obtain amine-functionalized RGO powder.³¹ Further decoration of NH₂-RGO with TCNC-Au@Pd NFs were done by mixing of 20 wt% TCNC-Au@Pd NFs colloid with well dispersed NH₂-RGO in DI water by 30 min ultra-sonication. The sediments were collected and washed thoroughly and dried at 80 °C in a vacuum oven for 24 h. Samples were stored in desiccator for further measurements. For comparison purpose, TSC-Au@Pd NPs/NH₂-RGO, and TCNC-Pd NPs/ NH₂-RGO and were also fabricated.

4.2.5. Electrocatalytic Oxygen Reduction Reaction (ORR)

TCNC-Au@Pd NFs/NH₂-RGO modified working electrode was constructed by dropping 10 μL of homogeneous suspension of catalyst on a rotating disc electrode (RDE) having 3mm diameter. Homogeneous suspension of catalyst was prepared by mixing 1mg of the material per mL of 3:2 IPA:water mixture water and 40 μL of Nafion solution (20 wt%). The mixture was then sonicated for about one hour to obtain a homogeneous suspension. ORR measurements were conducted in a three electrode system consisting of a working electrode (TCNC-Au@Pd NFs/NH₂-RGO; RDE), counter electrode (graphite rod) and a reference electrode (Hg/HgO) in oxygen saturated alkaline medium (0.1 M KOH). For comparison purpose, commercial Pd/C (20 wt%), TSC-Au@Pd NPs/ NH₂-RGO, and TCNC-Pd NPs/ NH₂-RGO were also utilized as catalysts in same manner as above. LSV measurements were from negative to positive direction at 10 mV/s. All the potentials measured were transformed to the reversible hydrogen electrode (RHE) scale.

4.2.6. 4-Nitrophenol (4-NP) Catalytic Reduction

Catalytic reduction of 4-NP was done in a quartz cuvette by adding specific amount of TCNC-Au@Pd NFs/NH₂-RGO catalyst to a mixture of 3 mL freshly prepared 15 mM NaBH₄ solution and 0.25 mM 4-NP solution with constant shaking. Both visual and spectrometric analysis of reduction were carried out at regular interval of time by UV-Vis absorption spectroscopy. After completion of 4-NP reduction, the catalyst was recovered by centrifugation and reused after washing step.

4.2.7. Characterization Methods

TEM analysis was performed using FEI-Tecnai 30 G2S-TWIN transmission electron microscope with a 300 kV acceleration voltage. Zeta potentials of the all samples were obtained from Zetasizer Nano ZS, Malvern equipment. The crystalline structure of the TCNC-Au, TCNC-Au@Pd NFs were determined using PANalytical X'pert pro, powder X-ray diffractometer (XRD) equipped with Cu K α ($\lambda=1.54$ Å), 45 kV. X-ray photoelectron spectroscopy (XPS) study was performed using PHI 5000 VersaProbe II, ULVAC-PHI Inc., USA. The binding energies of XPS peaks were referenced to C1s peak at 284.8 eV. The FTIR spectrometer (PerkinElmer) was used to study the chemical structure of TCNC and TCNC-Au@Pd NFs by scanning in the range from 4000-400 cm⁻¹. Total Au and Pd contents were estimated with an inductively coupled plasma mass spectrometry (ICP-MS) (Thermo Scientific iCAP-RQ). All UV-Visible absorption spectra were acquired using Shimadzu UV-2700, Shimadzu, Japan UV-Visible absorption spectrometer. Oxygen reduction reaction measurements of the synthesized catalysts and commercial standard were performed using the Pine Research Instruments rotating disk electrode (RDE) setup connected to a potentiostat.

4.3. RESULTS AND DISCUSSION

4.3.1. TCNC Bounded Au@Pd Nanoflowers

The Turkevich method for the preparation of Au NPs by utilizing trisodium citrate is well-established over half century ago. Whereas the astonishing reducing and capping actions of nanocellulose have been founded only few years back. TEMPO-oxidized cellulose nanocrystals (TCNC) bounded Au@Pd nanoflowers were synthesized as described in **Figure 4.1**. Utilizing the combined actions of both TCNC and TSC as stabilizing and reducing agents, isotropic spherical Au NPs with size about 15 ± 2 nm bounded by well-dispersed network TCNC were synthesized. Induced carboxyl functionalization in nanocellulose not only to establish better aqueous solubility but also for creation of nucleation sites for metal nanoparticles by the electrostatic interaction between COO⁻ and M⁺ ions.³² Nearly an array of Au NPs of controlled size and geometries

TCNC-Au@Pd Nanoflowers

signifies the action carboxyl ends as nucleation sites in the TCNC support. Thereby hanging of Au (0) NPs preferably at the carboxyl groups by replacing Na^+ ions of linear cellulose chains were obtained as shown in **Figure 4.2**. High scope of formation of an intercalated network bed by both inter and intramolecular hydrogen bonds of TCNC in aqueous media create a perfect permanent seats for Au NPs without any coagulation indicated by the zeta-potential value of about -33 mV shown in **Table 4.1**. Later, the as-prepared TCNC-Au seeds were directly used for Pd shell coating without any further purifications. Five aliquots of as prepared TCNC-Au seeds were mixed with five different quantities (50, 100, 150, 200, and 250 μL) of equimolar ascorbic acid (AA) and Pd precursor at a pH of about 8. Our expectation was a uniform Pd shell coating preferably over the TCNC bounded Au seeds since Pd can grow a layer by layer on Au as from the literature.^{8, 33}

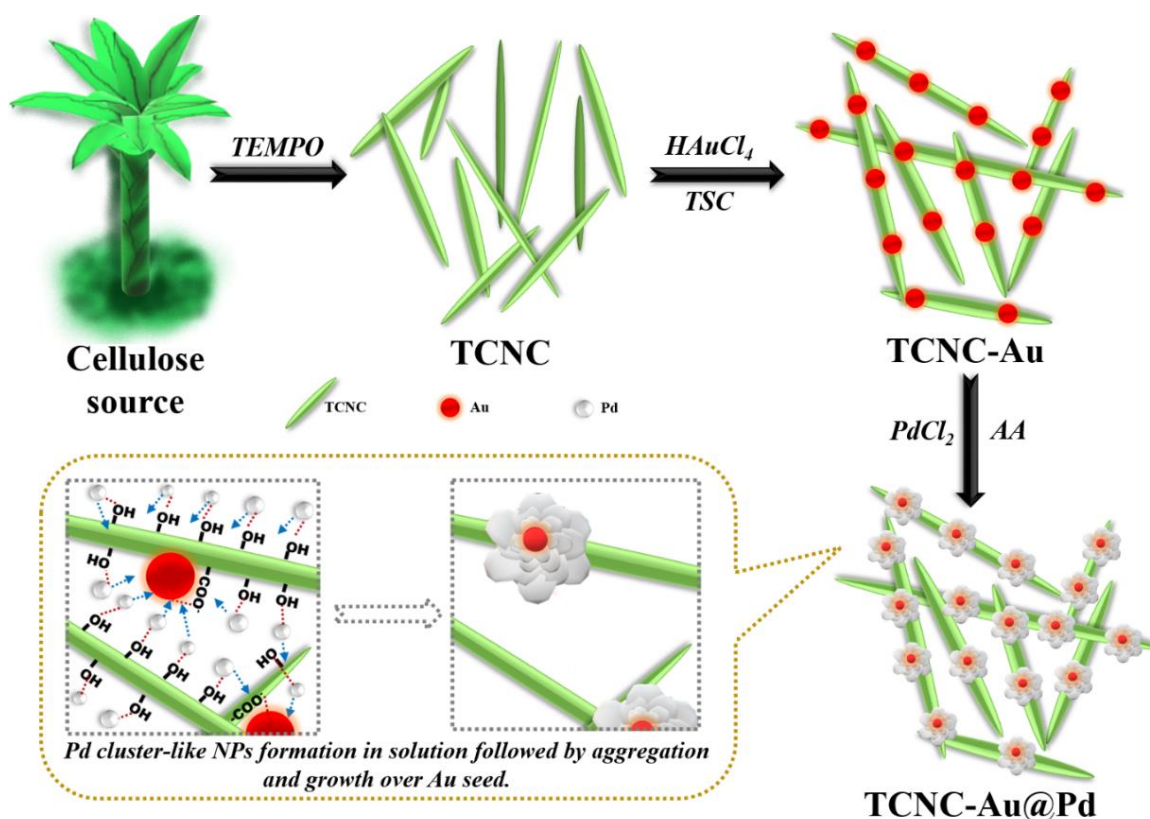


Figure 4.1. Cartoon describing various steps for synthesis of Au@Pd nanoflowers bounded with the TCNC.

After the subsequent additions of 50 μL Ascorbic acid and Pd precursor, the color of colloid changed from wine red to light brownish-black. However, no distinguishable Pd shell formation was observed as shown in **Figure 4.3b**. Succeeding to the addition of 100 μL of the reagents formed in a petal-like island Pd shell over Au core (**Figure 4.3c**). This was clearly distinguishable by high contrast difference arises due to difference in electron density between Au and Pd instead of epitaxial growth of Pd layer over Au core as described elsewhere.³⁴

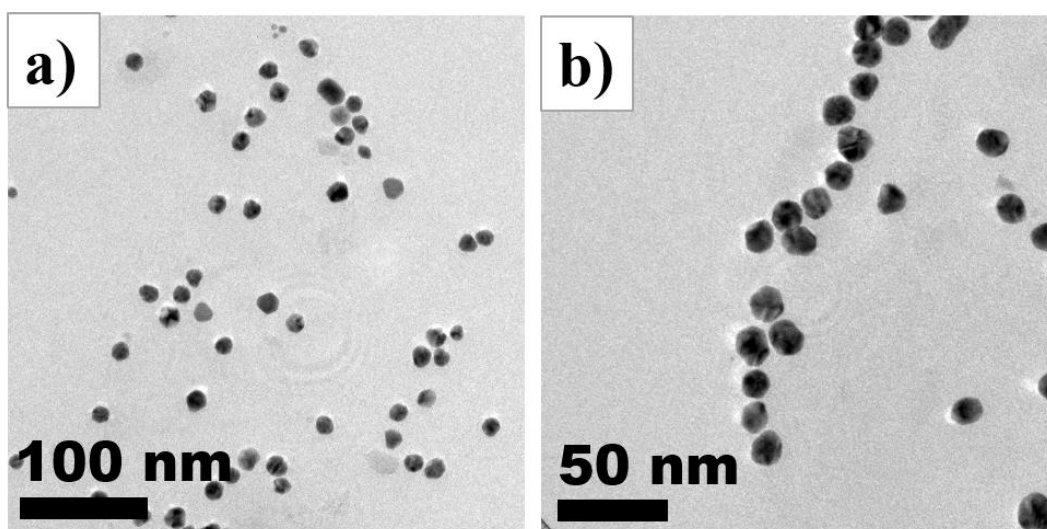


Figure 4.2. TEM images of TCNC-Au NPs seed.

Samples	Zeta potential (mV)
TCNC	-52.0
TCNC-Au (Pd-0)	-33.0
TCNC-Au@Pd (Pd-50)	-36.7
TCNC-Au@Pd (Pd-100)	-39.8
TCNC-Au@Pd (Pd-150)	-45.2
TCNC-Au@Pd (Pd-200)	-50.0
TCNC-Au@Pd (Pd-250)	-47.8

Table 4.1. Zeta-potential values of TCNC-Au@Pd NFs with different Pd shell thickness.

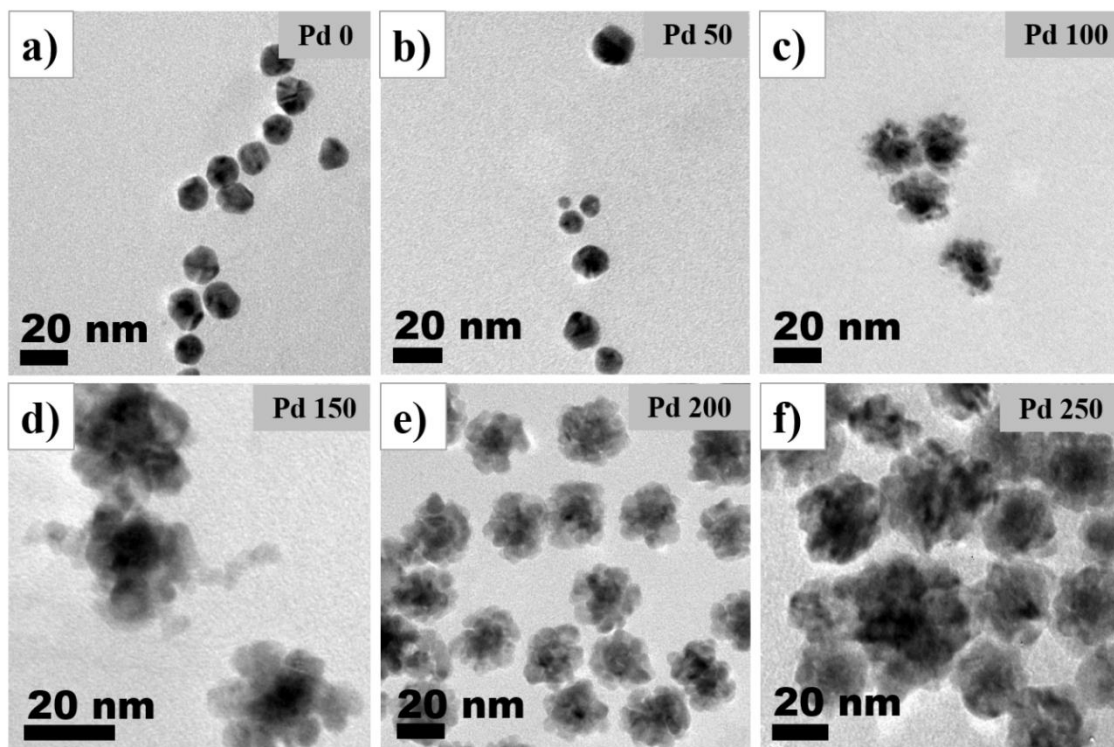


Figure 4.3. TEM images (a) TCNC-Au NP seeds, (b-f) TCNC-Au@Pd NFs containing an Au core and Pd petal-like shells obtained after mixing of different quantities of equimolar ascorbic acid (50, 100, 150, 200 and 250 μL) and Pd precursor at pH, 8.

Presence of TCNC cannot be witness in all TEM images since no heavy metal staining agents were used to distinguish between nanocellulose and metal nanoparticles. Nevertheless, a network of TCNC may be visible even at low magnification in a few regions due to the presence of metal NPs (**Figure 4.4**). Further, an increase in the amounts of reagents, from 150-250 μL resulted an incremental increase in the number of petals of size range, 3-5 nm as revealed from **Figure 4.3(d-f)**. The HR-TEM image and FFT pattern of TCNC-Au@Pd NF structures obtained during the initial stages of Pd shell growth after the addition of 50 μL ascorbic acid and Pd precursor (**a-c**); and the Pd petals growth after the addition of 200 μL (**d-g**) are shown in **Figure 4.5**.

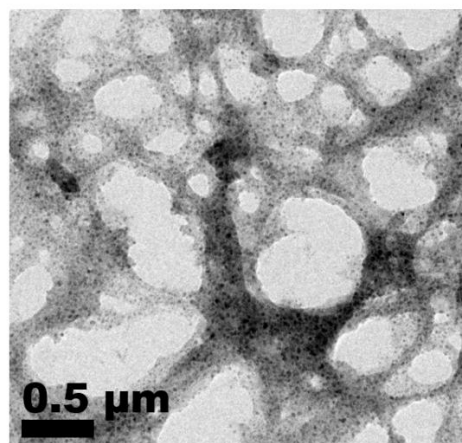


Figure 4.4. TEM image of TCNC-Au NPs seed at low magnification.

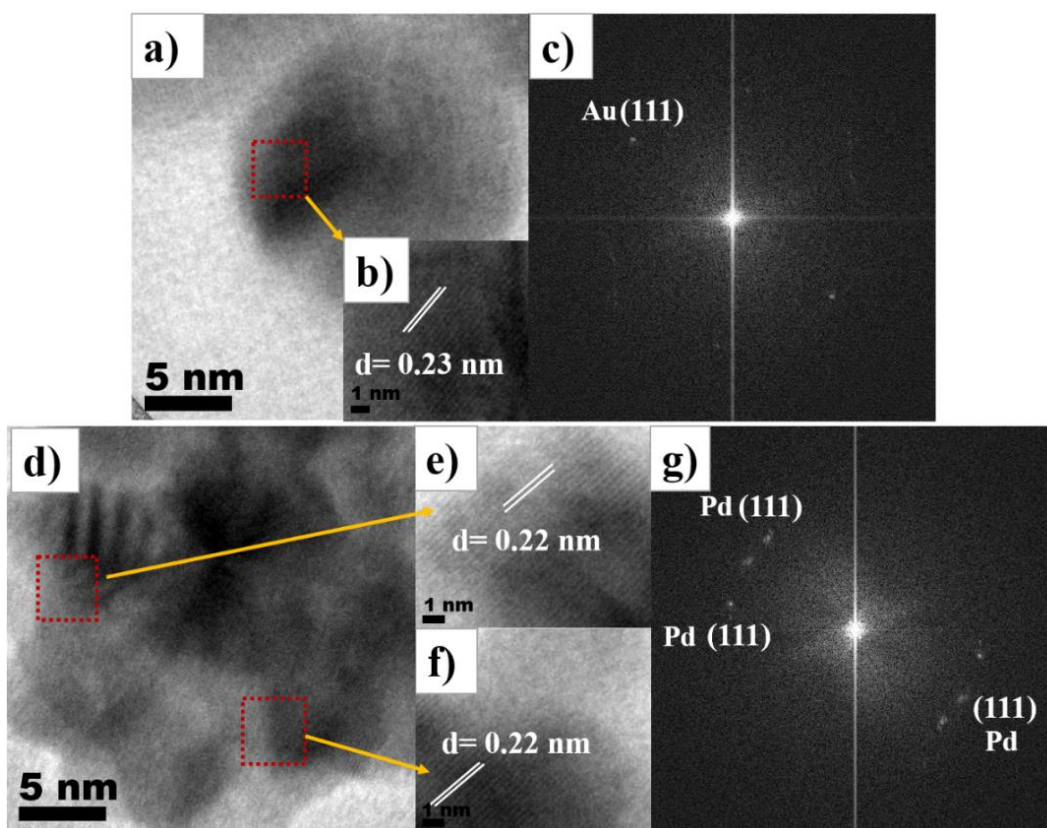


Figure 4.5. HR-TEM images and their corresponding FFT patterns of TCNC-Au@Pd NFs at various Pd shell coating: Pd-50 (a-c) and Pd-200 (d-g).

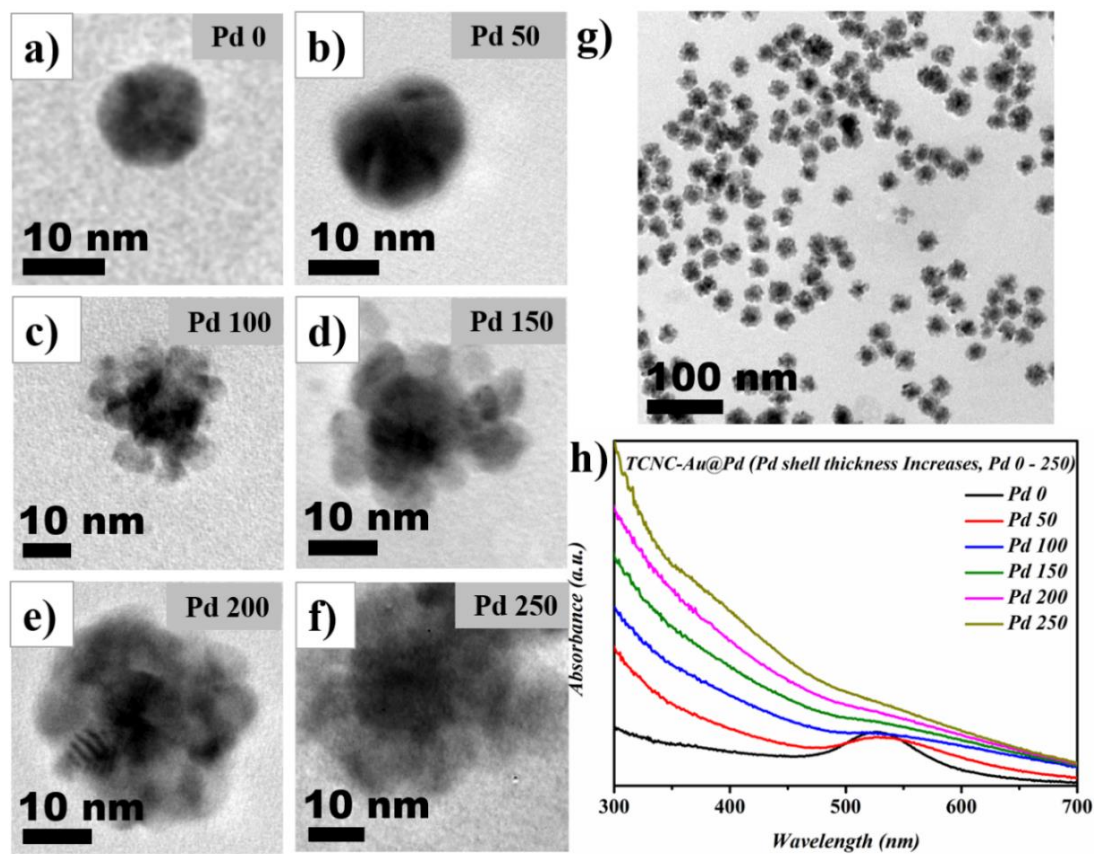


Figure 4.6. (a-f) The TEM images of single TCNC-Au@Pd NF showing an increment in the number of the Pd petals obtained after the coating with different quantities of the Pd precursors, (g) TCNC-Au@Pd NFs at low magnification and (h) the corresponding UV-Visible absorption spectra.

We observed that at lower Pd precursor concentrations, the shell was indistinguishable, and the lattice fringes observed in the higher magnification images and FFT spot pattern signifies the presence of the (111) crystalline plane as the dominant plane corresponds to Au. Whereas in **Figure 4.5d**, a fully formed Pd petals over Au surface, camouflaging TCNC-Au seed was observed. As a result, the lattice fringes of Au core were unattainable, whereas the lattice fringes corresponding to (111) planes of Pd were obtained from petals areas as shown in **Figure 4.5(d-f)**. The corresponding FFT patterns obtained from these petals supports the above findings (**Figure 4.5c, and 4.5g**). In general, the HR-TEM images of initial and intermediate shell thickness (petals) confirmed that Au is present as core and Pd as petal-like shell in the TCNC-Au@Pd NF structures, and significant

alloying has not occurred. As the number of Pd petals augmented, the average size of the TCNC-Au@Pd NF structures varies from 18 ± 2 nm to 32 ± 2 nm (**Figure 4.6(a-f)**). **Figure 4.6g** shows the low magnification TEM image of TCNC-Au@Pd NFs which present the distribution of the Au@Pd NFs with uniform geometry in the entire area. To further affirm the formation of TCNC-Au@Pd NFs, UV-Visible absorption spectra were recorded (**Figure 4.6h**). It is observed that an obvious surface plasmon absorption at 527 nm which is characteristic for Au NPs. Interestingly, this surface plasmon band of Au gradually diminishes up on increasing the amounts of Pd precursors from 50-250 μ L, and finally no observable plasmonic band in the visible region corresponding to Pd nanoparticles.⁹ These results suggest that the morphology of TCNC-Au@Pd NFs having Au confined in the core with Pd shell coating on the of nanostructure.^{14,35} Besides, as-synthesized TCNC-Au@Pd NF structures with different Pd compositions maintained excellent colloidal stability as revealed by the zeta potential values (**Table 4.1**). The TCNC-Au@Pd NFs (Pd-200) colloid revealed the highest zeta potential value of -50.0 mV, and we have not observed any significant sedimentation even after six months (**Figure 4.7a**). The yield of TCNC-Au@Pd NFs is estimated to be about 75% using ICP-MS and quantified the ratio of Au:Pd and found to be approximately 1:2 ratio for TCNC-Au@Pd NFs (Pd-200), which was reported for the better catalytic performance of this bimetallic system.³⁶

Figure 4.7b illustrates the XRD pattern of synthesized TCNC-Au NPs seed which includes diffraction peaks corresponding to nanocellulose and metallic Au. The peaks at $2\theta = 12.36^\circ$, 20.28° , and 22.23° are due to the characteristic diffraction peaks of cellulose II, indexing the planes (1-10), (110) and (200), respectively. The diffraction peaks observed after $2\theta = 35^\circ$, exactly at 38.28° , 44.61° , 64.48° , 77.4° and 81.35° indicate significant matching with the typical diffraction pattern of *fcc* Au NPs corresponded to the planes (111), (200), (220), (311), and (222), respectively (JCPDS no. 00-004-0784). The overall narrow and prominent XRD patterns validated the complete formation of crystalline Au NPs embedded in the intercalated TCNC network. **Figure 4.7c**, XRD pattern of TCNC-Au@Pd NFs demonstrates a slight shift in the peak positions of above-signified planes after Pd shell coating, which nearly matches with the standard diffraction pattern for metallic *fcc* Pd (JCPDS no. 00-005-0681) with diffraction peaks corresponding to TCNC.

TCNC-Au@Pd Nanoflowers

The prominent crystalline peak of (111) plane at 38.28° in TCNC-Au and TCNC-Au@Pd affirmed that the TCNC well covered this plane, which is in consensus with the TEM observations. Compared to the diffraction pattern of TCNC-Au NPs seed and TCNC-Au@Pd NFs (**Figure 4.7b and 4.7c**), after Pd shell coating a significant decrease in the intensity diffraction peaks of TEMPO-oxidized cellulose nanocrystals (TCNC) was observed. These random decrease in the crystallinity of semi-crystalline polymer arises mainly due to the disturbance in crystallinity by the coordination interaction between polymer and the metal introduced to the composite.³⁷ This would infer that here occurs a strong intermolecular interaction between the Pd NPs and TEMPO-oxidized cellulose nanocrystals resulting from the oxophilicity of Pd.^{17d} Therefore, our XRD results suggest an inevitable role of the TEMPO-oxidized cellulose nanocrystals for directing the flower-like morphology instead of the epitaxial growth of Pd over Au NPs.

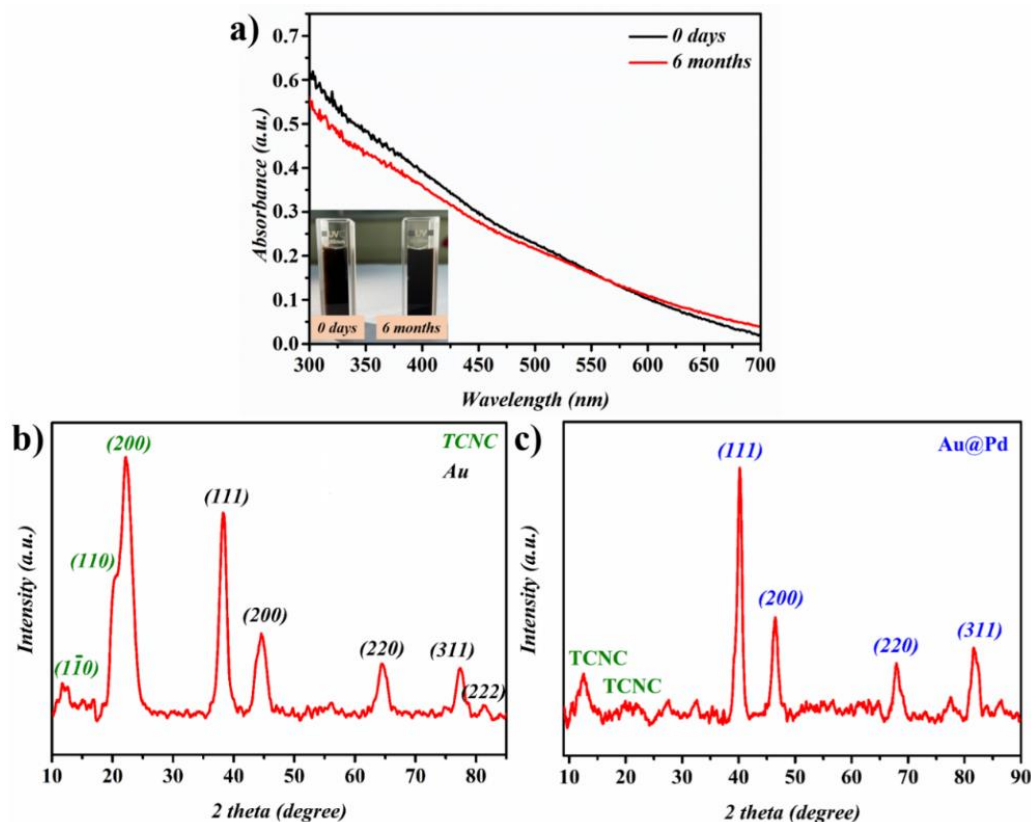


Figure 4.7. (a) UV-Visible absorption spectra of TCNC-Au@Pd NFs (Pd-200) suspension at different time durations (inset: the photographs showing the stability of TCNC-Au@Pd NFs colloid); XRD patterns of (b) TCNC-Au NPs seed and (c) TCNC-Au@Pd NFs (Pd-200).

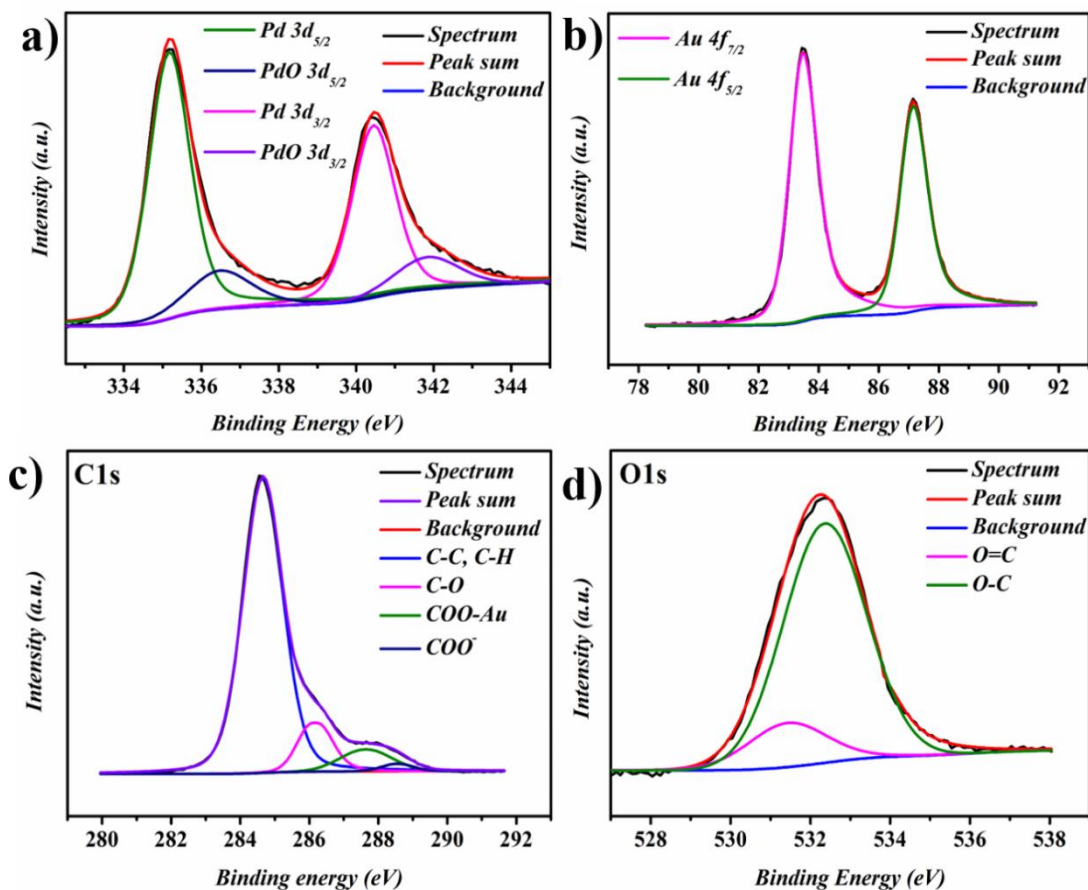


Figure 4.8. XPS narrow scans of TCNC-Au@Pd NFs (Pd-200) (a) deconvoluted spectra of Pd 3d, (b) Au 4f, (c) C1s, and (d) O1s, respectively.

The chemical states of the major elements present in the TCNC-Au@Pd NFs system were investigated by XPS. The narrow scans of major elements of TCNC-Au@Pd NFs are given in **Figure 4.8(a-d)**. Particularly, the narrow scan of Pd3d showed two doublets (**Figure 4.8a**) with relatively high intensity at 335.15 and 340.45 eV with a binding energy separation of 5.30 eV are assumed to have originated from 3d_{5/2} and 3d_{3/2} of Pd (0). The deconvolution of doublet pairs can be fitted with an additional peak of low intensity at 336.48 and 341.84 eV, attributed to the binding energy of Pd²⁺ species. These low intense Pd²⁺ species were unlikely due to the surface partial oxidation of Pd NPs during the sample preparation while drying since Pd is very sensitive to oxygen. **Figure 4.8b** is

the deconvoluted spectrum of Au 4f region of Au NPs showing Au(0) 4f_{7/2} and Au(0) 4f_{5/2} doublets situated at 83.5 and 87.2 eV, respectively with an energy separation of 3.6 eV, which is consistent with the typical spectrum for metallic Au(0).³⁸ Further the narrow-scans of C1s and O1s obtained (**Figure 4.8c and 4.8d**) indicate the presence of TEMPO-oxidized nanocellulose crystals as the template for Au NPs. The C1s spectrum is composed of four distinct peaks at 284.6 (C-C, C-H), 286.18 (C-O), 287.62 (COO-Au), and 288.7 eV (COO⁻), respectively. The peak at 288.7 eV is assigned to carboxyl functionalization during the TEMPO-oxidation. The peak at 287.62 eV strongly supported the fact that the Au NPs are connected to carboxyl groups of TCNC since these two peak positions are attributed to free carboxyl moieties and coordinated carboxylates, respectively.³⁹ The core-level spectrum of O1s also be deconvoluted to two peaks with binding energies, 531.4 (O=C) and 532.4 eV (O-C).⁴⁰ The nature of binding of Au NPs and TCNC is further analyzed by comparing the deconvoluted spectra of Au4f of nanocellulose capped Au NPs (seed) and TSC capped Au NPs (synthesized in absence of TCNC). **Figure 4.9a** shows two distinct peaks of Au(0) 4f_{7/2} and Au(0) 4f_{5/2} assigned to 83.55 and 87.15 eV for TCNC-Au NPs; and 83.3 and 86.9 eV for TSC-Au NPs, respectively. This slight shift in the binding energies of the spin-orbit components of the TCNC capped Au NPs compared to that of the TSC capped Au NPs towards higher binding energies supports the effectual wrapping of Au NPs by TCNC and only possess lower electron density than TSC-Au NPs.³² These XPS results further confirmed the applicability of the carboxyl functional groups as nucleation sites for Au ions, and thereby generation of immobilized Au NPs embedded in the TCNC intercalated network resulted in unprecedented colloidal stability.

Figure 4.9b shows the FTIR spectra of TCNC and TCNC-Au@Pd NFs represent the qualitative analysis of interactions between TCNC and Au@Pd NFs formed on the TCNC templates. First, the FTIR spectrum of TCNC shows peaks at 3446 cm⁻¹ (broad; -OH stretching), 2908 cm⁻¹ (C-H stretching), 1612 cm⁻¹ (C=O stretching of COO⁻ group), 1414 cm⁻¹ (C-O stretching of COO⁻ group), and 1056 cm⁻¹ (C-O-C stretching).⁴¹ After *in-situ* synthesis of Au@Pd NFs over TCNC, the FTIR spectrum of TCNC-Au@Pd NFs also includes the above characteristic vibrational peaks of cellulose indicates the minor change in the chemical structure of cellulose by incorporating nanoparticles to TCNC template. In closer observation, the intensities of all characteristic IR absorption peaks, especially

cellulose, were diminished in TCNC-Au@Pd NFs, which indicates the adhesion of Au@Pd NFs on the hydroxyl groups of the nanocellulose crystals.⁴¹ A significant reduction in the intensity and shift in the –OH stretching vibration from 3446 to 3434 cm^{-1} was also observed which can be resulted from the interaction between Au@Pd NFs and –OH groups of TCNC.⁴²

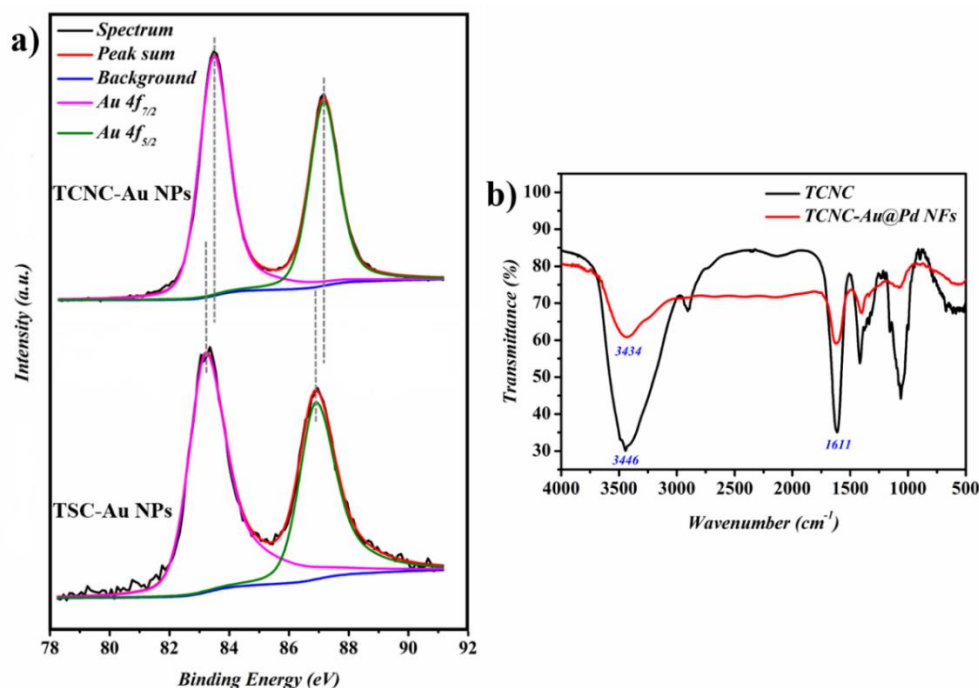


Figure 4.9. (a) Deconvoluted XPS spectra of Au(0) 4f of TCNC-Au NPs and TSC-Au NPs, and (b) FTIR spectra of TCNC and TCNC-Au@Pd NFs.

4.3.2. Role of TCNC in Morphology Evolution of TCNC-Au@Pd Nanoflowers

We investigated the basis of the structure-directing capabilities of TCNC for the shape selective colloidal synthesis of distinct flower-like Au@Pd NPs. To investigate this hypothesis, the synthesis of Au@Pd NPs was carried in the absence of TCNC, keeping all other parameters constant. A comparison between the TEM micrographs of Au@Pd synthesized with and without TEMPO-oxidized cellulose nanocrystals shine light on the shape-directing capability of TCNC. **Figures 4.10a** and **4.10b** show the TEM images of TCNC-Au@Pd NFs whereas **Figures 4.10c** and **4.10d** present the bare Au@Pd NPs in the absence of TCNC. Initially, the carboxyl functional groups in TCNC could tightly bound

the Au NPs followed by the capping of Au NPs. Subsequently, the electron-rich hydroxyl groups present in nanocellulose will function as the nucleation or anchoring sites for Pd clusters in the solution by ascorbic acid (AA) reduction during the shell coating. The Pd cluster-like small NPs (3-5 nm) formed by the AA reduction in the solution can be quantitatively deposited at the surface hydroxyl groups of TCNC that collectively capped the Au NPs, then comprehensively ad-layers on Au core.⁴³ A successful formation of cluster-like small Pd NPs in solution before the aggregation over the Au NPs seed was observed from some of the TEM images captured during the Pd shell coating process by seed-mediated synthesis route (**Figure 4.10b**). A more or less similar cluster mediated growth mechanism was reported by Xu *et al.* and Lim *et al.*, respectively for the growth of Au@Pd NFs and Pt dendrites capped Pd core by utilizing high molecular weight PVP.^{14, 44} In our study, the epitaxial growth of Pd shell, about 7-8 nm over citrate capped Au seed was observable without any formation of anisotropic morphologies by Pd coating (**Figure 4.10c** and **4.10d**). Based on the above observations, a possible morphology evolution mechanism and shape-directing capability of TCNC is proposed (**Figure 4.1**).

The shape-directing ability of TCNC for nanoengineered core-shell Au@Pd NFs arises from the fact that the inherent –OH groups that electrostatically bound to Pd clusters could enable the merging of Pd clusters, thereby inhibiting the growth of perfect epitaxial Pd shell over Au seed. Nucleation and subsequent growth process of a bound Pd or any metal clusters would progress slowly followed by release and migration towards Au seed or any metal core, leading to the generation of anisotropic morphology.⁴⁵ The constrained capture of Pd clusters by the electrostatic interaction of oxygen atoms of polar –OH groups of TCNC resulted in a gradual reduction in the overall crystallinity of TCNC after the Pd shell coating^{15, 17c}, which was evident from the XRD analysis. Concisely, numerous hydroxyl functional groups present in the TCNC hinder the direct epitaxial deposition of Pd shell over Au core, directing to the creation of small clusters like Pd NPs of 3-5 nm size, which will further be aggregated as petals around Au NPs. Whereas in the absence of TCNC, free Pd clusters were formed in the solution, preferably deposit in the (111) plane of Au core and grow quickly into a uniform shell. Even though the shape regulating ability of TEMPO-oxidized nanocellulose fibers was first mentioned by Jiang *et al.* to form Ag

nanoprisms using H_2O_2 as an etching agent.⁴⁵ Our study is the initial step for presenting TCNC as a potential and bio-sourced shape-directing and capping agent for the preparation of bimetallic core-shell NPs, especially Au@Pd NFs, without the presence of any etching or co-capping agents.

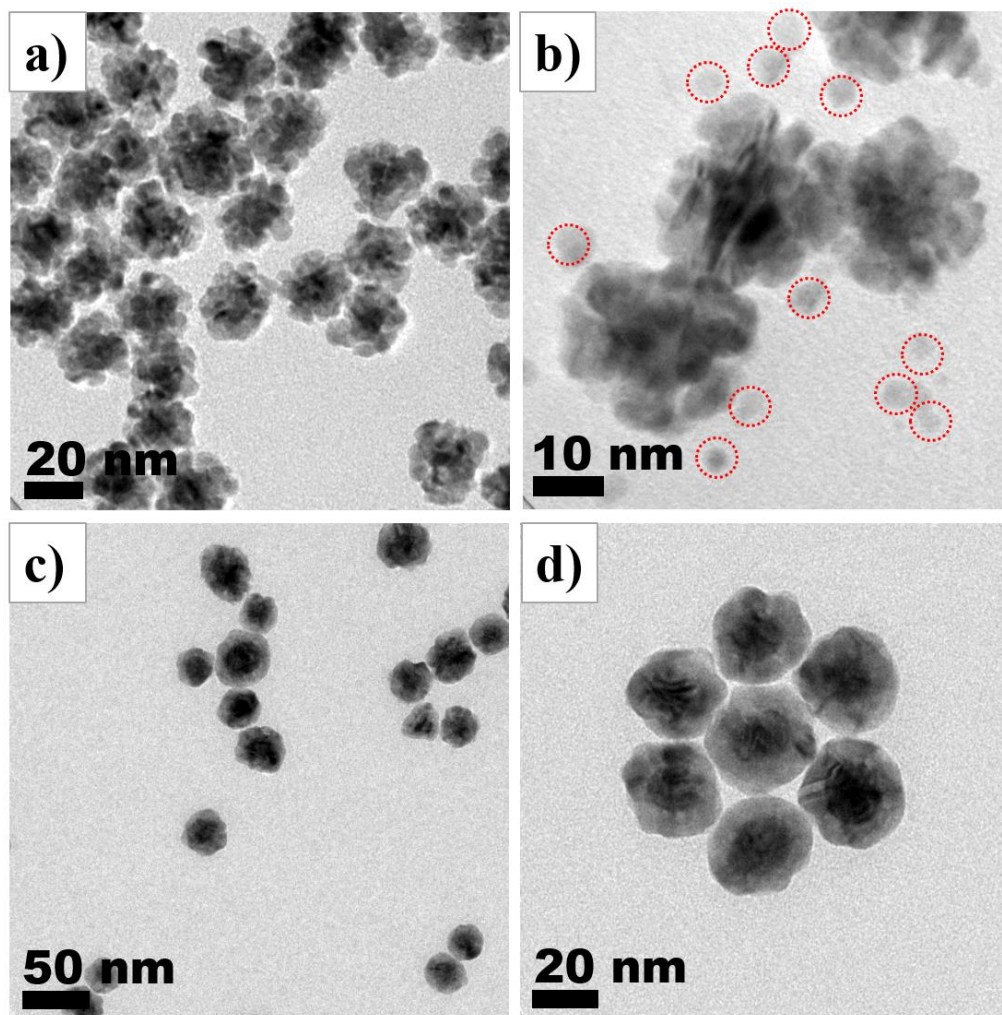


Figure 4.10. TEM images of (a) TCNC-Au@Pd NFs (Pd-200); (b) cluster-like small Pd NPs (3-5 nm) captured during Pd shell coating over Au NPs seed solution and (c-d) citrate capped Au@Pd NPs (Pd-200).

4.3.3. Catalytic Performance of TCNC-Au@Pd NFs

A reduction in the size of Pd-based metal catalysts is extremely desirable since shorter dimensions may provide more number of catalytically active sites by unit mass.

TCNC-Au@Pd Nanoflowers

The TCNC-Au@Pd NFs system nanoengineered in our study may catalytically be more active because it is enriched with a large count of small petal-like Pd NPs around the TCNC bounded core. Since the hydrophilic nature of the catalyst may hinder its catalytic activity and recyclability, we amalgamated amine functionalized reduced graphene oxide (NH₂-RGO) as an acceptable support for the system. Therefore, the TCNC-Au@Pd NFs were decorated over NH₂-RGO nanosheets by the electrostatic interaction without losing any structural change and stability. Thus the heterogeneous TCNC-Au@Pd NFs/NH₂-RGO catalyst was fashioned by an aqueous solvent assisted mixing of TCNC-Au@Pd NFs with NH₂-RGO (obtained from RGO prepared by Hummers method followed by amino functionalization). **Figure 4.11(a-c)** shows the successful functionalization of TCNC-Au@Pd NFs over NH₂-RGO sheets uniformly without any significant change in structure and sign of aggregation.

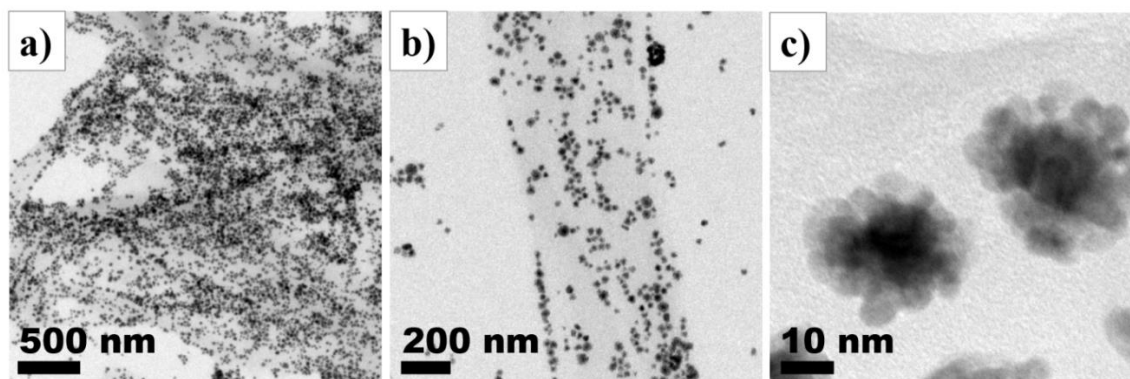


Figure 4.11. (a-c) TEM images of TCNC-Au@Pd NFs decorated NH₂-RGO nanosheets.

4.3.4. Oxygen Reduction Reaction in Alkaline Medium (ORR)

Electrocatalytic performance of our synthesized catalysts and standard was measured towards ORR by rotating disc electrode (RDE) method in 0.1 M KOH at 1600 rpm of the working electrode by saturating the solution with O₂. The ORR polarization curves (LSV curves) recorded for a series of the catalysts, including commercial 20 wt% Pd/C (control sample) profiled in **Figure 4.12**. All the potentials were reported on the RHE scale and the current densities got were normalized to the geometric area of the electrode. Both the onset potential and half-wave potential (E_{1/2}) showed a positive trend in the order

TCNC-Pd NPs/NH₂-RGO < TSC-Au@Pd NPs/NH₂-RGO < TCNC-Au@Pd NFs/NH₂-RGO \approx Pd/C (Std.). Compared to TCNC-Pd NPs/NH₂-RGO, both TSC-Au@Pd NPs/NH₂-RGO and TCNC-Au@Pd NFs/NH₂-RGO exhibited a positive shift in both onset potentials and E_{1/2}, revealing the effect of the bimetallic system (Au@Pd) towards the electrocatalytic activity. Whereas further enhancement in the TCNC-Au@Pd NFs/NH₂-RGO system compared to TSC-Au@Pd NPs/NH₂-RGO may evolve from its flower-like constructs with a high electrochemically active surface area which improves the ORR kinetics and reduces the overpotential. Additionally, decoration of Au@Pd NFs over amino functionalized graphene oxide nanosheets induced long-term stability of the catalyst without any agglomerations. The TCNC-Au@Pd NFs/NH₂-RGO system performed as a better electrocatalyst towards ORR compared to its counterpart systems with an onset potential of about 0.94 V, which is almost close to that of the standard Pd/C. This enhancement may have resulted from the consecutive effects of strain (lattice mismatch), ligand effect, and electronic modifications.⁴⁶ The diffusion limiting current density (mA/cm²) obtained for TCNC-Au@Pd NFs/ NH₂-RGO of about -4.4 mA/cm² at 1600 rpm stands out as another important performance indicator, implying the promising activity of the system. Also, this limiting current density is slightly higher compared to that of the standard Pd/C (-3.5 mA/cm²), and that obtained for homogeneous TCNC-Au@Pd NFs colloids during our primary ORR studies signified the importance of further modifications in the system by optimizing graphene content. It has been reported that, higher graphene content will reduce the limiting current density.⁴⁷ In this report, however, more detailed investigations in the TCNC-Au@Pd NFs/NH₂-RGO catalyst toward ORR performance were not included since our primary aim was to highlight on the evolution of shape-directing capability of nanocellulose, as a bio-sourced alternative to the conventional capping agents.

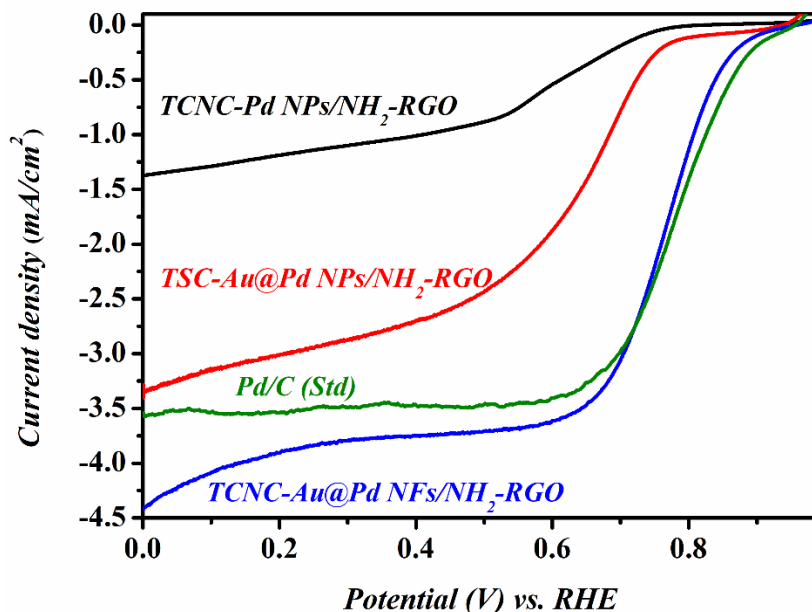


Figure 4.12. The ORR polarization curves of commercial Pd/C (20 wt%), TCNC-Au@Pd NFs/NH₂-RGO, TSC-Au@Pd NPs/ NH₂-RGO, and TCNC-Pd NPs/ NH₂-RGO catalysts in 0.1 M KOH solution recorded at a scan rate of 10 mV/s and an electrode rotation speed of 1600 rpm.

4.3.5. Catalytic 4-Nitrophenol (4-NP) Reduction

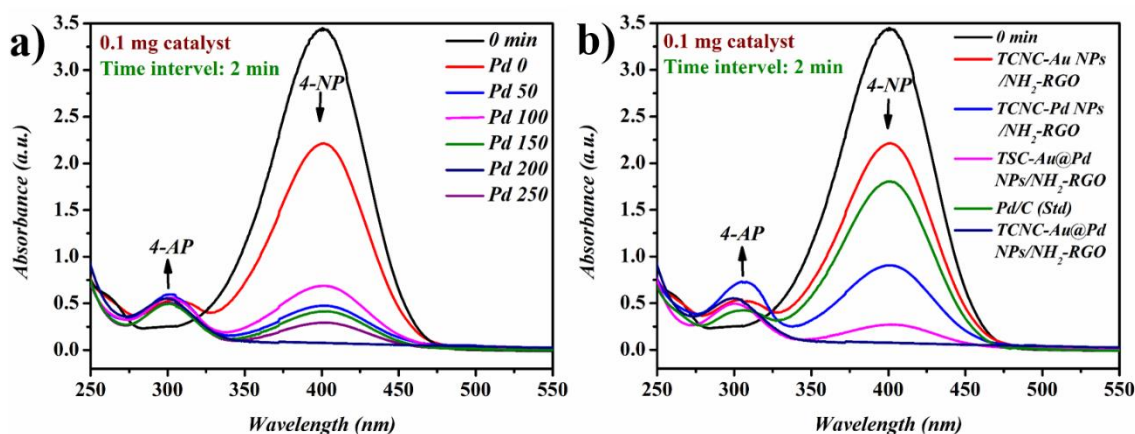


Figure 4.13. UV–Vis absorption spectra of 4-NP reduction catalyzed with (a) varying shell thickness of TCNC-Au@Pd NFs/NH₂-RGO, (b) comparison with different control and standard catalysts in same amount and at same time interval.

4-Nitrophenol to 4-Aminophenol (4-AP) reduction is a conventional catalytic reduction reaction and still outweighed as the benchmark to demonstrate the efficacies of newly proposed catalysts. Since both 4-NP (4-Nitrophenolate ions) and 4-AP exhibit evident absorption in the UV-Visible region, monitoring of the reduction process is studied using UV-Visible absorption spectroscopy. 4-NP showed an absorption band at 400 nm in the presence of NaBH₄ as a reducing agent, and the newborn 4-AP could show an absorption maximum at 300 nm. Au, Pd, especially Au-Pd metal NPs are the best candidates to catalyze the 4-NP reduction.²³ However, template-supported metal NPs will improve the catalytic properties and relieve the soaring price of catalysts by recycling them as heterogeneous catalysts.

The ultimate selection of most active Pd shell thickness over TCNC-Au core in TCNC-Au@Pd NFs/NH₂-RGO catalyst for the 4-NP reduction was done by the spectral monitoring of 4-NP reduction by using constant quantity of catalysts (0.1 mg) and at exact time interval, 2 min (**Figure 4.13a**). As indicated by the highest zeta potential value, excellent stable geometry with high surface area and adequate Au:Pd composition ratio suitable for catalysis; TCNC-Au@Pd NFs/NH₂-RGO with Pd-200 shell thickness came to first place with best catalytic activity. 4-NP reduction was also monitored with a series of catalysts used earlier in the ORR section and it also profiled the superior catalytic activity of our TCNC-Au@Pd NFs/NH₂-RGO. The order of the catalytic activity from the lowest to the highest is, TCNC-Au NPs/NH₂-RGO < Pd/C (Std.) < TCNC-Pd NPs/NH₂-RGO < TSC-Au@Pd NPs/NH₂-RGO < TCNC-Au@Pd NFs/NH₂-RGO (**Figure 4.13b**). The superior catalytic activity of TCNC-Au@Pd NFs/NH₂-RGO might have rightfully come from the synergic influence of the size, shape, stability, composition of nanoparticles as well as the presence of specific templates or supports which supplemented the detrimental effect of some conventional capping agents.⁴⁸

Figure 4.14(a-b) depicts the successful demonstration of TCNC-Au@Pd NFs/NH₂-RGO as an efficient catalyst towards 4-NP reduction. The reduction reaction was completed within 3 min even in the presence of a minute quantity of catalyst (0.05 mg) and showed significant enhancement upon increasing the amount to 0.1 mg. Reaction proceedings could be monitored by a gradual drop in the absorption maxima of 4-NP and

concomitant appearance of absorption of 4-AP and by the bleaching of the yellow color of 4-NP.

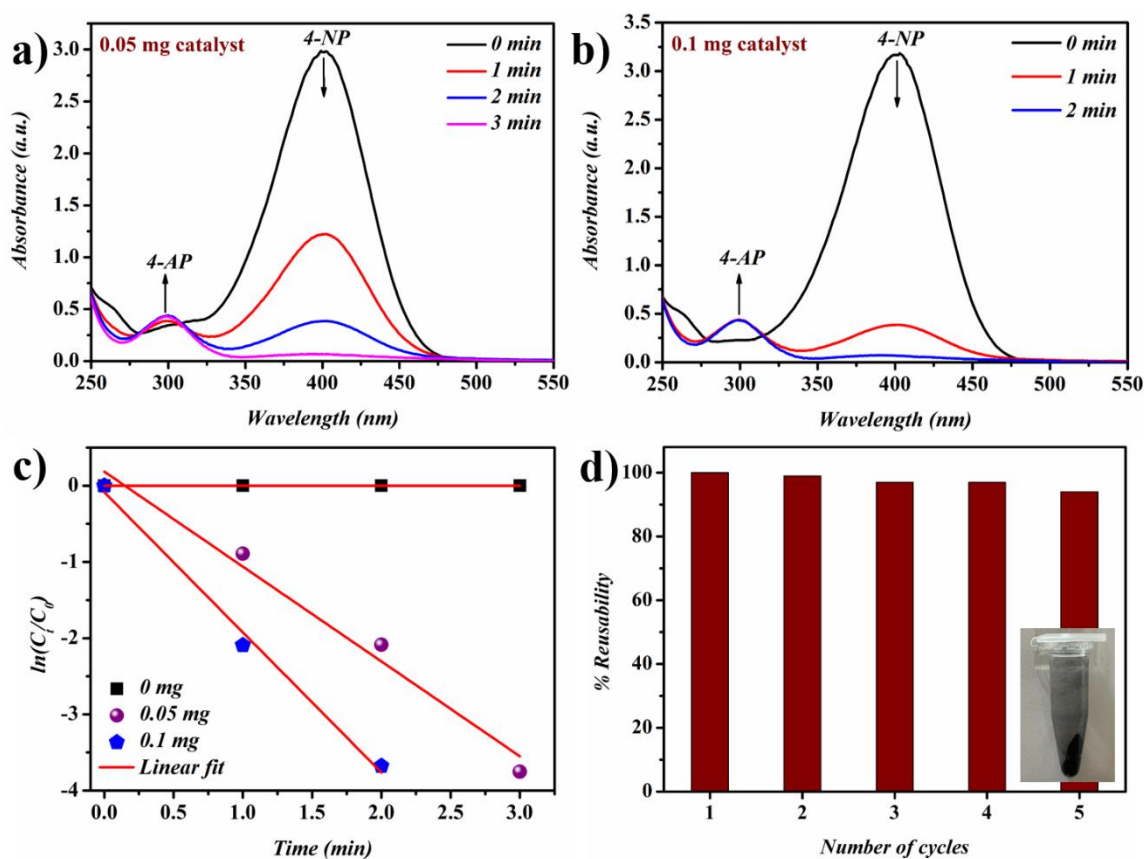


Figure 4.14. Real-time spectroscopic monitoring of 4-NP catalyzed by (a) 0.05 mg, (b) 0.1 mg of TCNC-Au@Pd NFs/NH₂-RGO, (c) corresponding reaction kinetic plots, and (d) recyclability of TCNC-Au@Pd NFs/NH₂-RGO for 4-NP reduction (inset shows the photograph of catalyst recovered by centrifugation after the completion of the 5th cycle).

Figure 4.14c shows the linear correlation of $\ln(C_t/C_0)$ versus reaction completion time (minute) since reaction rate independent of the concentration of reducing agent, and linear fitting was successful with correlation coefficients 0.9714 (0.05mg) and 0.9874 (0.1 mg) consistent with the fact that catalytic 4-NP reduction followed pseudo-first-order kinetics.²⁹ The rate constant of the reduction, estimated from the slope of the plot $\ln(C_t/C_0)$ versus time, was $30.63 \times 10^{-3} \text{ s}^{-1}$ for 0.1 mg of TCNC-Au@Pd NFs/NH₂-RGO catalyst. **Table 4.2** compares the efficiency of our catalyst with the results reported by other researchers, especially with nanocellulose supported catalysts. It is remarkable that the

excellent catalytic activity of TCNC-Au@Pd NFs/NH₂-RGO in 4-NP reduction; therefore, it is a burgeoning environmental benign candidate in the realm of catalysis. Electron transfer between electron-rich Au to Pd, relatively high surface area, backbone made by electron-rich amino-functionalized reduced graphene oxide, and prevention of self-aggregating during synthesis and storage are the answers to why this catalyst shows superior catalytic activity. TCNC-Au@Pd NFs/NH₂-RGO can be effortlessly recovered by centrifugation after completion of the reaction and can be reused at least five times without any remarkable reduction in the catalytic efficiency (**Figure 4.14d**).

Catalyst systems	Catalyst loading	Rate constant k_{app} (s⁻¹) x 10⁻³	Reaction time	Reference
CNF/Pd	5 mg	8.8	5 min	49
CNF/Ag	1 mg	4.6	8 min	50
CNC/Au	1 mL, (total Au content: 0.2 μmol)	2.06	14 min	51
CNC/PDDA/Au	4.1 x 10 ⁻² μmol (1mg/mL)	5.1	10 min	52
CNC/Au	50 mg	4	15 min	42
CNC/Ag@Au	1.5 g	22.83	3 min	53
Au@Ag/GO	100 μl	142.6	30 sec	54
Pd-Ni/rGO	0.2 mg	2.66	8 min	55
Au@Pd/PNIPAM	11 mg/L	16	4.2 min	56
Au@Pd/ PEO-b-P4VP-b-PNIPAM	0.24 mg/L	0.531	33.3 min	57
TCNC-Au@Pd NFs /NH₂-RGO	0.1 mg	30.63	2 min	Present work

Table 4.2. An overview of different catalysts for 4-NP reduction with rate constants.

4.4. CONCLUSIONS

In summary, we demonstrated a biomass-derived TEMPO-oxidized cellulose nanocrystal as a structure directing agent to synthesize intricate Pd-based bimetallic nanostructures which exhibited competent electrocatalytic activity. Firstly, the spherical Au NPs of diameter, 15 ± 2 nm were formed on the TCNC which served as seed for the subsequent petal-like epitaxial growth of Pd resulted in the formation of flower-shaped Au@Pd nanostructures of size, 32 ± 2 nm. Our results revealed that the presence of -OH rich TCNC pursued a key role in the systematic evolution of nanoparticle morphology. The -OH groups in the TCNC that are not bound to the Au seed surface further serve as the binding sites for Pd nanoclusters (NCs). Consequently, the TCNC promoted the coalescence of cluster-like Pd NPs to a certain size and stabilized them against further agglomeration. Furthermore, a heterogeneous catalyst was designed by adorning TCNC-Au@Pd on NH₂-RGO nanosheets and successfully demonstrated in ORR and 4-NP reduction reactions. Comparison of the electrocatalytic activity with citrate capped Au@Pd nanostructures revealed that TCNC-Au@Pd/NH₂-RGO system exhibited enhanced ORR catalytic behavior. Our study could pave way for further research on the potential use of green sustainable nanocellulose as a benign, shape-regulating agent in the realm of nanochemistry for the development of bio-sourced fuel cell components, however, more research is underway.

4.5. REFERENCES

1. Aslam, U.; Chavez, S.; Linic, S., Controlling energy flow in multimetallic nanostructures for plasmonic catalysis. *Nature nanotechnology* **2017**, *12* (10), 1000.
2. Rodríguez-Lorenzo, L.; de La Rica, R.; Álvarez-Puebla, R. A.; Liz-Marzán, L. M.; Stevens, M. M., Plasmonic nanosensors with inverse sensitivity by means of enzyme-guided crystal growth. *Nature materials* **2012**, *11* (7), 604-607.
3. Kauranen, M.; Zayats, A. V., Nonlinear plasmonics. *Nature photonics* **2012**, *6* (11), 737-748.
4. Howes, P. D.; Rana, S.; Stevens, M. M., Plasmonic nanomaterials for biodiagnostics. *Chemical Society Reviews* **2014**, *43* (11), 3835-3853.
5. Ferrando, R.; Jellinek, J.; Johnston, R. L., Nanoalloys: from theory to applications of alloy clusters and nanoparticles. *Chemical reviews* **2008**, *108* (3), 845-910.

6. Burda, C.; Chen, X.; Narayanan, R.; El-Sayed, M. A., Chemistry and properties of nanocrystals of different shapes. *Chemical reviews* **2005**, *105* (4), 1025-1102.
7. Fan, F.-R.; Liu, D.-Y.; Wu, Y.-F.; Duan, S.; Xie, Z.-X.; Jiang, Z.-Y.; Tian, Z.-Q., Epitaxial growth of heterogeneous metal nanocrystals: from gold nano-octahedra to palladium and silver nanocubes. *Journal of the American Chemical Society* **2008**, *130* (22), 6949-6951.
8. Yang, C.-W.; Chanda, K.; Lin, P.-H.; Wang, Y.-N.; Liao, C.-W.; Huang, M. H., Fabrication of Au–Pd core–shell heterostructures with systematic shape evolution using octahedral nanocrystal cores and their catalytic activity. *Journal of the American Chemical Society* **2011**, *133* (49), 19993-20000.
9. Lee, Y. W.; Kim, N. H.; Lee, K. Y.; Kwon, K.; Kim, M.; Han, S. W., Synthesis and characterization of flower-shaped porous Au–Pd alloy nanoparticles. *The Journal of Physical Chemistry C* **2008**, *112* (17), 6717-6722.
10. Thomas, B.; Raj, M. C.; Joy, J.; Moores, A.; Drisko, G. L.; Sanchez, C. m., Nanocellulose, a versatile green platform: from biosources to materials and their applications. *Chemical reviews* **2018**, *118* (24), 11575-11625.
11. Yuan, T.; Zeng, J.; Wang, B.; Cheng, Z.; Gao, W.; Xu, J.; Chen, K., Silver nanoparticles immobilized on cellulose nanofibrils for starch-based nanocomposites with high antibacterial, biocompatible, and mechanical properties. *Cellulose* **2021**, *28* (2), 855-869.
12. Abdelgawad, A. M.; El-Naggar, M. E.; Elsherbiny, D. A.; Ali, S.; Abdel-Aziz, M. S.; Abdel-Monem, Y. K., Antibacterial carrageenan/cellulose nanocrystal system loaded with silver nanoparticles, prepared via solid-state technique. *Journal of Environmental Chemical Engineering* **2020**, *8* (5), 104276.
13. Zhou, Y.; Saito, T.; Bergström, L.; Isogai, A., Acid-free preparation of cellulose nanocrystals by TEMPO oxidation and subsequent cavitation. *Biomacromolecules* **2018**, *19* (2), 633-639.
14. Xu, J.; Wilson, A. R.; Rathmell, A. R.; Howe, J.; Chi, M.; Wiley, B. J., Synthesis and catalytic properties of Au–Pd nanoflowers. *ACS nano* **2011**, *5* (8), 6119-6127.
15. Azizi, S.; Ahmad, M. B. H.; Hussein, M. Z.; Ibrahim, N. A., Synthesis, antibacterial and thermal studies of cellulose nanocrystal stabilized ZnO-Ag heterostructure nanoparticles. *Molecules* **2013**, *18* (6), 6269-6280.
16. Xu, C.; Chen, W.; Gao, H.; Xie, X.; Chen, Y., Cellulose nanocrystal/silver (CNC/Ag) thin-film nanocomposite nanofiltration membranes with multifunctional properties. *Environmental Science: Nano* **2020**, *7* (3), 803-816.
17. (a) Cirtiu, C. M.; Dunlop-Briere, A. F.; Moores, A., Cellulose nanocrystallites as an efficient support for nanoparticles of palladium: application for catalytic hydrogenation and Heck coupling under mild conditions. *Green Chemistry* **2011**, *13* (2), 288-291; (b) Kaushik, M.; Basu, K.; Benoit, C.; Cirtiu, C. M.; Vali, H.; Moores, A., Cellulose nanocrystals as chiral inducers: enantioselective catalysis and transmission electron microscopy 3D characterization. *Journal of the American Chemical Society* **2015**, *137* (19), 6124-6127; (c) Wu, X.; Lu, C.; Zhang, W.; Yuan, G.; Xiong, R.; Zhang, X., A novel reagentless approach for synthesizing cellulose nanocrystal-supported palladium nanoparticles with enhanced catalytic performance. *Journal of Materials Chemistry A* **2013**, *1* (30), 8645-8652; (d) Rezaayat, M.; Blundell, R. K.; Camp, J. E.; Walsh, D. A.; Thielemans, W., Green

- one-step synthesis of catalytically active palladium nanoparticles supported on cellulose nanocrystals. *ACS Sustainable Chemistry & Engineering* **2014**, 2 (5), 1241-1250; (e) Wang, B.; Ran, M.; Fang, G.; Wu, T.; Tian, Q.; Zheng, L.; Romero-Zerón, L.; Ni, Y., Palladium nano-catalyst supported on cationic nanocellulose–alginate hydrogel for effective catalytic reactions. *Cellulose* **2020**, 27, 6995-7008.
18. (a) Thompson, D. T., Catalysis by gold/platinum group metals. *Plat. Metals Rev* **2004**, 48, 169-172; (b) Marx, S.; Baiker, A., Beneficial interaction of gold and palladium in bimetallic catalysts for the selective oxidation of benzyl alcohol. *The Journal of Physical Chemistry C* **2009**, 113 (15), 6191-6201; (c) Zhang, L.; Zhang, J.; Kuang, Q.; Xie, S.; Jiang, Z.; Xie, Z.; Zheng, L., Cu²⁺-assisted synthesis of hexoctahedral Au–Pd alloy nanocrystals with high-index facets. *Journal of the American Chemical Society* **2011**, 133 (43), 17114-17117.
 19. Cortie, M. B.; McDonagh, A. M., Synthesis and optical properties of hybrid and alloy plasmonic nanoparticles. *Chemical reviews* **2011**, 111 (6), 3713-3735.
 20. Pan, W.; Zhang, X.; Ma, H.; Zhang, J., Electrochemical synthesis, voltammetric behavior, and electrocatalytic activity of Pd nanoparticles. *The Journal of Physical Chemistry C* **2008**, 112 (7), 2456-2461.
 21. Lin, X.-X.; Zhang, X.-F.; Wang, A.-J.; Fang, K.-M.; Yuan, J.; Feng, J.-J., Simple one-pot aqueous synthesis of AuPd alloy nanocrystals/reduced graphene oxide as highly efficient and stable electrocatalyst for oxygen reduction and hydrogen evolution reactions. *Journal of colloid and interface science* **2017**, 499, 128-137.
 22. Han, J.; Zhou, Z.; Yin, Y.; Luo, X.; Li, J.; Zhang, H.; Yang, B., One-pot, seedless synthesis of flowerlike Au–Pd bimetallic nanoparticles with core-shell-like structure via sodium citrate coreduction of metal ions. *CrystEngComm* **2012**, 14 (20), 7036-7042.
 23. Chen, X.; Cai, Z.; Chen, X.; Oyama, M., AuPd bimetallic nanoparticles decorated on graphene nanosheets: their green synthesis, growth mechanism and high catalytic ability in 4-nitrophenol reduction. *Journal of Materials Chemistry A* **2014**, 2 (16), 5668-5674.
 24. (a) Xiong, Y.; Yang, Y.; DiSalvo, F. J.; Abruña, H. c. D., Pt-decorated composition-tunable Pd–Fe@ Pd/C core–shell nanoparticles with enhanced electrocatalytic activity toward the oxygen reduction reaction. *Journal of the American Chemical Society* **2018**, 140 (23), 7248-7255; (b) Wang, D.; Xin, H. L.; Yu, Y.; Wang, H.; Rus, E.; Muller, D. A.; Abruña, H. D., Pt-decorated PdCo@ Pd/C core–shell nanoparticles with enhanced stability and electrocatalytic activity for the oxygen reduction reaction. *Journal of the American Chemical Society* **2010**, 132 (50), 17664-17666.
 25. Darabdhara, G.; Amin, M. A.; Mersal, G. A.; Ahmed, E. M.; Das, M. R.; Zakaria, M. B.; Malgras, V.; Alshehri, S. M.; Yamauchi, Y.; Szunerits, S., Reduced graphene oxide nanosheets decorated with Au, Pd and Au–Pd bimetallic nanoparticles as highly efficient catalysts for electrochemical hydrogen generation. *Journal of Materials Chemistry A* **2015**, 3 (40), 20254-20266.
 26. Wang, M.; Ma, Z.; Li, R.; Tang, B.; Bao, X.-Q.; Zhang, Z.; Wang, X., Novel flower-like PdAu (Cu) anchoring on a 3D rGO-CNT sandwich-stacked framework for highly efficient methanol and ethanol electro-oxidation. *Electrochimica Acta* **2017**, 227, 330-344.

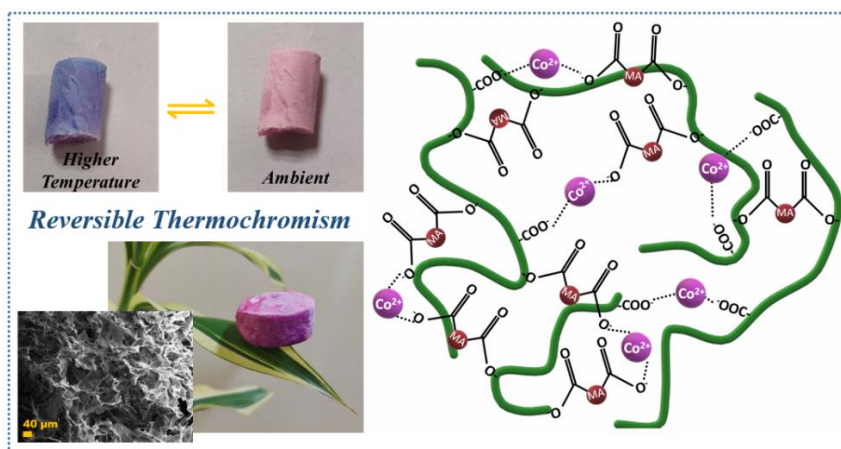
27. Sun, Y.; Wu, Q.; Shi, G., Graphene based new energy materials. *Energy & Environmental Science* **2011**, *4* (4), 1113-1132.
28. Ren, L.; Yang, L.; Yu, P.; Wang, Y.; Mao, L., Electrochemical post-treatment of infinite coordination polymers: An effective route to preparation of Pd nanoparticles supported onto carbon nanotubes with enhanced electrocatalytic activity toward ethanol oxidation. *ACS applied materials & interfaces* **2013**, *5* (21), 11471-11478.
29. Hakkeem, H. M. A.; Babu, A.; Pal, S. K.; Mohamed, A. P.; Ghosh, S. K.; Pillai, S., Cellulose nanocrystals directed in-situ assembly of Au@ Ag nanostructures with multifunctional activities. *Microchemical Journal* **2021**, *168*, 106393.
30. Navaee, A.; Salimi, A., Efficient amine functionalization of graphene oxide through the Bucherer reaction: an extraordinary metal-free electrocatalyst for the oxygen reduction reaction. *Rsc Advances* **2015**, *5* (74), 59874-59880.
31. Lai, L.; Chen, L.; Zhan, D.; Sun, L.; Liu, J.; Lim, S. H.; Poh, C. K.; Shen, Z.; Lin, J., One-step synthesis of NH₂-graphene from in situ graphene-oxide reduction and its improved electrochemical properties. *Carbon* **2011**, *49* (10), 3250-3257.
32. Zhang, L.; Lu, H.; Chu, J.; Ma, J.; Fan, Y.; Wang, Z.; Ni, Y., Lignin-Directed Control of Silver Nanoparticles with Tunable Size in Porous Lignocellulose Hydrogels and Their Application in Catalytic Reduction. *ACS Sustainable Chemistry & Engineering* **2020**, *8* (33), 12655-12663.
33. (a) Lu, C.-L.; Prasad, K. S.; Wu, H.-L.; Ho, J.-a. A.; Huang, M. H., Au nanocube-directed fabrication of Au– Pd core– shell nanocrystals with tetrahedral, concave octahedral, and octahedral structures and their electrocatalytic activity. *Journal of the American Chemical Society* **2010**, *132* (41), 14546-14553; (b) Chen, H.; Li, Y.; Zhang, F.; Zhang, G.; Fan, X., Graphene supported Au-Pd bimetallic nanoparticles with core-shell structures and superior peroxidase-like activities. *Journal of Materials Chemistry* **2011**, *21* (44), 17658-17661.
34. Fang, P.-P.; Duan, S.; Lin, X.-D.; Anema, J. R.; Li, J.-F.; Buriez, O.; Ding, Y.; Fan, F.-R.; Wu, D.-Y.; Ren, B., Tailoring Au-core Pd-shell Pt-cluster nanoparticles for enhanced electrocatalytic activity. *Chemical Science* **2011**, *2* (3), 531-539.
35. Scott, R. W.; Wilson, O. M.; Oh, S.-K.; Kenik, E. A.; Crooks, R. M., Bimetallic palladium– gold dendrimer-encapsulated catalysts. *Journal of the American Chemical Society* **2004**, *126* (47), 15583-15591.
36. Kelly, C. H.; Benedetti, T. M.; Alinezhad, A.; Schuhmann, W.; Gooding, J. J.; Tilley, R. D., Understanding the effect of Au in Au–Pd bimetallic nanocrystals on the electrocatalysis of the methanol oxidation reaction. *The Journal of Physical Chemistry C* **2018**, *122* (38), 21718-21723.
37. (a) Farea, M.; Abdelghany, A.; Oraby, A., Optical and dielectric characteristics of polyethylene oxide/sodium alginate-modified gold nanocomposites. *RSC Advances* **2020**, *10* (62), 37621-37630; (b) Ragab, H.; Rajeh, A., Structural, thermal, optical and conductive properties of PAM/PVA polymer composite doped with Ag nanoparticles for electrochemical application. *Journal of Materials Science: Materials in Electronics* **2020**, *31* (19), 16780-16792.
38. Yang, C.; Qing, C.; Wang, Q.; Zhang, X.; Lou, J.; Liu, Y., Synthesis of the hybrid CdS/Au flower-like nanomaterials and their SERS application. *Sensors and Actuators B: Chemical* **2020**, *304*, 127218.

39. (a) Park, J.-W.; Shumaker-Parry, J. S., Structural study of citrate layers on gold nanoparticles: role of intermolecular interactions in stabilizing nanoparticles. *Journal of the American Chemical Society* **2014**, *136* (5), 1907-1921; (b) Caporali, S.; Muniz-Miranda, F.; Pedone, A.; Muniz-Miranda, M., SERS, XPS and DFT study of xanthine adsorbed on citrate-stabilized gold nanoparticles. *Sensors* **2019**, *19* (12), 2700.
40. Sadri, R.; Hosseini, M.; Kazi, S.; Bagheri, S.; Zubir, N.; Solangi, K.; Zaharinie, T.; Badarudin, A., A bio-based, facile approach for the preparation of covalently functionalized carbon nanotubes aqueous suspensions and their potential as heat transfer fluids. *Journal of colloid and interface science* **2017**, *504*, 115-123.
41. Purwidyantri, A.; Karina, M.; Hsu, C.-H.; Srikandace, Y.; Prabowo, B. A.; Lai, C.-S., Facile Bacterial Cellulose Nanofibrillation for the Development of a Plasmonic Paper Sensor. *ACS Biomaterials Science & Engineering* **2020**, *6* (5), 3122-3131.
42. Eisa, W. H.; Abdelgawad, A. M.; Rojas, O. J., Solid-state synthesis of metal nanoparticles supported on cellulose nanocrystals and their catalytic activity. *ACS Sustainable Chemistry & Engineering* **2018**, *6* (3), 3974-3983.
43. Shin, Y.; Bae, I.-T.; Arey, B. W.; Exarhos, G. J., Facile stabilization of gold-silver alloy nanoparticles on cellulose nanocrystal. *The Journal of Physical Chemistry C* **2008**, *112* (13), 4844-4848.
44. Lim, B.; Jiang, M.; Yu, T.; Camargo, P. H.; Xia, Y., Nucleation and growth mechanisms for Pd-Pt bimetallic nanodendrites and their electrocatalytic properties. *Nano Research* **2010**, *3* (2), 69-80.
45. Jiang, F.; Hsieh, Y.-L., Synthesis of cellulose nanofibril bound silver nanoprism for surface enhanced Raman scattering. *Biomacromolecules* **2014**, *15* (10), 3608-3616.
46. Xue, Q.; Bai, J.; Han, C.; Chen, P.; Jiang, J.-X.; Chen, Y., Au nanowires@ Pd-polyethylenimine nanohybrids as highly active and methanol-tolerant electrocatalysts toward oxygen reduction reaction in alkaline media. *ACS Catalysis* **2018**, *8* (12), 11287-11295.
47. Das, S. K.; Mohanty, B.; Sahu, S. C.; Chakraborty, B.; Basu, S.; Jena, B. K., The experimental and theoretical insights on the interaction of AuPd bimetallic nanoentities on graphene: A study on electrocatalytic activity towards oxygen reduction reaction. *Electrochimica Acta* **2020**, *356*, 136820.
48. Menumerov, E.; Hughes, R. A.; Neretina, S., Catalytic reduction of 4-nitrophenol: a quantitative assessment of the role of dissolved oxygen in determining the induction time. *Nano letters* **2016**, *16* (12), 7791-7797.
49. Meng, J.; Liu, Y.; Shi, X.; Chen, W.; Zhang, X.; Yu, H., Recyclable nanocellulose-confined palladium nanoparticles with enhanced room-temperature catalytic activity and chemoselectivity. *Science China Materials* **2021**, *64* (3), 621-630.
50. Zhang, P.; Shao, C.; Zhang, Z.; Zhang, M.; Mu, J.; Guo, Z.; Liu, Y., In situ assembly of well-dispersed Ag nanoparticles (AgNPs) on electrospun carbon nanofibers (CNFs) for catalytic reduction of 4-nitrophenol. *Nanoscale* **2011**, *3* (8), 3357-3363.
51. Wu, X.; Lu, C.; Zhou, Z.; Yuan, G.; Xiong, R.; Zhang, X., Green synthesis and formation mechanism of cellulose nanocrystal-supported gold nanoparticles with enhanced catalytic performance. *Environmental Science: Nano* **2014**, *1* (1), 71-79.

52. Lam, E.; Hrapovic, S.; Majid, E.; Chong, J. H.; Luong, J. H., Catalysis using gold nanoparticles decorated on nanocrystalline cellulose. *Nanoscale* **2012**, *4* (3), 997-1002.
53. Gopiraman, M.; Saravanamoorthy, S.; Baskar, R.; Ilangovan, A.; Ill-Min, C., Green synthesis of Ag@ Au bimetallic regenerated cellulose nanofibers for catalytic applications. *New Journal of Chemistry* **2019**, *43* (43), 17090-17103.
54. Wu, T.; Zhang, L.; Gao, J.; Liu, Y.; Gao, C.; Yan, J., Fabrication of graphene oxide decorated with Au–Ag alloy nanoparticles and its superior catalytic performance for the reduction of 4-nitrophenol. *Journal of materials chemistry A* **2013**, *1* (25), 7384-7390.
55. Revathy, T.; Dhanavel, S.; Sivaranjani, T.; Narayanan, V.; Maiyalagan, T.; Stephen, A., Highly active graphene-supported palladium-nickel alloy nanoparticles for catalytic reduction of 4-nitrophenol. *Applied Surface Science* **2018**, *449*, 764-771.
56. Zhao, D.; Chen, X.; Liu, Y.; Wu, C.; Ma, R.; An, Y.; Shi, L., Thermosensitive and pH-sensitive Au–Pd bimetallic nanocomposites. *Journal of colloid and interface science* **2009**, *331* (1), 104-112.
57. Xiong, D. a.; Li, Z.; An, Y.; Ma, R.; Shi, L., Novel Au–Pd bimetallic core–shell nanocomplex and its catalytic activity modulation. *Journal of colloid and interface science* **2010**, *350* (1), 260-267.

CHAPTER 5

Reversible Thermochromic Cobalt(II) Coordinated Malonic Acid-Nanocellulose Hybrid Aerogels



ABSTRACT

Nanocellulose has long been seen as a green choice for a variety of applications due to the growing worldwide concern for sustainability. In this chapter we illustrate Co²⁺ cation induced malonic acid/nanocellulose aerogel that shows reversible thermochromism. Thermochromism is caused by the shift from tetrahedral to octahedral geometry upon contact with water molecules. This effect is accentuated by the high surface area of aerogel structures. Co(II) ions and malonic acid as components assured the coordination and cross-linking activities by through interactions with an extrinsic number of functional groups in TEMPO-oxidized cellulose nanofibers (TCNF) to construct hierarchically porous aerogel structures. Detailed characterisations of synthesised aerogels were carried out to evaluate the overall properties and performance. Reversible thermochromism performance of this hybrid aerogels were utilized for the visual sensing of humidity as demonstrated with an android mobile app interface. The nanocellulose-based green synthesis of aerogel can be adopted for other applications with diverse metal ions and additives upon requirements.

5.1. INTRODUCTION

The time to choose green and biodegradable polymer materials instead of petroleum-based polymers, which are responsible for most of the white pollution, has already passed. Cellulose is most abundant semi-crystalline natural polymer but its utility is always pressed down by its poor processibility and compactability. Arrival of the nano prototype of cellulose with variant functionalities named ‘nanocellulose’ made a huge turn to the road to the uncountable applications of this sustainable material.¹ Lot of researchers are worshipping in this area to spread this network of nanocellulose materials in mesmerizing outlooks for innovative ideas. These outlooks include photonic materials ², flexible films ³, packaging materials ⁴, hydrogels ⁵, aerogels ⁶, fibers ⁷, biomedical scaffolds ⁸, etc.

Thermochromic CoMNC aerogels

TEMPO-oxidized nanocellulose fibers, a sub-division of nanocellulose materials, are born with ultra-aqueous stability at nano-level imparted by the inter and intra-molecular hydrogen bonds, and induced carboxyl functionalization proven by a zeta potential of about -70 mV.⁹ Thixotropic behavior of nanocellulose, especially cellulose nanofibers (CNF) even in low concentrations always delivered the signal for the applicability of these sustainable materials in the realm of hydrogels and aerogels with its significant asset like entangled fibrous structure with high aspect ratio.¹⁰ This important property can be successfully tuned and transformed into a stable hydrogel by impregnating metal cations especially divalent metal cations into the nanocellulose hosting matrices.¹¹ Both induced carboxyl and inherent hydroxyl groups of nanocellulose fibers enables the distribution of the metal ions homogeneously throughout the network by coordination followed by immediate transformation into hydrogel. Metal ions coordinated nanocellulose stable hydrogels can be captured into lightweight aerogels by different cryogenic drying processes. Only a few appreciable research attempts are there to fabricate fast hydrogels of TEMPO-oxidised nanocellulose by incorporating metal ions by coordinating with carboxyl functional groups. Zander *et al.* demonstrated the fabrication of Ca^{2+} and Fe^{2+} cross-linked cellulose nanofiber hydrogels for tissue engineering applications.^{11a} Hai *et al.* reported the latent fingerprint detection and encryption using luminescent Tb^{3+} nanocellulose complex hydrogels.^{11b} Dong *et al.* also discussed Ca^{2+} , Zn^{2+} , Cu^{2+} , Al^{3+} , and Fe^{3+} intermediated hydrogelation of entangled TEMPO-oxidised cellulose nanofibers in detail.¹² The properties like homogeneity and strong binding of this nanocellulose metal ions hybrid gels can be upgraded by the addition of simple organic dicarboxylic acids like malonic acid, maleic, oxalic, succinic acid, etc. Surprisingly, these combinations that can trigger the overall properties of metal ions induced nanocellulose gels have rarely been explored in the literature.

Thermochromic materials are unique and invariant thermoresponsive materials that change its color to another and have been widely applied in areas such as temperature sensors, anti-counterfeiting, modern electronic devices, etc.¹³ If the thermochromic material is reversible, it can owe to more sackful applicability in various fields. Nanocellulose can act as a successful hosting matrix in different physical appearances,

such as films, gels, etc., to thermochromic materials towards novel applications. Recently, Jaiswal *et al.* reported creating thermoresponsive devices by incorporating black thermochromic pigment for optical modulation devices.¹⁴ Humidity sensors are important category of sensors that can make a huge impact in the agricultural, food processing, and pharmaceutical industry.¹⁵ A variety of humidity sensors are available in market, and new products are arising day by day with fascinating features and improved efficacies.¹⁶ Even though the ideal capabilities of a humidity sensor needs to be more improved in terms of its sensitivity, low response and recovery time, eco-friendliness thermal stability, etc., ceramics, organic polymers, and inorganic-polymer hybrids are the main rulers in this realm of humidity sensors.¹⁷ Cobalt based metal-organic frameworks (MOFs) are recent inmates in the humidity sensor economy by the inherent visual color based humidity sensing property of Cobalt metal.¹⁸ Colourimetric change arises through the change in coordination number of Co(II) with the H₂O in moisture as a ligand is behind this visual magic treat.¹⁷ Co(II) based MOFs can act as a vital determinant in the efficiency of humidity sensors, whereas poor processibility of MOFs always becomes hurdle for the designing and practical applicability of humidity sensor devices. Compared with the above mentioned common ceramic humidity sensors, especially porous silica based materials are well known for of their surface area, pore size, and distribution.¹⁹ Even though these pore structures are well suitable for providing more binding sites for water molecules, recovery time of ceramic based humidity sensors are too long.²⁰ Since polymer based materials are popular for lightweight and more flexible with better mechanical properties, these features can provide more merits to the polymer based humidity sensor products but suffers from slow response.¹⁷ This limitation of polymer based humidity sensors can be covered by impregnating Co(II), and the surface area and porosity of ceramic humidity sensors can be achieved by aerogel structure nanocellulose. In addition, comparing to dense solid material substrates, aerogels known by 99% air contact can show more accessibility to the water molecules to the fifth and sixth free coordination sites of Co(II) by the surface area and porosity.

Thermochromic CoMNC aerogels

In this chapter, we demonstrate a sustainable synthetic strategy for Co(II) coordinated malonic acid/nanocellulose hybrid aerogels that shows interesting property of thermochromism. Water molecules in the moisture plays a key role in this Co(II) based system and hence this property of reversible thermochromism can be tuned and utilized for humidity sensing. The novelty of this work is the unique approach that modified the comprehensive properties of Co(II) coordinated nanocellulose aerogels by incorporating a simple dicarboxylic acid, malonic acid as an additive. To the best of our knowledge, this combination of three distinct components has never before been documented in the literature for applications like humidity sensing. We also tried to demonstrate the real life applicability of this humidity sensing material by developing a specific and robust android application.

5.2. EXPERIMENTAL SECTION

5.2.1. Materials

Chemically treated (sodium hydroxide, NaOH) banana pseudo-stem fibers were used as cellulose source. Sodium chlorite (NaClO_2), 2,2,6,6-tetramethyl piperidine-1-oxyl radical (TEMPO; $\text{C}_9\text{H}_{18}\text{NO}$), sodium hypochlorite (NaClO), sodium hydroxide (NaOH), sodium bromide (NaBr) used for oxidation were procured from Sigma-Aldrich, India. Cobalt(II) acetate anhydrous ($\text{C}_4\text{H}_6\text{CoO}_4$) (98%) was purchased from Alfa Aesar and malonic acid ($\text{C}_3\text{H}_4\text{O}_4$) was from Sigma-Aldrich. All other chemicals, such as sodium hydroxide (NaOH), hydrochloric acid (HCl), lithium chloride (LiCl), magnesium chloride (MgCl_2), magnesium nitrate [$\text{Mg}(\text{NO}_3)_2$], Sodium chloride (NaCl), potassium chloride (KCl), potassium sulfate (K_2SO_4) were of analytical grade. Ultrapure deionized (DI) water (Milli-Q purifier system, Merck, Germany) was consumed as solvent in the complete synthesis procedure and tert-butanol ($\text{C}_4\text{H}_{10}\text{O}$) was utilized for the washing procedure.

5.2.2. Preparation of TEMPO-oxidised Cellulose Nanofibers (TCNF)

Same typical protocol of TEMPO-oxidation for the synthesis of TEMPO-oxidised nanocellulose described in Chapter 2, section 2.2 was adopted with a slight change in processing where homogenization was used instead of ultra-sonication to obtain fibers.²¹

The whole reaction system was transferred to the homogenizer only for a one pass at 50 MPa. The gel-like product obtained was thoroughly washed and stored at 4 °C in wet conditions for further modifications.

5.2.3. Synthesis of Cobalt(II) Induced Malonic acid-Nanocellulose Hybrid Aerogels (CoMNC)

A mixture 3 mL of 0.033 g malonic acid and 1.5 wt% nanocellulose dispersion was taken in a cultural tube. Instant white color gel formed on shaking and it was then incubated in an aqueous solution containing almost 0.063 g of cobalt acetate for 24 h. The obtained pink-colored mechanically stable hydrogels were placed in a preheated oven at 90 °C for 10 min followed by washing thoroughly with water, water: tert-butanol mixture to exchange the solvent to t-BuOH followed by freeze-drying. The resultant violet color aerogels were labeled as CoMNC aerogels. Aerogels fabricated by simply mixing similar amount of cobalt acetate to nanocellulose dispersion without malonic acid also prepared in the same procedure as control sample, was labeled as CoNC.

5.2.4. Physical Characterization of Aerogels

The carboxyl content of TCNF was determined by standard conductometric titration on a lab scale. O/C ratio and chemical states of TCNF samples, CoMNC, and CoNC aerogels were evaluated employing X-ray photoelectron spectroscopy (XPS) by PHI 5000 VersaProbe II, ULVAC-PHI Inc., USA. FTIR spectroscopic transmittance of samples were recorded from PerkinElmer FTIR spectrometer in the 4000-500 cm^{-1} region operated at a resolution of 4 cm^{-1} and 16 scans. Particle distribution by dynamic light scattering (DLS) and zeta potential of TCNF were studied by accessing Zetasizer Nano ZS, Malvern equipment using a sample concentration of 0.1 % (w/v). Morphology of TCNF was monitored by Atomic force microscopy (AFM) by Multimode 8 atomic force microscope; Nanoscope V controller (Bruker, Santa Barbara, CA) under tapping mode. Samples for AFM were prepared by coating and drying TCNF dispersion over mica sheet as substrate. PANalytical X'pert pro equipped with Cu $K\alpha$ ($\lambda=1.54 \text{ \AA}$), 45 kV is being used to obtain powder X-ray diffraction (XRD) pattern of all samples. Scanning electron micrographs

Thermochromic CoMNC aerogels

were acquired by subjecting fraction of aerogel samples to Zeiss EVO 18 cryo-SEM at 15 kV. Density of aerogels samples were formulated from mass by volume ratio. Nitrogen adsorption-desorption studies were performed to find out Brunauer-Emmett-Teller (BET) surface area and Barrett-Joyner-Halenda (BJH) pore-size distributions using Gemini 2375, Micromeritics, Norcross, USA. A minimum 12 h of degassing prior to surface area studies of aerogels is required. Thermogravimetric analysis (TGA) analysis were conducted with simultaneous thermogravimetric analyzer (STA 7300, Hitachi, Japan) in the range from 50 to 700 °C at a rate of 5 °C/min in the air. Mechanical specifically compression strength of aerogel samples were evaluated by a universal testing machine (Hounsfield, H5KS UTM, Redhill, U.K.); crosshead speed- 1.0 mm min⁻¹. UV- visible absorption maxima of CoMNC aerogel samples were measured from UV-Visible spectrophotometer (Shimadzu UV-2700, Shimadzu, Japan).

5.2.5. Formulation of Humidity Sensor Android Application

A prototype of Java-based android mobile app edited using Android studio as an IDE (integrated development environment) for humidity sensing was developed. The application design detail is shown in (section 5.3.5). Visible light spectrum corresponding to λ_{\max} obtained from UV-Visible absorption spectroscopy of CoMNC samples at different humidity environment were collected and utilized as input in the programming. Test standards and known humidity environments were created in glass desiccators having saturated solutions of LiCl, MgCl₂, Mg(NO₃)₂, NaCl, KCl, and K₂SO₄, which provides the humidity levels of 11%, 33%, 53%, 75%, 85%, and 97%, respectively.²² Absorption maxima (λ_{\max}) were recorded at 25 °C and relative humidity of 50-52%.

5.3. RESULTS AND DISCUSSION

5.3.1. Cobalt(II) Coordinated Malonic acid-Nanocellulose Hybrid Aerogels

TEMPO-oxidation is desirable for the fabrication of metal ion coordinated aerogels since it evokes the carboxyl functionalization in cellulose that ensure the coordination with metal ions. According to the experimental section, TEMPO-oxidation followed a mild

homogenization process to exfoliate cellulose nanofibers (TCNF) from banana pseudo-stem fibers. After being oxidized by TEMPO-mediated oxidation, the C6 hydroxy groups of cellulose selectively converted to carboxyl group which is determined to be 1.06 mmol/g by conductometric titrations and an O/C ratio of about 0.6 was obtained from XPS analysis which is higher than that of holocellulose (O/C ratio= 0.41) obtained from banana pseudo-stem fibers. Qualitative confirmation of introduced carboxyl groups in cellulose is done with FTIR analysis and confirmed from the new sharp peak arising at 1600 cm^{-1} .²³ Electrostatic repulsions between the carboxyl groups and inter and intra-molecular hydrogen bonding will always provide stable aqueous suspensions of TCNF as shown by the value of the zeta potential, -60.02 mV.

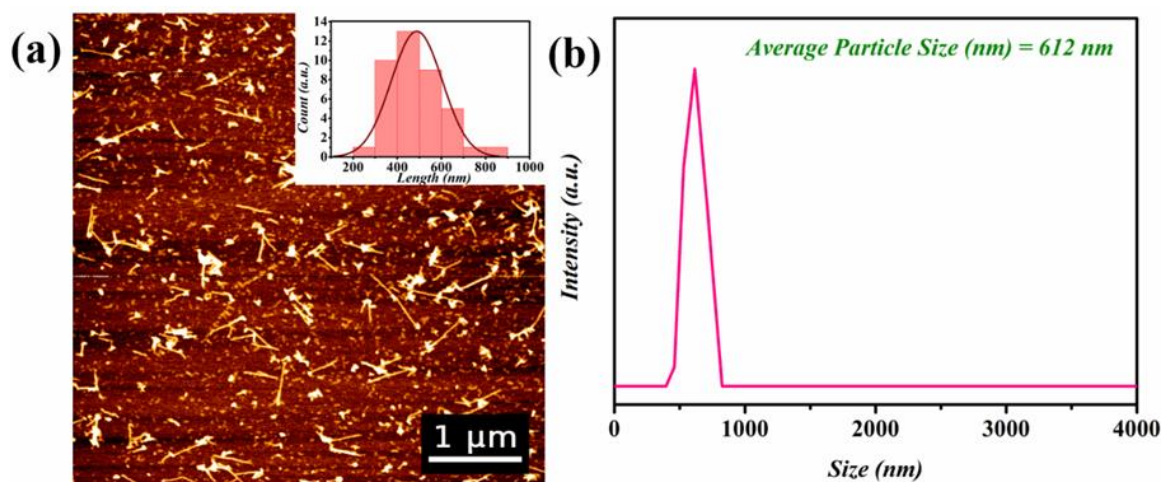


Figure 5.1. (a) AFM height image and (b) DLS spectrum of TCNF.

The size distribution and morphology of TCNF were confirmed by AFM and DLS analyses (**Figure 5.1**). Visual detection of morphology of TCNF were done using AFM in tapping mode in air. **Figure 5.1a**, the AFM height image, depicts the existence of individual fibers having width, 15 ± 2 nm and width, and length of a few hundred nanometers according to the high aspect ratio of cellulose nanofiber. Peak in the size distribution pattern located at 390 to 830 nm region having an average particle size as 612 nm with a PDI of 0.2 gave information about the fibrous structure of TEMPO-oxidized nanocellulose with almost uniform size (**Figure 5.1b**).

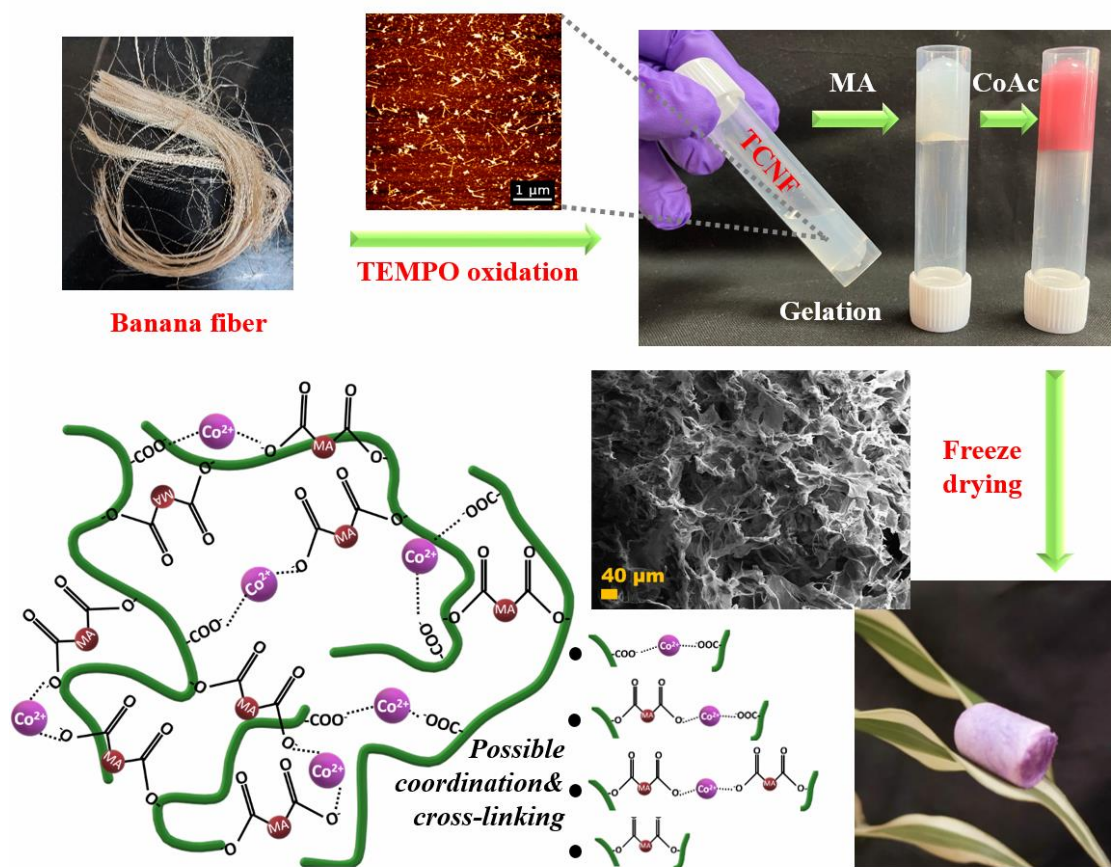


Figure 5.2. Synthesis of Cobalt(II) coordinated malonic acid/nanocellulose hybrid aerogels and schematic illustration of possible coordination and cross-linking in the formed aerogels.

Fluidity of 1.5 wt% TCNF dispersion was discarded by the addition of anhydrous Co (II) acetate salt denoted as CoNC. This rapid gelation is happened due to the bonding affinity of metal in +2 oxidation states to the carboxyl groups induced by the TEMPO oxidation in TCNF. Hence the strength of hydrogels will ultimately depend upon the degree of carboxylation in TCNF which will vary by several factors including source of cellulose.²⁴ As a preliminary step, we added 1.2 M anhydrous cobalt acetate to 1.5 wt% TCNF suspension and mixed in a vertex mixer for 30 s and denoted as CoNC. After instant mixing, there is small extent of fluidity and inhomogeneity in the physical appearance of pink hydrogel was observed. Despite the fact that full gel formation was detected after 24

hours, homogeneity was not achieved. Even though some literature discussed instant homogeneous gel formation with other metal ions like Ca^{2+} , Fe^{2+} , Al^{3+} , Cu^{2+} etc., our investigations led us to believe that this phenomenon is solely dependent on the degree of carboxylation, which is susceptible to vary due to individual experimental error.¹¹⁻¹² Therefore, another alternative option is required in such cases to form ultra-stable and sustainable hydrogels.

Adding ligands that can form MOF with Cobalt is one option and it has been employed by several researchers.⁶ However, these ligands are expensive and toxic in nature. Selective and versatile functionalization of nanocellulose with carboxyl groups enabled the binding of metal ions to the sustainable nanocellulose matrix and resulted in to rapid build mechanically stable aerogels. In addition to TEMPO-oxidation, formation of semi-acid esters resulted from the reaction of cellulose with polycarboxylic acids or their derivatives is an alternative or additional pathway to increase the carboxylic contents to an extent. Among the organic polycarboxylic acids, dicarboxylic acids are potential candidates to form an ester linkage between hydroxy groups of cellulose and one carboxyl group with the other end carboxyl group remaining free. Under some conditions these free carboxyl ends of dicarboxylic acids also react with the cellulose hydroxyl groups and gave cross-linkage between cellulose chains.²⁵ Cross-linking of cellulose chains can be utilized in mechanical strength of nanocellulose based hydrogels and aerogels to an extent, whereas concerned maximization of cross-linking without free carboxyl groups can be hindered in presence of Co^{2+} metal ions and water as solvent in the system. Dicarboxylic acids like citric acid, malonic acid, maleic acid etc., are also recognized by the researchers as organic acid catalyst for the exfoliation of nanocellulose fibers from holocellulose at optimum reaction conditions.²⁶ These optimum conditions includes high acid concentration, elevated temperature etc., that minimize cellulose cross-linking acids and acids can be recovered after the reaction.^{26b} Selection of malonic acid as the organic carboxylic acid in the development of mechanically stable Co^{2+} coordinated nanocellulose aerogels raised the coordination affinity of Co^{2+} with malonic acid and also the less possibility of effective cross-linking by the second carboxyl group of dicarboxylic is very less compared to the cross-linking efficiency of polycarboxylic acids.²⁷

Thermochromic CoMNC aerogels

Main five types of possible chemical interactions in the Co^{2+} induced malonic acid/nanocellulose aerogels (CoMNC) includes coordination between two carboxyl groups of TCNF formed by TEMPO oxidation and Co^{2+} ion ($\text{TCNF-COO}^- \dots \text{Co}^{2+} \dots \text{OOC-TCNF}$), coordination between one carboxyl group of TCNF formed by TEMPO oxidation and one free carboxyl end of semi acid ester of cellulose made by the malonic acid with Co^{2+} ion ($\text{TCNF-COO}^- \dots \text{Co}^{2+} \dots \text{OOC-CH}_2\text{-COO-TCNF}$), two free carboxyl end of semi acid ester of cellulose made by the malonic acid and Co^{2+} ion ($\text{TCNF-COO-CH}_2\text{-COO}^- \dots \text{Co}^{2+} \dots \text{OOC-CH}_2\text{-COO-TCNF}$) and the last one is cross-linking between cellulose chains by malonic acid as depicted in **Figure 5.2**. Coordination between Co^{2+} and two carboxyl groups of same malonic acid or different malonic acid is negligible here hence it will form insoluble coordination crystal forms (MOFs) in aqueous media depending upon the severity of reaction conditions.

The FT-IR spectra of MA, TCNF, CoNC and CoMNC aerogels were collected to evaluate the interaction between carboxylated nanocellulose, MA and Co^{2+} ions (**Figure 5.3a**). TEMPO-oxidised cellulose nanofibers showed a peak at 1600 cm^{-1} that typical for the carboxyl group. In the FT-IR spectra of CoNC aerogels shows a narrow shift in the peak corresponding to carboxy groups to 1603 cm^{-1} . After the formation of aerogel with MA and Co^{2+} ions, this peak underwent a high frequency shift to 1608 cm^{-1} with an additional peak at 1735 cm^{-1} . This shift happened by coordination of carboxyl groups with the metal ions. There is a small new-born peak at 1735 cm^{-1} validates the formation of ester groups in the system to some extent that theoretically has vibration peak at higher frequency than the carboxylic acids.²⁸ While considering the $-\text{OH}$ stretching vibration peak of nanocellulose at 3361 cm^{-1} became broadened, low-frequency shift was observed with a significant decrement in the intensity. This characteristic change can be explained by the coordination of numerous $-\text{OH}$ groups of cellulose with Cobalt ion which impart a cross-linked gel morphology.⁶ The utilization of hydroxy groups of cellulose for the formation of semi acid ester of cellulose also in agreement with noticeable decrement in the $-\text{OH}$ symmetric stretching peak intensity. The absorption bands between 500 and 700 cm^{-1} can be identified of M-O bonds on the sample which were observed in both TCNF and CoMNC resulted from the $\text{COO}^- \text{---} \text{Na}^+$ in TCNF and $\text{COO}^- \text{---} \text{Co}^{2+}$ coordination interactions in

Thermochromic CoMNC aerogels

CoMNC, respectively. Overall information obtained from FT-IR spectra of variant samples qualified the formation of different coordination interactions and cross-linking mentioned above, which are possible behind the formation of stable CoMNC aerogels.

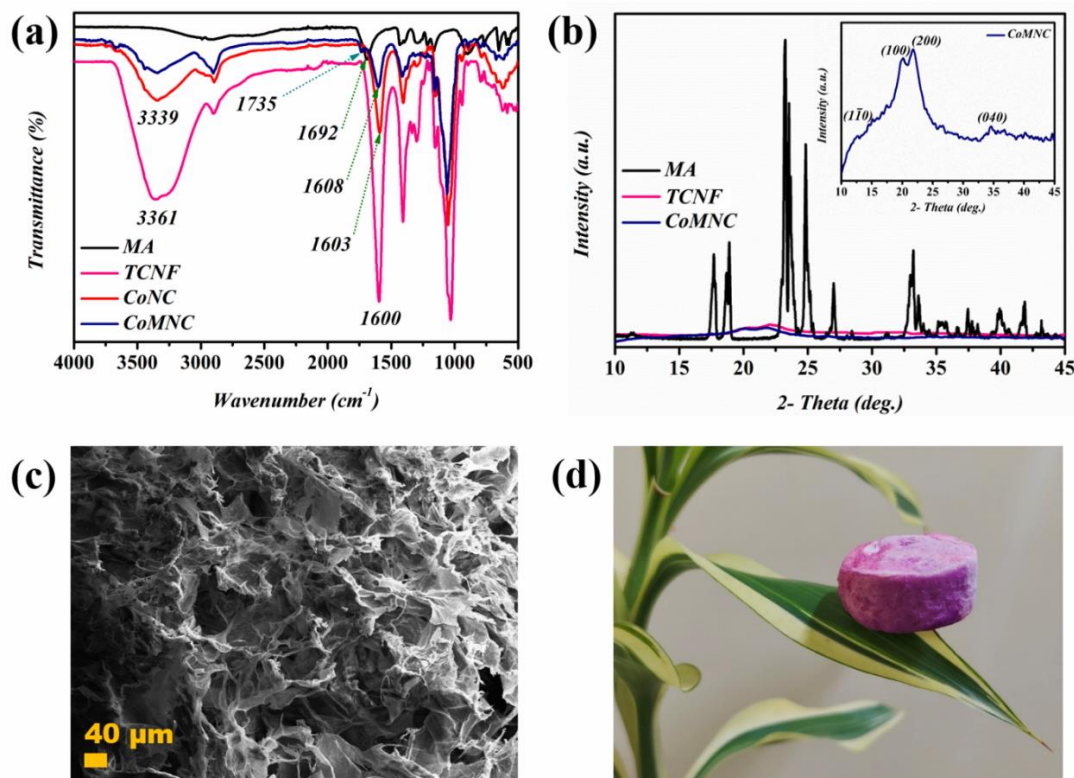


Figure 5.3. (a) FT-IR spectra, (b) PXRD of malonic acid (MA), TEMPO-oxidised nanocellulose (TCNF), CoNC and CoMNC aerogels, (c) SEM micrographs and (d) physical appearance of fibrous CoMNC aerogels.

The PXRD patterns of MA, TCNF and CoMNC aerogels were presented in **Figure 5.3b**. Typical XRD patterns of Cellulose II contains characteristic peaks at $2\theta = 12.6^\circ$, 20.03° , and 21.89° corresponding to the planes (1-10), (110) and (200), respectively. PXRD pattern of CoMNC aerogels obtained was exactly similar to the diffraction pattern of Cellulose II and great difference from the PXRD pattern of MA crystals. These PXRD observations illustrated that MA must be reacted with TCNF and Co^{2+} ions and malonate moiety must be introduced into amorphous coordinated polymer form successfully and no Cobalt malonate MOFs are formed. CoMNC aerogels have irregularly shaped and sized

Thermochromic CoMNC aerogels

pores as shown in the SEM image (**Figure 5.3c**) created by the layered sheets like structures of assembled cellulose nanofibers cross-linked by MA and Co^{2+} ions. The CoMNC aerogels formed were structurally strong and lightweight having a density of about 0.04 g/cm^3 (**Figure 5.3d**).

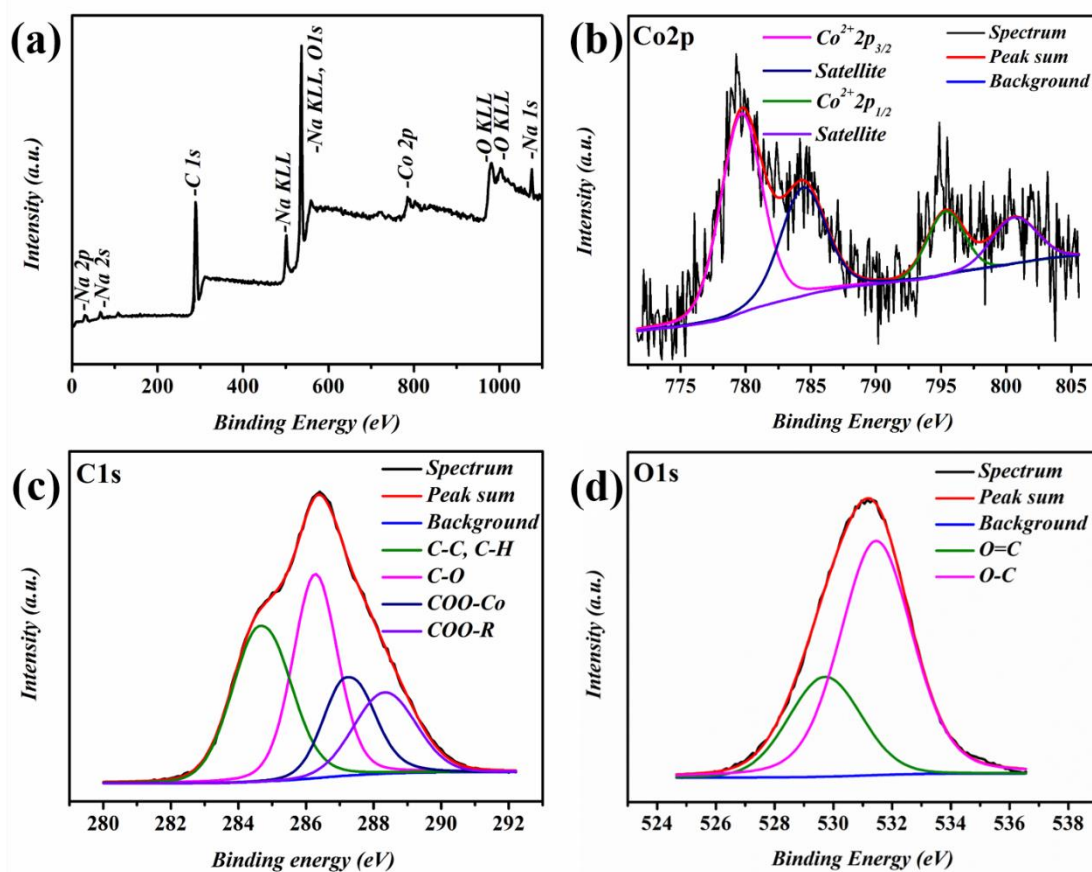


Figure 5.4. (a) XPS survey, deconvoluted XPS spectra of (b) Co2p, (c) C1s and (d) O1s of CoMNC aerogels.

In order to examine the chemical states of elemental constituents of CoMNC aerogels, XPS analysis were done and resultant survey spectrum shows the major elemental constituents of aerogels as Co, O, C and small amounts of Na that arises from the TCNF due to exfoliation of nanocellulose from plant source (**Figure 5.4a**). The deconvoluted XPS spectra of core-levels of Co2p, C1s and O1s were showed in **Figure 5.4b**, **5.4c**, and **5.4d**. The prominent Co2p core-level signal contained two coexhibited doublets corresponding to Co^{2+} species ($\text{Co}^{2+} 2p_{3/2}$ at 779.9 and $\text{Co}^{2+} 2p_{1/2}$ at 795.2 eV with a spin-orbital splitting

of ~ 15.4 eV), satellite peaks (784.5 and 800.6 eV), respectively.²⁹ **Figure 5.5a** shows the deconvoluted Co2p spectra of CoMNC aerogels along with the Co2p spectra of CoNC, control samples synthesized in absence of malonic acid for comparison. Co2p in CoMNC has shifted to a lower binding energy compared to corresponding in CoNC, this shift indicates that electronic or coordination interactions between the Co^{2+} ions and the supporting matrix is turned to more strong.³⁰ These corroborate the necessity of malonic acid in the formation of this mechanically stable CoMNC hydrogels and aerogels.

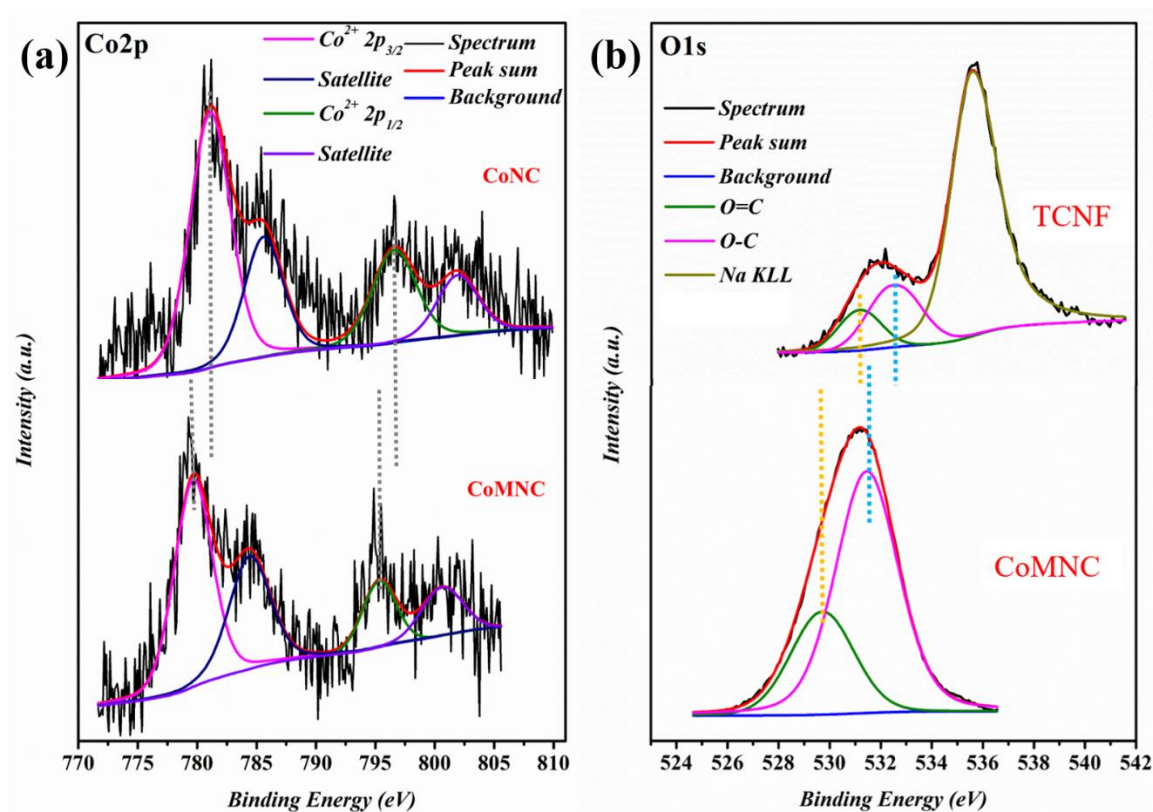


Figure 5.5. Deconvoluted XPS spectra for (a) Co2p of CoNC and CoMNC aerogels, and (b) O1s spectra of TCNF and CoMNC aerogels showing the shift in terms of binding energy after gel formation.

The deconvoluted XPS spectra of C1s for CoMNC found to be entirely different in proportions of all four distinct peaks for characteristic bonds from usually obtained C1s spectra for TEMPO-oxidised nanocellulose envisaged the presence of malonic acid also in the backbone aerogel scaffold (chapter 2, section 2.3.2).³¹ Distinct peak at 287.0 eV

Thermochromic CoMNC aerogels

signifies the strong coordination between Co^{2+} ions (metal ions) and carboxyl groups in the TCNF/MA template.³¹ The noticeable peak at 288.3 eV can be assigned to ester moiety formation in CoMNC and it cannot be able to differentiate from that for TCNF since free COOH groups will also show peak in this region of C1s XPS spectra.²⁸ However, increment in the intensity of this peak is considerable. The O1s spectrum can be fitted with two distinct peaks at 529.7 (O=C), and 531.4 (O-C) respectively. Low shift in the O1s characteristic peaks strongly promoted the fact of strong interaction between oxygen and metal present in the system (**Figure 5.5b**).

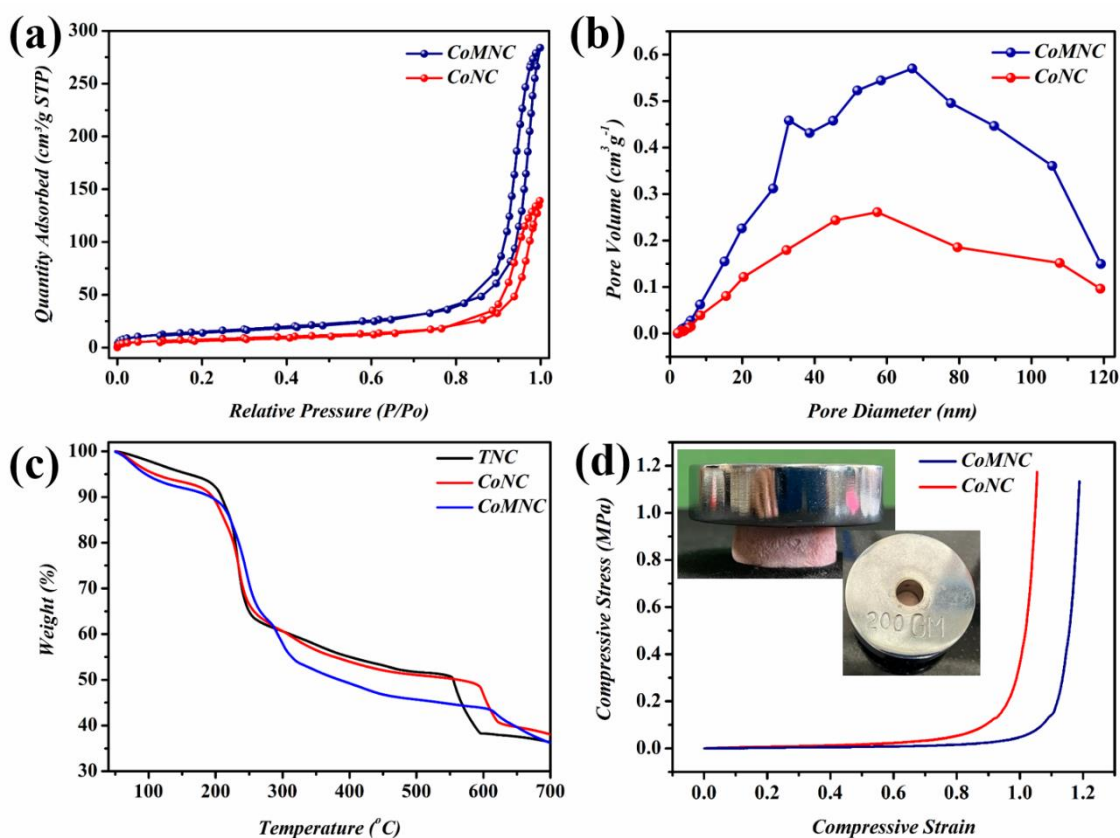


Figure 5.6. (a) BET N_2 adsorption–desorption analysis, (b) corresponding BJH pore-size distribution curves, (c) TG curves, and (d) Compression performance of CoNC and CoMNC aerogels.

The inherent and impressive high surface area and lightweight of these materials, called aerogels, make them applicable in a variety of industries. **Figure 5.6a** presented the BET N_2 adsorption- desorption loops for CoMNC and CoNC aerogels. Both curves

exhibited typical type II adsorption isotherms with H3 hysteresis loop characteristics of the monolayer-multilayer adsorption.³² CoMNC aerogels displays considerable variation in BET surface area compared to CoNC aerogels project the highlights of CoMNC aerogel system. CoMNC have a high BET surface area of $88.03 \text{ m}^2 \text{ g}^{-1}$ straddle that of CoNC aerogel ($28.66 \text{ m}^2 \text{ g}^{-1}$). In BJH pore-size distribution curves (**Figure 5.6b**) pore diameters are irregular and distributed in a wide range from minor amount of micro to some macropores which covers the entire mesoporous region as generally observed in nanocellulose based aerogels.³³ When considering the pore volume, major fraction of apparent pores were lies in the mesoporous sector having BJH adsorption average pore diameter of 30 nm and 27 nm for CoMNC and CoNC, respectively. Taking into account previous research, the BET surface area reported in this study is an average for nanocellulose based aerogels, and high values may be attained using a vacuum-assisted N_2 adsorption-desorption assay setup since both aerogels are very sensitive to moisture.³⁴ This high affinity of CoMNC and CoNC aerogels towards water molecules will extensively retard the N_2 adsorption thereby actual surface area will be higher than the measured BET surface area.

Figure 5.6c shows the thermal stability of TCNF, CoNC and CoMNC aerogels measured by thermogravimetric analysis (TGA) under air from 50 to 700 °C. Both TCNF and CoNC aerogels exhibited similar thermal degradation behaviour different from CoMNC manifested due to the change in composition or structure of nanocellulose after the addition of malonic acid that not visible in PXRD. Moisture absorption characteristics of aerogels are visible from the initial weight loss (5-8.2%) from 50 to almost 150 °C in TGA which shows an increasing trend from TCNF < CoNC < CoMNC. The polymer decomposition stage (about 50% weight loss) started at about 200 to 350 °C followed by subsequent residual substance decomposition stage up to about 600 °C.³⁵ Mechanical properties of CoNC and CoMNC aerogels were studied by compression measurements and the corresponding stress–strain curves are given in **Figure 5.6d**. Without shattering of specimen, both CoNC and CoMNC aerogels revealed a buckling to a dense solid film appearance at higher loads. CoMNC shows more improvement in the mechanical properties than CoNC aerogels without forming any fracture or disruption of aerogels

offered us the meaningful knowledge about the key role of malonic acid in the nanocellulose/Co²⁺ cross-linked aerogels.

5.3.2. Mechanism of Gel Formation

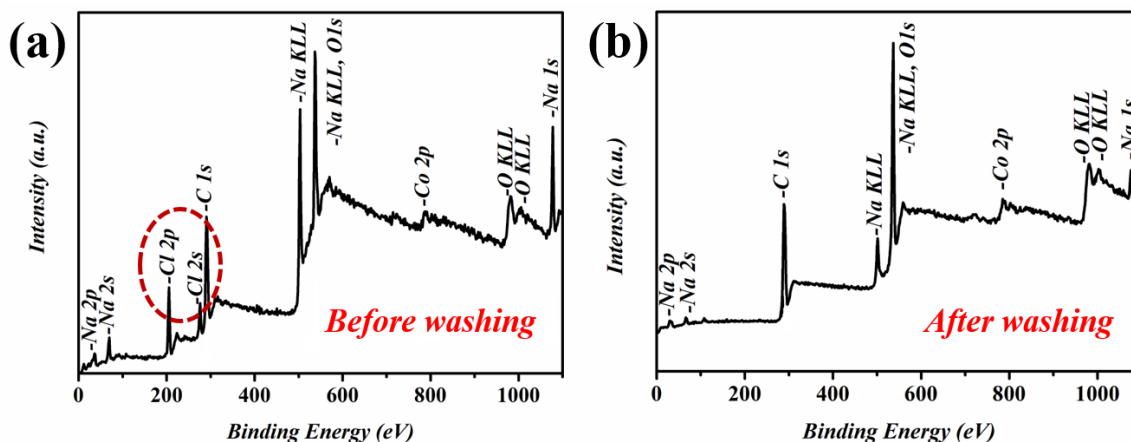


Figure 5.7. XPS survey spectra of CoMNC aerogels (a) before and (b) after washing step.

Isolation of Cellulose nanofibers (TCNF) was achieved from banana pseudo-stem fibers, agricultural waste through mainly three major intermediate chemical steps; pretreatment by NaOH, bleaching and followed by TEMPO-oxidation. Enormous utilization of Na and Cl contained reagents for these process ultimately leave noticeable amount of Na and Cl in the end product which can be confirmed from the prominent peak of Na KLL in the XPS spectra of TCNF (**Figure 5.7**). It is explicitly known that carboxyl groups created at C6 hydroxyl groups of cellulose chains by TEMPO-oxidation is existing and stable by the interaction between COO⁻ and Na⁺ ions in TCNF. Instant gel formation by addition of salts of metals in to TCNF matrix is fully governed by the complexation interaction between the COO⁻ groups and metal ions. For example, addition of weak salt like Cobalt acetate will promote the instant hydro-gelation by coordinating with COO⁻, replacing the Na⁺ ions in the current position. If the hydrogel formation mechanism is following this pathway, there should be the formation of NaCl as by-product which can be removed by purification.

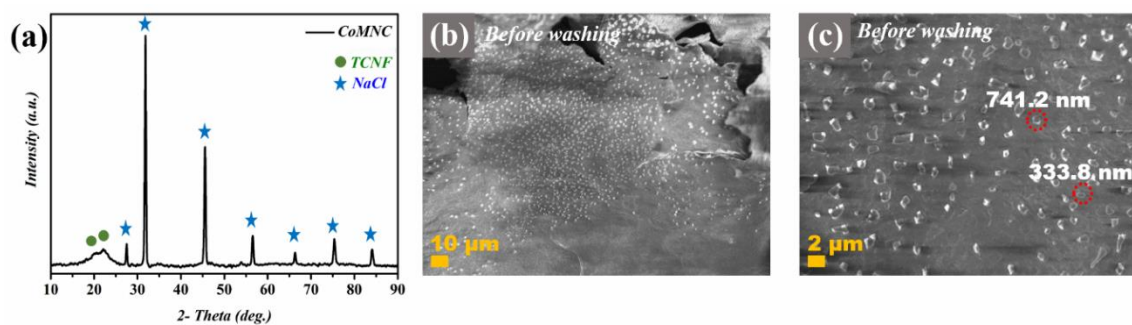


Figure 5.8. Physical characterization of CoMNC aerogels without washing step before freeze drying. a) XRD pattern, b-c) SEM micrographs.

Physical characterizations such as PXRD, SEM, and XPS analysis were performed prior to sample purification in order to investigate the mechanism. **Figure 5.8a** displayed the PXRD pattern of CoMNC fabricated without any washing or purification step which shows some extra peaks apart from typical trend of Cellulose II originated in the 2θ range 27- 85 ° compared to PXRD pattern of CoMNC with purification step (**Figure 5.3b**). The diffraction peaks precisely recorded at 27.45°, 31.79°, 45.54°, 53.92°, 56.52° 66.36° 75.38°, and 84.11° showed substantial similarity with the typical diffraction pattern of *fcc* NaCl crystals, which matched to the planes (111), (200), (220), (311), (222), (400), (420) and (422), respectively (JCPDS no. 00-078-0751), confirmed the presence of NaCl crystal formed during the hydro-gelation process. These diffraction patterns of NaCl in the aerogel PXRD patterns got eliminated after several washing steps leaving behind the XRD diffraction of Cellulose II (**Figure 5.3b**).

This intriguing evidence was further clarified by capturing surface morphology of CoMNC aerogel layers by SEM prior to the purification step. In the SEM micrographs of CoMNC aerogels before purification (**Figure 5.8b-c**), we observed a few crystals of several hundred nanometer size, decorated over the aerogel surface revealed the formation of NaCl crystals during the hydro-gelation process and these independent crystals can be removed by purifications. XPS survey spectrum also attempted to understand this mechanism of binding efficiency of carboxyl groups to Co^{2+} ions displayed both the presence of Na and Cl elements in the original aerogels, and peak of Cl element was

vanished after leaving small amount of Na element after washing step (**Figure 5.7**). These results considerable evidence towards the mechanism of gelation and important roles of carboxyl groups in the binding of metal ions.

5.3.3. Humidity Absorption of Aerogels

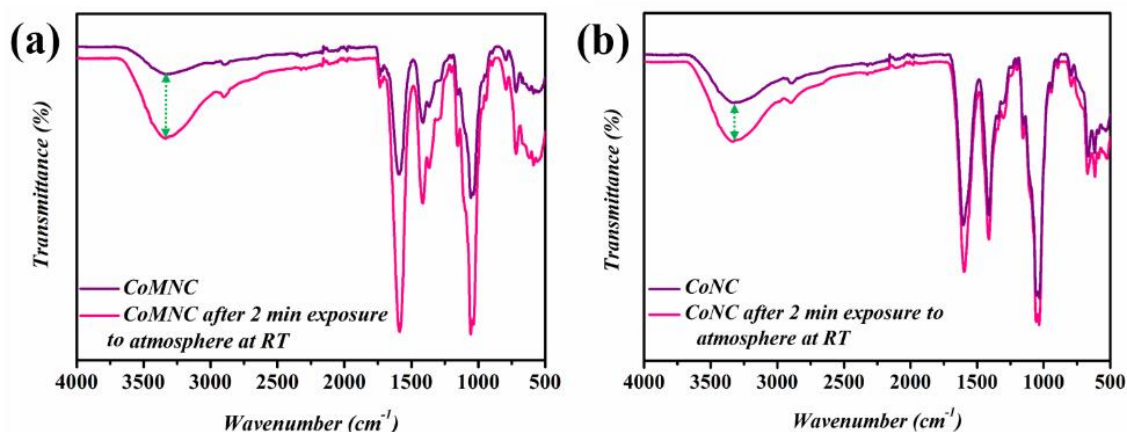


Figure 5.9. (a-b) FT-IR spectra of CoMNC and CoNC aerogels after 2 min exposure to atmosphere at room temperature for humidity absorption rate comparison.

The FT-IR measurements CoMNC and CoNC aerogels received special attention because both displayed significant change in the intensity of -OH symmetric stretching vibration peak at 3361 cm^{-1} within minutes (**Figure 5.9a-b**). This intensification in the -OH stretching is vastly raised and contributed by the absorbed water molecules from the surrounding atmosphere. This explicitly put forward the capability of aerogels absorption of water from humidity absorption and becomes imperative to study further. For comparison studies, FT-IR spectra measured for both CoMNC and CoNC aerogels at a fixed interval of 2 minutes under room temperature (**Figure 5.9a-b**). It has already been witnessed that both showing considerable absorption of atmospheric water whereas CoMNC aerogels achieved more absorption at fixed time of interval resulted in the more positive deviation in the -OH stretching peak intensity.

5.3.4. Reversible Thermochromism

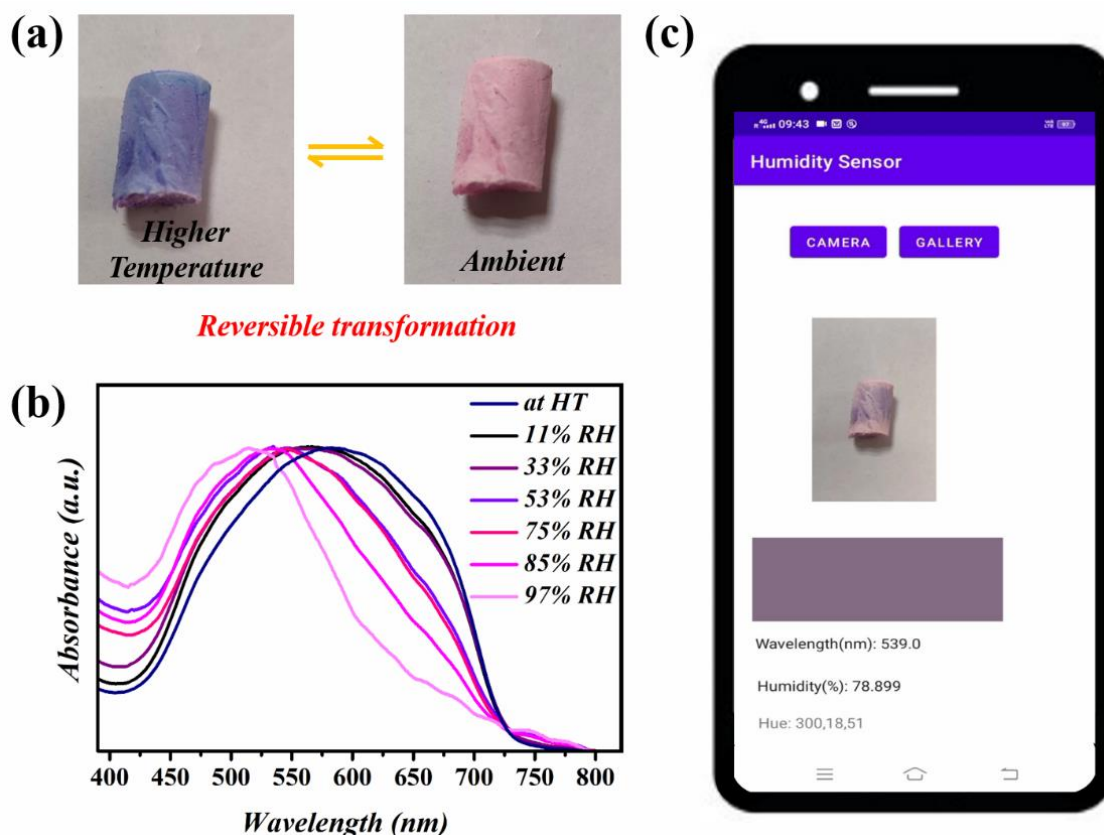


Figure 5.10. (a) Reversible thermochromism of CoMNC aerogels, (b) UV-Visible absorption spectrum of CoMNC aerogels at different standard humidity, and (c) developed a prototype of Java-based android mobile app for humidity sensing utilizing CoMNC aerogels.

It is rational that along with water molecule absorption of CoMNC aerogels, one would expect a distinguishable color change in the CoMNC aerogels from violet to pink as shown in **Figure 5.10a**. This allied color change has exactly resulted from the change in coordination of Co^{2+} coordination from dark colored tetrahedral to light colored octahedral by coordinating with water molecules at fifth and sixth coordination valencies. Coordination with water molecules is very weak in the case of CoMNC aerogels and can be removed by keeping it at elevated temperature of about 90 °C for several minutes without harming the structure and humidity absorption properties of aerogels. In fact, the

fabricated CoMNC aerogels are highly humidity sensitive and it shows relevant reversible thermochromism. These realizations lead to the applicability of CoMNC towards a visual humidity sensing platform.

5.3.5. Development of Humidity Sensor

Rate of visible chromic response to the change in humidity was evaluated by monitoring the UV-Visible absorption spectrum at different standard humidity created by the saturated salt solutions (**Figure 5.10b**). After keeping CoMNC aerogels in a desiccator containing saturated salt solutions of known humidity for 30 seconds, the UV-Visible absorption spectra was measured. Different humidity surroundings were set in the different glass desiccators by keeping saturated solutions of LiCl, MgCl₂, Mg(NO₃)₂, NaCl, KCl, and K₂SO₄ solutions, which provides standard and known humidity levels of 11%, 33%, 53%, 75%, 85%, and 97%, respectively. This time-dependent UV-Vis absorption analysis were repeated with several samples, and found out the accurate and precise λ_{\max} at the standard humidity levels. An android application was designed based on these λ_{\max} values and corresponding visible light spectrum of colors which enables the digital and easy sensing of humidity without any complex instruments (**Figure 5.10c**). Since the color change of these Co(II) coordinated malonic acid/nanocellulose hybrid aerogels materials were time-dependent, immediate measurements within one minute is essential for the accurate values. This constraint was solved by the developed android application which enables the humidity sensing of CoMNC aerogel photographs captured by the camera even long time before. Therefore, a simple snapshot of CoMNC aerogels allows instantaneous monitoring of ambient humidity from smartphones at any moment. A short time heating of used CoMNC aerogels at 90 °C will make the system active for reuse for further sensing. Detailed criteria and steps for the formulation of humidity sensor android application were shown below.

5.3.6. Development of an Android Mobile Application for Humidity Sensing Based on CoMNC Aerogels

1. Explanation of Program Listings

1.1. Capturing Image Using Camera

The given program is written in *Main_Activity.kt* file and inside the *onCreate()* function. In line 2, the app is instructed to recognize the camera button through its ID, which was defined while creating the *activity_main.xml* file. Lines 5 and 6 are written to clear the cache after every new image is loaded by the user. In the next line, an intent is defined which acts as a messenger and requests another app component (here, camera) to launch the requested activity. If camera returns the request, then the function *startActivityForResult()* launches the camera of the android phone.

```
1
2 camera=findViewById(R.id.capImage)
3
4 camera.setOnClickListener {
5     imageView.setImageBitmap(null)
6     imageView.destroyDrawingCache()
7     val takePictureIntent = Intent(MediaStore.ACTION_IMAGE_CAPTURE)
8
9     if (takePictureIntent.resolveActivity(this.packageManager)!=null) {
10        startActivityForResult(takePictureIntent, requestCode)
11    }else{
12        Toast.makeText(this, "Unable To Open Camera", Toast.LENGTH_SHORT).show()
13    }
14 }
```

The function *onActivityResult()* is declared outside the *onCreate()* function. After the intent is launched and the camera captures the image, the image is stored in form of a bitmap 'takenImage'. The *ImageView* is then set to the recorded bitmap to display the loaded image.

```
1 override fun onActivityResult(requestCode: Int, resultCode: Int, data: Intent?) {
2     if(requestCode==requestCode && resultCode== Activity.RESULT_OK){
3         val takenImage = data?.extras?.get("data") as Bitmap
4         imageView.setImageBitmap(takenImage)
5     }else {
6         super.onActivityResult(requestCode, resultCode, data)
7     }
8 }
```

1.2. Selecting Image from Gallery

The *registerForActivityResult()* function registers the user's callback and sets the image URI to the *ImageView*. The *setOnClickListener()* button has the same function as in the case of camera button that is it redirects the user to the gallery once it is clicked. The chosen image is then displayed on the *ImageView*.

Thermochromic CoMNC aerogels

```
1     val pickImage =
2         registerForActivityResult (ActivityResultContracts.GetContent (),
3             ActivityResultCallback {
4                 imageView.setImageURI(it)
5             })
6     button.setOnClickListener {
7         imageView.setImageBitmap(null)
8         imageView.destroyDrawingCache()
9         pickImage.launch("image/*")
10    }
```

1.3. Main Program

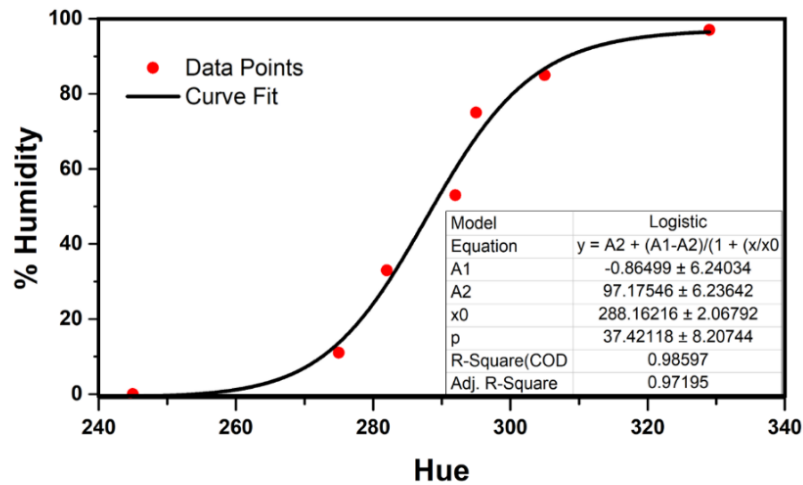


Figure 5.11. Logistic curve fit for the data between humidity and *hue* along with the parameters

The RGB value of the pixel where our finger is placed currently is recorded. Since every wavelength does not have a corresponding RGB value, the RGB value is converted to HSV value using the function *RGBtoHSV()*. Further, two variables of double type lambda and humidity are declared. For *hue* values between 200 to 350, we are calculating the wavelength value for the complementary colour (*hue*-180). The equation relating humidity and *hue* is obtained by first converting the wavelength values in the data to their corresponding *hue* values and doing a curve fit between humidity and *hue* data.

$$\text{Humidity} = 97.17546 + (-0.86499 - 97.17546)/(1 + (\text{Hue}/288.16216)^{37.42118})$$


```
1     imageView.setOnTouchListener { v, event ->
2         if (event.action==MotionEvent.ACTION_DOWN || event.action==
MotionEvent.ACTION_MOVE){
3             bitmap=imageView.drawingCache
4             val pixel = bitmap.getPixel(event.x.toInt(),event.y.toInt())
5
6             val r = Color.red(pixel)
7             val g = Color.green(pixel)
8             val b = Color.blue(pixel)
9
10            colorView.setBackgroundColor(Color.rgb(r,g,b))
11
12            val hsv = FloatArray(3)
13            Color.RGBToHSV(r,g,b,hsv)
14
15            val hue = hsv[0].toInt()
16            val sat = (hsv[1]*100).toInt()
17            val value =(hsv[2]*100).toInt()
18
19            var lambda: Double=0.00
20            var humidity: Double=0.00
21
22            if(hue in 200..350){
23                lambda = 650-(0.925*(hue-180))
24                humidity = 97.17546 + (-0.86499 - 97.17546)/(1 + (hue
/288.16216).pow(37.42118))
25            }
26
27            val dec = DecimalFormat("##.000")
28            humidity = dec.format(humidity).toDouble()
29            lambda=dec.format(lambda).toDouble()
30
31            if(humidity<100 && humidity>0) {
32                display1.text = "Wavelength(nm): $lambda"
33                display2.text = "Humidity(%): $humidity"
34                display3.text = "Hue: $hue,$sat,$value"
35            }
36
37            else if(humidity<0){
38                display1.text = "Wavelength(nm): $lambda"
39                display2.text = "Humidity(%): 0.0"
40                display3.text = "Hue: $hue,$sat,$value"
41            }else{
42                display1.text = "Wavelength(nm): $lambda"
43                display2.text = "Humidity(%): 100.0"
44                display3.text = "Hue: $hue,$sat,$value"
45            }
46            true
47        }
```

5.4. CONCLUSIONS

In brief, a reversible thermochromic Cobalt(II) coordinated malonic acid/nanocellulose hybrid aerogels was developed by utilizing the synergic action of coordinating power of Co(II) ions and malonic acid assisted cross-linking. Induced carboxyl groups from TEMPO-oxidation and handful hydroxy groups played beneficial

Thermochromic CoMNC aerogels

role in the coordination with Co(II) ions and ester moiety based linkage between fibers by utilizing malonic acid. These cobalt(II) coordinated malonic acid/nanocellulose hybrid aerogels exhibited the intrinsic thermochromic property of Co(II) based materials. Moreover, the fibrous and flexible nature of aerogels with high specific surface area enhanced this phenomenon by reducing the time for these reversible thermochromism process. The enhanced reversible thermochromism of these hybrid aerogels eluted from its high accessible surface contact with the moisture can be utilized as a visible humidity sensor. More specific humidity sensing was enabled by developing an android mobile application for reading the color coordinates of aerogels from its spectroscopic absorption characteristics. This sustainable pathway can be ideal for many broad applications that required incorporation of different metal based additives with exciting properties.

5.5. REFERENCES

1. Thomas, B.; Raj, M. C.; Joy, J.; Moores, A.; Drisko, G. L.; Sanchez, C. m., Nanocellulose, a versatile green platform: from biosources to materials and their applications. *Chemical reviews* **2018**, *118* (24), 11575-11625.
2. Giese, M.; Spengler, M., Cellulose nanocrystals in nanoarchitectonics—towards photonic functional materials. *Molecular Systems Design & Engineering* **2019**, *4* (1), 29-48.
3. Xu, X.; Liu, F.; Jiang, L.; Zhu, J.; Haagenon, D.; Wiesenborn, D. P., Cellulose nanocrystals vs. cellulose nanofibrils: a comparative study on their microstructures and effects as polymer reinforcing agents. *ACS applied materials & interfaces* **2013**, *5* (8), 2999-3009.
4. Hubbe, M. A.; Ferrer, A.; Tyagi, P.; Yin, Y.; Salas, C.; Pal, L.; Rojas, O. J., Nanocellulose in thin films, coatings, and plies for packaging applications: A review. *BioResources* **2017**, *12* (1), 2143-2233.
5. Guccini, V.; Phiri, J.; Trifol, J.; Rissanen, V.; Mousavi, S. M.; Vapaavuori, J.; Tammelin, T.; Maloney, T.; Kontturi, E., Tuning the Porosity, Water Interaction, and Redispersion of Nanocellulose Hydrogels by Osmotic Dehydration. *ACS applied polymer materials* **2021**.
6. Zhu, L.; Zong, L.; Wu, X.; Li, M.; Wang, H.; You, J.; Li, C., Shapeable fibrous aerogels of metal–organic-frameworks templated with nanocellulose for rapid and large-capacity adsorption. *ACS nano* **2018**, *12* (5), 4462-4468.
7. Varghese, H.; Hakkeem, H. M. A.; Chauhan, K.; Thouti, E.; Pillai, S.; Chandran, A., A high-performance flexible triboelectric nanogenerator based on cellulose acetate nanofibers and micropatterned PDMS films as mechanical energy harvester and self-powered vibrational sensor. *Nano Energy* **2022**, *98*, 107339.
8. Ferreira, F. V.; Otoni, C. G.; Kevin, J.; Barud, H. S.; Lona, L. M.; Cranston, E. D.; Rojas, O. J., Porous nanocellulose gels and foams: Breakthrough status in the

- development of scaffolds for tissue engineering. *Materials Today* **2020**, *37*, 126-141.
9. Isogai, A.; Saito, T.; Fukuzumi, H., TEMPO-oxidized cellulose nanofibers. *nanoscale* **2011**, *3* (1), 71-85.
 10. Li, M. C.; Wu, Q.; Moon, R. J.; Hubbe, M. A.; Bortner, M. J., Rheological aspects of cellulose nanomaterials: Governing factors and emerging applications. *Advanced Materials* **2021**, *33* (21), 2006052.
 11. (a) Zander, N. E.; Dong, H.; Steele, J.; Grant, J. T., Metal cation cross-linked nanocellulose hydrogels as tissue engineering substrates. *ACS applied materials & interfaces* **2014**, *6* (21), 18502-18510; (b) Hai, J.; Li, T.; Su, J.; Liu, W.; Ju, Y.; Wang, B.; Hou, Y., Anions Reversibly Responsive Luminescent Tb (III) Nanocellulose Complex Hydrogels for Latent Fingerprint Detection and Encryption. *Angew. Chem., Int. Ed* **2018**, *57* (23), 6786-6790.
 12. Dong, H.; Snyder, J. F.; Williams, K. S.; Andzelm, J. W., Cation-induced hydrogels of cellulose nanofibrils with tunable moduli. *Biomacromolecules* **2013**, *14* (9), 3338-3345.
 13. Cheng, Y.; Zhang, X.; Fang, C.; Chen, J.; Wang, Z., Discoloration mechanism, structures and recent applications of thermochromic materials via different methods: A review. *Journal of Materials Science & Technology* **2018**, *34* (12), 2225-2234.
 14. Jaiswal, A. K.; Hokkanen, A.; Kumar, V.; Makela, T.; Harlin, A.; Orelma, H., Thermoresponsive Nanocellulose Films as an Optical Modulation Device: Proof-of-Concept. *ACS Applied Materials & Interfaces* **2021**, *13* (21), 25346-25356.
 15. Guo, X.; Kuang, D.; Zhu, Z.; Ding, Y.; Ge, L.; Wu, Z.; Du, B.; Liang, C.; Meng, G.; He, Y., Humidity Sensing by Graphitic Carbon Nitride Nanosheet/TiO₂ Nanoparticle/Ti₃C₂T_x Nanosheet Composites for Monitoring Respiration and Evaluating the Waxing of Fruits. *ACS Applied Nano Materials* **2021**, *4* (10), 11159-11167.
 16. Lin, J.; Fang, H.; Tan, X.; Sun, B.; Wang, Z.; Deng, H.; Liu, H.; Tang, Z.; Liao, G.; Shi, T., Ultrafast self-assembly MoS₂/Cu (OH) 2 nanowires for highly sensitive gamut humidity detection with an enhanced self-recovery ability. *ACS Applied Materials & Interfaces* **2019**, *11* (49), 46368-46378.
 17. Tsigara, A.; Mountrichas, G.; Gatsouli, K.; Nichelatti, A.; Pispas, S.; Madamopoulos, N.; Vainos, N. A.; Du, H.; Roubani-Kalantzopoulou, F., Hybrid polymer/cobalt chloride humidity sensors based on optical diffraction. *Sensors and Actuators B: Chemical* **2007**, *120* (2), 481-486.
 18. Zhang, D.; Luo, N.; Xue, Z.; Bai, Y.-L.; Xu, J., Effect of Open Metal Sites in Cobalt-Based Bimetallic Metal–Organic Framework Nanoparticles-Coated Quartz Crystal Microbalance (QCM) for Humidity Detection. *ACS Applied Nano Materials* **2022**.
 19. He, X.; Geng, W.; Zhang, B.; Jia, L.; Duan, L.; Zhang, Q., Ultrahigh humidity sensitivity of NaCl-added 3D mesoporous silica KIT-6 and its sensing mechanism. *RSC advances* **2016**, *6* (44), 38391-38398.

20. Zhang, S.; Geng, W.; He, X.; Tu, J.; Ma, M.; Duan, L.; Zhang, Q., Humidity sensing performance of mesoporous CoO (OH) synthesized via one-pot hydrothermal method. *Sensors and Actuators B: Chemical* **2019**, *280*, 46-53.
21. Hakkeem, H. M. A.; Babu, A.; Pal, S. K.; Mohamed, A. P.; Ghosh, S. K.; Pillai, S., Cellulose nanocrystals directed in-situ assembly of Au@ Ag nanostructures with multifunctional activities. *Microchemical Journal* **2021**, *168*, 106393.
22. Zhang, D.; Luo, N.; Xue, Z.; Bai, Y.-L.; Xu, J., Effect of Open Metal Sites in Cobalt-Based Bimetallic Metal–Organic Framework Nanoparticles-Coated Quartz Crystal Microbalance (QCM) for Humidity Detection. *ACS Applied Nano Materials* **2022**, *5* (2), 2147-2155.
23. Nabeela, K.; Thomas, R. T.; Nair, J. B.; Maiti, K. K.; Warriar, K. G. K.; Pillai, S., TEMPO-oxidized nanocellulose fiber-directed stable aqueous suspension of plasmonic flower-like silver nanoconstructs for ultra-trace detection of analytes. *ACS Applied Materials & Interfaces* **2016**, *8* (43), 29242-29251.
24. Zhou, Y.; Saito, T.; Bergström, L.; Isogai, A., Acid-free preparation of cellulose nanocrystals by TEMPO oxidation and subsequent cavitation. *Biomacromolecules* **2018**, *19* (2), 633-639.
25. Allen, T. C.; Cuculo, J. A., Cellulose derivatives containing carboxylic acid groups. *Journal of Polymer Science: Macromolecular Reviews* **1973**, *7* (1), 189-262.
26. (a) Bian, H.; Luo, J.; Wang, R.; Zhou, X.; Ni, S.; Shi, R.; Fang, G.; Dai, H., Recyclable and reusable maleic acid for efficient production of cellulose nanofibrils with stable performance. *ACS Sustainable Chemistry & Engineering* **2019**, *7* (24), 20022-20031; (b) Chen, L.; Zhu, J.; Baez, C.; Kitin, P.; Elder, T., Highly thermal-stable and functional cellulose nanocrystals and nanofibrils produced using fully recyclable organic acids. *Green Chemistry* **2016**, *18* (13), 3835-3843.
27. Yang, C. Q.; Wang, X., Formation of cyclic anhydride intermediates and esterification of cotton cellulose by multifunctional carboxylic acids: An infrared spectroscopy study. *Textile Research Journal* **1996**, *66* (9), 595-603.
28. Benkaddour, A.; Jradi, K.; Robert, S.; Daneault, C., Study of the effect of grafting method on surface polarity of tempo-oxidized nanocellulose using polycaprolactone as the modifying compound: Esterification versus click-chemistry. *Nanomaterials* **2013**, *3* (4), 638-654.
29. Petitto, S.; Langell, M., Surface composition and structure of Co₃O₄ (110) and the effect of impurity segregation. *Journal of Vacuum Science & Technology A: Vacuum, Surfaces, and Films* **2004**, *22* (4), 1690-1696.
30. Ashok, A.; Kumar, A.; Tarlochan, F., Surface alloying in silver-cobalt through a second wave solution combustion synthesis technique. *Nanomaterials* **2018**, *8* (8), 604.
31. Hakkeem, H. M. A.; Babu, A.; Shilpa, N.; Venugopal, A. A.; Mohamed, A.; Kurungot, S.; Pillai, S., Tailored synthesis of ultra-stable Au@ Pd nanoflowers with enhanced catalytic properties using cellulose nanocrystals. *Carbohydrate Polymers* **2022**, *292*, 119723.
32. Meng, Y.; Young, T. M.; Liu, P.; Contescu, C. I.; Huang, B.; Wang, S., Ultralight carbon aerogel from nanocellulose as a highly selective oil absorption material. *Cellulose* **2015**, *22* (1), 435-447.

33. Li, Y.; Tanna, V. A.; Zhou, Y.; Winter, H. H.; Watkins, J. J.; Carter, K. R., Nanocellulose aerogels inspired by frozen tofu. *ACS Sustainable Chemistry & Engineering* **2017**, *5* (8), 6387-6391.
34. Cervin, N. T.; Aulin, C.; Larsson, P. T.; Wågberg, L., Ultra porous nanocellulose aerogels as separation medium for mixtures of oil/water liquids. *Cellulose* **2012**, *19* (2), 401-410.
35. Jiang, F.; Hsieh, Y.-L., Cellulose nanofibril aerogels: synergistic improvement of hydrophobicity, strength, and thermal stability via cross-linking with diisocyanate. *ACS applied materials & interfaces* **2017**, *9* (3), 2825-2834.

CHAPTER 6

Summary and Future Perspectives

6.1. SUMMARY OF THE THESIS

Currently, we rely mostly on depleting petroleum-based resources with a higher carbon footprint. The use of alternate renewable resources and sustainable materials with manageable pollution side effects has to be steadily and effectively encouraged. Primarily, abundant natural lignocellulosic is a suitable alternative that we can focus on and convert to value-added products. The present dissertation focuses on the isolation of cellulose nanoforms from banana pseudo-stem fibers, an agricultural waste, and the development of different functional hybrids derived from it.

Chapter 1 briefly discusses the diverse forms of nanocellulose, including their abundant resources, systematic synthetic procedures, physicochemical properties, etc. Furthermore, as a sustainable and multifunctional material, applications of nanocellulose for the template-assisted synthesis of metal nanostructures and aerogels are described. This chapter provides a more fundamental knowledge of understanding pertaining the sustainable nanocellulose.

In **Chapter 2**, which serves as the core of the thesis, it is emphasized a simplified and energy-efficient approach to synthesize cellulose nanocrystals (CNC). Since the plant kingdom is diverse and hierarchical, the extraction of nanocellulose will be more unique to its origin. Our choice targeted banana pseudo-stem fibers as the source of nanocellulose, which will be produced in huge amounts in a tropical country like India, one of the world's largest banana growers. Fibers with linear cellulose chains are an excellent choice for the synthesis of CNC with ease of functionalization and low mechanical energy input. In addition, acid-free CNC was synthesized via TEMPO-mediated oxidation followed by ultrasonication as a post-mechanical treatment. Effect of ultrasonication time was studied for the CNC synthesis and physicochemical properties and compiled for high yield. The efficacy of banana pseudo-stem fibers was compared with areca nut leaf sheaths and mahogany hardwood which represent different plant parts for the preparation of CNC.

Chapter 3 describes the facile synthesis method for generating Au@Ag core-shell nanoparticles with interparticle distance controllable in ~ 1 nm. This chain-like coupled

Summary and Future perspectives

Au@Ag NPs were achieved by immobilizing Au seed by TEMPO-oxidized cellulose nanocrystals (TCNC), as-synthesized in the previous chapter, and then by tuning the Ag shell thickness. TCNC assumed to provide profound colloidal stability and shelf-life to the colloidal metal nanoparticles, as shown by the zeta potential value, -49.7 mV. Further, we investigated the optoelectronic properties of TCNC- Au@Ag NPs, especially in SERS, and 4-nitrophenol (4-NP) reduction. The thickness of Ag shell is tuned from 3.5 to 10 nm and investigated their SERS enhancement. Our research outcome clearly indicated that TCNC- Au@Ag NPs having ~ 8.5 nm Ag shell thickness exhibited the prime enhancement, which is several fold higher than citrate capped Au@Ag NPs. We also observed an exceptional SERS enhancement with TCNC- Au@Ag NPs in solid state that is 45-times higher than in solution state. This led us to understand the role of TCNC were not only simply the stabilization of the colloidal system but also acts as a nanoengineer that can tune the inter particle distance by immobilization and assembly formation in the solid state. Further, SERS sensitivity studies showed that TCNC- Au@Ag NPs (~ 8.5 nm) could detect pesticides like malachite green and methylene blue, a concentration down to 10 fM and 100 fM, respectively. The finite element modeling (FEM) studies were conducted to theoretically validate our experimental results. According to FEM studies, the enhanced electric field concentrates at the junction of two adjacent TCNC-Au@Ag NPs as the origin of augmentation in the SERS signals. Also, the theoretical estimated $EF \sim |E_4|$ is in agreement with the experimentally calculated EF (10^5). Finally, in catalytic application, TCNC-Au@Ag NPs showed superior catalytic activity towards 4-nitrophenol reduction with a rate constant of $32.33 \times 10^{-3} \text{ s}^{-1}$.

In **Chapter 4**, we explored the shape-directing and capping ability of TCNC in the synthesis of bimetallic Au@Pd core-shell nanoparticles, ensuring an eco-friendly approach. Interestingly, we could achieve anisotropic flower-like morphology with a spherical Au NPs core of ~ 14 nm size and small petal-like bunch of Pd NPs of ~ 5 nm. The evolution of flower-like morphology is endorsed by TCNC resulting from the carboxyl group of TCNC that binds selectively to Au NPs, and the free hydroxyl groups which serve as the binding sites for cluster-like small Pd NPs. Flower-like nanostructures of TCNC-Au@Pd were decorated on amino-functionalized graphene (NH_2 -RGO) without losing

their unique structure, allowing them to be deployed as an efficient, reusable, and green alternative heterogeneous catalyst. The feasibility of the bio-supported catalyst has been investigated in two concurrently prevalent model catalytic reactions, namely the oxygen reduction reaction (ORR) and the reduction of 4-nitrophenol, the best model reactions in fuel cell and industrial catalytic applications, respectively.

Finally, in **Chapter 5**, we have demonstrated a simple and efficient strategy for the fabrication of Co(II) coordinated nanocellulose aerogel that exhibits reversible thermochromism. Long and entangled cellulose nanofibers (TCNF) with low crystallinity were chosen by aiming towards a more stable aerogel structure instead short TCNC. TCNF were successfully prepared by changing the ultrasonication process discussed in chapter 2 by a mild homogenization. Successful coordination, crosslinking, and mechanical strength were attained by introducing malonic acid, an organic dicarboxylic acid, into the system. Developed Co(II) cation induced malonic acid/nanocellulose (CoMNC) aerogels exhibited a reversible thermochromism eloped from the change in coordination of Co(II) by interacting with moisture. This reversible property of CoMNC aerogels is utilized for the development of an android application which able to sense the humidity. This investigation proposes and foresee the extensive applicability of nanocellulose aerogels with organic carboxylic acids and diverse metal ions upon requirements.

6.2. FUTURE PERSPECTIVES

- More advancement in the nanocellulose synthesis with energy-saving strategies
- Pilot-scale synthesis of cellulose nanocrystals and fibers
- Nanocellulose capped different metal nanoparticles having extended shelf-life
- Utilization of nanocellulose bounded metal nanostructure for applications like energy harvesting, electronic devices, flexible electronics, healthcare, etc.
- Development of nanocellulose based sustainable membranes for air and water purification
- Fabrication and exploration of nanocellulose based composites in 4D printing, green H₂ production, and packaging materials, etc.

ABSTRACT

Name of the Student: Hasna M A

Registration No. :

10CC18J39005

Faculty of Study: Chemical Sciences

Year of Submission: 2023

AcSIR academic centre/CSIR Lab: CSIR-

Name of the Supervisor(s):

National Institute for Interdisciplinary Science
and Technology, Thiruvananthapuram

Dr. Saju Pillai

Title of the Thesis: Biomass-derived Cellulose Nanoforms and their Functional Hybrids

The present thesis focuses on the development of multifunctional hybrids based on nanocellulose, while emphasizing sustainability for various applications. The thesis is organized into six chapters, with the introduction serving as the first chapter. There are then four working chapters, and the final sixth chapter concludes with a summary and future perspectives. In Chapter 2, the efficient and energy-saving synthesis of cellulose nanocrystals from banana pseudo-stem fibers is discussed. This strategy also incorporates source comparison and yield optimization. The focus of Chapter 3 is on the carboxylated cellulose nanocrystal as a bio-template for assembling Au@Ag NPs with excellent colloidal stability and tailored plasmonic nanogaps for SERS-based ultra-trace level analyte detection. It also examines the theoretical validity of the nanocrystal's catalytic activity towards 4-NP reduction. Chapter 4 illustrates more insight into the shape-directing and stabilizing properties of TEMPO-oxidized cellulose nanocrystals for Au@Pd flower-like nanostructures towards catalysis. In Chapter 5, the potential for usage as a humidity sensor is discussed in relation to the development of reversible thermochromic Cobalt(II) coordinated malonic acid/nanocellulose hybrid aerogels.

LIST OF PUBLICATIONS

Emanating from thesis work

1. Cellulose nanocrystals directed in-situ assembly of Au@Ag nanostructures with multifunctional activities; **Hasna M. Abdul Hakkeem**, Aswathy Babu, Sudip Kumar Pal, A. Peer Mohamed., Sujit Kumar Ghosh, and Saju Pillai*, *Microchemical Journal*, 2021, 168, 106393.
2. Tailored synthesis of ultra-stable Au@Pd nanoflowers with enhanced catalytic properties using cellulose nanocrystals; **Hasna M. Abdul Hakkeem**, Aswathy Babu, Nagaraju Shilpa, Adithya A Venugopal, A. P. Mohamed, Sreekumar Kurungot, and Saju Pillai*, *Carbohydrate Polymers*, 2022, 292, 119723.
3. High performance Au nanorod as SERS substrates for environmental monitoring facilitated by the organizing power of nanocellulose from agave palm leaves, a biowaste; **Hasna M Abdul Hakkeem**, Aswathy Babu, Saju Pillai*, Sustainable Energy-Water-Environment Nexus in Deserts, *Springer Nature Applied Sciences*, 2022, 649-656.
4. Reversible thermochromic Cobalt(II) coordinated malonic acid/nanocellulose hybrid aerogels as a humidity sensor; **Hasna M. Abdul Hakkeem**, Ardra V.S., Adrija De, Aswathy Babu, M. Padmanabhan, and Saju Pillai* (Manuscript communicated).
5. Banana Pseudostem fibers as efficient and energy saving source for the acid free synthesis of cellulose nanocrystals; **Hasna M. Abdul Hakkeem**, Aswathy Babu, Kallayi Nabeela and Saju Pillai* (Manuscript under preparation).

Not related to thesis

1. A high-performance flexible triboelectric nanogenerator based on cellulose acetate nanofibers and micropatterned PDMS films as mechanical energy harvester and self-powered vibrational sensor; Harris Varghese, **Hasna M. Abdul Hakkeem**, Kanika Chauhan, Eshwar Thouti*, Saju Pillai* and Achu Chandran*, *Nano Energy*, 2022, 98, 107339.

2. Self-powered Flexible Triboelectric Touch Sensor with Micro-pyramidal PDMS Films and Cellulose Acetate Nanofibers; Harris Varghese, **Hasna M. Abdul Hakkeem**, Mohd Farman, Eshwar Thouti*, Saju Pillai* and Achu Chandran*, *Results in Engineering*, 2022, 16, 100550.
3. Highly luminescent, fast switching display device based on core-shell bimetallic nanoparticles/ ferroelectric liquid crystal composites; Abilash T K, **Hasna M. Abdul Hakkeem**, Saju Pillai* and Achu Chandran* (under revision in *Nanoscale*).
4. Zinc (II) coordinated cellulose nanofibrous metal organic frame works for antimicrobial coatings and fibers; **Hasna M. Abdul Hakkeem**, Velayudhanpillai Adarsh, Sukumaran RK, M. Padmanabhan* and Saju Pillai* (Manuscript under preparation).
5. Phthalate rich water soluble Zn(II) coordination polymers with unprecedented structural features, emission properties and semi-conductive behaviour; Sujesh Baby, **Hasna M. Abdul Hakkeem**, K. C. Joseph, Saju Pillai, and M. Padmanabhan* (Manuscript under preparation).
6. Flexible printed triboelectric nanogenerator of Boron nitride nanosheets-PVP composites against electrospun nanocellulose; Ainikulangara Sundaran Bhavya, **Hasna M. Abdul Hakkeem**, Saju Pillai, Achu Chandran*, and Kuzhichalil Peethambharan Surendran* (Manuscript under preparation).
7. Shape and Color Memory Effects and Associated Properties of PVA film by in-situ Polymerization of 2D Metal-Organic Compound; Aswathy Babu, Praveena P, **Hasna M. Abdul Hakkeem**, M. Padmanabhan* and Saju Pillai* (Manuscript under preparation).

LIST OF CONFERENCE PRESENTATIONS

1. **Hasna M. Abdul Hakkeem**, Reny Thankam Thomas, Parvathy R Chandran, Nabeela Kallayi and Saju Pillai, 'Nanocellulose: a versatile support for the growth of anisotropic metal nanostructures as SERS substrate for environmental monitoring', First Indian Materials Conclave and 30th AGM of MRSI, 2019 held at IISC Bengaluru, India (Poster presentation).
2. **Hasna M. Abdul Hakkeem**, Aswathy Babu and Saju Pillai, 'High-Performance Au Nanorods as SERS Substrates for Environmental Monitoring Facilitated by the Organizing Power of Nanocellulose from Agave Palm Leaves, a Bio-waste', 1st International Conference on Sustainable Energy-Water-Environment Nexus In Desert Climate, (QEERI IC-SEWEN'19), 2019 held at Qatar National Convention Centre, Hamad Bin Khalifa University, Doha, Qatar (Poster presentation).
3. **Hasna M. Abdul Hakkeem**, Aswathy Babu and Saju Pillai, 'TEMPO-oxidised nanocellulose fiber supported Au@Ag core-shell green platform for trace level detection of analytes by SERS', 14th International Conference on Ecomaterials (ICEM-14), 2020, held at CSIR-NIIST, Thiruvananthapuram, India (Poster presentation).
4. **Hasna M. Abdul Hakkeem**, Aswathy Babu and Saju Pillai, 'TEMPO-oxidised nanocellulose fiber supported Au@Ag core-shell scaffolds for ultra-trace level detection of analytes', 2nd Indian Materials Conclave and 31st AGM of MRSI, 2020, held at CSIR-CGCRI, Kolkata, India (Poster presentation).
5. **Hasna M. Abdul Hakkeem**, Aswathy Babu and Saju Pillai, 'Necklace-like Assembly of Au@Ag Core-shell Nanostructures on Cellulose Nanocrystals with Tailored Plasmonic Nanogaps', Recent Advances in Physics of Materials (RAPM-2021) held at CSIR-NIIST, Thiruvananthapuram, India (Poster presentation).
6. **Hasna M. Abdul Hakkeem**, Nagaraju Shilpa, Sreekumar Kurungot, Saju Pillai, 'Decisive Role of TEMPO-Oxidized Cellulose Nanocrystals as Structure Directing Agent for Ultra-Stable Au@Pd Nanoflowers with Enhanced Catalytic Properties', Advances in Materials & Processing: Challenges & Opportunities (AMPCO-2022), held at IIT Roorkee, India (Oral presentation).



Cellulose nanocrystals directed in-situ assembly of Au@Ag nanostructures with multifunctional activities

Hasna M. Abdul Hakkeem^{a,b,1}, Aswathy Babu^{a,1}, Sudip Kumar Pal^c, A. Peer Mohamed^a,
Sujit Kumar Ghosh^c, Saju Pillai^{a,b,*}

^a Materials Science and Technology Division, CSIR-National Institute for Interdisciplinary Science and Technology (CSIR-NIIST), Thiruvananthapuram 695 019, Kerala, India

^b Academy of Scientific and Innovative Research (AcSIR), Ghaziabad 201 002, Uttar Pradesh, India

^c Department of Chemistry, Assam University, Silchar 788 011, Assam, India

ARTICLE INFO

Keywords:

Au@Ag core-shell nanostructures
TEMPO-oxidised cellulose nanocrystal (TCNC)
Nano-assemblies
Bio-template
Plasmonic hotspots
FEM simulation

ABSTRACT

Bio-template-directed synthesis of shell-engineered plasmonic nano-assemblies has attracted extensive research interest due to their profound opto-electronic properties. Herein, we report TEMPO-oxidized cellulose nanocrystals (TCNC) as a promising bio-template for the in-situ preparation and assembly of Au_{core}-Ag_{shell} nanoparticles (Au@Ag NPs) having excellent colloidal stability with tunable optical and catalytic properties. By modulating Ag shell thickness, TCNC promoted the assembly of Au@Ag nanostructures and resulted in abundant plasmonic hotspots. Thereby as-formed TCNC payloads could enhance its solid-state SERS activity in detecting malachite green and methylene blue concentration down to 10 fM and 100 fM, respectively. The finite element modelling (FEM) studies further supported the observed results, revealing the enhanced electric field concentrates at the junction of two adjacent TCNC-Au@Ag NPs as the origin of augmentation in the SERS signals. Further, TCNC-Au@Ag NPs assemblies showed superior catalytic activity towards 4-nitrophenol reduction with a rate constant of $32.33 \times 10^{-3} \text{ s}^{-1}$.

1. Introduction

Morphology-dependent plasmonic features of gold and silver nanoparticles empower them to fit interdisciplinary areas such as SERS [1], catalysis [2], sensing [3], and biomedicine [4,5], etc. Due to their excellent optoelectronic properties, bimetallic Au-Ag nanostructures have attracted much attention in recent years. These properties result from the bifunctional or synergic electronic effects dissimilar from their monometallic counterparts [6]. The fact that surface-enhanced Raman scattering (SERS) is highly reliant on the morphology of nanostructures, extensive studies were carried out to optimize nanoparticle size, shape, and composition to achieve high SERS enhancement. Among the several bimetallic nanostructures, Au@Ag core-shell NPs with higher chemical stability, tunable plasmonic properties, and excellent electromagnetic enhancement in the visible region is widely used in the field of SERS [7]. Besides, when these plasmonic core-shell nanostructures are positioned adjacent to each other to form organized assemblies, the coupling of

localized surface plasmon resonances of individual core-shell nanoparticles will occur. It brings exceptionally high electric field enhancements at the junctions of nanoparticles [8,9]. It is being established that the SERS activity relies heavily on the electromagnetic (EM) field enhancement generated at the nanogap junctions between the plasmonic nanostructures [10,11].

Despite the SERS application of bimetallic Au-Ag NPs, it is known that the Au@Ag systems having a variable surface composition and particle size will modify the overall electronic and ensemble effects of its catalytic property [6]. Results have shown that the diameter of the core and thickness of the shell play a prominent part in the catalytic efficiencies as well as SERS properties of Au@Ag NPs [12]. The efficacy of Au-Ag bimetallic nanoparticles in various catalytic applications has been investigated in quite a few studies [12,13]. However, the greater tendency of nanostructures towards agglomeration may significantly deteriorate their plasmonic properties and catalytic activity [14]. Plasmonic nanostructures with long shelf-life which hold their plasmonic

* Corresponding author at: Materials Science and Technology Division, CSIR-National Institute for Interdisciplinary Science and Technology (CSIR-NIIST), Thiruvananthapuram 695 019, Kerala, India.

E-mail address: pillai_saju@niist.res.in (S. Pillai).

¹ Equal contribution.

<https://doi.org/10.1016/j.microc.2021.106393>

Received 8 March 2021; Received in revised form 20 April 2021; Accepted 10 May 2021

Available online 13 May 2021

0026-265X/© 2021 Elsevier B.V. All rights reserved.

properties and high surface area are essential for catalytic activity. Even though some progress was made in the area of spherically shaped Au@Ag NPs, controlled growth of nanostructures with stability, uniformity in size, and morphology remains a challenge. Further, the use of shape directing surfactants such as CTAB, CTAC, PVP, etc., may reduce the catalytic or SERS activities of nanostructures since they avert the adsorption of target molecules on the nanoparticle surface [15]. Hence, for any practical application, an efficient SERS substrate is required to have i) superior stability, ii) a large number of hotspots to ensure ultrahigh sensitivity, iii) uniform dissemination of the hotspots to achieve better reproducibility of the signal, and iv) fabrication method should be easy and eco-friendly. On the other hand, for catalytic applications, high surface area, optimum size, and stability of nanostructures are relevant.

In this context, nanocellulosic materials are emerging as a promising sustainable biomaterial for the in-situ synthesis of plasmonic nanostructures. TEMPO-oxidized cellulose nanofiber with high-densities of carboxylate groups on the surface offers an anchor site for the metal nanoparticles. Apart from nanocellulose fibers produced by TEMPO-oxidation followed by homogenization, TEMPO-oxidised cellulose nanocrystals (TCNC) were recently proposed by Isogai *et al.* with spindle-like morphology (low aspect ratio) by replacing homogenization with ultra-sonication [16]. The higher surface area, a greater yield of anionic group (carboxylic), and good water dispersibility enable TCNC as the right option for minimizing the amount of the materials needed for surface-mediated nanoparticle synthesis [17–20]. There have been several reports dealing with cellulose nanocrystals (CNC) to prepare metallic nanoparticles; limited studies have been reported for the synthesis of bimetallic Au-Ag nanostructures [21]. Recently, Asgari *et al.* prepared Au@Ag/cellulose nanofibers (CNF) nanocomposite by simply mixing CNF suspension with Au@Ag nanoparticles in an equimolar ratio for SERS applications [22]. In another report, Gopiraman *et al.* utilized CNF produced by electrospinning of cellulose acetate to prepare bimetallic Ag@Au nanocomposites for catalytic application [23]. However, none of these studies has investigated the utility of CNF or CNC for the in-situ preparation of Au@Ag NPs due to the complexity in achieving control over the morphology in the nanocellulose matrix. The advantage of in-situ synthesis of core-shell nanoparticles on TCNC bio-template would be the control over the assembly of plasmonic nanostructures, which allows for maximum SERS enhancement.

In this perspective, we report a facile bio-supported method for the in-situ preparation and assembly of Au@Ag core-shell NPs on carboxylated cellulose nanocrystals and demonstrated its dual role as a susceptible SERS platform and catalytic support. The synthesis procedure relies on the controlled reduction of Ag(I) ions over TCNC stabilized Au NPs through a seed-mediated method, resulting in Au@Ag nanostructures with tunable optical properties. Subsequently, the resultant Au@Ag nanostructures are effectively assigned as a substrate for the trace-level SERS detection of two carcinogenic adulterant dyes: malachite green and methylene blue, widely used as colorants and biocides in the aquaculture industry. Furthermore, the catalytic properties of optimized TCNC-Au@Ag nano-assemblies are studied kinetically following the reduction of 4-nitrophenol as a typical catalytic reduction reaction. This report would also bring new insights into the various functions of TCNC, such as (1) environmentally benign template for the synthesis of Au@Ag NPs with excellent colloidal stability and longer shelf-life, (2) astounding enhancement in SERS, especially in solid-state, and (3) superior catalytic performance. To the best of our knowledge, this is the first report on using TCNC as a bio-template for the in-situ synthesis and controlled assembly of Au@Ag NPs having high-density hotspot junctions.

2. Materials and methods

2.1. Chemicals

For the preparation of TEMPO-oxidized cellulose nanocrystals,

chemically extracted banana pseudo-stem fibers were used. Sodium chlorite (NaClO_2), sodium hypochlorite (NaClO), sodium hydroxide (NaOH), 2,2,6,6-tetramethyl piperidine-1-oxyl radical (TEMPO; $\text{C}_9\text{H}_{18}\text{NO}$), sodium bromide (NaBr), aurochloric acid ($\text{HAuCl}_4 \cdot 2\text{H}_2\text{O}$), trisodium citrate tribasic dihydrate (TSC; $\text{C}_6\text{H}_5\text{Na}_3\text{O}_7 \cdot 2\text{H}_2\text{O}$), silver nitrate (AgNO_3), L-ascorbic acid ($\text{C}_6\text{H}_8\text{O}_6$), malachite green (MG; $\text{C}_{23}\text{H}_{25}\text{N}_2$), methylene blue (MB; $\text{C}_{16}\text{H}_{18}\text{ClN}_3\text{S} \cdot 3\text{H}_2\text{O}$), 4-nitrophenol (4-NP; $\text{C}_6\text{H}_5\text{NO}_3$) and sodium borohydride (NaBH_4) and were bought from Sigma-Aldrich, India. Ultrapure deionized (DI) water (Milli-Q purifier system, Merck, Germany) was utilized throughout the synthesis.

2.2. Extraction of holocellulose

The ultimate strategy for extracting holocellulose by abolishing both lignin and hemicellulose content explained in literature has been slightly modified as adequate as starting material. Banana pseudo-stem fibers were initially pre-treated with excess NaOH during the extraction process. Subsequently, bleaching was done at a minimum of two times with 1.7 wt% NaClO_2 at pH 4 at 150°C until the biomass turned as a white cotton-like substance. The obtained holocellulose was washed thoroughly with DI water, dried, and kept for further experiments.

2.3. Preparation of TEMPO-oxidised cellulose nanocrystals (TCNC)

TEMPO-oxidation was performed by the procedure put forward by Isogai and co-workers [24,25]. Concisely, a catalytic quantity of TEMPO (0.032 g) was accurately weighed and dissolved in DI water by stirring for 5 min in a 500 mL flat bottom flask. Then 0.32 g of NaBr and 1.00 g of holocellulose were added, and the water content was increased to 270 mL by adding additional DI water. The oxidation process was initiated by adding a 30 mL ice-cooled NaClO solution at pH 10–11 range. Due to the presence of excess NaOH in the holocellulose, further addition of NaOH was not needed. The reaction was conducted for 1 h. During the reaction, regioselective conversion of carbon-6 (C6) hydroxyl to carboxyl group as monitored from the way of consumption of NaOH or pH measured at regular 5 min intervals. After the completion of oxidation, the whole system was ultra-sonicated for 2 h. After 2 h of ultra-sonication, the oxidation process was quenched by adding 5 mL of ethanol. The final product was separated by washing and followed by freeze-drying.

2.4. Synthesis of TCNC capped Au NPs seed (TCNC-Au NPs)

TCNC initiated the synthesis of Au seed solution, and the reduction process was augmented with the addition of trisodium citrate (TSC). Briefly, 750 μL of 0.01 M HAuCl_4 was gradually added to 60 mL aqueous solution of 0.1 wt% TCNC taken in a 250 mL conical flask followed by heating up to 100°C with continuous magnetic stirring. When the boiling was started, 1 mL of 1 wt% of citrate was added and heated for an extra 20 min. Upon boiling, the colorless solution gradually converted to purple, giving TCNC capped Au seed solution. The resulting solution had been cooled at room temperature and preserved at 5°C for further use to synthesize Au@Ag NPs. Further, to analyze the effect of TCNC, the synthesis was performed with different wt% of TCNC while keeping all other reagent concentrations constant. Henceforth, Au seeds of different sizes have been synthesized by varying the wt% of TCNC solution, ranging from 0.05 to 0.25 wt%.

2.5. Synthesis of TCNC stabilized Au@Ag NPs (TCNC-Au@Ag NPs)

TCNC stabilized Au@Ag NPs have been synthesized by employing a modified seed-mediated approach [26]. In brief, 150 μL of 0.01 M aqueous ascorbic acid solution (AA) was added to 3 mL TCNC capped Au NPs seed solution and magnetically stirred for 2 min. An equivalent volume (150 μL) of a 0.01 M AgNO_3 solution was added dropwise with vigorous stirring to this reaction mixture. Subsequently, the color of the

solution slowly shifted from purple to yellowish-orange within 10 min of magnetic stirring. The quantity of AA and AgNO₃ varied from 60 to 210 μ L, leads to the production of TCNC-Au@Ag NPs with various Ag shell thicknesses. The samples were stored at 5 °C in amber-colored storage bottles. For comparison, the standard Turkevich method adapted citrate stabilized Au, and Au@Ag NPs were synthesized [27]. Except for trisodium citrate, all other reaction parameters were kept constant for evaluating the role of TSC as a reducing and capping agent.

2.6. SERS sample preparation

Samples for SERS were prepared by mixing analytes and substrate colloids (without increasing the concentration by centrifugation) in a 1:3 (v/v) ratio one day before the measurement. For solution-phase measurements, 10 μ L samples were pipetted out on a pre-cleaned glass slide (cleaned by washing with chromic acid, sonicating in ethanol, acetone afterward accompanied by UV-Ozone treatment for 10 min) at the time of measurement. In the case of solid-state measurements, drops on a glass slide were dried under vacuum in a desiccator. Especially for SERS spectra in solid-state, Raman signals were captured from a minimum of five different positions and all repeated at least three times.

2.7. Catalytic studies with 4-nitrophenol (4-NP)

4 mL freshly prepared 15 mM NaBH₄ solution is well mixed with 80 μ L 4-NP solution (10 mM) in a quartz cuvette. A specific amount of TCNC-Au@Ag NPs colloid was added to the above and mixed well [23]. The reduction reaction is detected by a gradual change in color of 4-NP from yellow to colorless and was analyzed spectrometrically at a regular interval of time. Time-dependent UV-Vis absorption analysis was done until the completion of the reaction indicated by the absence of an absorption peak at 400 nm.

2.8. Characterization

The FEI-Tecnaï 30 G2S-TWIN transmission electron microscope (300 kV) is being used to obtain transmission electron microscopy (TEM) images of TCNC-Au NPs, TCNC-Au@Ag NPs, and related selected area electron diffraction (SAED). Atomic force microscopy (AFM) images of TCNC were collected through a Multimode 8 atomic force microscope linked to a Nanoscope V controller (Bruker, Santa Barbara, CA). Si cantilevers, with a 10 nm radius of curvature, were worked at a scan rate of 1 Hz in tapping mode (NSG 01, NT-MDT). The resonance frequencies ranged from 120 to 180 kHz, and the force constant of the AFM probe ranged from 2.5 to 10 N/m. Scan size from 10 \times 10 μ m² to 800 \times 800 nm² at 512 \times 512 pixel resolution were recorded. Using UV-Visible spectrophotometer (Shimadzu UV-2700, Shimadzu, Japan), the plasmonic properties of colloids of nanoparticles and catalytic reduction of 4-NP were monitored (spectral range of 200–700 nm; using 1 cm path length quartz cell). In the 4000–500 cm⁻¹ wavenumber region, the Fourier transform infrared (FTIR) spectra were acquired by PerkinElmer FTIR spectrometer. Powder X-ray diffraction (XRD) pattern of the TCNC, TCNC-Au, and TCNC-Au@Ag samples were taken using PANalytical X'pert pro equipped with Cu K α (λ = 1.54 Å), 45 kV.

X-ray photoelectron spectroscopic (XPS) studies were conducted using PHI 5000 VersaProbe II, ULVAC-PHI Inc., USA. Samples were prepared by concentrating colloidal samples on a pre-cleaned glass slide using an O-ring. Using Zetasizer Nano ZS, Malvern equipment, dynamic light scattering (DLS) study was conducted towards the particle size and zeta potential analysis. The elemental composition of Au and Ag has been measured via inductively coupled plasma mass spectrometry (ICP-MS) by Thermo Scientific iCAP-RQ. The carboxyl content of TCNC was experimentally estimated using conductometric titration. Surface-enhanced Raman scattering (SERS) analysis was done with a 20X objective Raman microscope (WITec, Inc. alpha 300R Germany) armed with Peltier-cooled charge-coupled detector; 600 g/mm grating; 633 nm

laser with a resolution of 1 cm⁻¹; integration time of 2 s; 5 accumulations in the range of 0–3000 cm⁻¹.

3. Results and discussion

3.1. Structural and morphological analysis of TCNCs

As described in the experimental section, carboxyl functionalized cellulose nanocrystals were obtained from banana pseudo-stem fibers via TEMPO-oxidation followed ultra-sonication. TEMPO is a water-soluble stable nitroxyl radical used as a catalyst to convert alcoholic hydroxyl groups to carboxyl acid under mild conditions. The absence of peaks at 1242 cm⁻¹, 1500 cm⁻¹, and 1700 cm⁻¹ in the FT-IR spectra of holocellulose fibers (Fig. 1a) confirmed that the pretreatment and bleaching processes could remove lignin and hemicellulose contents from the fiber [28]. The introduction of carboxyl functional groups by the regioselective oxidization of C6 primary hydroxyl group is evident from the intense peak at 1616 cm⁻¹ [29]. The absolute solubility of TCNC in aqueous solution imparted by the anionic carboxyl groups renders TCNC aqueous suspension highly stable, as revealed by the zeta potential value, -50.2 mV (Table S1). WAXS pattern (Fig. S1) of hollow cellulose and TCNC confirmed the modification of cellulose I to cellulose II phase by mercerization as indicated by three peaks at 2θ = 12.5°, 20.7°, and 22.1° that are indexed as (1 $\bar{1}$ 0), (110) and (200) planes of cellulose II [30].

The morphological characteristics of TCNC were studied using AFM (Fig. 1b). The AFM height image shows the formation of spindle-like morphology of TCNC, which differs to that of cellulose nanofibers and nanonetworks having a high aspect ratio [16]. The AFM height profile suggested TCNC having length, 150–200 nm and width, 15 \pm 2 nm. The carboxyl content of TCNC is estimated to be 1.23 mmol/g using conductometric titration [30].

3.2. TCNC templated synthesis of Au and Au@Ag NPs

Scheme 1 depicts the preparation of TCNC stabilized Au and Au@Ag nanostructures. Our synthetic approach relies on the convergence of two concepts: initially, TCNC templated synthesis of Au NPs as the core of the nanostructure on to which the growth of Ag shell occurs; secondly, the sequential variation of Ag ion concentration in the reaction mixture during synthesis. Initially, the size of the Au core formed was regulated by varying wt% of TCNC from 0.05 to 0.1, 0.15, 0.2, and 0.25 wt%, and all other reaction parameters were kept constant (Fig. S2). It is found that the wt% TCNC plays a critical role in the size distribution and morphology of resulting Au NPs. The carboxyl groups in TCNC offer reduction sites for Au³⁺ ion and provides nucleation sites for the newly formed Au monomers [31]. The reduction of Au precursor to Au NPs is facilitated by the combined reducing action of TCNC and citrate. Meanwhile, the TCNC network in aqueous media provides more steric stabilization to the resulting Au NPs by significantly preventing the fusion of Au NPs formed on the TCNC templates [32]. Such interaction promotes the creation of adjacent and tightly packed assembly of Au NPs in the TCNC matrix.

Due to the highly spherical morphology and monodispersed nature, 0.1 wt% TCNC stabilized Au NPs were chosen as an optimized seed system for the subsequent Ag shell growth. The as-prepared TCNC-Au NPs seed possesses a diameter of 25.0 \pm 5 nm and a surface plasmon resonance band at 524 nm (Fig. S3 and Fig. S2a). Additionally, the TCNC-Au colloid exhibited high stability not less than 8 months, as evident from the minor changes in the UV-vis absorption band (Fig. S4). It did not show any signs of aggregation and flocculation (Table S1) revealed by its high zeta potential value, -45.0 mV. Fig. 2a depicted a typical HR-TEM image of TCNC-Au@Ag NPs obtained with Au core size of 25.0 \pm 5 nm and Ag shell thickness around 3.5 nm. It has been proved that due to the fine match of both Ag and Au elements lattice constants,

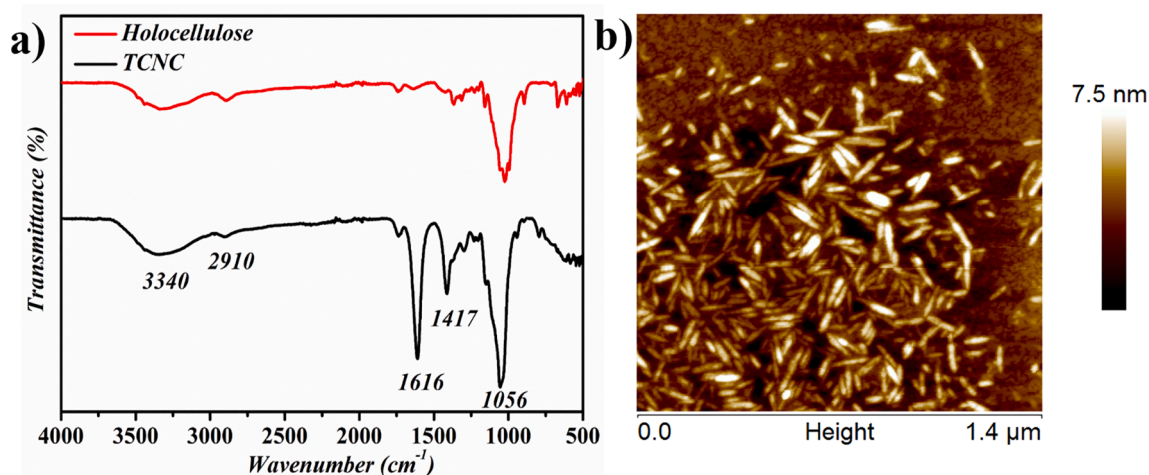
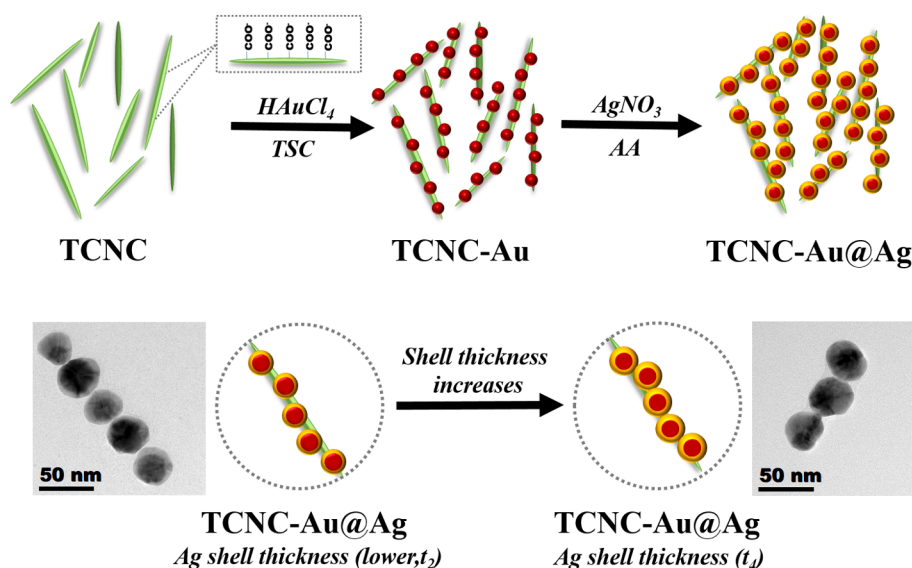


Fig. 1. (a) The FTIR spectra and (b) AFM image of TEMPO-oxidized cellulose nanocrystals (TCNC).



Scheme 1. The preparation procedure of TCNC stabilized Au@Ag nanostructures.

Ag can selectively adsorb and grown over the Au seeds to form the core-shell nanostructure [33]. However, the two components of the core-shell nanostructure can easily be distinguished by the contrast difference between Au (dark) and Ag (bright) due to the difference in electron density [34]. Further, HR-TEM and the FFT spot pattern (Fig. 2b) show that the Ag (0) formed typically along the direction of the Au (111) plane.

The XRD spectra were recorded for validation of Ag nanoshell growth over TCNC templated Au seed. XRD pattern of TCNC-Au NPs exhibited (Fig. S2b) four specific diffraction peaks at 38.42° , 44.39° , 64.93° , and 77.89° , respectively indexing the planes (111), (200), (220) and (311) of the cubic face-centered Au accompanied by a weak-intensity peak at 81.81° , indexed as (222) plane (JCPDS no. 00-004-0784). Meanwhile, the XRD pattern of TCNC-Au@Ag NPs (Fig. 2c) showed peaks at 38.9° , 44.9° , 65.3° , 78.2° , and 82.2° indicative of (111), (200), (220), (311) and (222) diffraction planes of FCC structure of Ag, respectively (JCPDS no. 00-004-0783). The diffraction patterns of both Au and Au@Ag NPs are almost identical, as Au and Ag possess comparable lattice parameters [34]. Nevertheless, the XRD patterns displayed sharper characteristic peaks for TCNC-Au@Ag NPs than that of TCNC-Au NPs, indicating Ag shell growth over Au seed surface with high crystallinity.

To elucidate the chemical composition and oxidation states of core-shell nanostructures, XPS study have been conducted. The XPS narrow scans of Au 4f core-level of TCNC-Au NPs (Fig. S5) showed two peaks due to spin-orbit splitting at binding energies (BEs) 83.4 eV (Au 4f_{7/2}) and 87.1 eV (Au 4f_{5/2}) with an energy difference of 3.7 eV inferring zero-valent state of Au NPs. In the case of TCNC-Au@Ag NPs, the narrow scan of Ag 3d core-level shows two distinct peaks due to spin-orbit splitting at BEs 367.4 eV (Ag 3d_{5/2}), and 373.4 eV (Ag 3d_{3/2}) with 6 eV difference confirms the formation of metallic Ag (Fig. 3a) [35]. Additionally, the narrow scan of Au 4f core-level exhibited two peaks at 83.8 eV (Au 4f_{7/2}) and 87.5 eV (Au 4f_{5/2}) (Fig. 3b). The relative peak intensity of bulk Au 4f spectrum gets suppressed compared to Au seed, which further authenticates the formation of core-shell nanostructures. Further, the carboxyl functionalization of cellulose nanocrystal (TCNC) was also investigated using XPS. The XPS survey spectrum shows carbon and oxygen as major elements with an O/C ratio of 0.77 which indicate the presence of TCNC template in our system. Fig. 3c presented the narrow scan of C1s of TCNC with deconvoluted peaks at 284.8, 285.9, 288, and 289.1 eV, assigned to the BEs of C-C/C-H, C-O, O-C-O/C=O, and O-C=O, respectively, which are the main chemical states of carboxyl functionalized cellulose [36]. The deconvoluted spectrum of O1s (Fig. 3d) revealed two peaks at 532.2 eV and 530.7 eV matching to O-C and O-C-

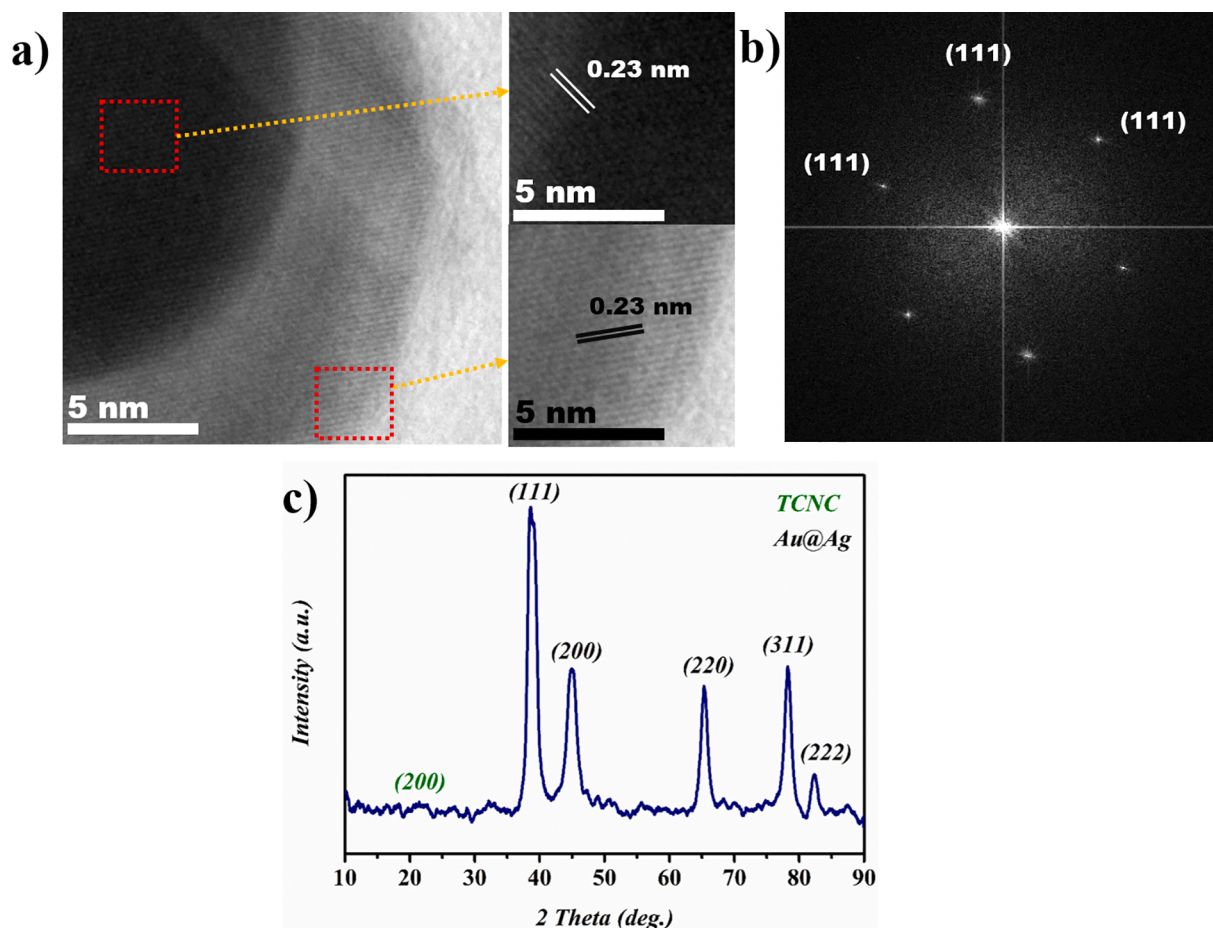


Fig. 2. (a) HR-TEM image of TCNC-Au@Ag nanostructures (average Ag shell thickness- 3.5 nm); inset shows the magnified images of red marked area; (b) FFT spot pattern of TCNC-Au@Ag nanostructures enclosed by (111) facets; (c) XRD pattern.

O/O=C also infer the existence of TCNC as the backbone of Au@Ag NPs [37].

3.3. Shell thickness-dependent optical and morphological properties of TCNC-Au@Ag nanostructures

TCNC-Au@Ag nanostructures with diverse shell thickness were prepared by adding different quantities of silver nitrate and ascorbic acid in equal volumes to TCNC-Au seed (25.0 ± 5 nm) colloids. The as-prepared TCNC-Au@Ag colloid exhibited a zeta potential value of -49.7 mV, indicating excellent stability and longer shelf-life (Fig. S6) required for various biomedical applications. Fig. 4a showed the UV-Visible absorption spectra of TCNC-Au@Ag colloids prepared with different amounts of Ag precursor and ascorbic acid (from 60, 90, 110, 150, and 210 μ L). After adding AgNO₃ solution, the resultant Au@Ag nanostructures displayed two plasmonic bands; one at 390 nm (Ag shell) and the other at 520 nm (Au core), which specifies the partial coverage of Au core by Ag NPs. With the gradual increase of Ag precursor volume, an increase in the plasmonic absorption intensity of the Ag part along with the typical redshift in plasmon absorption from 390 nm to 420 nm was observed. The steady reduction of the LSPR band of Au core and the prevalence of Ag band implies that the Ag salt reduction takes place on the previously formed Au core surface instead of creating additional nucleation sites.

Further, Fig. 4b and Fig. 5 demonstrate the TEM images of TCNC-Au@Ag nanostructures with varying shell thickness (t). With the increase of Ag precursor volume, a gradual upsurge in the Ag shell thickness from ~ 3.5 nm (t_1) to 5 (t_2), 7.5 (t_3), 8.5 (t_4), and 10 nm (t_5) can be observed with a subsequent rise in the total diameter of

nanoparticles from 28.5 ± 2 nm to 35.5 ± 2 nm. Further, a gradual reduction in the interparticle distance can be seen with an increase in shell thickness, offering numerous plasmonic hotspot junctions. Interestingly, highly cross-linked Au@Ag nanostructure assemblies were obtained onto TCNC templates with an Ag shell thickness of ~ 8.5 nm (t_4) (Fig. 5d-e). This morphological change of isolated Au@Ag NPs into necklace-like nanoassemblies could be well correlated with the gradual redshift of Ag plasmon band arises due to the interparticle coupling between adjacent core-shell nanoparticles. However, at higher shell thickness (~ 10 nm), the ordered arrangements were found to be slightly disrupted due to the formation of larger sized Au@Ag nanostructures on TCNC templates.

Subsequently, to get more insight into the role of TCNC in morphological transformation, we repeated the experiments with a higher wt% of TCNC (0.25 wt%) for preparing Au@Ag NPs. Interestingly, larger Au@Ag NPs were found with irregular morphology (Fig. S7) instead of forming spherical nanostructures. This could be ascribed to the presence of more nucleation sites offered by a higher amount of TCNC, and different reaction kinetics followed. These results imply that the formation of discrete and close-packed core-shell nanostructures could be efficiently tailored by altering the Ag shell thickness and wt% of TCNC.

From the above observations, we could infer that TCNC acted as a template introducing a new transformation to Au@Ag NPs in both properties and structural aspects. We highlight TCNC as a soft-template for constructing ordered assemblies of Au@Ag nanostructures by tuning the shell thickness. With an optimized TCNC content and Ag shell thickness, the interparticle coupling between core-shell NPs enabled the formation of ordered assemblies of Au@Ag over TCNC instead of forming bulk agglomerates. Therefore, our study can offer a versatile

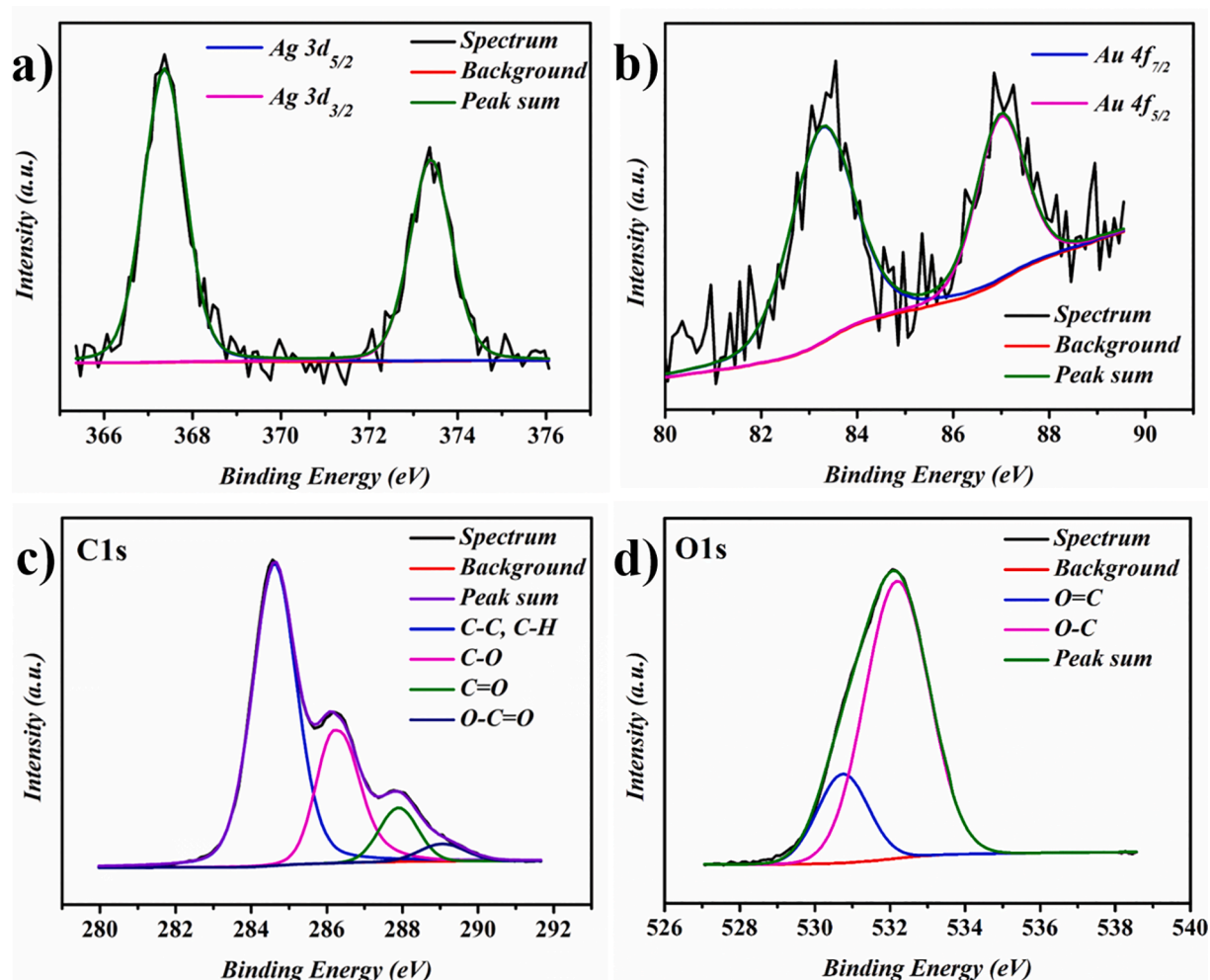


Fig. 3. XPS narrow scans corresponding to (a) Ag 3d; (b) Au 4f; (c) C 1s and (d) O 1s for TCNC-Au@Ag nanostructures.

method that introduces TCNC as a plasmonic engineer and shape directing template to prepare the discrete spherical Au@Ag NPs with diverse shell thicknesses and the coupled Au@Ag nanostructures with numerous plasmonic nanogaps.

3.4. SERS response of assembled Au@Ag nanostructures on TCNC templates

The plasmonic effect of TCNC-Au@Ag nanostructures in SERS enhancement was first evaluated using a cationic dye malachite green (MG), an antifungal and antiparasitic compound widely used in aquaculture, as the Raman probe molecule. TCNC templated Au@Ag nano assemblies offers numerous hotspots, which take a significant share in amplifying electromagnetic field compared to isolated nanoparticles. Moreover, the positively charged MG dye would readily get adsorbed on the surface of negatively charged TCNC via electrostatic interaction, which further contributes to SERS enhancement. Hence, the SERS spectra of MG recorded at least from five random spots of dried TCNC-Au@Ag substrate with different Ag shell thickness, ~ 3.5 nm to ~ 10 nm (t_1 – t_5), and are shown in Fig. 6a.

The significant bands at 1617, 1368, 1174, 918, and 445 cm^{-1} can be attributed to the in-plane stretching of the ring-C-C, N-phenyl stretching, N-C stretching vibration coupled with the C-C and C-H in-plane motions at 1394 cm^{-1} , aromatic C-H in-plane bending vibrations, ring skeletal vibrations of the phenyl-C modes of MG [38]. The peak at 1617 cm^{-1} was used to assess the enhancement in Raman signal intensity, and the bar diagram (Fig. 6b) shows relative intensity. With shell thickness

rising from ~ 3.5 to 10 nm, SERS intensity of MG adsorbed on TCNC-Au@Ag nanostructures underwent a gradual increase and reached a maximum of 8.5 nm. However, further increase of the Ag shell thickness caused a decrease of Raman signal intensity since the LSPR properties of Au core became masked at higher Ag shell thickness (>8.5 nm) [26]. This is because the incident light penetrates through the Ag shell only up to a specific thickness [39]. All these experimental outcomes are in line with the results published for nanoparticles and nanocubes of Au@Ag [40,41].

The analytical enhancement factor (AEF) for different shell thickness is calculated based on the specific equation,

$$\text{AEF} = \frac{I_{\text{SERS}}}{I_{\text{RAMAN}}} \times \frac{C_{\text{RAMAN}}}{C_{\text{SERS}}}$$

where I_{SERS} is the intensity of sample with concentration C_{SERS} in the presence of metal nanoparticles as a substrate, while I_{RAMAN} and C_{RAMAN} are in the absence of nanoparticle substrate [42]. Focused on the intense peak of MG at 1617 cm^{-1} , AEFs for different TCNC-Au@Ag NPs were estimated to be 2.01×10^5 , 3.3×10^5 , 3.61×10^5 , 4.03×10^5 , 6.85×10^5 , and 5.08×10^5 for t_0 , t_1 , t_2 , t_3 , t_4 , and t_5 , respectively. Accordingly, in the present study, it is assumed that when the mean Ag shell thickness exceeds 8.5 nm (t_4), the excitation of Au core electrons will be difficult, resulting in lesser SERS. Also, the TCNC-Au@Ag nanostructures become unstable when the Ag shell, coated over the surface of Au NPs was too thick [26]. Hence, considering that the SERS behavior and stability, the TCNC-Au@Ag (t_4) nanostructures with ~ 8.5 nm Ag shell thickness have been chosen as the optimized SERS substrate for further studies.

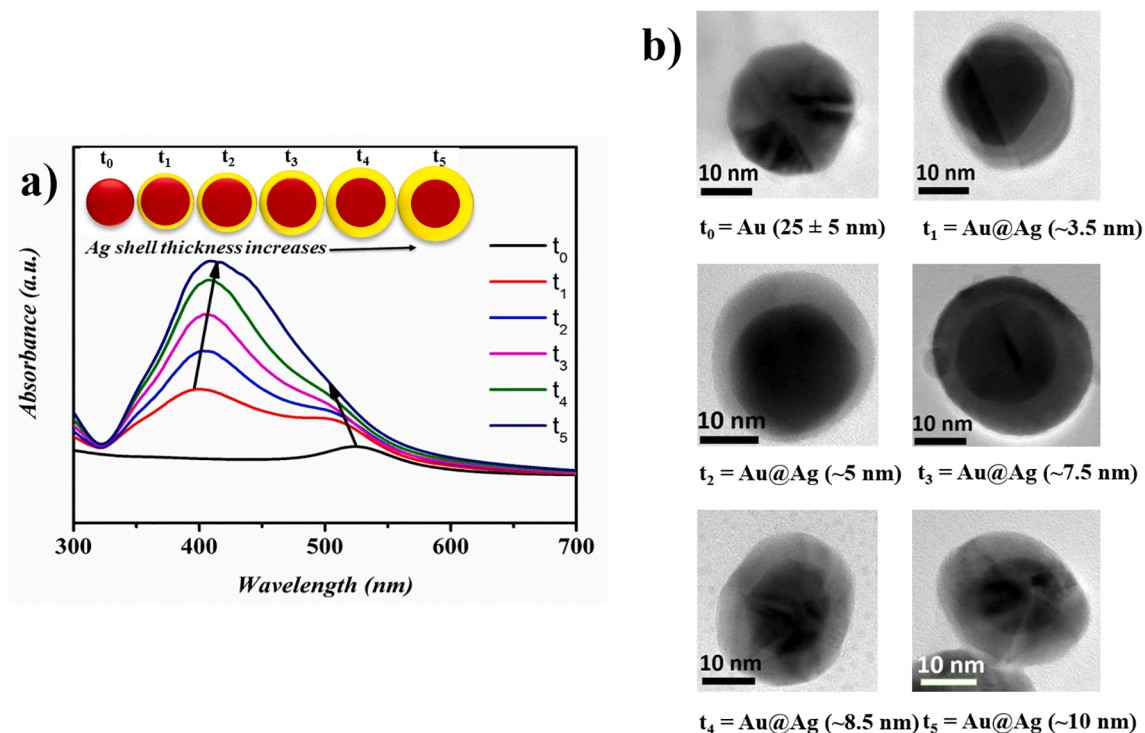


Fig. 4. (a) UV-Vis spectra of TCNC-Au@Ag nanostructures with varying shell thickness 't' (t_0 , t_1 , t_2 , t_3 , t_4 , and t_5) obtained by adding 0, 60, 90, 110, 150, and 210 μL 0.01 M AgNO_3 to 3 mL Au seed solution; (b) equivalent magnified TEM images.

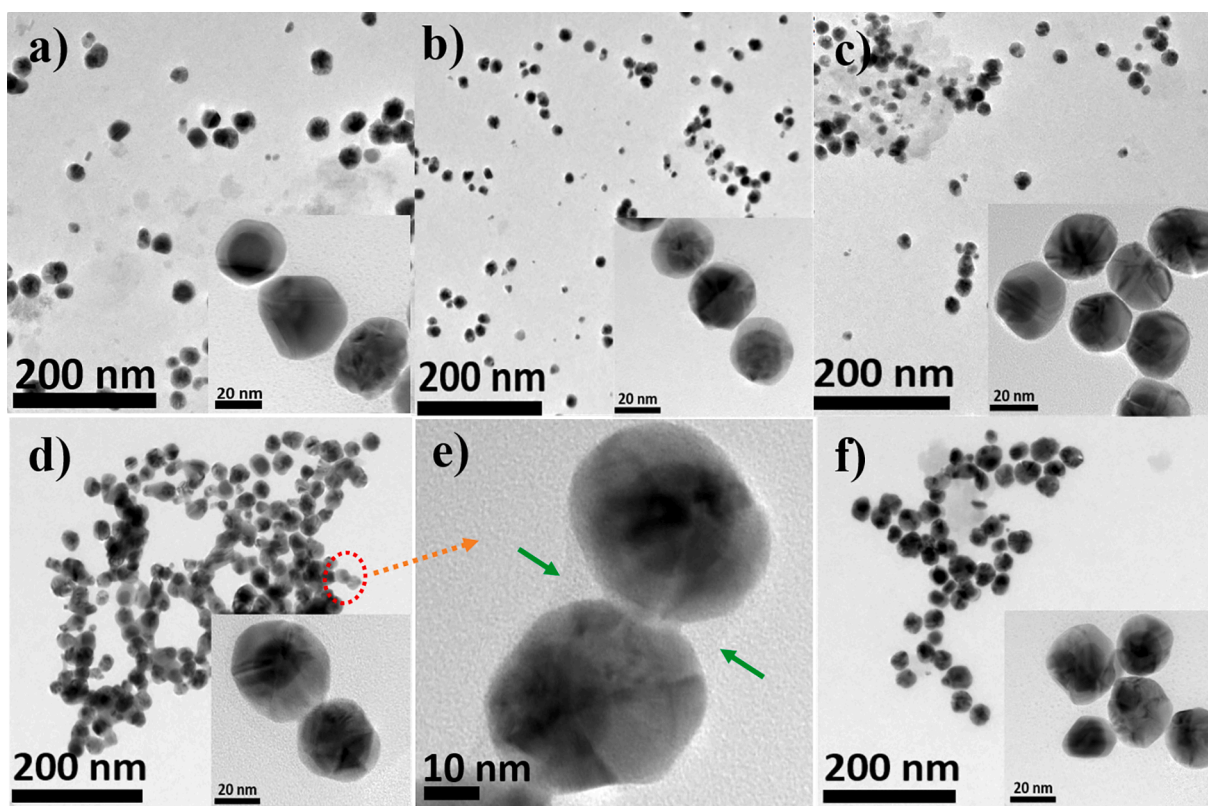


Fig. 5. TEM images of TCNC-Au@Ag nanostructures prepared by adding (a) 60, (b) 90, (c) 110, (d-e) 150, and (f) 210 μL 0.01 M AgNO_3 to 3 mL Au seed solutions; insets in (a-d and f) shows corresponding magnified TEM images.

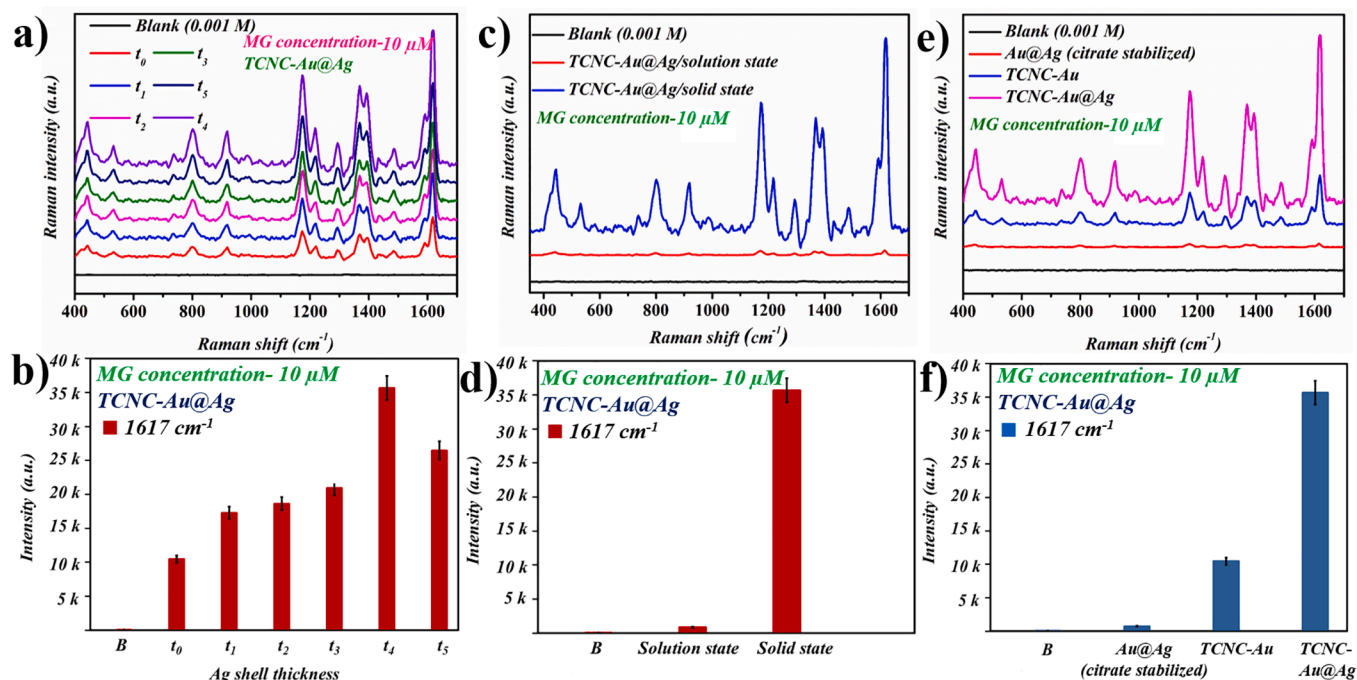
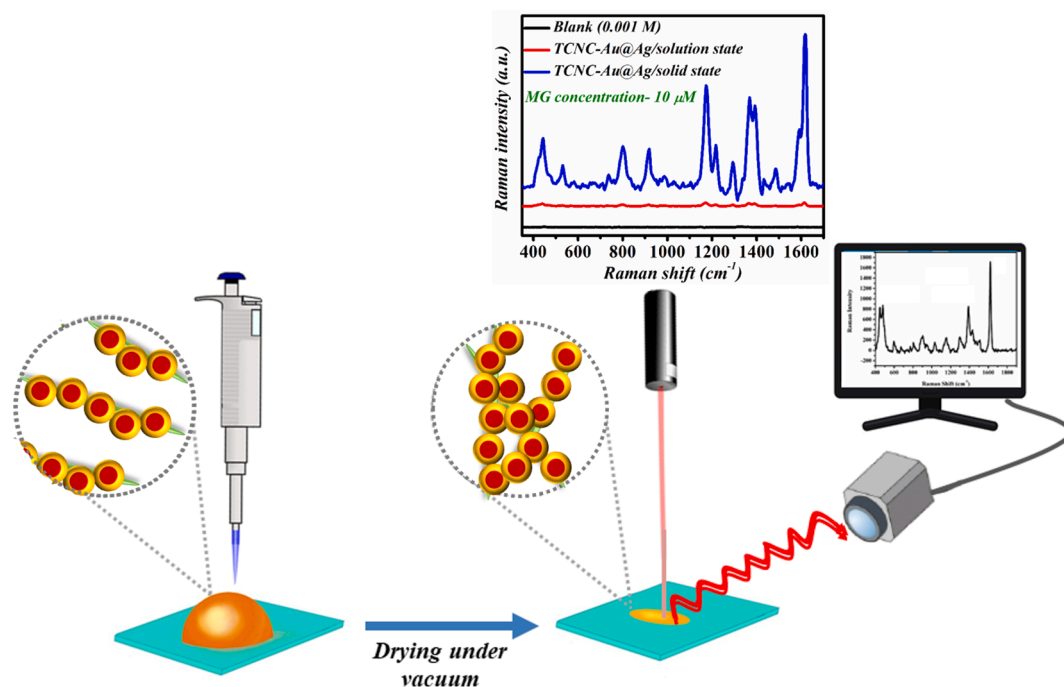


Fig. 6. SERS response of malachite green (a and b) in solid-state with varying shell thickness of TCNC-Au@Ag nanostructures; comparison of SERS sensing in dispersion solution and solid-state (c and d); comparison of solid-state SERS sensing (e and f) with control substrates (TCNC-Au and citrate stabilized Au@Ag NPs).

Subsequently, we compared the SERS efficiency of this optimized substrate in the solution phase using the same probe molecule, MG, and are presented in Fig. 6c-d. Interestingly, it is seen that the SERS peak intensity of MG in dried substrate exhibited 45 times enhancement when compared with the SERS signal intensity in the solution state. Further, to elucidate the role of carboxylated cellulose nanocrystals in hotspot generation, SERS spectra of MG were compared with control substrates such as citrate capped-Au@Ag NPs (total size $\sim 35 \text{ nm}$, shell thickness $\sim 8.5 \text{ nm}$) in the dried state (Fig. 6e-f). The peak intensity at 1617 cm^{-1} versus different substrates revealed the role of TCNC in SERS, which is

several times higher than that of other control systems. It is evident that TCNC-Au and TCNC-Au@Ag nanostructures exhibited 10- and 30-fold enhancement in signal intensity when compared with citrate stabilized Au@Ag NPs. This shows that the TCNC template and the shell thickness play a key role in controlling the amplified electric fields created near the core-shell nanoparticles. Further, the higher SERS enhancement of the t_4 substrate could be a consequence of the enhanced near-field produced either by a single core-shell NPs or from the hotspots produced within the core-shell NP assemblies having an interparticle distance less than 1 nm . Upon drying, the entangled Au@Ag NPs decorated



Scheme 2. Mechanism of SERS detection using TCNC-Au@Ag nanostructures with numerous hotspot regions.

TCNC payloads come close together inherited by its self-assembling property. From the AFM analysis, we could see numerous Au@Ag nanoparticles (bright contract) adhering over TCNC surface even after drying [Fig. S8]. This leads to creation of a highly dense hotspot region augmented electromagnetic field and the dramatic enhancement in SERS signal intensity [43,44]. The hotspot engineering ability of TCNC in SERS has been illustrated in Scheme 2. The effective preconcentration of the targeted analytes while drying and creating high-density hotspot regions facilitated by the closely packed array of TCNC-Au@Ag plasmonic payloads is an added advantage. Such findings shed light on the significance of TCNC in modulating the plasmonic effects while comparing with the plasmonic properties of classical mono or bimetallic systems prepared with conventional capping agents.

We further evaluated the applicability of the optimized TCNC-Au@Ag substrate for the trace-level detection of MG. This ominous chemical can be readily absorbed by fish tissues, which causes many genetical mutations and cancer in animals [42]. With a decrease in concentration, the intensity of MG Raman peaks gradually decreased as expected (Fig. 7a-b) with a practical limit of detection (LOD) of 10 fM. Plot for comparison of the SERS intensity at 1617 cm^{-1} versus concentration of MG with standard deviation also given (Fig. 7b). Furthermore, the practical application of the substrate solely depends on the reproducibility criterion. Hence, the reproducibility of the developed substrate has been evaluated using methylene blue (MB), as shown in Fig. 7c with the plot of intensity versus concentration of MB by choosing the characteristic band of MB at 1623 cm^{-1} (Fig. 7d). It could be found that blank MB solution Raman spectra with a concentration of 10^{-3} M are not qualitative and recognizable, whereas SERS spectra in the presence of 0.1 wt% TCNC-Au@Ag (t_4) NPs in solid-state displayed strongly amplified SERS signals even at a concentration below 100 fM. An

overview of the sensitivity studies with the lowest detection limit of MG and MB with various types of Au@Ag substrates has been tabulated (Table S2 and S3). It is worthy of notice that the SERS platform specified in this report exhibits higher sensitivity when compared with other substrates. It suggests that our method is green, cost-effective, nontoxic, and afford sustainable alternatives to known methods and their applicability in biomedical, diagnosis, and environmental monitoring.

3.5. Finite element modelling (FEM) of TCNC-Au@Ag nanostructures

For plasmonic nanomaterials like Au@Ag NPs, augmented electromagnetic fields are the key factor for SERS applications. Hence, it is vital to examine how well the silver shell affects the near-field properties. Therefore, we calculated the rate of electromagnetic energy (W) experienced by the analyte molecule near the isolated Au@Ag NPs surface and at the junctions of two Au@Ag NPs, referring to the entire wavelength region via finite element modelling (FEM) utilizing commercially accessible COMSOL Multiphysics software [45]. Primarily, we have used the RF module to articulate and solve the differential form of Maxwell equations in conjunction with the initial and boundary conditions. In conjunction with state-of-the-art algorithms for preconditioning and solution, the equations are formulated by using a finite element approach, including numerically stable edge element discretization. The scattering amplitude at the far-field (E_{far}) is invoked in the prologue of this calculation as a limiting extrapolation of their near-field action, commonly described as $E_{far} = \lim_{r \rightarrow \infty} r E_{sca}$. Therefore, the extent of electromagnetic energy dissipation could be obtained by adding the incident scattering amplitude and integrating over the Poynting vector over the whole surface as,

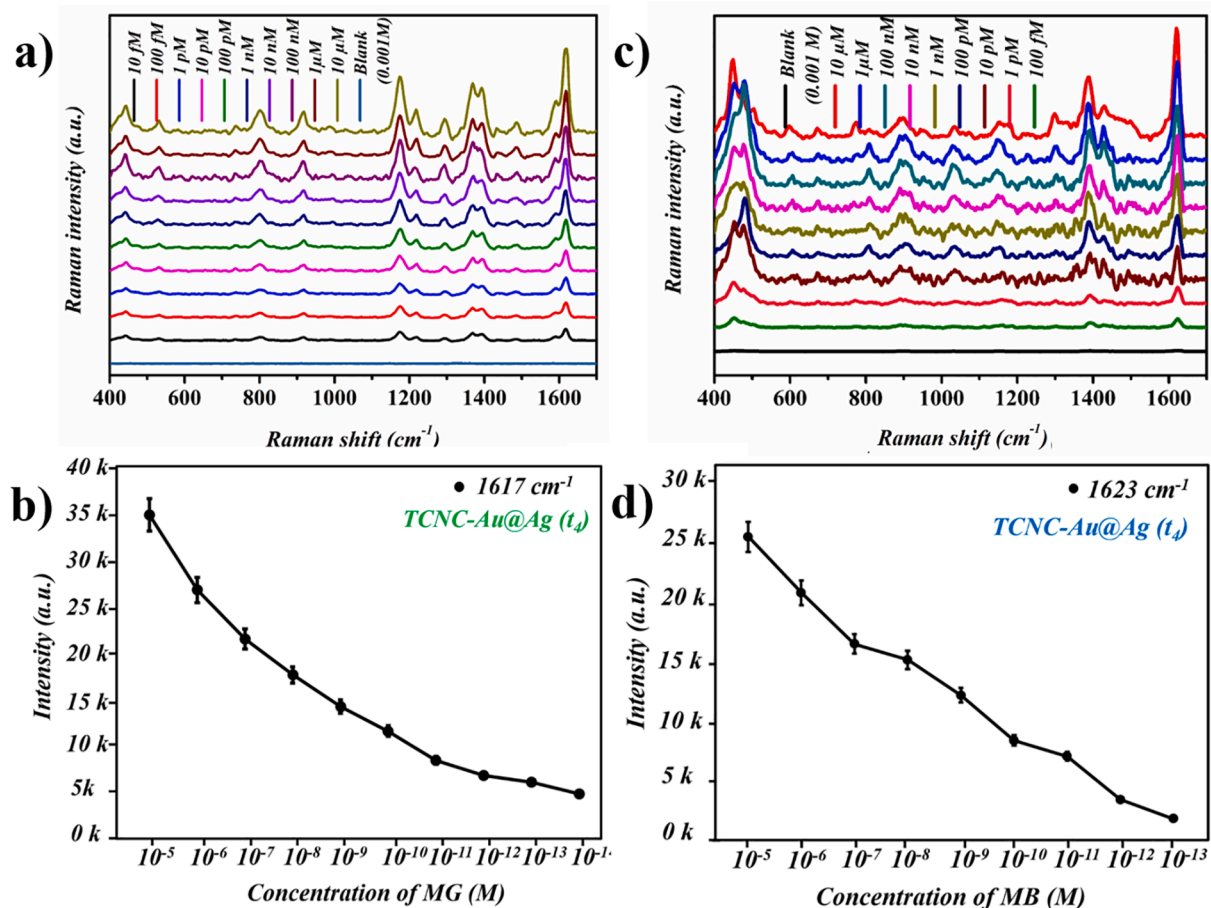


Fig. 7. Sensitivity of TCNC-Au@Ag (t_4) nanostructures towards SERS detection of malachite green (a and b) and methylene blue (c and d).

$$W_{abs} = \frac{1}{2} \int_0^a \int_0^b \int_0^c \text{Re}[J_{tot} \cdot E^* + i\omega B \cdot H^*] dv \quad (1)$$

$$W_{sca} = \frac{1}{2} \iint_s \text{Re}[E_{sca} \times H_{sca}] nds \quad (2)$$

That is correlated with the optical cross-section $\sigma = W/P$; where P is the incident irradiance. The electric field patterns calculated through FEM showing the surface plots corresponding to the 2D geometry of Au core, isolated, and dimers of Au@Ag nanostructures were presented in Fig. 8. The surface profile corresponding to TCNC-Au@Ag (Fig. 8b) displays strong localization of surface charge at the Au-Ag interface. It is observed that the enhanced local field concentrates on the outer surface of the Ag-shell (for $\lambda = 410$ nm) and polarizes parallel to the incident polarization. The electric field's strength on the Ag outer shell surface is greater than that of the Au NPs of the same size (Fig. 8a). This would be due to the interaction of the various kinds of charges centered on the Ag shell interface and surface along with the incident polarization and can be ascribed to the electron transfer from the Au core to the silver shell in the nanostructures. It was observed that the maximum $|E^2|$ value is 19.20- eV at the outer surface of the silver shell. However, in the case of bare TCNC-Au NPs ($\lambda = 524$ nm), the electric field is shown only at the two sides of the outer surface with a maximum of $|E^2|$ value at 5.03 eV, which is lesser than the core-shell nanostructures.

Further, the electric field distribution in the vicinity of two TCNC-Au@Ag (t_4) NPs was shown in Fig. 8c-e. The field polarization value is higher at the junctions of two Au@Ag NPs, which shows that electromagnetic coupling is more sensitive than the isolated core-shell NPs. It could be noted that the region at the junctions of TCNC-Au@Ag ($t = 8.5$ nm) nanostructures with a nanogap ~ 1 nm, concentrates the highest electric field (hotspots). When caught at these hotspots, the analyte

molecules give rise to incredible Raman intensities. Further, it shows a maximum $|E^2|$ value of 39.23 eV at the junction of the two core-shell NPs and is two orders of magnitude higher than that of isolated Au@Ag NPs and eight-fold higher than that of monometallic Au NPs. The simulated SERS enhancement factor ($EF \sim |E^4|$) agrees with the experimentally calculated EF ($\sim 10^5$) values of TCNC-Au@Ag nanostructures.

3.6. Catalytic activity of TCNC-Au@Ag NPs

Catalytic reduction of 4-nitrophenol by sodium borohydride is known to be one of the foremost model systems for evaluating the performance of catalysts by real-time spectroscopic monitoring. Due to the toxic, carcinogenic nature of nitrophenols, conversion followed by disposal is a major environmental issue. The aminophenols formed during the reduction of nitrophenols by NaBH_4 are inevitable components in the pharmaceutical industry, and the conversion is simple and efficient [46]. We compared the catalytic activities of bare TCNC-Au with that of TCNC-Au@Ag (~ 8.5 nm) in the 4-nitrophenol (4-NP) reduction reaction to assess the influence of the Ag shell on the catalytic properties of core-shell plasmonic nanostructures. The reduction progress has been evaluated by comparing the UV-Visible absorption spectra with one-minute intervals (Fig. 9).

The absorption maximum of 4-NP in the presence of NaBH_4 is 400 nm, attributed to the generation of 4-nitrophenolate ions [47]. On adding small aliquots (24 μL) of TCNC-Au@Ag ($t_4 \sim 8.5$ nm) to the reaction mixture, a steady decline of the absorption peak at 400 nm and the subsequent appearance of 4-aminophenol absorption at 300 nm is noted [48]. Although, in the presence of pure 25 nm TCNC-Au (t_0), negligible variation in the absorption band of 4-NP observed, indicates a weak 4-NP reduction. The catalytic reaction efficacy is estimated as 11% for TCNC-Au (t_0) and 91% TCNC-Au@Ag (t_4) nanostructures.

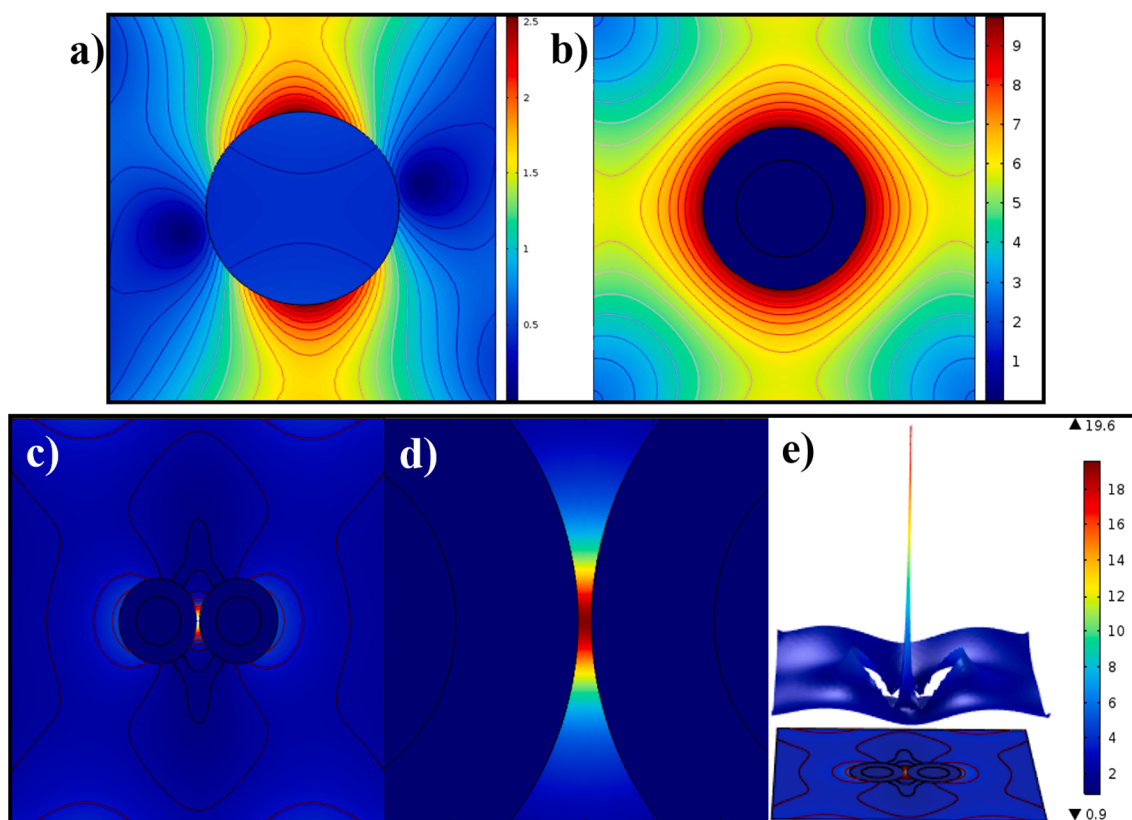


Fig. 8. Finite element modelling showing the electric field distribution corresponding to the 2D geometry of (a) TCNC-Au and (b) isolated TCNC-Au@Ag nanostructures; (c-d) at the junction between two TCNC-Au@Ag nanostructures; (d) represents the magnified image of (c); and (e) depicts the surface with height expression where it shows a sharp peak at the junction between two core-shell nanostructures.

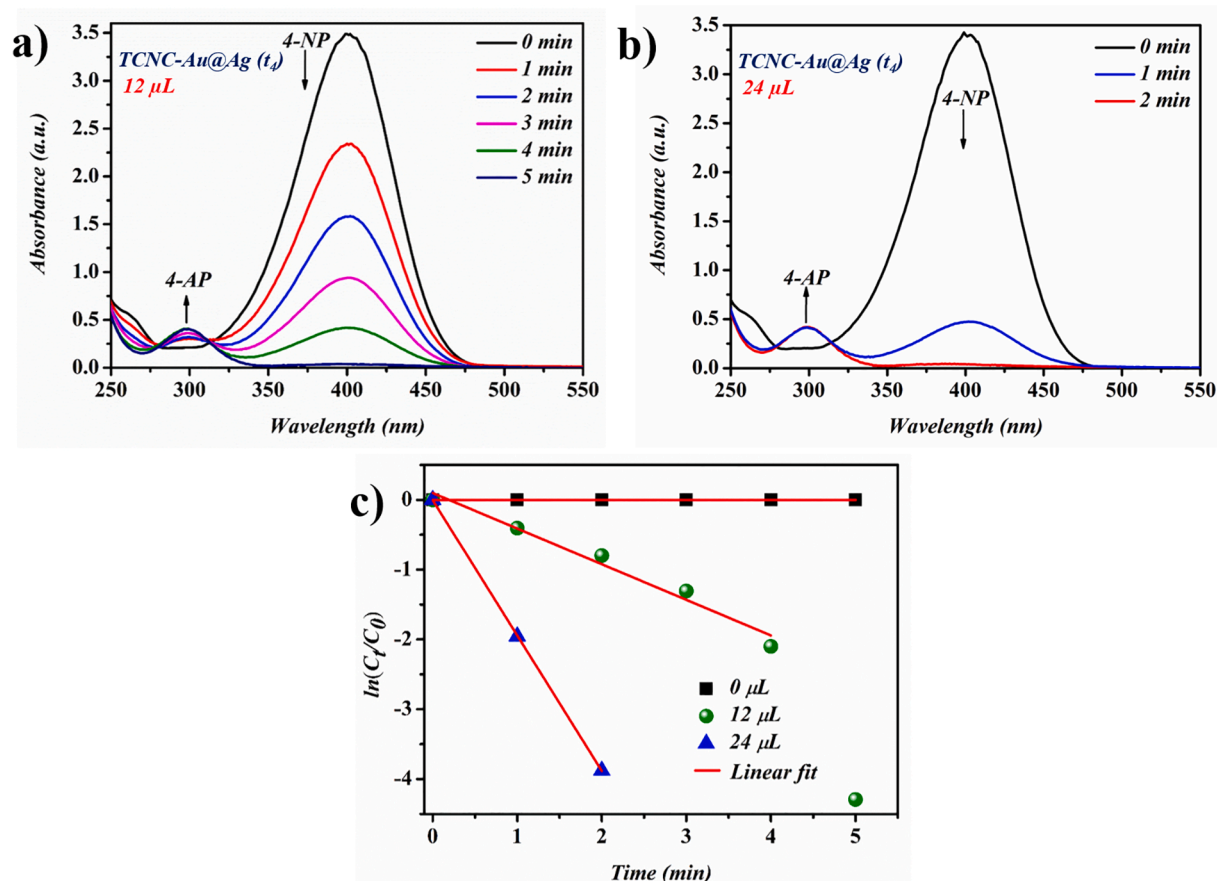


Fig. 9. (a-b) The time-dependent UV-Vis absorption spectra of 4-NP reduction with NaBH₄ catalyzed by different amounts of TCNC-Au@Ag (t₄) nanostructures and (c) corresponding kinetic plots of the reduction reaction.

Fig. 9a and 9b display the absorption spectra of the nitrophenol-borohydride mixture at various intervals of time in the presence of TCNC-Au@Ag (t₄ ~8.5 nm) catalyst. It is evident from the spectrum that, with the addition of 12 μL (~0.1 mg) of catalyst, the absorption intensity of 4-NP declines to nearly zero within 5 min. The termination of the reduction can be assured not only by the diminishing of the absorption peak at 400 nm but also by a visual change from yellow to colorless. With an increased amount of catalyst (24 μL, 0.2 mg), the reduction reaction was completed within 3 min. This short period for the reduction process, even with very minute quantities of TCNC-Au@Ag (t₄), signifies its applicability in the domain of catalysis (Table S4).

Reaction kinetics of this reduction was analyzed from ln C_t/C₀ versus time plot, and the linear fit was done with a correlation coefficient of 0.9672 (12 μL) and 0.9999 (24 μL), which revealed that 4-NP reduction by NaBH₄ obeys pseudo-first-order kinetics (Fig. 9c). The rate constant (k_{app}) of the reaction was derived from the slope of the plot ln (C_t/C₀) over time [49]. A high k_{app} value of 32.33 × 10⁻³ s⁻¹ was obtained for 24 μL (~0.2 mg) of TCNC-Au@Ag (t₄) catalyzed reduction of 4-nitrophenol. The superior catalytic action of TCNC-Au@Ag (t₄) nano assemblies could be ascribed to the synergistic electronic effect, size, and composition [50,51]. Since the Fermi level for Au (-5.0 eV) is slightly lesser than that of Ag (-4.6 eV), an electron-rich area near the Au@Ag interface is created by the transfer of electrons from Ag to Au [52].

Moreover, the electron transfer between Au and Ag is ambiguous, which could be further explained by the electron compensation effect [53]. The distorted electron balance between Au and Ag is compensated for back-donation of electrons from Au to Ag, causes reduced d-electron in Au core with an augmented d-electron in Ag shell, which is predominant at interfaces of Au and Ag. Hence, for TCNC templated Au@Ag nano-assemblies with Ag shell thickness of ~ 8.5 nm, numerous

accessible electron-rich regions could be present on TCNC surface. These highly active surface sites lead to more adsorption of 4-NP, thus leading to an enhanced catalytic rate. However, in the case of bare Au NPs (TCNC-Au NPs), such localization of electrons does not occur, and the electron density is distributed throughout the entire particle. Besides that, the catalytic effects are indeed reliant on the surface area of the catalyst. Here, the large surface area associated with the coupled nanostructures provides an active surface for the reduction and serves as a dynamic electron transfer mediator. After the reaction, the newly produced 4-aminophenol molecules rapidly desorb from the catalyst's surface [23,54]. Hence, the merits of the large surface area of TCNC, along with the presence of numerous electron-dense regions profited from Au@Ag nanostructures, will provide novel avenues for homogeneous catalysis.

4. Conclusions

In summary, we reported the synthesis of discrete as well as assembled Au@Ag core-shell nanostructures on carboxylated cellulose nanocrystal templates using a facile seed-mediated approach. Here, TCNC is critical to obtain core-shell nano-assemblies having abundant plasmonic hotspot junctions resulting in excellent SERS activity in solid-state with remarkable colloidal shelf-life. Correlation with theoretical FEM field simulations confirmed an enhanced local field at the junctions of adjacent TCNC-Au@Ag nanostructures, which can significantly enhance the Raman intensities. Moreover, the presence of several electron-dense regions in the assembled TCNC-Au@Ag nanostructures enabled enhanced catalytic activity. We envisage that our method could pave way for designing innovative complex nano-architectures of core-shell systems decorated on TCNC bio-templates with dense plasmonic

hotspots and exceptional colloidal stability. This could open up enormous possibilities for maneuvering various multifunctional plasmonic bimetallic nano-systems suitable for biomedical, energy, and environmental applications.

Declaration of Competing Interest

The authors declare that they have no known competing financial interests or personal relationships that could have appeared to influence the work reported in this paper.

Acknowledgment

Financial support from the UGC and KSCSTE for this research is greatly appreciated.

Appendix A. Supplementary data

Supplementary data to this article can be found online at <https://doi.org/10.1016/j.microc.2021.106393>.

References

- X. Zhang, X. Xiao, Z. Dai, W. Wu, X. Zhang, L. Fu, C. Jiang, Ultrasensitive SERS performance in 3D "sunflower-like" nanoarrays decorated with Ag nanoparticles, *Nanoscale* 9 (2017) 3114–3120.
- Y. Yao, X. Zhang, J. Peng, Q. Yang, One-pot fabrication of yolk-shell nanospheres with ultra-small Au nanoparticles for catalysis, *Chem. Commun.* 51 (2015) 3750–3753.
- W. Kim, J.-C. Lee, J.-H. Shin, K.-H. Jin, H.-K. Park, S. Choi, Instrument-free synthesizable fabrication of label-free optical biosensing paper strips for the early detection of infectious keratoconjunctivitis, *Anal. Chem.* 88 (2016) 5531–5537.
- F.-Y. Kong, J.-W. Zhang, R.-F. Li, Z.-X. Wang, W.-J. Wang, W. Wang, Unique roles of gold nanoparticles in drug delivery, targeting and imaging applications, *Molecules* 22 (2017) 1445.
- T. Miclăuș, C. Beer, J. Chevallier, C. Scavenius, V.E. Bochenkov, J.J. Enghild, D. S. Sutherland, Dynamic protein coronas revealed as a modulator of silver nanoparticle sulphidation in vitro, *Nat. Commun.* 7 (2016) 1–10.
- N. Arora, A. Mehta, A. Mishra, S. Basu, 4-Nitrophenol reduction catalysed by Au-Ag bimetallic nanoparticles supported on LDH: Homogeneous vs. heterogeneous catalysis, *Appl. Clay Sci.* 151 (2018) 1–9.
- R. Guo, F. Yin, Y. Sun, L. Mi, L. Shi, Z. Tian, T. Li, Ultrasensitive simultaneous detection of multiplex disease-related nucleic acids using double-enhanced surface-enhanced Raman scattering nanosensors, *ACS Appl. Mater. Interfaces* 10 (2018) 25770–25778.
- S.K. Ghosh, T. Pal, Interparticle coupling effect on the surface plasmon resonance of gold nanoparticles: from theory to applications, *Chem. Rev.* 107 (2007) 4797–4862.
- M. Shanthil, R. Thomas, R. Swathi, K. George Thomas, Ag@ SiO₂ core-shell nanostructures: distance-dependent plasmon coupling and SERS investigation, *J. Phys. Chem. Lett.* 3 (2012) 1459–1464.
- T. Jiang, X. Wang, J. Tang, S. Tang, Seed-mediated synthesis of fluorinated Ag nanoplates as surface enhanced Raman scattering substrate for in situ molecular detection, *Mater. Res. Bull.* 97 (2018) 201–206.
- M. Rycenga, C.M. Cobley, J. Zeng, W. Li, C.H. Moran, Q. Zhang, D. Qin, Y. Xia, Controlling the synthesis and assembly of silver nanostructures for plasmonic applications, *Chem. Rev.* 111 (2011) 3669–3712.
- Y.-C. Tsao, S. Rej, C.-Y. Chiu, M.H. Huang, Aqueous phase synthesis of Au–Ag core-shell nanocrystals with tunable shapes and their optical and catalytic properties, *J. Am. Chem. Soc.* 136 (2014) 396–404.
- Y. Sun, C. Lei, Synthesis of Out-of-Substrate Au–Ag Nanoplates with Enhanced Stability for Catalysis, *Angew. Chem.* 121 (2009) 6956–6959.
- X. Wu, L. Qiu, Z. Yang, F. Yan, Imidazolium functionalized NT-Im-Au-Ag hybrids for surface-enhanced Raman scattering and catalytic reduction of 4-nitrophenol, *Appl. Catal. A* 478 (2014) 30–37.
- A.K. Samal, L. Polavarapu, S. Rodal-Cedeira, L.M. Liz-Marzán, J. Pérez-Juste, I. Pastoriza-Santos, Size tunable Au@ Ag core-shell nanoparticles: synthesis and surface-enhanced Raman scattering properties, *Langmuir* 29 (2013) 15076–15082.
- A. Isogai, Y. Zhou, Diverse nanocelluloses prepared from TEMPO-oxidized wood cellulose fibers: Nanonetworks, nanofibers, and nanocrystals, *Curr. Opin. Solid State Mater. Sci.* 23 (2019) 101–106.
- K.M.A. Uddin, A.R. Lokanathan, A. Liljeström, X. Chen, O.J. Rojas, J. Laine, Silver nanoparticle synthesis mediated by carboxylated cellulose nanocrystals, *Green Mater.* 2 (2014) 183–192.
- D. Musino, C. Rivard, G. Landrot, B. Novales, T. Rabilloud, I. Capron, Hydroxyl groups on cellulose nanocrystal surfaces form nucleation points for silver nanoparticles of varying shapes and sizes, *J. Colloid Interface Sci.* 584 (2020) 360–371.
- F. Hoeng, A. Denneulin, C. Neuman, J. Bras, Charge density modification of carboxylated cellulose nanocrystals for stable silver nanoparticles suspension preparation, *J. Nanopart. Res.* 17 (2015) 244.
- L. Liu, L. Wang, S. Luo, Y. Qing, N. Yan, Y. Wu, Chiral nematic assemblies of silver nanoparticles in cellulose nanocrystal membrane with tunable optical properties, *J. Mater. Sci.* 54 (2019) 6699–6708.
- Y. Shin, I.-T. Bae, B.W. Arey, G.J. Exarhos, Facile stabilization of gold-silver alloy nanoparticles on cellulose nanocrystal, *The Journal of Physical Chemistry C* 112 (2008) 4844–4848.
- S. Asgari, L. Sun, J. Lin, Z. Weng, G. Wu, Y. Zhang, M. Lin, Nanofibrillar cellulose/Au@ Ag nanoparticle nanocomposite as a SERS substrate for detection of paraquat and thiram in lettuce, *Microchim. Acta* 187 (2020) 1–11.
- M. Gopiraman, S. Saravanamoorthy, R. Baskar, A. Ilangoan, C. Ill-Min, Green synthesis of Ag@ Au bimetallic regenerated cellulose nanofibers for catalytic applications, *New J. Chem.* 43 (2019) 17090–17103.
- Y. Zhou, T. Saito, L. Bergström, A. Isogai, Acid-free preparation of cellulose nanocrystals by TEMPO oxidation and subsequent cavitation, *Biomacromolecules* 19 (2018) 633–639.
- Y. Zhou, S. Fujisawa, T. Saito, A. Isogai, Characterization of concentration-dependent gelation behavior of aqueous 2, 2, 6, 6-tetramethylpiperidine-1-oxyl-cellulose nanocrystal dispersions using dynamic light scattering, *Biomacromolecules* 20 (2018) 750–757.
- B. Liu, G. Han, Z. Zhang, R. Liu, C. Jiang, S. Wang, M.-Y. Han, Shell thickness-dependent Raman enhancement for rapid identification and detection of pesticide residues at fruit peels, *Anal. Chem.* 84 (2012) 255–261.
- T.Y. Olson, A.M. Schwartzberg, C.A. Orme, C.E. Talley, B. O'Connell, J.Z. Zhang, Hollow gold–silver double-shell nanospheres: structure, optical absorption, and surface-enhanced Raman scattering, *J. Phys. Chem. C* 112 (2008) 6319–6329.
- C.K. Saurabh, R. Dungani, A. Owlabi, N.S. Atiqah, A. Zaidon, N.S. Aprilia, Z. M. Sarker, H.A. Khalil, Effect of hydrolysis treatment on cellulose nanowhiskers from oil palm (*Elaeis guineensis*) fronds: Morphology, chemical, crystallinity, and thermal characteristics, *BioResources* 11 (2016) 6742–6755.
- K. Nabeela, R.T. Thomas, J.B. Nair, K.K. Maiti, K.G.K. Warriar, S. Pillai, TEMPO-oxidized nanocellulose fiber-directed stable aqueous suspension of plasmonic flower-like silver nanoconstructs for ultra-trace detection of analytes, *ACS Appl. Mater. Interfaces* 8 (2016) 29242–29251.
- Z. Tang, W. Li, X. Lin, H. Xiao, Q. Miao, L. Huang, L. Chen, H. Wu, TEMPO-oxidized cellulose with high degree of oxidation, *Polymers* 9 (2017) 421.
- H. He, R. Chen, L. Zhang, W. Shen, Growth of gold nanoparticles on cellulose nanofibers, *Cellulose* 27 (2020) 5041–5053.
- H. Fukuzumi, R. Tanaka, T. Saito, A. Isogai, Dispersion stability and aggregation behavior of TEMPO-oxidized cellulose nanofibrils in water as a function of salt addition, *Cellulose* 21 (2014) 1553–1559.
- M.C.G. Toro, J.P. Schlegel, C.H. Giraldo, Radioactive Bimetallic Gold-Silver Nanoparticles Production in a Research Nuclear Reactor, *ChemistrySelect* 3 (2018) 8936–8941.
- S. Mahmud, S.S. Satter, A.K. Singh, M.M. Rahman, M.Y.A. Mollah, M.A.B.H. Susan, Tailored Engineering of Bimetallic Plasmonic Au@ Ag Core@ Shell Nanoparticles, *ACS Omega* 4 (2019) 18061–18075.
- K. Jia, M.Y. Khaywah, Y. Li, J.L. Bijeon, P.M. Adam, R.g. Dêturche, B. Guelorget, M. François, G. Louarn, R.E. Ionescu, Strong improvements of localized surface plasmon resonance sensitivity by using Au/Ag bimetallic nanostructures modified with polydopamine films, *ACS Appl. Mater. Interf.*, 6 (2014) 219–227.
- F. Sun, W. Liu, Z. Dong, Y. Deng, Underwater superoleophobicity cellulose nanofibril aerogel through regioselective sulfonation for oil/water separation, *Chem. Eng. J.* 330 (2017) 774–782.
- J. Yang, C. Ma, J. Tao, J. Li, K. Du, Z. Wei, C. Chen, Z. Wang, C. Zhao, M. Ma, Optimization of polyvinylamine-modified nanocellulose for chlorpyrifos adsorption by central composite design, *Carbohydr. Polym.* (2020), 116542.
- K. Zhang, J. Zhao, H. Xu, Y. Li, J. Ji, B. Liu, Multifunctional paper strip based on self-assembled interfacial plasmonic nanoparticle arrays for sensitive SERS detection, *ACS Appl. Mater. Interfaces* 7 (2015) 16767–16774.
- Y. Ma, W. Li, E.C. Cho, Z. Li, T. Yu, J. Zeng, Z. Xie, Y. Xia, Au@ Ag core–shell nanocubes with finely tuned and well-controlled sizes, shell thicknesses, and optical properties, *ACS Nano* 4 (2010) 6725–6734.
- H. Wang, X. Guo, S. Fu, T. Yang, Y. Wen, H. Yang, Optimized core-shell Au@ Ag nanoparticles for label-free Raman determination of trace Rhodamine B with cancer risk in food product, *Food Chem.* 188 (2015) 137–142.
- Y. Liu, J. Zhou, B. Wang, T. Jiang, H.-P. Ho, L. Petti, P. Mormile, Au@ Ag core-shell nanocubes: epitaxial growth synthesis and surface-enhanced Raman scattering performance, *PCCP* 17 (2015) 6819–6826.
- W. Kim, Y.-H. Kim, H.-K. Park, S. Choi, Facile fabrication of a silver nanoparticle immersed, surface-enhanced Raman scattering imposed paper platform through successive ionic layer adsorption and reaction for on-site bioassays, *ACS Appl. Mater. Interfaces* 7 (2015) 27910–27917.
- H. Wei, K. Rodríguez, S. Rennecker, W. Leng, P.J. Vikesland, Preparation and evaluation of nanocellulose–gold nanoparticle nanocomposites for SERS applications, *Analyst* 140 (2015) 5640–5649.
- K. Nabeela, R.T. Thomas, A. Mohamed, S. Pillai, Nanocellulose-silver ensembles for ultrasensitive SERS: An investigation on the role of nanocellulose fibers in the generation of high-density hotspots, *Appl. Mater. Today* 20 (2020), 100672.
- K. Yee, Numerical solution of initial boundary value problems involving Maxwell's equations in isotropic media, *IEEE Trans. Antennas Propag.* 14 (1966) 302–307.
- Y. Tian, Y.-Y. Cao, F. Pang, G.-Q. Chen, X. Zhang, Ag nanoparticles supported on N-doped graphene hybrids for catalytic reduction of 4-nitrophenol, *RSC Adv.* 4 (2014) 43204–43211.

- [47] M. Ma, Y. Yang, W. Li, R. Feng, Z. Li, P. Lyu, Y. Ma, Gold nanoparticles supported by amino groups on the surface of magnetite microspheres for the catalytic reduction of 4-nitrophenol, *J. Mater. Sci.* 54 (2019) 323–334.
- [48] Y. Liu, G. Jiang, L. Li, H. Chen, Q. Huang, T. Jiang, X. Du, W. Chen, Preparation of Au/PAN nanofibrous membranes for catalytic reduction of 4-nitrophenol, *J. Mater. Sci.* 50 (2015) 8120–8127.
- [49] M. Liang, R. Su, W. Qi, Y. Yu, L. Wang, Z. He, Synthesis of well-dispersed Ag nanoparticles on eggshell membrane for catalytic reduction of 4-nitrophenol, *J. Mater. Sci.* 49 (2014) 1639–1647.
- [50] D. Wang, Y. Li, Bimetallic nanocrystals: liquid-phase synthesis and catalytic applications, *Adv. Mater.* 23 (2011) 1044–1060.
- [51] X. Guo, Q. Zhang, Y. Sun, Q. Zhao, J. Yang, Lateral etching of core-shell Au@metal nanorods to metal-tipped Au nanorods with improved catalytic activity, *ACS Nano* 6 (2012) 1165–1175.
- [52] Y. Yang, J. Shi, G. Kawamura, M. Nogami, Preparation of Au–Ag, Ag–Au core-shell bimetallic nanoparticles for surface-enhanced Raman scattering, *Scr. Mater.* 58 (2008) 862–865.
- [53] Y. Feng, G. Wang, Y. Chang, Y. Cheng, B. Sun, L. Wang, C. Chen, H. Zhang, Electron Compensation Effect Suppressed Silver Ion Release and Contributed Safety of Au@Ag Core-Shell Nanoparticles, *Nano Lett.* 19 (2019) 4478–4489.
- [54] E. Menumov, R.A. Hughes, S. Neretina, Catalytic reduction of 4-nitrophenol: a quantitative assessment of the role of dissolved oxygen in determining the induction time, *Nano Lett.* 16 (2016) 7791–7797.



Tailored synthesis of ultra-stable Au@Pd nanoflowers with enhanced catalytic properties using cellulose nanocrystals

Hasna M. Abdul Hakkeem^{a,b}, Aswathy Babu^a, Nagaraju Shilpa^c, Adithya A. Venugopal^a,
A.P. Mohamed^a, Sreekumar Kurungot^{b,c}, Saju Pillai^{a,b,*}

^a Materials Science and Technology Division, CSIR-National Institute for Interdisciplinary Science and Technology (CSIR-NIIST), Thiruvananthapuram 695 019, Kerala, India

^b Academy of Scientific and Innovative Research (AcSIR), Ghaziabad 201 002, India

^c Physical and Materials Chemistry Division, CSIR-National Chemical Laboratory, Dr. Homi Bhabha Road, Pune 411008, India

ARTICLE INFO

Keywords:

Cellulose nanocrystals
Au@Pd
Nanoflowers
Oxygen reduction reaction
Catalysis

ABSTRACT

A green strategy for the synthesis of bimetallic core-shell Au@Pd nanoflowers (NFs) employing banana pseudo-stem-derived TEMPO-oxidized cellulose nanocrystals (TCNC) as both capping and shape-directing agent via seed-mediated method is presented. Flower-like nanostructures of Au@Pd bound to TEMPO-oxidized cellulose nanocrystals (TCNC-Au@Pd) were decorated on amino-functionalized graphene (NH₂-RGO) without losing their unique structure, allowing them to be deployed as an efficient, reusable and a green alternative heterogeneous catalyst. The decisive role of TCNC in the structural metamorphosis of nanoparticle morphology were inferred from the structural and morphology analyses. According to our study, the presence of -OH rich TCNC appears to play a pivotal role in the structured evolution of intricate nanostructure morphology. The feasibility of the bio-supported catalyst has been investigated in two concurrently prevalent model catalytic reactions, namely the oxygen reduction reaction (ORR) and the reduction of 4-nitrophenol, the best model reactions in fuel cell and industrial catalytic applications, respectively.

1. Introduction

Bimetallic nanoparticles with tailored morphologies were widely explored due to their unprecedented demand in a variety of fields like catalysis (Aslam, Chavez, & Linic, 2017), sensing (Rodríguez-Lorenzo, de La Rica, Álvarez-Puebla, Liz-Marzán, & Stevens, 2012), plasmonics (Kauranen & Zayats, 2012), biomedical (Howes, Rana, & Stevens, 2014), etc., owing to their excellent optical and electronic properties of monometallic counterparts (Ferrando, Jellinek, & Johnston, 2008). Apart from isotropic spherical morphologies, the anisotropic morphologies have a profound influence on their intrinsic physicochemical properties (Burda, Chen, Narayanan, & El-Sayed, 2005). Various methodologies like electrodeposition, sonochemical, co-precipitation, etc. are reported regarding the preparation of nanomaterials. However, achieving controllable geometries with good colloidal stability is questionable; most of these methods are expensive and have low yield. Chemical reduction methods, especially colloidal synthesis utilizing various capping agents, are generally employed to synthesize metallic

nanostructures of well-defined morphologies with comparable shelf-life. CTAB (Fan et al., 2008), CTAC (Yang et al., 2011) and PVP (Lee et al., 2008) are a few well-explored capping as well as shape-directing agents for modulating specific geometries of nanoparticles. Many of the synthesis methods utilizing conventional capping agents are complex, time-consuming, require high temperatures and utilize toxic organic solvents. Nevertheless, the above-mentioned conventional capping agents are the pillars of the synthesis of anisotropic nanostructures. However, there exist only a few promising eco-friendly or sustainable strategies capable of the controlled morphology generation of metallic nanoparticles that perform with completely inherent properties. Presenting them as a sustainable alternative to conventional shape-directing agents is a challenge in the realm of nanotechnology, which is completely ruled by conventional ones.

Nano version of the most abundant biopolymer cellulose with less amorphous nature known as cellulose nanocrystals (CNC), upsurged in recent years. Realm of CNC goes far beyond merely due to the applicability arises from the congregate of remarkable properties like easy

* Corresponding author at: Materials Science and Technology Division, CSIR-National Institute for Interdisciplinary Science and Technology (CSIR-NIIST), Thiruvananthapuram 695 019, Kerala, India.

E-mail address: pillai_saju@niist.res.in (S. Pillai).

<https://doi.org/10.1016/j.carbpol.2022.119723>

Received 25 January 2022; Received in revised form 4 June 2022; Accepted 7 June 2022

Available online 11 June 2022

0144-8617/© 2022 Elsevier Ltd. All rights reserved.

functionalization (Thomas et al., 2018), mechanical properties (Yuan et al., 2021), sustainability, and high surface area (Abdelgawad et al., 2020), etc. Regardless of labyrinth acid hydrolysis synthetic way, Zhou et al. proposed a modified method, TEMPO-mediated oxidation followed by cavitation which enables the ease of formation of CNC (Zhou, Saito, Bergström, & Isogai, 2018). Carboxyl groups confined by TEMPO-mediated oxidation and inborn abundant hydroxy groups ascertained the robustness of TCNC towards good carriers of metal nanoparticles avoiding any undesirable aggregation that crevasse its performances (Xu et al., 2011). Moreover, apart from conventional polymer capping agents, the criteria of desirable surface area for both nanoparticles and template (TCNC) is well ascertained due to the nano range physical dimensions (Azizi, Ahmad, Hussein, & Ibrahim, 2013). Electrostatic interactions between metal ions and functionalized hydrophilic TCNC confine metal nanoparticles controlled growth and distribution over TCNC with high surface area (Xu, Chen, Gao, Xie, & Chen, 2020). There are several reports on CNC-assisted synthesis of ultra-stable metal nanoparticles, especially Au and Ag, for various applications (Nabeela, Thomas, Mohamed, & Pillai, 2020). Notably, Kaushik et al. integrated the template, stabilizer, reducing actions of CNC reported in the area of catalysis (Xu et al., 2011). To the best of our knowledge, there are only a few researches on the preparation of CNC supported Pd nanoparticles for its application in advanced catalysis that made an upsurge in activity however, morphology control and desired surface modification are still a challenge (Cirtiu, Dunlop-Briere, & Moores, 2011; Kaushik et al., 2015; Rezayat, Blundell, Camp, Walsh, & Thielemans, 2014; Wang et al., 2020; Wu et al., 2013).

Au@Pd anisotropic nanoparticles unambiguously showed their catalytic properties in various fields endowed from electronic couplings and geometric effects (Marx & Baiker, 2009; Thompson, 2004; Zhang et al., 2011). Bimetallic Au–Pd nanostructures can be designed as alloys or core-shell morphologies by co-reduction and seed-mediated synthesis, respectively. The seed-mediated synthesis for core-shell morphology is complex and pronounced due to the judicious control over the intrinsic physicochemical properties simply by tuning the composition, shell morphology, and thickness (Cortie & McDonagh, 2011). Numerous novel strategies are evolved to synthesis Au@Pd core-shell NPs with flower-like morphologies utilizing shape-directing agents through seed-mediated synthesis envisioned from the pronounced applicability of this bimetallic system in the field of catalysis. Xu et al. demonstrated the development of Au–Pd NFs by the formation of Pd petal-like shell over PVP capped Au seed (Xu et al., 2011). Lee et al. explained the preparation of flower-like Au–Pd alloy nanostructures by the reduction property of ascorbic acid and employing PVP as stabilizing agent (Lee et al., 2008).

Apart from Pt catalyst, Pd is a recent addition, an efficient metal catalyst with excellent electrochemical activity in fuel cells (FCs) (Pan, Zhang, Ma, & Zhang, 2008). Moreover, bimetallic NPs comprising Pd and other metals generally outperform in terms of electro-catalytic efficacies than monometallic counterparts of them. Au@Pd NPs are well known as an alternative for expensive and scarce Pt catalysts (Lin et al., 2017). Several reports exist demonstrating this bimetallic system having dramatic electrocatalytic activity emerging from the cooperative catalytic properties of both Au and Pd (Au acts as a promoter to electron transfer to Pd) (Han et al., 2012). Au–Pd bimetallic NPs also adequately recognized for their catalytic efficiency towards the 4-NP to 4-AP reduction, a miniature catalytic reaction that took as the backbone of the pharmaceutical industry (Chen, Cai, Chen, & Oyama, 2014).

Incorporation of Au@Pd NPs onto a carbon support material is required for the development of heterogeneous recyclable catalysis applications. Researchers adopted simple mixing of metallic NPs and Vulcan carbon for the fabrication of the heterogeneous recyclable catalysts (Wang et al., 2010; Xiong, Yang, DiSalvo, & Abruña, 2018). However, this could be a formidable challenge for the stability of catalyst prepared. These might be the reason for choosing reduced graphene oxide (RGO) (Darabdhara et al., 2015) and CNT (Wang et al., 2017) as

the versatile support for the metal NPs which further improves the catalytic activity and immobilizes NPs (Sun, Wu, & Shi, 2011). Furthermore, there arises another difficulty: metal NPs have a tendency of spontaneous aggregation at the edges of defects of these materials that may lead to the destruction of the anisotropic morphology of metal nanoparticles. The addition of suitable surfactants can overcome these challenges; however, it may result in the reduction in catalytic activity (Ren, Yang, Yu, Wang, & Mao, 2013).

Herein, we demonstrate a bio-supported synthetic strategy for bimetallic Au@Pd NFs resembles to that of a flower garland enabled by TEMPO-oxidized cellulose nanocrystals that impart ultra-stability to the colloidal system. The novelty of the present report is the remarkable shape-directing and capping activity of a bio-derived material, nanocellulose as a new competitor to conventional capping agents. For the applicability as an efficient, reusable and a green alternative heterogeneous catalyst, TEMPO-oxidized cellulose nanocrystal bounded Au@Pd (TCNC-Au@Pd) flower-like nanostructures have been decorated over amino-functionalized graphene (NH₂-RGO) without losing its unique structure. The feasibility of the bio-derived catalyst in two prevailing model catalytic reactions, that is oxygen reduction reaction (ORR) in alkaline electrolyte solution and reduction of 4-nitrophenol, has been investigated.

2. Materials and methods

2.1. Materials

Chemically extracted banana pseudo-stem fibers (from banana plant waste) were utilized for TCNC preparation. Gold(III) chloride trihydrate (HAuCl₄·2H₂O), trisodium citrate tribasic dihydrate (TSC; C₆H₅Na₃O₇·2H₂O), palladium chloride (PdCl₂), L-ascorbic acid (C₆H₈O₆), graphite powder <150 μm, sodium nitrite (NaNO₂), sulphuric acid (H₂SO₄, 98 %), hydrogen peroxide (H₂O₂, 30 wt%), 4-nitrophenol (4-NP; C₆H₅NO₃) and sodium borohydride (NaBH₄) were bought from Sigma-Aldrich (U.S.) and were used as obtained. Hydrochloric acid (HCl, 35 %) was purchased from Rankem, whereas potassium permanganate (KMnO₄), ethylene glycol (C₆H₆O₂), and ammonia solution (NH₄OH, 99 %) were purchased from TCI chemicals. Ultrapure deionized (DI) water (Milli-Q purifier system, Merck, Germany) was used as solvents for all experiments.

2.2. Synthesis of TEMPO-oxidized cellulose nanocrystals (TCNC)

A chemo-mechanical treatment was employed for the synthesis of TEMPO-oxidized cellulose nanocrystals. Briefly, TEMPO-mediated oxidation followed by ultrasonication for 2 h. A detailed experimental procedure can be found elsewhere (Hakkeem et al., 2021).

2.3. Preparation of TCNC bounded Au NPs seed (TCNC-Au NPs)

A typical preparation method of carboxyl functionalized cellulose nanocrystal bounded Au seed solution proceeded by the combined reduction capabilities of both TCNC and TSC with minor modifications (Hakkeem et al., 2021). Briefly, 600 μL of 0.05 M HAuCl₄ mixed with 50 mL 0.1 wt% TCNC solution in a 100 mL RB flask by sonication followed by boiling and slow stirring at 400 rpm. Subsequently, 4 mL of 0.04 M of citrate was added to the boiling solution which turned to purple color solution after 20 min. As-formed TCNC bounded Au seed solution was cooled and stored at 4 °C for further use. Wine red colored Au seed was used for the preparation of Pd shell coating after the solution was let to reach ambient temperature.

2.4. Synthesis of TCNC bounded Au@Pd nanoflowers (TCNC-Au@Pd NFs)

To synthesis TCNC bounded Au@Pd NFs, a seed-mediated approach

was employed with minor modifications by adding 400 μL of 0.05 M ascorbic acid solution (AA) and 0.05 M PdCl_2 to as-prepared 6 mL TCNC-Au NPs seed solution dropwise with slow stirring. Progress of the reaction was monitored by a visible change in color of the solution from purple to blackish brown within a few seconds of magnetic stirring. Variable amounts equimolar AA and PdCl_2 from 50 to 250 μL lead to the development of TCNC-Au@Pd NFs with the increasing number of Pd petals. The samples were stored after dialysis at 4 $^\circ\text{C}$ for a longer duration. To compare nanostructure formations, the std. Turkevich method was opted: citrate capped Au@Pd NPs and TCNC bounded Pd NPs were also prepared.

2.5. Synthesis of heterogeneous TCNC-Au@Pd decorated NH_2 -RGO catalyst

GO was prepared by modified Hummers procedure (Navaee & Salimi, 2015), amine-functionalized and reduced in one-step hydrothermal treatment. Here we adopted an in-situ hydrothermal reduction technique utilizing ethylene glycol as solvent. The amine functionalization was done using ammonia solution. Briefly, 30 mg GO was mixed with 30 mL ethylene glycol solvent and was made into a uniform solution by sonication for 15 min. The uniform solution was added to the Teflon lined autoclave after adding 0.5 mL ammonia solution at 170 $^\circ\text{C}$ for 10 h. The dark brown colored solution was filtered, washed, and dried at 60 $^\circ\text{C}$ for 24 h to obtain amine-functionalized RGO powder (Lai et al., 2011). Further decoration of NH_2 -RGO with TCNC-Au@Pd NFs was obtained by mixing 20 wt% TCNC-Au@Pd NFs colloid with well-dispersed NH_2 -RGO in DI water for 30 min ultra-sonication. The sediments were collected and washed thoroughly and dried at 80 $^\circ\text{C}$ in a vacuum oven for 24 h. Samples were stored in a desiccator for further experiments. For comparison, TSC-Au@Pd NPs/ NH_2 -RGO and TCNC-Pd NPs/ NH_2 -RGO were also prepared.

2.6. Electrocatalytic oxygen reduction reaction (ORR)

TCNC-Au@Pd NFs/ NH_2 -RGO-based working electrode was constructed by dropping 10 μL of homogeneous suspension of TCNC-Au@Pd NFs/ NH_2 -RGO catalyst on a rotating disc electrode (RDE) having 3 mm diameter. Catalyst slurry was prepared by dispersing 1 mg of the material in 1 mL of 3:2 IPA:water mixture and 40 μL of Nafion solution (20 wt%). The mixture was then sonicated for about 1 h to obtain a homogeneous suspension. ORR measurement was conducted in a three-electrode system comprising of a working electrode coated with TCNC-Au@Pd NFs/ NH_2 -RGO, counter electrode (graphite rod), and a reference electrode (Hg/HgO) in oxygen saturated alkaline medium (0.1 M KOH). Linear sweep voltammetry (LSV) measurements were taken after 50 cycles of CV measurements in 0.1 M KOH over the potential range from 0.05 to 1.1 V at 50 mV/s to eliminate surface contamination. For comparison purposes, commercial Pd/C (20 wt%), TSC-Au@Pd NPs/ NH_2 -RGO, and TCNC-Pd NPs/ NH_2 -RGO were also utilized as catalysts in the same manner as above. LSV measurements were from negative to positive direction at 10 mV/s. All the potentials measured were transformed to the reversible hydrogen electrode (RHE) scale.

2.7. 4-Nitrophenol (4-NP) catalytic reduction

Catalytic reduction of 4-NP was done in a quartz cuvette by adding a specific amount of TCNC-Au@Pd NFs/ NH_2 -RGO catalyst system to a mixture of 3 mL freshly prepared 15 mM NaBH_4 solution and 0.25 mM 4-NP solution with constant shaking. Spectrometric analysis of reduction was carried out at regular intervals of time by UV-Vis absorption spectroscopy. After completion of 4-NP reduction, the catalyst was recovered by centrifugation and reused after washing step.

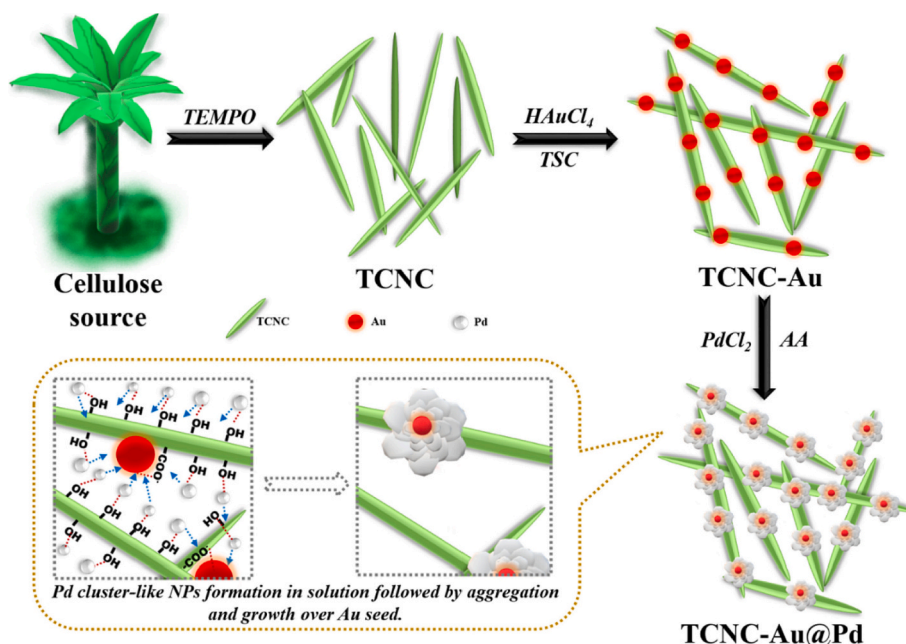
2.8. Characterization methods

Tapping mode AFM height images were obtained from a Multimode 8 atomic force microscope equipped with a Nanoscope V controller (Bruker, Santa Barbara, CA). Samples were deposited on mica substrate by drying under vacuum for 24 h prior to AFM measurements. The dynamic light scattering (DLS) data and zeta potential were obtained from Zetasizer Nano ZS, Malvern equipment. The FTIR spectrometer (PerkinElmer) was used to study the chemical structure of TCNC and TCNC-Au@Pd NFs by scanning in the range from 4000 to 400 cm^{-1} . Wide-angle X-ray scattering (WAXS) pattern of TCNC and holocellulose were captured by XEUS SAXS/WAXS system from Xenocs operated with $\text{Cu K}\alpha$ ($\lambda = 1.54 \text{ \AA}$), 50 kV. The crystalline structure of the TCNC-Au, TCNC-Au@Pd NFs were determined using PANalytical X'pert pro, powder X-ray diffractometer (XRD) equipped with $\text{Cu K}\alpha$ ($\lambda = 1.54 \text{ \AA}$), 45 kV. TEM analysis was performed using FEI-Tecna 30 G2S-TWIN transmission electron microscope with a 300 kV acceleration voltage. X-ray photoelectron spectroscopy (XPS) study was performed using PHI 5000 VersaProbe II, ULVAC-PHI Inc., USA. The binding energies of XPS peaks were referenced to C1s peak at 284.8 eV. Total Au and Pd contents were estimated with an inductively coupled plasma mass spectrometry (ICP-MS) (Thermo Scientific iCAP-RQ). All UV-Visible absorption spectra were acquired using Shimadzu UV-2700, Shimadzu, Japan UV-Visible absorption spectrometer. Oxygen reduction reaction measurements of the synthesized catalysts and commercial standard were performed using the Pine Research Instruments rotating disk electrode (RDE) setup connected to a potentiostat.

3. Results and discussion

3.1. Synthesis of Au@Pd nanoflowers bounded with the TCNC

The Turkevich method for preparing Au NPs by utilizing trisodium citrate was well-established over five decades ago. Whereas the astonishing reducing and capping actions of nanocellulose for the shape-directed synthesis of nanoparticles have been reported only a few years back (Kaushik & Moores, 2016). Scheme 1 shows the preparation of Au@Pd nanoflowers bounded with TEMPO-oxidized cellulose nanocrystals (TCNC). Initially, needle-like carboxyl functionalized cellulose nanocrystals having an average diameter, $13 \pm 2 \text{ nm}$ and length, $150 \pm 20 \text{ nm}$ were prepared by TEMPO-oxidation followed by ultra-sonication. The size reduction of cellulose fibers to nanocellulose with needle-like morphology was revealed in AFM height images and the DLS spectra analysis showed TCNC with an average size, 160 nm, Fig. S1a and 1b (Supplementary data). Further, FTIR spectra and WAXS pattern of holocellulose before TEMPO oxidation and TCNC were also recorded as the basic characterizations of TCNC and obtained similar results discussed in our previous report (Hakkeem et al., 2021). The carboxyl functionalization of nanocellulose was carried out to achieve better colloidal solubility and to create nucleation sites for the metal nanoparticles due to the electrostatic interaction between COO^- and M^+ ions (Lili Zhang et al., 2020). By adopting the combined stabilizing and reducing actions of TCNC and TSC, isotropic spherical Au NPs with size about $15 \pm 2 \text{ nm}$ bounded to well-dispersed network of TCNC were synthesized. Nearly an array of Au NPs of uniform size and shape signifies the action of carboxyl ends as nucleation sites in the TCNC support. The preferential anchoring of Au (0) NPs at the carboxyl groups by replacing Na^+ ions of nanocellulose chains were obtained as shown in Fig. S2a and b. The high probability of formation of an intercalated network bed by both inter and intramolecular hydrogen bonds of TCNC in aqueous media creates perfect anchoring sites for Au NPs without any coagulation as indicated by the zeta potential value, -33 mV (Table S1). Later, the as-prepared Au seeds bounded with TCNC were used for Pd shell coating without any purification. Five aliquots of as-prepared TCNC-Au seeds were mixed with different quantities (50, 100, 150, 200, and 250 μL) of equimolar ascorbic acid (AA) and Pd precursor at pH, 8. As expected a



uniform Pd shell growth, preferably over the TCNC bounded Au seeds was formed since Pd can form layer by layer on Au core (Chen, Li, Zhang, Zhang, & Fan, 2011; Lu, Prasad, Wu, Ho, & Huang, 2010; Yang et al., 2011).

After subsequent additions of 50 μL , ascorbic acid, and Pd precursors, the color of colloid changed from wine red to light brownish-black; however, no apparent Pd shell formation was observed, as evident from Fig. 1b. Succeeding to the addition of 100 μL of the reagents

resulted in a petal-like Pd shell appearance over the Au core (Fig. 1c). This was distinguishable by the contrast variations arises due to the discrepancy in electron density between Au and Pd, instead of epitaxial growth of Pd layer over the Au core as described elsewhere (Fang et al., 2011). Presence of TCNC could not be witness from the TEM images since no heavy metal staining agents were used to distinguish between the nanocellulose and metal nanoparticles. Nevertheless, a network of TCNC may be visible even at low magnification in a few regions due to

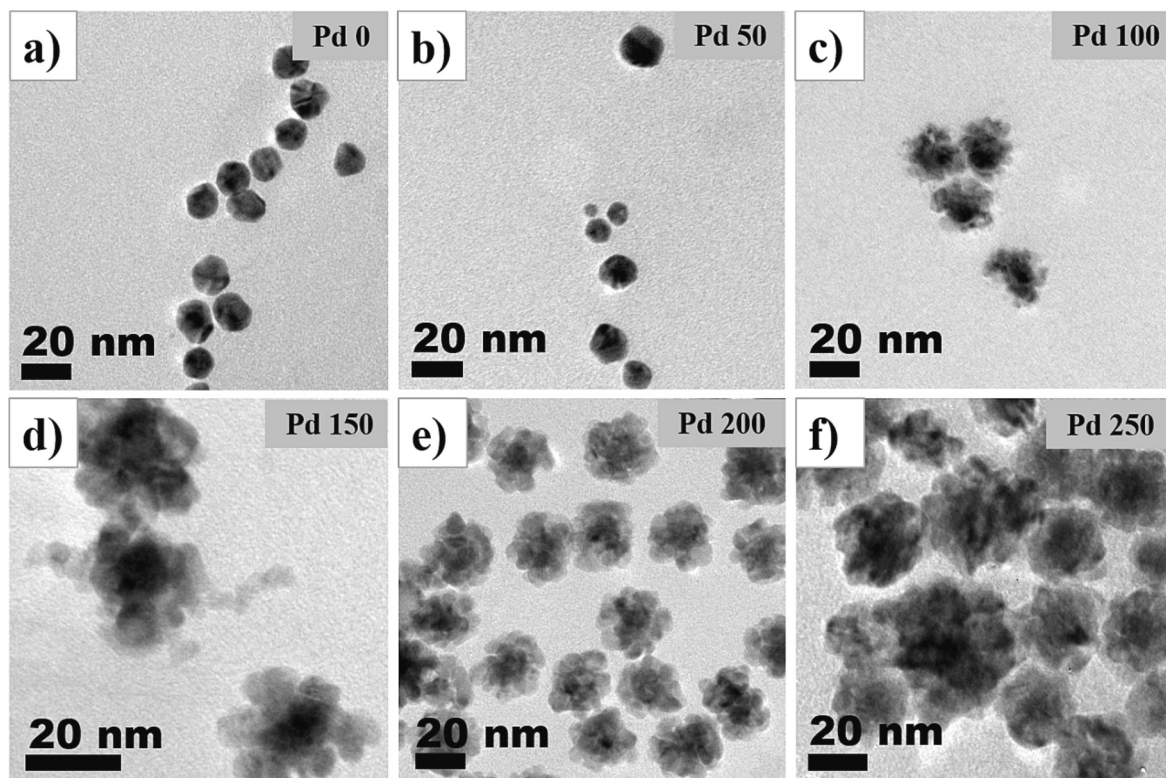


Fig. 1. TEM images (a) TCNC-Au NP seeds, (b–f) TCNC-Au@Pd NFs containing an Au core and Pd petal-like shells obtained after mixing of different quantities of equimolar ascorbic acid (50, 100, 150, 200 and 250 μL) and Pd precursor at pH, 8.

the presence of metal NPs (Fig. S3). Further an increase in the amounts of reagents, from 150 to 250 μL resulted an incremental increase in the number of petals of size range, 3–5 nm as revealed from Fig. 1 (d–f). The HR-TEM image and FFT pattern of TCNC-Au@Pd NF structures obtained during the initial stages of Pd shell growth after the addition of 50 μL ascorbic acid and Pd precursor (a–c); and the Pd petals growth after the addition of 200 μL (d–g) are shown in Fig. 2.

We observed that at lower Pd precursor concentrations, the shell was indistinguishable, and the lattice fringes observed in the higher magnification images and FFT spot pattern signifies the presence of the (111) crystalline plane as the dominant plane corresponds to Au. Whereas in Fig. 2d, a fully formed Pd petals over Au surface, camouflaging TCNC-Au seed was observed. As a result, the lattice fringes of Au core were unattainable, whereas the lattice fringes corresponding to (111) planes of Pd were obtained from petals areas as shown in Fig. 2 (d–f). The corresponding FFT patterns obtained from these petals supports the above findings (Fig. 2c, and g). In general, the HR-TEM images of initial and intermediate shell thickness (petals) confirmed that Au is present as core and Pd as petal-like shell in the TCNC-Au@Pd NF structures, and significant alloying has not occurred.

As the number of Pd petals augmented, the average size of the TCNC-Au@Pd NF structures varies from 18 ± 2 nm to 32 ± 2 nm [Fig. 3(a–f)]. Fig. 3g shows the low magnification TEM image of TCNC-Au@Pd NFs which present the distribution of the Au@Pd NFs with uniform geometry in the entire area. To further affirm the formation of TCNC-Au@Pd NFs, UV-Visible absorption spectra were recorded (Fig. 3h). It is observed that an obvious surface plasmon absorption at 527 nm which is characteristic for Au NPs. Interestingly, this surface plasmon band of Au gradually diminishes up on increasing the amounts of Pd precursors from 50 to 250 μL , and finally no observable plasmonic band in the visible region corresponding to Pd nanoparticles (Lee et al., 2008). These results suggest that the morphology of TCNC-Au@Pd NFs having Au confined in the core with Pd shell coating on the of nanostructure (Scott, Wilson, Oh, Kenik, & Crooks, 2004; Xu et al., 2011). Besides, as-synthesized TCNC-Au@Pd NF structures with different Pd compositions maintained excellent colloidal stability as revealed by the zeta potential values (Table S1). The TCNC-Au@Pd NFs (Pd-200) colloid revealed the

highest zeta potential value of -50.0 mV, and we have not observed any significant sedimentation even after six months (Fig. S4). The yield of TCNC-Au@Pd NFs is estimated to be about 75 % using ICP-MS and quantified the ratio of Au:Pd and found to be approximately 1:2 ratio for TCNC-Au@Pd NFs (Pd-200), which was reported for the better catalytic performance of this bimetallic system (Kelly et al., 2018).

Fig. 4a illustrates the XRD pattern of synthesized TCNC-Au NPs seed which includes diffraction peaks corresponding to nanocellulose and metallic Au. The peaks at $2\theta = 12.36^\circ$, 20.28° , and 22.23° are due to the characteristic diffraction peaks of cellulose II, indexing the planes (1–10), (110) and (200), respectively. The diffraction peaks observed after $2\theta = 35^\circ$, exactly at 38.28° , 44.61° , 64.48° , 77.4° and 81.35° indicate significant matching with the typical diffraction pattern of *fcc* Au NPs corresponded to the planes (111), (200), (220), (311), and (222), respectively (JCPDS no. 00-004-0784). The overall narrow and prominent XRD patterns validated the complete formation of crystalline Au NPs embedded in the intercalated TCNC network. Fig. 4b, XRD pattern of TCNC-Au@Pd NFs demonstrates a slight shift in the peak positions of above-signified planes after Pd shell coating, which nearly matches with the standard diffraction pattern for metallic *fcc* Pd (JCPDS no. 00-005-0681) with diffraction peaks corresponding to TCNC. The prominent crystalline peak of (111) plane at 38.28° in TCNC-Au and TCNC-Au@Pd affirmed that the TCNC well covered this plane, which is in consensus with the TEM observations. Compared to the diffraction pattern of TCNC-Au NPs seed and TCNC-Au@Pd NFs (Fig. 4), after Pd shell coating a significant decrease in the intensity diffraction peaks of TEMPO-oxidized cellulose nanocrystals (TCNC) was observed. These random decrease in the crystallinity of semi-crystalline polymer arises mainly due to the disturbance in crystallinity by the coordination interaction between polymer and the metal introduced to the composite (Farea, Abdelghany, & Oraby, 2020; Ragab & Rajeh, 2020). This would infer that here occurs a strong intermolecular interaction between the Pd NPs and TEMPO-oxidized cellulose nanocrystals resulting from the oxophilicity of Pd (Rezayat et al., 2014). Therefore, our XRD results suggest an inevitable role of the TEMPO-oxidized cellulose nanocrystals for directing the flower-like morphology instead of the epitaxial growth of Pd over Au NPs.

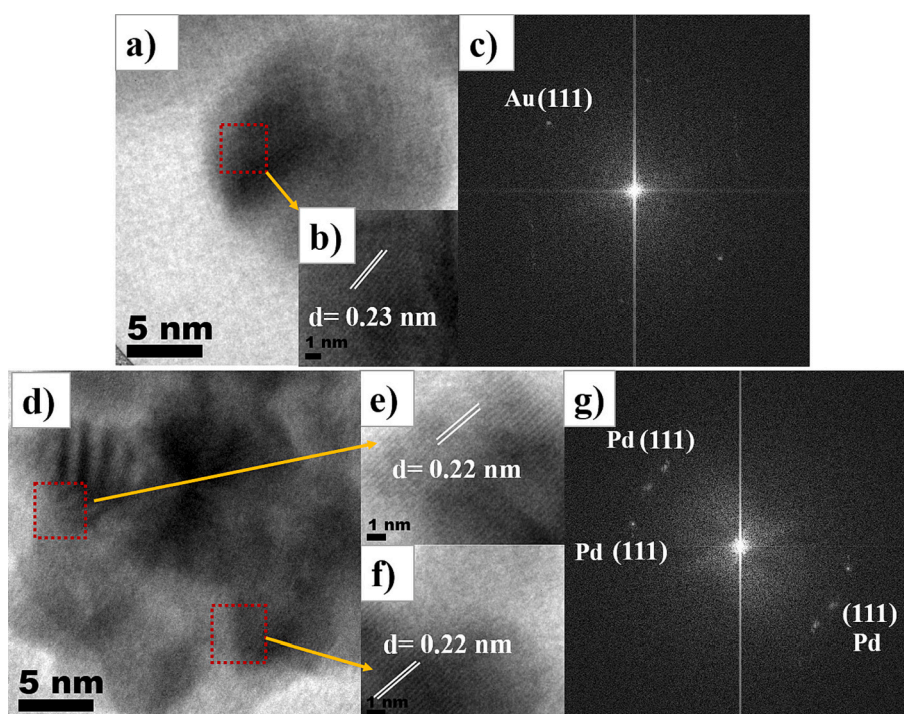


Fig. 2. HR-TEM images and their corresponding FFT patterns of TCNC-Au@Pd NFs at various Pd shell coating: Pd-50 (a–c) and Pd-200 (d–g).

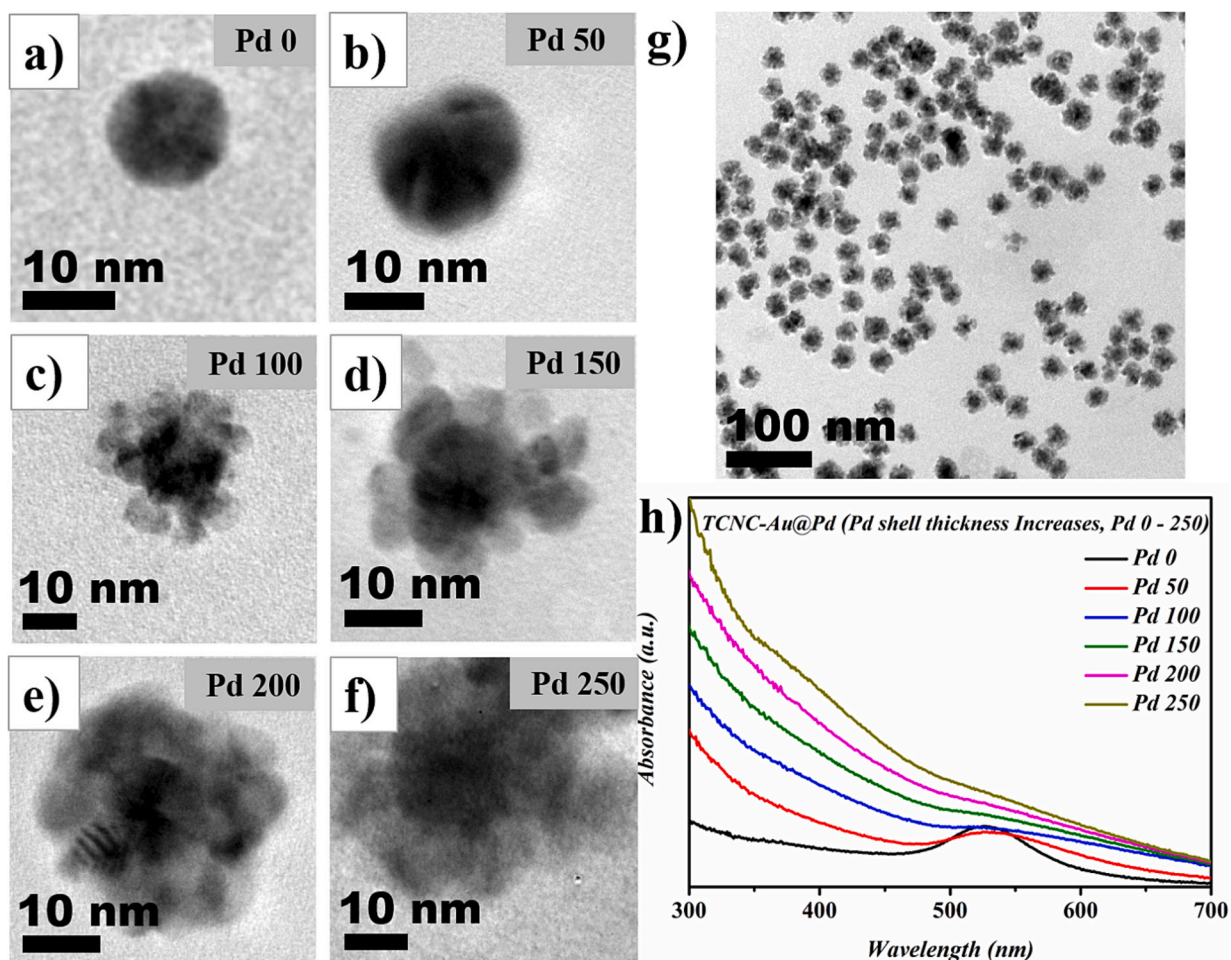


Fig. 3. (a–f) The TEM images of single TCNC-Au@Pd NF showing an increment in the number of the Pd petals obtained after the coating with different quantities of the Pd precursors, (g) TCNC-Au@Pd NFs at low magnification and (h) the corresponding UV-Visible absorption spectra.

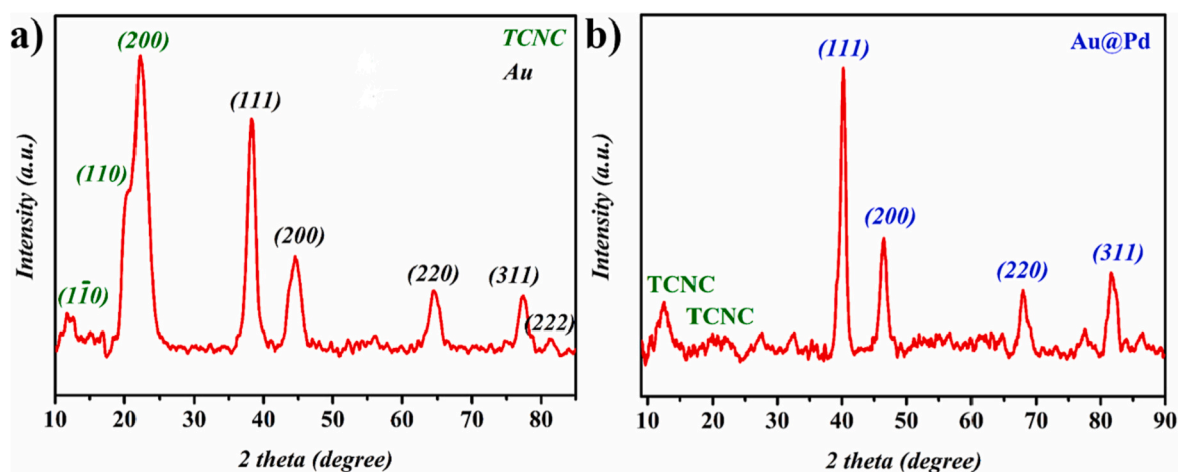


Fig. 4. XRD patterns of (a) TCNC-Au NPs seed and (b) TCNC-Au@Pd NFs (Pd-200).

The chemical states of the major elements present in the TCNC-Au@Pd NFs system were investigated by XPS. The narrow scans of major elements of TCNC-Au@Pd NFs are given in Fig. 5(a–d). Particularly, the narrow scan of Pd3d showed two doublets (Fig. 5a) with relatively high intensity at 335.15 and 340.45 eV with a binding energy separation of 5.30 eV are assumed to have originated from $3d_{5/2}$ and $3d_{3/2}$ of Pd (0). The deconvolution of doublet pairs can be fitted with an

additional peak of low intensity at 336.48 and 341.84 eV, attributed to the binding energy of Pd^{2+} species. These low intense Pd^{2+} species were unlikely due to the surface partial oxidation of Pd NPs during the sample preparation while drying since Pd is very sensitive to oxygen. Fig. 5b is the deconvoluted spectrum of Au 4f region of Au NPs showing Au(0) $4f_{7/2}$ and Au(0) $4f_{5/2}$ doublets situated at 83.5 and 87.2 eV, respectively with an energy separation of 3.6 eV, which is consistent with the typical

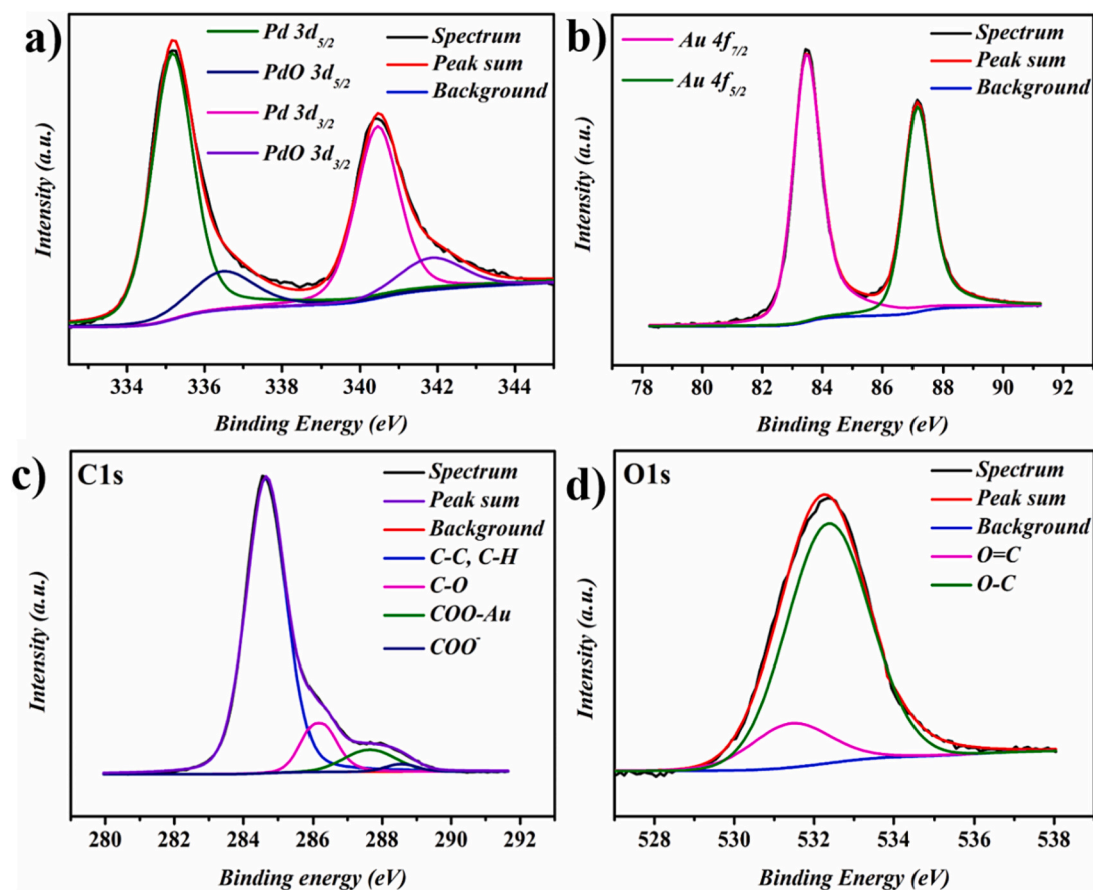


Fig. 5. XPS narrow scans of TCNC-Au@Pd NFs (Pd-200) (a) deconvoluted spectra of Pd 3d, (b) Au 4f, (c) C1s, and (d) O1s, respectively.

spectrum for metallic Au(0) (Yang et al., 2020). Further the narrow-scans of C1s and O1s obtained (Fig. 5c and d) indicate the presence of TEMPO-oxidized nanocellulose crystals as the template for Au NPs. The C1s spectrum is composed of four distinct peaks at 284.6 (C—C, C—H), 286.18 (C—O), 287.62 (COO—Au), and 288.7 eV (COO⁻), respectively. The peak at 288.7 eV is assigned to carboxyl functionalization during the TEMPO-oxidation. The peak at 287.62 eV strongly supported the fact that the Au NPs are connected to carboxyl groups of TCNC since these two peak positions are attributed to free carboxyl moieties and coordinated carboxylates, respectively (Caporali, Muniz-Miranda, Pedone, & Muniz-Miranda, 2019; Park & Shumaker-Parry, 2014). The core-level spectrum of O1s also be deconvoluted to two peaks with binding energies, 531.4 (O=C) and 532.4 eV (O—C) (Sadri et al., 2017). The nature of binding of Au NPs and TCNC is further analyzed by comparing the deconvoluted spectra of Au4f of nanocellulose capped Au NPs (seed) and TSC capped Au NPs (synthesized in absence of TCNC). Fig. S5 shows two distinct peaks of Au(0) 4f_{7/2} and Au(0) 4f_{5/2} assigned to 83.55 and 87.15 eV for TCNC-Au NPs; and 83.3 and 86.9 eV for TSC-Au NPs, respectively. This slight shift in the binding energies of the spin-orbit components of the TCNC capped Au NPs compared to that of the TSC capped Au NPs towards higher binding energies supports the effectual wrapping of Au NPs by TCNC and only possess lower electron density than TSC-Au NPs (Lili Zhang et al., 2020). These XPS results further confirmed the applicability of the carboxyl functional groups as nucleation sites for Au ions, and thereby generation of immobilized Au NPs embedded in the TCNC intercalated network resulted in unprecedented colloidal stability.

Fig. S6 shows the FTIR spectra of TCNC and TCNC-Au@Pd NFs represent the qualitative analysis of interactions between TCNC and Au@Pd NFs formed on the TCNC templates. First, the FTIR spectrum of TCNC shows peaks at 3446 cm⁻¹ (broad; -OH stretching), 2908 cm⁻¹

(C—H stretching), 1612 cm⁻¹ (C=O stretching of COO⁻ group), 1414 cm⁻¹ (C—O stretching of COO⁻ group), and 1056 cm⁻¹ (C—O—C stretching) (Purwidyantri et al., 2020). After in-situ synthesis of Au@Pd NFs over TCNC, the FTIR spectrum of TCNC-Au@Pd NFs also includes the above characteristic vibrational peaks of cellulose indicates the minor change in the chemical structure of cellulose by incorporating nanoparticles to TCNC template. In closer observation, the intensities of all characteristic IR absorption peaks, especially cellulose, were diminished in TCNC-Au@Pd NFs, which indicates the adhesion of Au@Pd NFs on the hydroxy groups of the nanocellulose crystals (Purwidyantri et al., 2020). A significant reduction in the intensity and shift in the -OH stretching vibration from 3446 to 3434 cm⁻¹ was also observed which can be resulted from the interaction between Au@Pd NFs and -OH groups of TCNC (Eisa, Abdelgawad, & Rojas, 2018).

3.2. Role of TCNC in morphology evolution of TCNC-Au@Pd nanoflowers

We investigated the basis of the structure-directing capabilities of TCNC for the shape selective colloidal synthesis of distinct flower-like Au@Pd NPs. To investigate this hypothesis, the synthesis of Au@Pd NPs was carried in the absence of TCNC, keeping all other parameters constant. A comparison between the TEM micrographs of Au@Pd synthesized with and without TEMPO-oxidized cellulose nanocrystals shine light on the shape-directing capability of TCNC. Fig. 6a and b shows the TEM images of TCNC-Au@Pd NFs whereas Fig. 6c and d presents the bare Au@Pd NPs in the absence of TCNC. Initially, the carboxyl functional groups in TCNC could tightly bound the Au NPs followed by the capping of Au NPs. Subsequently, the electron-rich hydroxy groups present in nanocellulose will function as the nucleation or anchoring sites for Pd clusters in the solution by ascorbic acid (AA) reduction

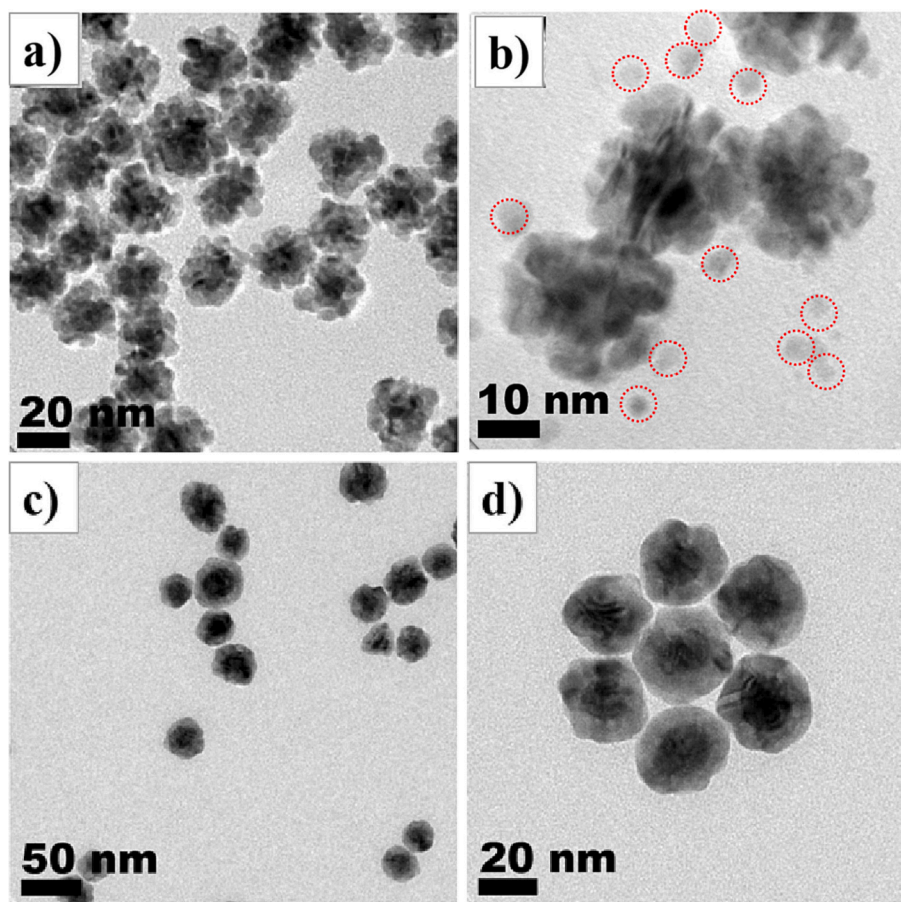


Fig. 6. TEM images of (a) TCNC-Au@Pd NFs (Pd-200); (b) cluster-like small Pd NPs (3–5 nm) captured during Pd shell coating over Au NPs seed solution and (c–d) citrate capped Au@Pd NPs (Pd-200).

during the shell coating. The Pd cluster-like small NPs (3–5 nm) formed by the AA reduction in the solution can be quantitatively deposited at the surface hydroxy groups of TCNC that collectively capped the Au NPs, then comprehensively ad-layers on Au core (Shin, Bae, Arey, & Exarhos, 2008). A successful formation of cluster-like small Pd NPs in solution before the aggregation over the Au NPs seed was observed from some of the TEM images captured during the Pd shell coating process by seed-mediated synthesis route (Fig. 6b). A more or less similar cluster mediated growth mechanism was reported by Xu et al. and Lim et al., respectively for the growth of Au@Pd NFs and Pt dendrites capped Pd core by utilizing high molecular weight PVP (Lim, Jiang, Yu, Camargo, & Xia, 2010; Xu et al., 2011). In our study, the epitaxial growth of Pd shell, about 7–8 nm over citrate capped Au seed was observable without any formation of anisotropic morphologies by Pd coating (Fig. 6c and d). Based on the above observations, a possible morphology evolution mechanism and shape-directing capability of TCNC is proposed (Scheme 1).

The shape-directing ability of TCNC for nanoengineered core-shell Au@Pd NFs arises from the fact that the inherent –OH groups that electrostatically bound to Pd clusters could enable the merging of Pd clusters, thereby inhibiting the growth of perfect epitaxial Pd shell over Au seed. Nucleation and subsequent growth process of a bound Pd or any metal clusters would progress slowly followed by release and migration towards Au seed or any metal core, leading to the generation of anisotropic morphology (Jiang & Hsieh, 2014). The constrained capture of Pd clusters by the electrostatic interaction of oxygen atoms of polar –OH groups of TCNC resulted in a gradual reduction in the overall crystallinity of TCNC after the Pd shell coating (Azizi et al., 2013; Wu et al., 2013), which was evident from the XRD analysis. Concisely, numerous

hydroxy functional groups present in the TCNC hinder the direct epitaxial deposition of Pd shell over Au core, directing to the creation of small clusters like Pd NPs of 3–5 nm size, which will further be aggregated as petals around Au NPs. Whereas in the absence of TCNC, free Pd clusters were formed in the solution, preferably deposit in the (111) plane of Au core and grow quickly into a uniform shell. Even though the shape regulating ability of TEMPO-oxidized nanocellulose fibers was first mentioned by Jiang et al. to form Ag nanoprisms using H_2O_2 as an etching agent (Jiang & Hsieh, 2014). Our study is the initial step for presenting TCNC as a potential and bio-sourced shape-directing and capping agent for the preparation of bimetallic core-shell NPs, especially Au@Pd NFs, without the presence of any etching or co-capping agents.

3.3. Catalytic performance of TCNC-Au@Pd NFs

A reduction in the size of Pd-based metal catalysts is extremely desirable since shorter dimensions may provide more number of catalytically active sites by unit mass. The TCNC-Au@Pd NFs system nanoengineered in our study may catalytically be more active because it is enriched with a large count of small petal-like Pd NPs around the TCNC bounded core. Since the hydrophilic nature of the catalyst may hinder its catalytic activity and recyclability, we amalgamated amine functionalized reduced graphene oxide (NH_2 -RGO) as an acceptable support for the system. Therefore, the TCNC-Au@Pd NFs were decorated over NH_2 -RGO nanosheets by the electrostatic interaction without losing any structural change and stability. Thus the heterogeneous TCNC-Au@Pd NFs/ NH_2 -RGO catalyst was fashioned by an aqueous solvent assisted mixing of TCNC-Au@Pd NFs with NH_2 -RGO (obtained from RGO prepared by Hummers method followed by amino functionalization). Fig. 7

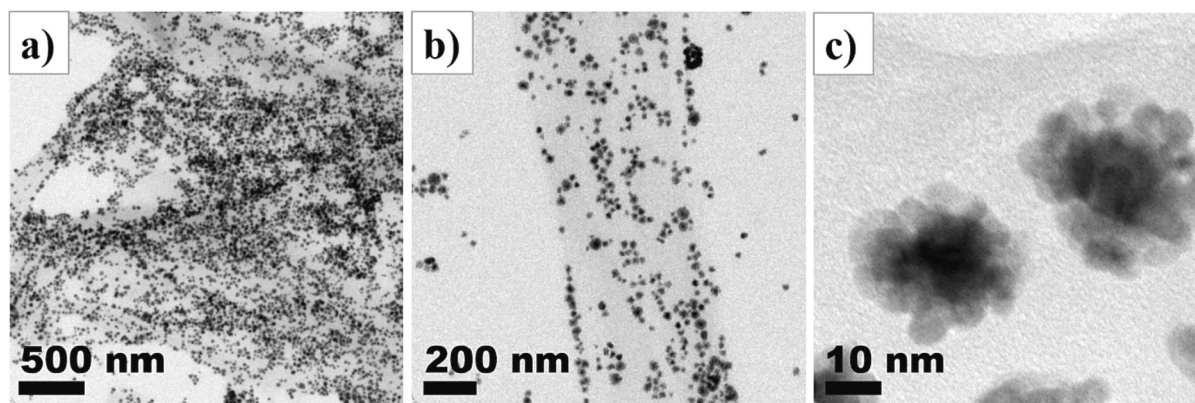


Fig. 7. (a–c) TEM images of TCNC-Au@Pd NFs decorated NH_2 -RGO nanosheets.

(a–c) shows the successful functionalization of TCNC-Au@Pd NFs over NH_2 -RGO sheets uniformly without any significant change in structure and sign of aggregation.

3.4. Oxygen reduction reaction in alkaline medium (ORR)

Electrocatalytic performance of our synthesized catalysts and standard was measured towards ORR by rotating disc electrode (RDE) method in 0.1 M KOH at 1600 rpm of the working electrode by saturating the solution with O_2 . The ORR polarization curves (LSV curves) recorded for a series of the catalysts, including commercial 20 wt% Pd/C (control sample) profiled in Fig. 8. All the potentials were reported on the RHE scale and the current densities got were normalized to the geometric area of the electrode. Both the onset potential and half-wave potential ($E_{1/2}$) showed a positive trend in the order TCNC-Pd NPs/ NH_2 -RGO < TSC-Au@Pd NPs/ NH_2 -RGO < TCNC-Au@Pd NFs/ NH_2 -RGO \approx Pd/C (Std.). Compared to TCNC-Pd NPs/ NH_2 -RGO, both TSC-Au@Pd NPs/ NH_2 -RGO and TCNC-Au@Pd NFs/ NH_2 -RGO exhibited a positive shift in both onset potentials and $E_{1/2}$, revealing the effect of the bimetallic system (Au@Pd) towards the electrocatalytic activity.

Whereas further enhancement in the TCNC-Au@Pd NFs/ NH_2 -RGO system compared to TSC-Au@Pd NPs/ NH_2 -RGO may evolve from its flower-like constructs with a high electrochemically active surface area which improves the ORR kinetics and reduces the overpotential. Additionally, decoration of Au@Pd NFs over amino functionalized graphene oxide nanosheets induced long-term stability of the catalyst without any agglomerations. The TCNC-Au@Pd NFs/ NH_2 -RGO system performed as a better electrocatalyst towards ORR compared to its counterpart systems with an onset potential of about 0.94 V, which is almost close to that of the standard Pd/C. This enhancement may have resulted from the consecutive effects of strain (lattice mismatch), ligand effect, and electronic modifications (Xue et al., 2018). The diffusion limiting current density (mA/cm^2) obtained for TCNC-Au@Pd NFs/ NH_2 -RGO of about $-4.4 \text{ mA}/\text{cm}^2$ at 1600 rpm stands out as another important performance indicator, implying the promising activity of the system. Also, this limiting current density is slightly higher compared to that of the standard Pd/C ($-3.5 \text{ mA}/\text{cm}^2$), and that obtained for homogeneous TCNC-Au@Pd NFs colloids during our primary ORR studies signified the importance of further modifications in the system by optimizing graphene content. It has been reported that, higher graphene content will

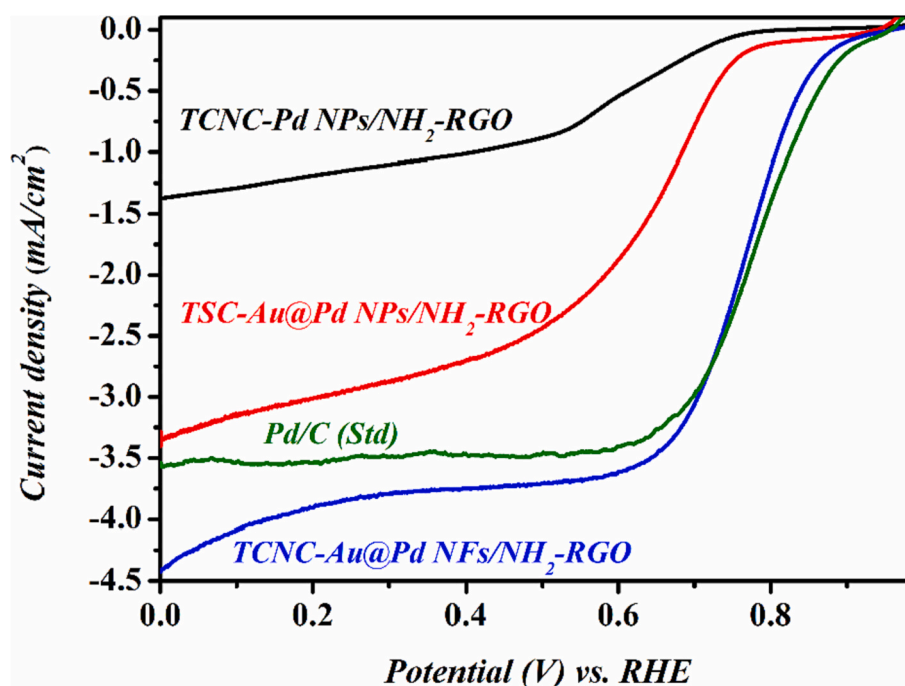


Fig. 8. The ORR polarization curves of commercial Pd/C (20 wt%), TCNC-Au@Pd NFs/ NH_2 -RGO, TSC-Au@Pd NPs/ NH_2 -RGO, and TCNC-Pd NPs/ NH_2 -RGO catalysts in 0.1 M KOH solution recorded at a scan rate of 10 mV/s and an electrode rotation speed of 1600 rpm.

reduce the limiting current density (Das et al., 2020). In this report, however, more detailed investigations in the TCNC-Au@Pd NFs/NH₂-RGO catalyst towards ORR performance were not included since our primary aim was to highlight on the evolution of shape-directing capability of nanocellulose, as a bio-sourced alternative to the conventional capping agents.

3.5. Catalytic 4-nitrophenol (4-NP) reduction

4-Nitrophenol to 4-aminophenol (4-AP) reduction is a conventional catalytic reduction reaction and still outweighed as the benchmark to demonstrate the efficacies of newly proposed catalysts. Since both 4-NP (4-nitrophenolate ions) and 4-AP exhibit evident absorption in the UV-Visible region, monitoring of the reduction process is studied using UV-Visible absorption spectroscopy. 4-NP showed an absorption band at 400 nm in the presence of NaBH₄ as a reducing agent, and the newborn 4-AP could show an absorption maximum at 300 nm. Au, Pd, especially Au-Pd metal NPs are the best candidates to catalyze the 4-NP reduction (Chen et al., 2014). However, template-supported metal NPs will improve the catalytic properties and relieve the soaring price of catalysts by recycling them as heterogeneous catalysts. The ultimate selection of most active Pd shell thickness over TCNC-Au core in TCNC-Au@Pd NFs/NH₂-RGO catalyst for the 4-NP reduction was done by the spectral monitoring of 4-NP reduction by using constant quantity of catalysts (0.1 mg) and at exact time interval, 2 min (Fig. S7a). As indicated by the highest zeta potential value, excellent stable geometry with high surface area and adequate Au:Pd composition ratio suitable for catalysis; TCNC-Au@Pd NFs/NH₂-RGO with Pd-200 shell thickness came to first place with best catalytic activity. 4-NP reduction was also monitored with a series of catalysts used earlier in the ORR section and it also profiled the superior catalytic activity of our TCNC-Au@Pd NFs/NH₂-RGO. The order of the catalytic activity from the lowest to the highest is, TCNC-Au NPs/NH₂-RGO < Pd/C (Std.) < TCNC-Pd NPs/NH₂-

RGO < TSC-Au@Pd NPs/NH₂-RGO < TCNC-Au@Pd NFs/NH₂-RGO (Fig. S7b). The superior catalytic activity of TCNC-Au@Pd NFs/NH₂-RGO might have rightfully come from the synergic influence of the size, shape, stability, composition of nanoparticles as well as the presence of specific templates or supports which supplemented the detrimental effect of some conventional capping agents (Menumorov, Hughes, & Neretina, 2016).

Fig. 9(a–b) depicts the successful demonstration of TCNC-Au@Pd NFs/NH₂-RGO as an efficient catalyst towards 4-NP reduction. The reduction reaction was completed within 3 min even in the presence of a minute quantity of catalyst (0.05 mg) and showed significant enhancement upon increasing the amount to 0.1 mg. Reaction proceedings could be monitored by a gradual drop in the absorption maxima of 4-NP and concomitant appearance of absorption of 4-AP and by the bleaching of the yellow color of 4-NP.

Fig. 9c shows the linear correlation of $\ln(C_t/C_0)$ versus reaction completion time (min) since reaction rate independent of the concentration of reducing agent, and linear fitting was successful with correlation coefficients 0.9714 (0.05 mg) and 0.9874 (0.1 mg) consistent with the fact that catalytic 4-NP reduction followed pseudo-first-order kinetics (Hakkeem et al., 2021). The rate constant of the reduction, estimated from the slope of the plot $\ln(C_t/C_0)$ versus time, was $30.63 \times 10^{-3} \text{ s}^{-1}$ for 0.1 mg of TCNC-Au@Pd NFs/NH₂-RGO catalyst. Table S2 compares the efficiency of our catalyst with the results reported by other researchers, especially with nanocellulose supported catalysts. It is remarkable that the excellent catalytic activity of TCNC-Au@Pd NFs/NH₂-RGO in 4-NP reduction; therefore, it is a burgeoning environmental benign candidate in the realm of catalysis. Electron transfer between electron-rich Au to Pd, relatively high surface area, back-bone made by electron-rich amino-functionalized reduced graphene oxide, and prevention of self-aggregating during synthesis and storage are the answers to why this catalyst shows superior catalytic activity. TCNC-Au@Pd NFs/NH₂-RGO can be effortlessly recovered by centrifugation after

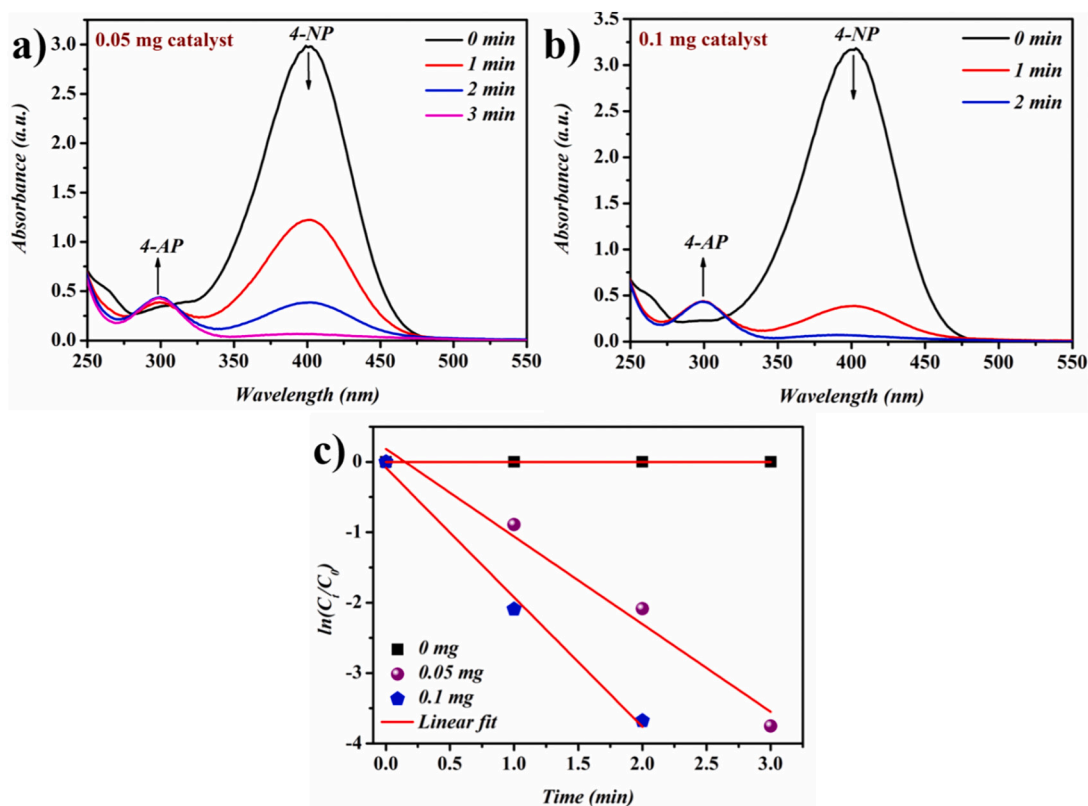


Fig. 9. Real-time spectroscopic monitoring of 4-NP catalyzed by (a) 0.05 mg, (b) 0.1 mg of TCNC-Au@Pd NFs/NH₂-RGO, and (c) corresponding reaction kinetic plots.

completion of the reaction and can be reused at least five times without any remarkable reduction in the catalytic efficiency (Fig. S7c).

4. Conclusions

In summary, we demonstrated a biomass-derived TEMPO-oxidized cellulose nanocrystal as a structure directing agent to synthesize intricate Pd-based bimetallic nanostructures which exhibited competent electrocatalytic activity. Firstly, the spherical Au NPs of diameter, 15 ± 2 nm were formed on the TCNC which served as seed for the subsequent petal-like epitaxial growth of Pd resulted in the formation of flower-shaped Au@Pd nanostructures of size, 32 ± 2 nm. Our results revealed that the presence of -OH rich TCNC pursue a key role in the systematic evolution of nanoparticle morphology. The -OH groups in the TCNC that are not bound to the Au seed surface further serve as the binding sites for Pd nanoclusters (NCs). Consequently, the TCNC promoted the coalescence of cluster-like Pd NPs to a certain size and stabilize them against further agglomeration. Furthermore, a heterogeneous catalyst was designed by adorning TCNC-Au@Pd on NH₂-RGO nanosheets and successfully demonstrated in ORR and 4-NP reduction reactions. Comparison of the electrocatalytic activity with citrate capped Au@Pd nanostructures revealed that TCNC-Au@Pd/NH₂-RGO system exhibited enhanced ORR catalytic behavior. Our study could pave way for further research on the potential use of green sustainable nanocellulose as a benign, shape-regulating agent in the realm of nanochemistry for the development of bio-sourced fuel cell components, however more research is underway.

Declaration of competing interest

The authors do not declare any competing financial interest.

CRedit authorship contribution statement

Hasna M. Abdul Hakkeem: Investigation, Formal analysis, Data curation, Writing – original draft. **Aswathy Babu:** Investigation, Data curation, Writing – review & editing. **Nagaraju Shilpa:** Investigation, Formal analysis, Writing – review & editing. **Adithya A. Venugopal:** Methodology, Writing – review & editing. **A.P. Mohamed:** Formal analysis, Data curation. **Sreekumar Kurungot:** Conceptualization, Methodology, Data curation, Writing – review & editing, Supervision. **Saju Pillai:** Conceptualization, Methodology, Data curation, Writing – review & editing, Supervision.

Data availability

No data was used for the research described in the article.

Acknowledgments

We thank Mr. Kiran Mohan (CSIR-NIIST) for TEM image acquisitions. Financial support from the UGC and KSCSTE for this research is greatly appreciated. This research was supported by DST project [DST/TMD/MES/2K17/17(G)/1].

Appendix A. Supplementary data

The Supporting Information related to this article can be found in the online version. AFM micrograph, DLS spectra, FTIR spectra and WAXS pattern of TCNC; TEM images of TCNC-Au NPs seed; Zeta-potential values of TCNC-Au@Pd NFs with different Pd shell thickness; TEM image of TCNC-Au NPs seed at low magnification; UV-Visible absorption spectra of TCNC-Au@Pd NFs (Pd-200) suspension at different time durations; Deconvoluted XPS spectra of Au(0) 4f of TCNC-Au NPs and TSC-Au NPs for BE comparison purpose; FTIR spectrum of TCNC and TCNC-Au@Pd NFs; UV-Vis absorption spectra of 4-NP reduction catalyzed with varying shell thickness of TCNC-Au@Pd NFs/NH₂-RGO, comparison with different control and standard catalysts in same

amount and at same time interval and recyclability of TCNC-Au@Pd NFs/NH₂-RGO for 4-NP reduction; Table consists of an overview of different catalysts for 4-NP reduction with rate constants. Supplementary data to this article can be found online at doi:<https://doi.org/10.1016/j.carbpol.2022.119723>.

References

- Abdelgawad, A. M., El-Naggar, M. E., Elsherbiny, D. A., Ali, S., Abdel-Aziz, M. S., & Abdel-Monem, Y. K. (2020). Antibacterial carrageenan/cellulose nanocrystal system loaded with silver nanoparticles, prepared via solid-state technique. *Journal of Environmental Chemical Engineering*, 8(5), Article 104276.
- Aslam, U., Chavez, S., & Linic, S. (2017). Controlling energy flow in multimetallic nanostructures for plasmonic catalysis. *Nature Nanotechnology*, 12(10), 1000.
- Azizi, S., Ahmad, M. B. H., Hussein, M. Z., & Ibrahim, N. A. (2013). Synthesis, antibacterial and thermal studies of cellulose nanocrystal stabilized ZnO-ag heterostructure nanoparticles. *Molecules*, 18(6), 6269–6280.
- Burda, C., Chen, X., Narayanan, R., & El-Sayed, M. A. (2005). Chemistry and properties of nanocrystals of different shapes. *Chemical Reviews*, 105(4), 1025–1102.
- Caporali, S., Muniz-Miranda, F., Pedone, A., & Muniz-Miranda, M. (2019). SERS, XPS and DFT study of xanthine adsorbed on citrate-stabilized gold nanoparticles. *Sensors*, 19(12), 2700.
- Chen, H., Li, Y., Zhang, F., Zhang, G., & Fan, X. (2011). Graphene supported au-pd bimetallic nanoparticles with core-shell structures and superior peroxidase-like activities. *Journal of Materials Chemistry*, 21(44), 17658–17661.
- Chen, X., Cai, Z., Chen, X., & Oyama, M. (2014). Au-Pd bimetallic nanoparticles decorated on graphene nanosheets: Their green synthesis, growth mechanism and high catalytic ability in 4-nitrophenol reduction. *Journal of Materials Chemistry A*, 2(16), 5668–5674.
- Cirtiu, C. M., Dunlop-Briere, A. F., & Moores, A. (2011). Cellulose nanocrystallites as an efficient support for nanoparticles of palladium: Application for catalytic hydrogenation and heck coupling under mild conditions. *Green Chemistry*, 13(2), 288–291.
- Cortie, M. B., & McDonagh, A. M. (2011). Synthesis and optical properties of hybrid and alloy plasmonic nanoparticles. *Chemical Reviews*, 111(6), 3713–3735.
- Darabdhara, G., Amin, M. A., Mersal, G. A., Ahmed, E. M., Das, M. R., Zakaria, M. B., & Szunert, S. (2015). Reduced graphene oxide nanosheets decorated with au, pd and Au-Pd bimetallic nanoparticles as highly efficient catalysts for electrochemical hydrogen generation. *Journal of Materials Chemistry A*, 3(40), 20254–20266.
- Das, S. K., Mohanty, B., Sahu, S. C., Chakraborty, B., Basu, S., & Jena, B. K. (2020). The experimental and theoretical insights on the interaction of AuPd bimetallic nanoentities on graphene: A study on electrocatalytic activity towards oxygen reduction reaction. *Electrochimica Acta*, 356, Article 136820.
- Eisa, W. H., Abdelgawad, A. M., & Rojas, O. J. (2018). Solid-state synthesis of metal nanoparticles supported on cellulose nanocrystals and their catalytic activity. *ACS Sustainable Chemistry & Engineering*, 6(3), 3974–3983.
- Fan, F.-R., Liu, D.-Y., Wu, Y.-F., Duan, S., Xie, Z.-X., Jiang, Z.-Y., & Tian, Z.-Q. (2008). Epitaxial growth of heterogeneous metal nanocrystals: From gold nano-octahedra to palladium and silver nanocubes. *Journal of the American Chemical Society*, 130(22), 6949–6951.
- Fang, P.-P., Duan, S., Lin, X.-D., Anema, J. R., Li, J.-F., Buriez, O., & Ren, B. (2011). Tailoring au-core pd-shell pt-cluster nanoparticles for enhanced electrocatalytic activity. *Chemical Science*, 2(3), 531–539.
- Farea, M., Abdelghany, A., & Oraby, A. (2020). Optical and dielectric characteristics of polyethylene oxide/sodium alginate-modified gold nanocomposites. *RSC Advances*, 10(62), 37621–37630.
- Ferrando, R., Jellinek, J., & Johnston, R. L. (2008). Nanoalloys: From theory to applications of alloy clusters and nanoparticles. *Chemical Reviews*, 108(3), 845–910.
- Hakkeem, H. M. A., Babu, A., Pal, S. K., Mohamed, A. P., Ghosh, S. K., & Pillai, S. (2021). Cellulose nanocrystals directed in-situ assembly of Au@ ag nanostructures with multifunctional activities. *Microchemical Journal*, 168, Article 106393.
- Han, J., Zhou, Z., Yin, Y., Luo, X., Li, J., Zhang, H., & Yang, B. (2012). One-pot, seedless synthesis of flowerlike Au-Pd bimetallic nanoparticles with core-shell-like structure via sodium citrate coreduction of metal ions. *CrystEngComm*, 14(20), 7036–7042.
- Howes, P. D., Rana, S., & Stevens, M. M. (2014). Plasmonic nanomaterials for diagnostics. *Chemical Society Reviews*, 43(11), 3835–3853.
- Jiang, F., & Hsieh, Y.-L. (2014). Synthesis of cellulose nanofibril bound silver nanoprisms for surface enhanced raman scattering. *Biomacromolecules*, 15(10), 3608–3616.
- Kauranen, M., & Zayats, A. V. (2012). Nonlinear plasmonics. *Nature Photonics*, 6(11), 737–748.
- Kaushik, M., Basu, K., Benoit, C., Cirtiu, C. M., Vali, H., & Moores, A. (2015). Cellulose nanocrystals as chiral inducers: Enantioselective catalysis and transmission electron microscopy 3D characterization. *Journal of the American Chemical Society*, 137(19), 6124–6127.
- Kaushik, M., & Moores, A. (2016). Nanocelluloses as versatile supports for metal nanoparticles and their applications in catalysis. *Green Chemistry*, 18(3), 622–637.
- Kelly, C. H., Benedetti, T. M., Alinezhad, A., Schuhmann, W., Gooding, J. J., & Tilley, R. D. (2018). Understanding the effect of au in Au-Pd bimetallic nanocrystals on the electrocatalysis of the methanol oxidation reaction. *The Journal of Physical Chemistry C*, 122(38), 21718–21723.
- Lai, L., Chen, L., Zhan, D., Sun, L., Liu, J., Lim, S. H., & Lin, J. (2011). One-step synthesis of NH₂-graphene from in situ graphene-oxide reduction and its improved electrochemical properties. *Carbon*, 49(10), 3250–3257.

- Lee, Y. W., Kim, N. H., Lee, K. Y., Kwon, K., Kim, M., & Han, S. W. (2008). Synthesis and characterization of flower-shaped porous Au–Pd alloy nanoparticles. *The Journal of Physical Chemistry C*, 112(17), 6717–6722.
- Lim, B., Jiang, M., Yu, T., Camargo, P. H., & Xia, Y. (2010). Nucleation and growth mechanisms for Pd–Pt bimetallic nanodendrites and their electrocatalytic properties. *Nano Research*, 3(2), 69–80.
- Lin, X.-X., Zhang, X.-F., Wang, A.-J., Fang, K.-M., Yuan, J., & Feng, J.-J. (2017). Simple one-pot aqueous synthesis of AuPd alloy nanocrystals/reduced graphene oxide as highly efficient and stable electrocatalyst for oxygen reduction and hydrogen evolution reactions. *Journal of Colloid and Interface Science*, 499, 128–137.
- Lu, C.-L., Prasad, K. S., Wu, H.-L., Ho, J.-A. A., & Huang, M. H. (2010). Au nanocube-directed fabrication of Au–Pd core–shell nanocrystals with tetrahedral, concave octahedral, and octahedral structures and their electrocatalytic activity. *Journal of the American Chemical Society*, 132(41), 14546–14553.
- Marx, S., & Baiker, A. (2009). Beneficial interaction of gold and palladium in bimetallic catalysts for the selective oxidation of benzyl alcohol. *The Journal of Physical Chemistry C*, 113(15), 6191–6201.
- Menumerov, E., Hughes, R. A., & Neretina, S. (2016). Catalytic reduction of 4-nitrophenol: A quantitative assessment of the role of dissolved oxygen in determining the induction time. *Nano Letters*, 16(12), 7791–7797.
- Nabeela, K., Thomas, R. T., Mohamed, A., & Pillai, S. (2020). Nanocellulose-silver ensembles for ultrasensitive SERS: An investigation on the role of nanocellulose fibers in the generation of high-density hotspots. *Applied Materials Today*, 20, Article 100672.
- Navae, A., & Salimi, A. (2015). Efficient amine functionalization of graphene oxide through the bucherer reaction: An extraordinary metal-free electrocatalyst for the oxygen reduction reaction. *RSC Advances*, 5(74), 59874–59880.
- Pan, W., Zhang, X., Ma, H., & Zhang, J. (2008). Electrochemical synthesis, voltammetric behavior, and electrocatalytic activity of Pd nanoparticles. *The Journal of Physical Chemistry C*, 112(7), 2456–2461.
- Park, J.-W., & Shumaker-Parry, J. S. (2014). Structural study of citrate layers on gold nanoparticles: Role of intermolecular interactions in stabilizing nanoparticles. *Journal of the American Chemical Society*, 136(5), 1907–1921.
- Purwidyantri, A., Karina, M., Hsu, C.-H., Srikanth, Y., Prabowo, B. A., & Lai, C.-S. (2020). Facile bacterial cellulose nanofibrillation for the development of a plasmonic paper sensor. *ACS Biomaterials Science & Engineering*, 6(5), 3122–3131.
- Ragab, H., & Rajeh, A. (2020). Structural, thermal, optical and conductive properties of PAM/PVA polymer composite doped with Ag nanoparticles for electrochemical application. *Journal of Materials Science: Materials in Electronics*, 31(19), 16780–16792.
- Ren, L., Yang, L., Yu, P., Wang, Y., & Mao, L. (2013). Electrochemical post-treatment of infinite coordination polymers: An effective route to preparation of Pd nanoparticles supported onto carbon nanotubes with enhanced electrocatalytic activity toward ethanol oxidation. *ACS Applied Materials & Interfaces*, 5(21), 11471–11478.
- Rezayat, M., Blundell, R. K., Camp, J. E., Walsh, D. A., & Thielemans, W. (2014). Green one-step synthesis of catalytically active palladium nanoparticles supported on cellulose nanocrystals. *ACS Sustainable Chemistry & Engineering*, 2(5), 1241–1250.
- Rodríguez-Lorenzo, L., de La Rica, R., Álvarez-Puebla, R. A., Liz-Marzán, L. M., & Stevens, M. M. (2012). Plasmonic nanosensors with inverse sensitivity by means of enzyme-guided crystal growth. *Nature Materials*, 11(7), 604–607.
- Sadri, R., Hosseini, M., Kazi, S., Bagheri, S., Zubir, N., Solangi, K., & Badarudin, A. (2017). A bio-based, facile approach for the preparation of covalently functionalized carbon nanotubes aqueous suspensions and their potential as heat transfer fluids. *Journal of Colloid and Interface Science*, 504, 115–123.
- Scott, R. W., Wilson, O. M., Oh, S.-K., Kenik, E. A., & Crooks, R. M. (2004). Bimetallic palladium–gold dendrimer-encapsulated catalysts. *Journal of the American Chemical Society*, 126(47), 15583–15591.
- Shin, Y., Bae, I.-T., Arey, B. W., & Exarhos, G. J. (2008). Facile stabilization of gold-silver alloy nanoparticles on cellulose nanocrystal. *The Journal of Physical Chemistry C*, 112(13), 4844–4848.
- Sun, Y., Wu, Q., & Shi, G. (2011). Graphene based new energy materials. *Energy & Environmental Science*, 4(4), 1113–1132.
- Thomas, B., Raj, M. C., Joy, J., Moores, A., Drisko, G. L., & Sanchez, C. M. (2018). Nanocellulose, a versatile green platform: From biosources to materials and their applications. *Chemical Reviews*, 118(24), 11575–11625.
- Thompson, D. T. (2004). Catalysis by gold/platinum group metals. *Platinum Metals Review*, 48, 169–172.
- Wang, B., Ran, M., Fang, G., Wu, T., Tian, Q., Zheng, L., & Ni, Y. (2020). Palladium nanocatalyst supported on cationic nanocellulose–alginate hydrogel for effective catalytic reactions. *Cellulose*, 27, 6995–7008.
- Wang, D., Xin, H. L., Yu, Y., Wang, H., Rus, E., Muller, D. A., & Abruna, H. D. (2010). Pt-decorated PdCo@Pd/C core–shell nanoparticles with enhanced stability and electrocatalytic activity for the oxygen reduction reaction. *Journal of the American Chemical Society*, 132(50), 17664–17666.
- Wang, M., Ma, Z., Li, R., Tang, B., Bao, X.-Q., Zhang, Z., & Wang, X. (2017). Novel flower-like PdAu (Cu) anchoring on a 3D rGO-CNT sandwich-stacked framework for highly efficient methanol and ethanol electro-oxidation. *Electrochimica Acta*, 227, 330–344.
- Wu, X., Lu, C., Zhang, W., Yuan, G., Xiong, R., & Zhang, X. (2013). A novel reagentless approach for synthesizing cellulose nanocrystal-supported palladium nanoparticles with enhanced catalytic performance. *Journal of Materials Chemistry A*, 1(30), 8645–8652.
- Xiong, Y., Yang, Y., DiSalvo, F. J., & Abruna, H. C. D. (2018). Pt-decorated composition-tunable Pd–Fe@Pd/C core–shell nanoparticles with enhanced electrocatalytic activity toward the oxygen reduction reaction. *Journal of the American Chemical Society*, 140(23), 7248–7255.
- Xu, C., Chen, W., Gao, H., Xie, X., & Chen, Y. (2020). Cellulose nanocrystal/silver (CNC/Ag) thin-film nanocomposite nanofiltration membranes with multifunctional properties. *Environmental Science: Nano*, 7(3), 803–816.
- Xu, J., Wilson, A. R., Rathmell, A. R., Howe, J., Chi, M., & Wiley, B. J. (2011). Synthesis and catalytic properties of Au–Pd nanoflowers. *ACS Nano*, 5(8), 6119–6127.
- Xue, Q., Bai, J., Han, C., Chen, P., Jiang, J.-X., & Chen, Y. (2018). Au nanowires@Pd-polyethylenimine nanohybrids as highly active and methanol-tolerant electrocatalysts toward oxygen reduction reaction in alkaline media. *ACS Catalysis*, 8(12), 11287–11295.
- Yang, C.-W., Chanda, K., Lin, P.-H., Wang, Y.-N., Liao, C.-W., & Huang, M. H. (2011). Fabrication of Au–Pd core–shell heterostructures with systematic shape evolution using octahedral nanocrystal cores and their catalytic activity. *Journal of the American Chemical Society*, 133(49), 19993–20000.
- Yang, C., Qing, C., Wang, Q., Zhang, X., Lou, J., & Liu, Y. (2020). Synthesis of the hybrid CdS/Au flower-like nanomaterials and their SERS application. *Sensors and Actuators B: Chemical*, 304, Article 127218.
- Yuan, T., Zeng, J., Wang, B., Cheng, Z., Gao, W., Xu, J., & Chen, K. (2021). Silver nanoparticles immobilized on cellulose nanofibrils for starch-based nanocomposites with high antibacterial, biocompatible, and mechanical properties. *Cellulose*, 28(2), 855–869.
- Zhang, L., Lu, H., Chu, J., Ma, J., Fan, Y., Wang, Z., & Ni, Y. (2020). Lignin-directed control of silver nanoparticles with tunable size in porous lignocellulose hydrogels and their application in catalytic reduction. *ACS Sustainable Chemistry & Engineering*, 8(33), 12655–12663.
- Zhang, L., Zhang, J., Kuang, Q., Xie, S., Jiang, Z., Xie, Z., & Zheng, L. (2011). Cu²⁺-assisted synthesis of hexoctahedral Au–Pd alloy nanocrystals with high-index facets. *Journal of the American Chemical Society*, 133(43), 17114–17117.
- Zhou, Y., Saito, T., Bergström, L., & Isogai, A. (2018). Acid-free preparation of cellulose nanocrystals by TEMPO oxidation and subsequent cavitation. *Biomacromolecules*, 19(2), 633–639.

High-Performance Au Nanorods as SERS Substrates for Environmental Monitoring Facilitated by the Organizing Power of Nanocellulose from Agave Palm Leaves, a Bio-Waste

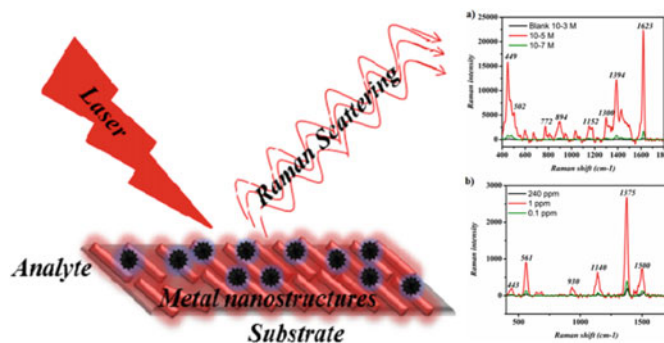
Hasna M. Abdul Hakkeem, Aswathy Babu, and Saju Pillai

Abstract

In search of a biocompatible and sustainable platform for surface-enhanced Raman scattering (SERS) studies, nanorods with a high aspect ratio of coinage metals such as gold, silver, and copper augment the peak intensity, but the shelf life of metal nanoparticles is questionable. Here, we report the synthetic strategy of parallelly aligned nanorods achieved by the synergetic action of carboxyl-functionalized nanocellulose fibers (TNCF) and cetyl trimethyl ammonium bromide (CTAB) as both reducing and capping agents. The synthesized parallel nanorods shows excellent SERS enhancement down to 10^{-7} M concentration of methylene blue and 0.1 ppm of thiram (pesticide). Additionally, TEMPO-oxidized nanocellulose fibers-supported nanorods colloid showed excellent shelf life. Our approach using TEMPO-oxidized nanocellulose fibers-supported Au nanorods can be considered an efficient and reproducible surface-enhanced Raman scattering substrate environmental monitoring.

Keywords

TEMPO-oxidized nanocellulose fiber • Au nanorods • Surface-enhanced Raman scattering (SERS) • Pesticide



Highlights

- We developed nanorods of gold of about 50 nm size supported with TEMPO-oxidized nanocellulose.
- The synthesized colloid of Au nanorods exhibited excellent Raman signal enhancement due to numerous hotspot generation.
- We demonstrated ultra-trace detection of analyte methylene blue up to 10^{-7} M and pesticide thiram up to 0.1 ppm with Au/TNCF nanorods as the solid-state substrate.

1 Introduction

Surface-enhanced Raman scattering (SERS) is an ingenious extension of plasmon resonance theory of metallic nanostructures (Betz et al. 2014; Fateixa et al. 2015; Ouyang et al. 2017). SERS becomes prominent by the sponsorship of coinage metals. These metals (Au, Ag, Cu) can be tailored into nano-dimensions with exhilarating light-reflecting properties, and that is an excellent platform for catalytic, drug delivery, bio-imaging, sensing, energy harvesting, etc. (Eo et al. 2013; Dharmatti et al. 2014; Chauhan et al. 2018; Song et al. 2015; Zhang et al. 2019; Maaza et al. 2005; Kana Kana et al. 2010; Dakka et al. 2000; Vijaya et al. 2017; Shah et al. 2018; Aisida

H. M. Abdul Hakkeem · A. Babu · S. Pillai (✉)
Materials Science and Technology Division, CSIR-National
Institute for Interdisciplinary Science and Technology (NIIST),
Thiruvananthapuram, Kerala 695019, India
e-mail: pillai_saju@niist.res.in

H. M. Abdul Hakkeem · S. Pillai
Academy of Scientific and Innovative Research (AcSIR),
Ghaziabad, 201002, India

et al. 2019). In which, SERS is a most conceivable technique that allows the detection of analytes in trace amounts enabled by the augmentation of electromagnetic fields created by the excitation conduction electrons (Jiang et al. 2018; Wu et al. 2015). The current world is passing through a merciless way of business, even in the food industry. Nowadays, the daily diet contains many toxic chemicals in addition to nutrients that are even capable of causing human death. These poisons are masked by nicknames such as food preservatives, adulterants, coloring agents, flavoring agents, acidity regulators, stabilizers, herbicides, and pesticides, with different codes and hides under ambrosial food items. These ominous chemicals may contain aflatoxins that are carcinogens. There are varieties of purposes to ensure the safety of food in different countries. The accuracy and precision of these analysis results decide whether these products are permitted or not. There are several methods such as liquid chromatography–mass spectrometry (LC–MS) (Jemal 2000), high-performance liquid chromatography (HPLC) (Neue and El Fallah 1997), gas chromatography–mass spectrometry (GC–MS) (Hübschmann 2015), enzyme-linked immunosorbent assays (ELISAs) (Crowther 1995), LC-MS/MS (Jemal 2000), and GC–MS/MS (Alder et al. 2006). However, these tandem techniques are expensive, arduous, and lower detection limits. Nevertheless, these chemicals tolerant levels are in ppm. Therefore, SERS is a new modest and efficient technique that detects analytes even in aM concentration, which is an interesting task for the research world, and several new ideas in sensing are published recently (Nabeela et al. 2016).

One of the crucial obstacles is the complexity in the fabrication of anisotropic metal nanostructures with high chemical stability and sensitivity. Of these metals, Ag plays a crucial role in most of the next-generation plasmonic technologies with the hurdle of instability due to fast sulfuration and oxidation (Rycenga et al. 2011). However, Au NPs are comparably chemically inert and biocompatible (Hu et al. 2006). Aforementioned, complexity in the tailoring of metal nanostructures is a severe dilemma. Morphology of metal nanostructures can be tuned by using capping agents such as CTAB (Rodríguez-Fernández et al. 2005; Chen et al. 2003; Moon et al. 2009), CTAC (Nezhad et al. 2008; Yoo and Jang 2013), PVP (Liu et al. 2010; Pastoriza-Santos and Liz-Marzán 2002), etc., that will fabricate particular nanostructures like rods (Sau and Murphy 2004; Qiu et al. 2010; Chang et al. 2005), prisms (Millstone et al. 2006; Lee et al. 2014), cubes (Skrabalak et al. 2007; Ma et al. 2010), and disks (Hong et al. 2011) by preferably attaching on specific crystal planes and suppress growth in that specific direction. For example, PVP adsorbs at {100} crystal plane, whereas citrate at {111} plane in the synthesis of nanostructures (Nabeela et al. 2016; Koczkur et al. 2015; Ji et al. 2007). Apart from this truncating property, the shelf life of metal nanostructures is still questionable. Au nanorods are

extensively utilized in SERS for both bio-sensing and environmental monitoring (Liu et al. 2018; Ou et al. 2018). Dimensions of nanoparticles, alignment, and aggregation were proven to have better SERS sensitivity. Au nanorods exhibit two plasmon bands known as longitudinal and transverse, sensitive to the aspect ratios of nanorods.

Xu et al. published a paper recently about enriching Au nanorods induced by the ultrasonic aggregation for bio-sensing (Xu et al. 2020). Peng et al. demonstrated the self-assembly of vertically aligned Au nanorods for the SERS detection of food contaminants (Peng et al. 2013). Martin et al. compared the enhancement in SERS by parallel and perpendicular aligned nanorods (Martin et al. 2014).

Here is the pivotal attraction of nanocellulose to create a complete network by hydrogen bonds that prevent aggregation of nanoparticles. Nanocellulose-mediated synthesis of metal nanoparticles is a burgeoning field and gained great attention due to its capability to design innocuous synthesis routes and unprecedented stability of metal nanoparticle colloids (Kaushik and Moores 2016). Many reports are dealing with metal NPs decorated nanocellulose fibers, and their applications were explored in catalysis (Chen et al. 2015; Eisa et al. 2018), hydrogels (Tang et al. 2018), antimicrobial research (Shi et al. 2015), SERS (Golmohammadi et al. 2017; Park et al. 2013), etc. TEMPO-oxidized nanocellulose is a sustainable bio-material that furnishes a platform for designing eye-catching anisotropic nanostructures metals by its inherent reducing and capping ability (Nabeela et al. 2016). Here, the carboxyl groups of TEMPO-oxidised nanocellulose acts as an anchoring site for the nanoparticles and fiber nature of nanocellulose fulfills the role of a complete capping agent, which imparts unpredictable stability. Only a few reports explored the nanocellulose-mediated synthesis of nanoparticles. However, Au nanorods synthesis with nanocellulose has not been explored.

In the present work, we have developed TEMPO-oxidized nanocellulose (TNCF) derived from agave palm leaves as a sustainable matrix for the growth of stable Au nanorods. This finding is novel in aspect that there is no other report regarding the highly reproducible method for preparing parallel Au nanorods supported by TNCF. Synthesised nanocellulose-supported noble metal nanoparticles competitive assay were used to establish the ultra-trace detection of analytes (methylene blue and thiram) enabled by SERS.

2 Experimental Section

2.1 Materials

Agave palm leaves were used for TNCF extraction. TEMPO (2,2,6,6-tetramethylpiperidine-1-oxyl) (99%), sodium bromide (99%), sodium hypochlorite (5% active chlorine), gold

(III) chloride trihydrate (99%), cetyl trimethyl ammonium bromide (CTAB), L-ascorbic acid, methylene blue, and thiram were bought from Sigma–Aldrich. All other chemicals used were analytical grade such as sodium hydroxide, hydrochloric acid, and acetic acid. All chemicals were used without further purification, as they were provided. Ultrapure 18.2 M resistivity deionized (DI) water was used throughout the synthesis.

3 Materials and Methods

3.1 Preparation of Nanocellulose

Pretreatment of crushed agave palm leaves generally proceeds with an aqueous alkali hydroxide, mostly sodium hydroxide treatment. Ten grams of crushed agave palm leaves was weighed accurately and soaked in 15 wt% NaOH. The mixture was stirred for 4 h. Bleaching of mercerized fiber was done by mixing with 1.7 wt% sodium chlorite at 150 °C at pH 4. The substance was collected, filtered, thoroughly washed, dried, and desiccated (Nabeela et al. 2016; Lani et al. 2014). TEMPO-mediated oxidation was done with 1 g of hollow cellulose, 0.032 g of TEMPO, 0.32 g of NaBr, and 10 mL of NaClO, and 290 ml DI water was well stirred at pH 10–11 using NaOH throughout the reaction, followed by 1-h ultra-sonication. After a one-hour reaction, it was quenched, washed, freeze-dried, and desiccated for further use (Saito et al. 2007; Isogai et al. 2011).

3.2 Synthesis of TNCF-Supported Au Nanorods

TNCF-supported Au nanorods were synthesized by using the synergic effect of TNCF, CTAB, and ascorbic acid. In brief, 250 ml mixture containing 0.25 wt.% well-dispersed TNCF, 9 g CTAB, 1 mM H₂AuCl₄, 0.06 M ascorbic acid, and Au seed solution of 3 nm was taken in a beaker and undisturbed overnight. The prepared gold nanoparticles were cooled and stored at 4 °C for further studies.

3.3 SERS Studies

Different concentrations of methylene blue (10^{-3} , 10^{-5} , and 10^{-7} M) and thiram (240, 1, and 0.1 ppm) were prepared and mixed with previously synthesized Au nanorods in a 1:3 ratio, and about 10 μ l of the solution was dropped in a pre-cleaned glass slide and dried in a vacuum. Glass slides for SERS studies were cleaned by sonicating washed glass slides in ethanol and acetone for 10 min, followed by cleaning by ozonizer for further 10 min. All the SERS studies are done only in solid state.

4 Results and Discussion

Nanocellulose fibers were isolated by TEMPO oxidation from the agave palm leaves accompanied by ultra-sonication. Apart from the FTIR spectra of holo-cellulose, there is an intense peak at 1606 cm^{-1} in the TEMPO-oxidized nanocellulose reflecting C=O stretching. This suggests that C-6 hydroxyl groups of D-glucose units were converted to carboxyl groups successfully (Nabeela et al. 2016). X-ray diffraction is a universal technique to investigate the crystal structure of cellulosic samples. Cellulose structure is not purely crystalline due to the presence of disordered (amorphous) domains. WAXS analysis of purified holo-cellulose and TNCF is presented in Fig. 1b. After the holo-cellulose was oxidized by TEMPO/NaBr/NaClO, a significant changes in the crystallinity indices and crystal size were not observed. These studies indicate that the COO-

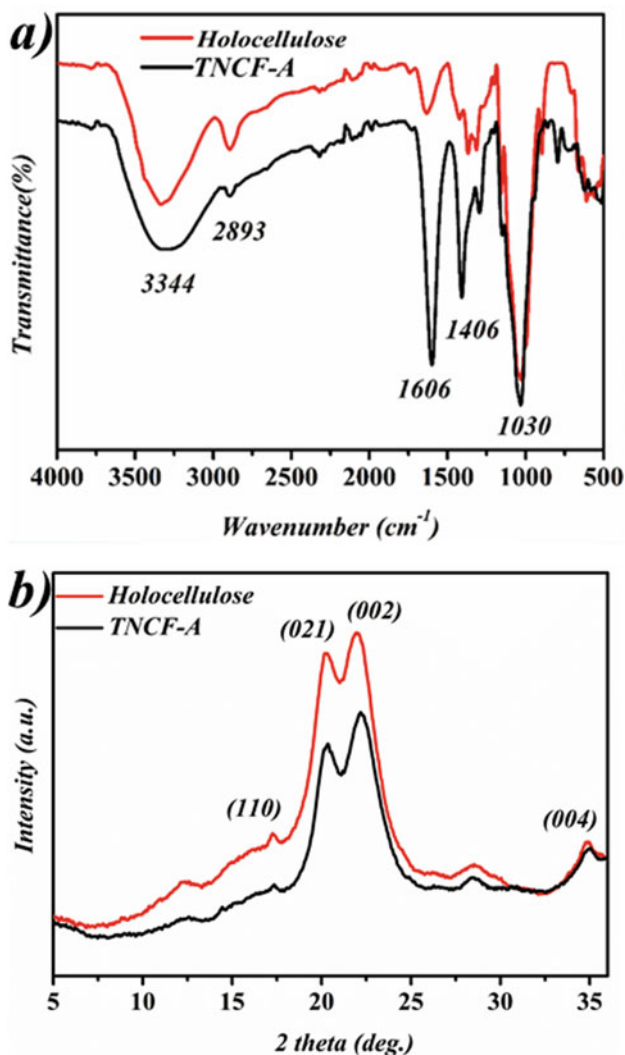


Fig. 1 a FTIR spectra and b WAXS pattern of holo-cellulose and TEMPO-oxidized nanocellulose

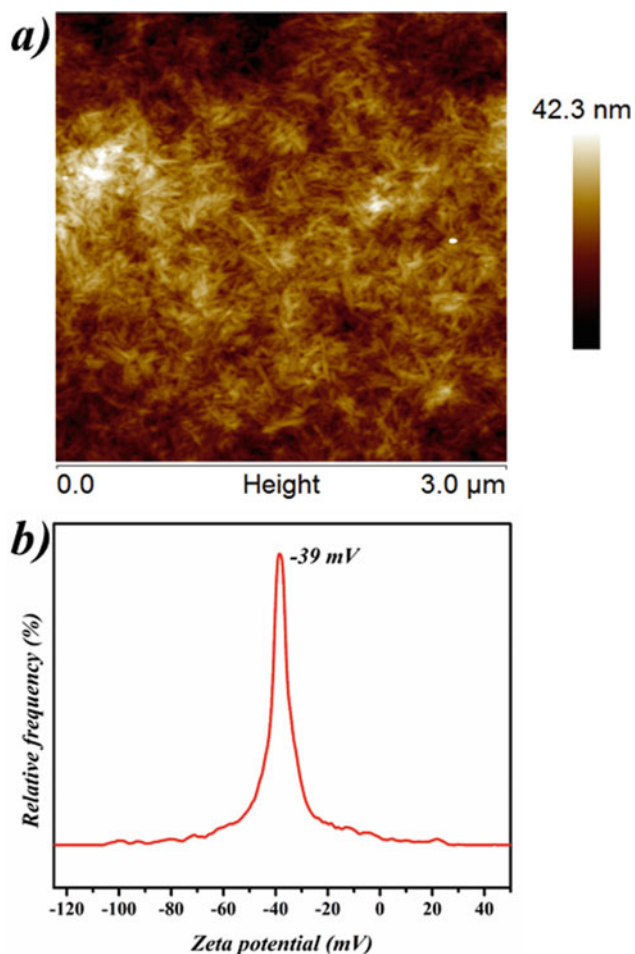


Fig. 2 a AFM images and b zeta potential of nanocellulose

groups are generated by the TEMPO-catalyzed oxidation and are selectively present in the cellulose microfibril surface without any change in the internal structure crystallite of cellulose (Isogai et al. 2011).

AFM did the morphological characterization of TNCF. AFM images of TEMPO-oxidized nanocellulose from agave palm leaves are shown in Fig. 2a. Dimensions of nanofiber has a wide range of distribution, but most of the rod-like nanofibers' size lies within the range 150 ± 50 nm length and 15 ± 5 nm width as confirmed. The stability of nanocellulose fibers was studied using zeta-potential measurements. The zeta-potential value of TEMPO-oxidized nanocellulose fiber obtained was -39.0 mV, confirming the high stability of nanocellulose.

UV-visible absorption spectroscopy is employed to investigate the optical properties of Au nanorods supported by TEMPO-oxidized nanocellulose fibers (Fig. 3a). It has been well understood that the shape, size, and composition of nanostructures confide the position and nature of the surface resonance peak, and all these factors ultimately affect the enhancement of the Raman signal in SERS. The UV-

visible spectrum shows SPR peaks of Au nanorods consist of two absorptions bands at 540 and 780 nm corresponding to transverse and longitudinal modes. By considering cost-effectiveness, simplicity in the synthesis, and plasmonic properties, Ag nanoparticles are preferable, but biocompatibility and low toxicity made Au nanoparticles chosen in this work (Vijaya et al. 2017; Shah et al. 2018; Aisida et al. 2019).

Figure 3b shows representative bright-field TEM images of Au nanorods of about 50 nm length and 15 nm width with parallel arrangements imparted by the organizing power of nanocellulose. The surface carboxyl groups donated this astral organizing power of TNCF to facilitate the hotspot generation. Au nanorods' SERS efficiency was studied by employing methylene blue (MB) as the model analyte molecule. Characteristic peaks at 449 and 502 cm^{-1} are correlated with the skeletal deformation mode C-N-C of methylene blue. Peaks perceived at 772 and 1152 cm^{-1} correspond to C-H's in-plane bending mode, while the peak at 1300 cm^{-1} attributed the C-H in-plane ring deformation mode. C-N symmetrical stretching and C-C ring stretching generate peaks at 1394 and 1623 cm^{-1} , respectively, which are prominent in the case of Raman spectra of methylene blue (Nabeela et al. 2016; Li et al. 2016).

Scheme 1 demonstrates the schematic model of SERS sensitivity studies by employing TNCF-supported Au nanorods as substrate. As shown in Fig. 4a, it is obvious that the Raman bands of methylene blue obtained from the blank solution (without Au nanorod substrate) of concentration 10^{-3} M were fragile. Additionally, the SERS spectra of methylene blue at concentration 10^{-5} and 10^{-7} M were also studied. Due to the high SERS enhancement efficiency of Au nanorods, the Raman intensity is thousand times increased in 10^{-5} and 10^{-7} M methylene blue and the characteristic Raman peaks are also prominent. These results indicate that the methylene blue molecules were adsorbed on the Au nanorods, hence experiencing a tremendous electromagnetic field.

Our substrate's reproducibility and social applicability are evaluated by selecting thiram, the pesticide used in an agricultural area with a 2 ppm tolerance level. The characteristic peaks of thiram at 561 cm^{-1} are reflected in the S-S stretch. Stretching vibrational mode of CH_3N is observed at 930 cm^{-1} , while that of C-N stretch and CH_3 rock is at 1300 cm^{-1} . Intense peaks around 1375 and 1500 cm^{-1} are dedicated to C-N symmetrical stretching and CH_3 deformation, respectively (Chen et al. 2016; Shizhuang et al. 2014). The Raman signal enhancement of a pesticide, thiram, was also studied using SERS in solid state. The SERS spectra of thiram at different concentrations (240, 1, and 0.1 ppm) are shown in Fig. 4b in which 240 ppm is blank (without Au nanorods). TNCF-supported Au nanorods are used as substrate to detect thiram beyond its tolerance level,

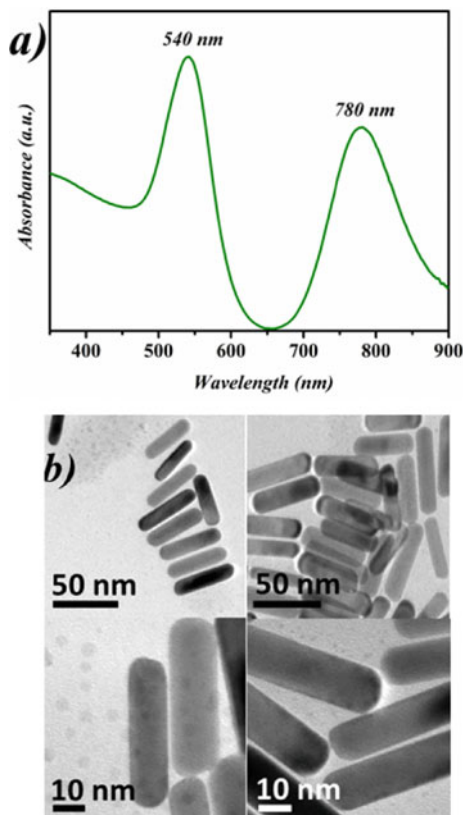


Fig. 3 a UV-visible absorption spectra and b TEM micrographs of TNCF-A-supported Au nanorods

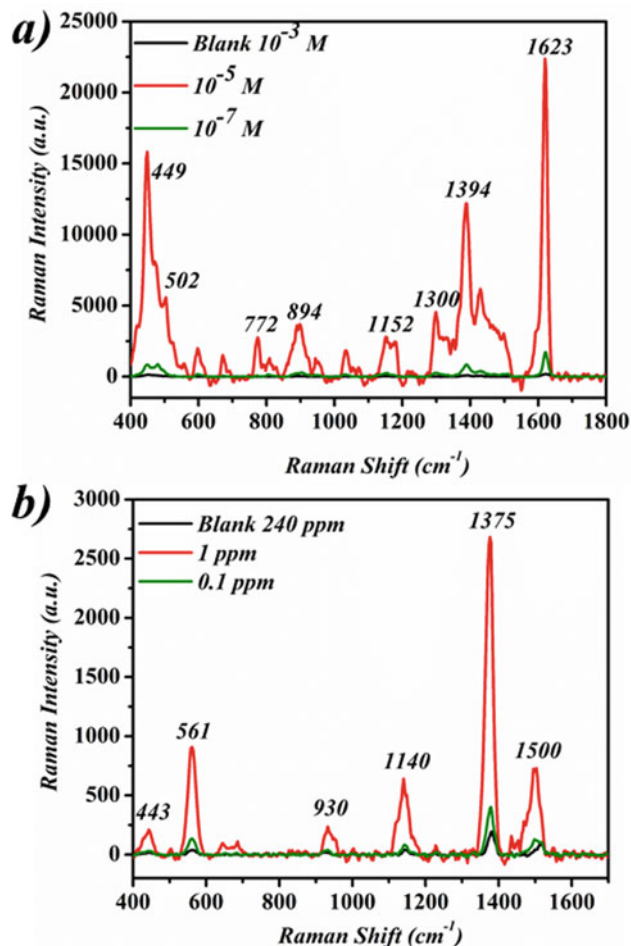
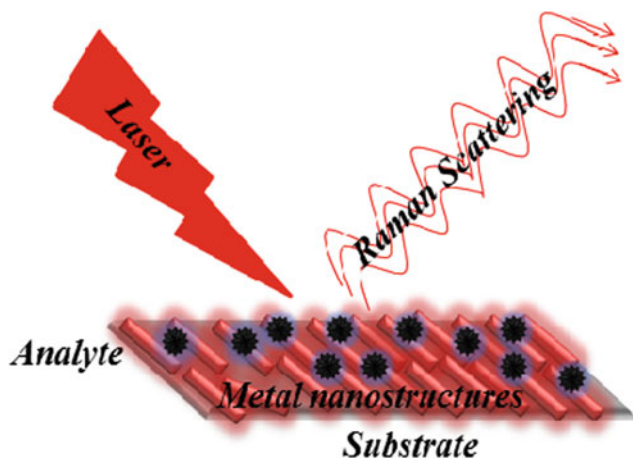


Fig. 4 SERS spectra of a methylene blue and b thiram



Scheme 1 Schematics of SERS-assisted sample detection by using Au nanorods

signifying its applicability in the environmental monitoring and food safety sectors. Multi-detection of multi-contaminants through SERS by using our substrate is also possible since every molecule had different Raman signals. We attained a lower detection limit (LOD) 10^{-7} M, 0.1 ppm for methylene blue and thiram, respectively, with an

analytical enhancement factor (AEF) computed based on the specific equation.

$$AEF = (I_{SERS}/I_{RAMAN})(C_{RAMAN}/C_{SERS})$$

where I_{SERS} is the intensity of SERS at concentration C_{SERS} obtained in metal nanoparticles' presence as a substrate, while I_{RAMAN} and C_{RAMAN} are in the absence of nanoparticle substrate (Li et al. 2016; Wei and Vikesland 2015). Focused on MB's intense peak at 1623 cm^{-1} and thiram at 1375 cm^{-1} , AEF for TNCF-supported Au nanorods was estimated to be 1.2×10^4 and 3.1×10^3 , respectively. A plot for comparing the SERS intensity versus concentration of MB and thiram was also given (Fig. 5), which enlightened our substrate's key role in SERS enhancement. The unusual SERS enhancement in MB's case can be attributed to the ionic interaction between cationic MB and negatively charged Au nanorods. Besides, when two Au nanorods are aligned parallel, their transverse plasmon oscillations couple each other, resulted in the maximum

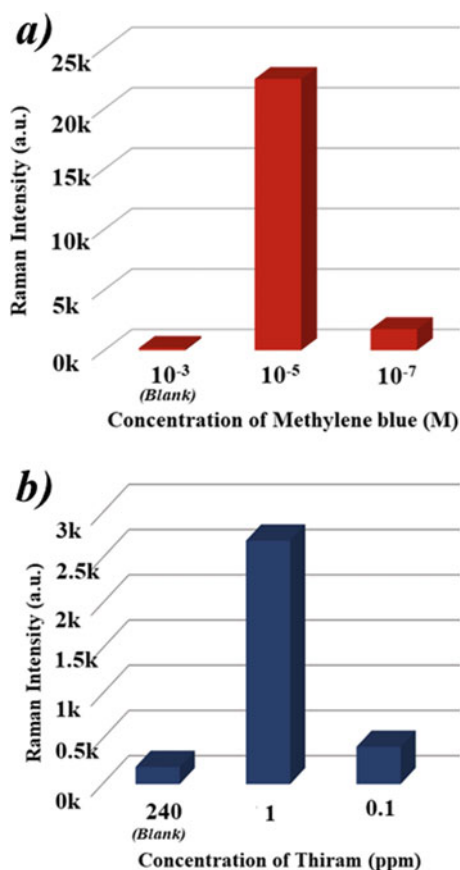


Fig. 5 Bar diagram of signal intensity of most intense peak versus concentration of methylene blue (peak at 1623 cm^{-1}) and thiram (peak at 1375 cm^{-1})

electromagnetic field in the vicinity of analytes molecules (Kumar and Thomas 2011).

5 Conclusion

We demonstrated a simple synthetic strategy for the Au nanorods derived from sustainable TNCF. Here, we have studied the role of nanocellulose as an anchoring site for the growth of Au nanorods and tailored into parallelly arranged Au nanorods for the easiness of hotspot generation. The optical and morphology of Au nanorods were successfully analyzed. Further, Au nanorods as SERS platform were used to demonstrate ultra-trace detection of analyte molecules (dye and pesticide). Modified Au nanorods aqueous colloid showed excellent Raman signal enhancement ascribed by Au and Ag's localized surface resonance action. Ultra-trace detections of methylene blue (up to 10^{-7} M) as a model analyte and pesticide thiram (up to 0.1 ppm) in solid state were demonstrated.

Acknowledgements The authors wish to thank AcSIR, UGC, and KSCSTE-PDF for funding.

References

- S.O. Aisida, K. Ugwu, P.A. Akpa, A.C. Nwanya, P.M. Ejikeme, S. Botha, I. Ahmad, M. Maaza, Biogenic synthesis and antibacterial activity of controlled silver nanoparticles using an extract of *Gongronema Latifolium*. *Chem. Phys.* **237**, 121859 (2019)
- L. Alder, K. Greulich, G. Kempe, B. Vieth, Residue analysis of 500 high priority pesticides: better by GC-MS or LC-MS/MS? *Mass Spectrom. Rev.* **25**, 838–865 (2006)
- J.F. Betz, W.Y. Wei, Y. Cheng, I.M. White, G.W. Rubloff, Simple SERS substrates: powerful, portable, and full of potential. *Phys. Chem. Chem. Phys.* **16**, 2224–2239 (2014)
- J.-Y. Chang, H. Wu, H. Chen, Y.-C. Ling, W. Tan, Oriented assembly of Au nanorods using biorecognition system. *Chem. Commun.* 1092–1094 (2005)
- D.S. Chauhan, P. Arunkumar, R. Prasad, S.K. Mishra, B.P.K. Reddy, A. De et al., Facile synthesis of plasmonic zein nanoshells for imaging-guided photothermal cancer therapy. *Mater. Sci. Eng. C* **90**, 539–548 (2018)
- F. Chen, G.-Q. Xu, T.A. Hor, Preparation and assembly of colloidal gold nanoparticles in CTAB-stabilized reverse microemulsion. *Mater. Lett.* **57**, 3282–3286 (2003)
- M. Chen, H. Kang, Y. Gong, J. Guo, H. Zhang, R. Liu, Bacterial cellulose supported gold nanoparticles with excellent catalytic properties. *ACS Appl. Mater. Interfaces* **7**, 21717–21726 (2015)
- J. Chen, Y. Huang, P. Kannan, L. Zhang, Z. Lin, J. Zhang et al., Flexible and adhesive surface enhance Raman scattering active tape for rapid detection of pesticide residues in fruits and vegetables. *Anal. Chem.* **88**, 2149–2155 (2016)
- J.R. Crowther, *ELISA: Theory and Practice*, vol. 42 (Springer Science & Business Media, 1995)
- A. Dakka, J. Lafait, C. Sella, S. Berthier, M. Abd-Lefdil, J.C. Martin, M. Maaza, Optical properties of Ag-TiO₂ nano-cermet films prepared by co-sputtering and multilayer deposition techniques. *Appl. Opt.* **39**(16), 2745–2753 (2000)
- R. Dharmatti, C. Phadke, A. Mewada, M. Thakur, S. Pandey, M. Sharon, Biogenic gold nano-triangles: cargos for anticancer drug delivery. *Mater. Sci. Eng. C* **44**, 92–98 (2014)
- W.H. Eisa, A.M. Abdelgawad, O.J. Rojas, Solid-state synthesis of metal nanoparticles supported on cellulose nanocrystals and their catalytic activity. *ACS Sustain. Chem. Eng.* **6**, 3974–3983 (2018)
- M. Eo, J. Baek, H.D. Song, S. Lee, J. Yi, Quantification of electron transfer rates of different facets on single gold nanoparticles during catalytic reactions. *Chem. Commun.* **49**, 5204–5206 (2013)
- S. Fateixa, H.I. Nogueira, T. Trindade, Hybrid nanostructures for SERS: materials development and chemical detection. *Phys. Chem. Chem. Phys.* **17**, 21046–21071 (2015)
- H. Golmohammadi, E. Morales-Narvaez, T. Naghdi, A. Merkoci, Nanocellulose in sensing and biosensing. *Chem. Mater.* **29**, 5426–5446 (2017)
- S. Hong, Y. Choi, S. Park, Shape control of Ag shell growth on Au nanodisks. *Chem. Mater.* **23**, 5375–5378 (2011)
- M. Hu, J. Chen, Z.-Y. Li, L. Au, G.V. Hartland, X. Li et al., Gold nanostructures: engineering their plasmonic properties for biomedical applications. *Chem. Soc. Rev.* **35**, 1084–1094 (2006)
- H.-J. Hübschmann, *Handbook of GC-MS: Fundamentals and Applications* (Wiley, 2015)

- A. Isogai, T. Saito, H. Fukuzumi, TEMPO-oxidized cellulose nanofibers. *Nanoscale* **3**, 71–85 (2011)
- M. Jemal, High-throughput quantitative bioanalysis by LC/MS/MS. *Biomed. Chromatogr.* **14**, 422–429 (2000)
- X. Ji, X. Song, J. Li, Y. Bai, W. Yang, X. Peng, Size control of gold nanocrystals in citrate reduction: the third role of citrate. *J. Am. Chem. Soc.* **129**, 13939–13948 (2007)
- T. Jiang, X. Wang, J. Tang, S. Tang, Seed-mediated synthesis of floriated Ag nanoplates as surface-enhanced Raman scattering substrate for in situ molecular detections. *Mater. Res. Bull.* **97**, 201–206 (2018)
- J.B. Kana Kana, J.M. Ndjaka, B.D. Ngom, N. Manyala, O. Nemraoui, A.Y. Fasasi, R. Nemitudi, A. Gibaud, D. Knoesen, M. Maaza, Thermochromic nanocrystalline Au-VO₂ composite thin films prepared by radiofrequency inverted cylindrical magnetron sputtering. *Thin Solid Films* **518**(6), 1641–1647 (2010)
- M. Kaushik, A. Moores, Review: nano-celluloses as versatile supports for metal nanoparticles and their applications in catalysis. *Green Chem.* **18**, 622–637 (2016)
- K.M. Koczur, S. Mourdikoudis, L. Polavarapu, S.E. Skrabalak, Polyvinylpyrrolidone (PVP) in nanoparticle synthesis. *Dalton Trans.* **44**, 17883–17905 (2015)
- J. Kumar, K.G. Thomas, Surface-enhanced Raman spectroscopy: investigations at the nanorod edges and dimer junctions. *J. Phys. Chem. Lett.* **2**, 610–615 (2011)
- N. Lani, N. Ngadi, A. Johari, M. Jusoh, Isolation, characterization, and application of nano-cellulose from oil palm empty fruit bunch fiber as nanocomposites. *J. Nanomater.* **2014** (2014)
- K.E. Lee, A.V. Hesketh, T.L. Kelly, Chemical stability and degradation mechanisms of triangular Ag, Ag@Au, and Au nano-prisms. *Phys. Chem. Chem. Phys.* **16**, 12407–12414 (2014)
- C. Li, Y. Huang, K. Lai, B.A. Rasco, Y. Fan, Analysis of trace methylene blue in fish muscles using ultra-sensitive surface-enhanced Raman spectroscopy. *Food Control* **65**, 99–105 (2016)
- H. Liu, P. Hou, W. Zhang, J. Wu, Synthesis of monosized core-shell Fe₃O₄/Au multifunctional nanoparticles by PVP-assisted nanoemulsion process. *Colloids Surf. A* **356**, 21–27 (2010)
- C. Liu, C. Chen, S. Li, H. Dong, W. Dai, T. Xu, Y. Liu, F. Yang, X. Zhang, Target-triggered catalytic hairpin assembly-induced core-satellite nanostructures for high-sensitive “off-to-on” SERS detection of intracellular microRNA. *Anal. Chem.* **90**, 10591–10599 (2018)
- Y. Ma, W. Li, E.C. Cho, Z. Li, T. Yu, J. Zeng et al., Au@Ag core-shell nanocubes with finely tuned and well-controlled sizes, shell thicknesses, and optical properties. *ACS Nano* **4**, 6725–6734 (2010)
- M. Maaza, O. Nemraoui, C. Sella, A.C. Beye, Surface plasmon resonance tunability in Au-VO₂ thermochromic nanocomposites. *Gold Bull.* **38**(3), 100–106 (2005)
- A. Martín, A. Pescagliani, C. Schopf, V. Scardaci, R. Coull, L. Byrne, D. Iacopino, Surface-enhanced Raman scattering of 4-aminobenzenethiol on au nanorod ordered arrays. *J. Phys. Chem. C* **118**, 13260–13267 (2014)
- J.E. Millstone, G.S. Métraux, C.A. Mirkin, Controlling the edge length of gold nano-prisms via a seed-mediated approach. *Adv. Funct. Mater.* **16**, 1209–1214 (2006)
- S.Y. Moon, T. Kusunose, T. Sekino, CTAB-assisted synthesis of size- and shape-controlled gold nanoparticles in SDS aqueous solution. *Mater. Lett.* **63**, 2038–2040 (2009)
- K. Nabeela, R.T. Thomas, J.B. Nair, K.K. Maiti, K.G.K. Warriar, S. Pillai, TEMPO-oxidized nano-cellulose fiber-directed stable aqueous suspension of plasmonic flower-like silver nano-constructs for ultra-trace detection of analytes. *ACS Appl. Mater. Interfaces* **8**, 29242–29251 (2016)
- U.D. Neue, M.Z. El Fallah, *HPLC Columns: Theory, Technology, and Practice*, vol. 415 (Wiley-VCH New York, 1997)
- M.R.H. Nezhad, M. Alimohammadi, J. Tashkhourian, S.M. Razavian, Optical detection of phenolic compounds based on the surface plasmon resonance band of Au nanoparticles. *Spectrochim. Acta Part A Mol. Biomol. Spectrosc.* **71**, 199–203 (2008)
- Y. Ou, X. Wang, K. Lai, Y. Huang, B.A. Rasco, Y. Fan, Gold nanorods as surface-enhanced Raman spectroscopy substrates for rapid and sensitive analysis of Allura red and sunset yellow in beverages. *J. Agric. Food Chem.* **66**, 2954–2961 (2018)
- L. Ouyang, W. Ren, L. Zhu, J. Irudayaraj, Prosperity to challenges: recent approaches in SERS substrate fabrication. *Rev. Anal. Chem.* **36** (2017)
- M. Park, H. Chang, D.H. Jeong, J. Hyun, Spatial deformation of nano-cellulose hydrogel enhances SERS. *BioChip J.* **7**, 234–241 (2013)
- I. Pastoriza-Santos, L.M. Liz-Marzán, Formation of PVP-protected metal nanoparticles in DMF. *Langmuir* **18**, 2888–2894 (2002)
- B. Peng, G. Li, D. Li, S. Dodson, Q. Zhang, J. Zhang, Y.H. Lee, H.V. Demir, X.Y. Ling, Q. Xiong, Vertically aligned gold nanorod monolayer on arbitrary substrates: self-assembly and femtomolar detection of food contaminants. *ACS Nano* **7**, 5993–6000 (2013)
- Y. Qiu, Y. Liu, L. Wang, L. Xu, R. Bai, Y. Ji et al., Surface chemistry and aspect ratio mediated cellular uptake of Au nanorods. *Biomaterials* **31**, 7606–7619 (2010)
- J. Rodríguez-Fernández, J. Perez-Juste, P. Mulvaney, L.M. Liz-Marzán, Spatially-directed oxidation of gold nanoparticles by Au (III)–CTAB complexes. *J. Phys. Chem. B* **109**, 14257–14261 (2005)
- M. Rycenga, C.M. Cobley, J. Zeng, W. Li, C.H. Moran, Q. Zhang et al., Controlling the synthesis and assembly of silver nanostructures for plasmonic applications. *Chem. Rev.* **111**, 3669–3712 (2011)
- T. Saito, S. Kimura, Y. Nishiyama, A. Isogai, Cellulose nanofibers prepared by TEMPO-mediated oxidation of native cellulose. *Biomacromolecules* **8**, 2485–2491 (2007)
- T.K. Sau, C.J. Murphy, Seeded high yield synthesis of short Au nanorods in aqueous solution. *Langmuir* **20**, 6414–6420 (2004)
- A. Shah, G. Lutfullah, K. Ahmad, A.T. Khalil, M. Maaza, *Daphne mucronata*-mediated photosynthesis of silver nanoparticles and their novel biological applications, compatibility, and toxicity studies. *Green Chem. Lett. Rev.* **11**(3), 318–333 (2018)
- Z. Shi, J. Tang, L. Chen, C. Yan, S. Tanvir, W.A. Anderson et al., Enhanced colloidal stability and antibacterial performance of silver nanoparticles/cellulose nanocrystal hybrids. *J. Mater. Chem. B* **3**, 603–611 (2015)
- W. Shizhuang, C. Sheng, L. Miao, Z. Xinhua, Z. Shouguo, Z. Jian et al., Quantitative analysis of thiram based on SERS and PLSR combined with wavenumber selection. *Anal. Methods* **6**, 242–247 (2014)
- S.E. Skrabalak, L. Au, X. Li, Y. Xia, Facile synthesis of Ag nanocubes and Au nanocages. *Nat. Protoc.* **2**, 2182 (2007)
- C. Song, N. Zhou, B. Yang, Y. Yang, L. Wang, Facile synthesis of hydrangea flower-like hierarchical gold nanostructures with tunable surface topographies for single-particle surface-enhanced Raman scattering. *Nanoscale* **7**, 17004–17011 (2015)
- L. Tang, F. Tang, M. Li, L. Li, Facile synthesis of Ag@AgCl-contained cellulose hydrogels and their application. *Colloids Surf. A* **553**, 618–623 (2018)
- J.J. Vijaya, N. Jayaprakash, K. Kombaiyah, K. Kaviyarasu, L. J. Kennedy, M. Maaza, Bioreduction potentials of dried root of *Zingiber officinale* for simple green synthesis of silver nanoparticles: antibacterial studies. *J. Photochem. Photobiol. B Biol.* **177**, 62–68 (2017)

- H. Wei, P.J. Vikesland, pH-triggered molecular alignment for reproducible SERS detection via an AuNP/nano-cellulose platform. *Sci. Rep.* **5**, 1–10 (2015)
- W. Wu, L. Liu, Z. Dai, J. Liu, S. Yang, L. Zhou et al., Low-cost, disposable, flexible and highly reproducible screen printed SERS substrates for the detection of various chemicals. *Sci. Rep.* **5**, 10208 (2015)
- T. Xu, Y. Luo, C. Liu, X. Zhang, S. Wang, Integrated ultrasonic aggregation-induced enrichment with Raman enhancement for ultrasensitive and rapid biosensing. *Anal. Chem.* **99**(11), 7816–7821 (2020)
- H. Yoo, M.H. Jang, Size-controlled synthesis of gold bipyramids using an aqueous mixture of CTAC and salicylate anions as the soft template. *Nanoscale* **5**, 6708–6712 (2013)
- B. Zhang, W. Li, M. Nogi, C. Chen, Y. Yang, T. Sugahara, Alloying and embedding of Cu-core/Ag-shell nanowires for ultrastable stretchable and transparent electrodes. *ACS Appl. Mater. Interfaces* **11**, 18540–18547 (2019)